



# MASTERARBEIT / MASTER'S THESIS

Titel der Masterarbeit / Title of the Master's Thesis

„Laser-induced Photodissociation of Heteroleptic Transition  
Metal Complexes: A Theoretical Challenge“

verfasst von / submitted by

Anna Karina Bäck BA BA BSc

angestrebter akademischer Grad / in partial fulfilment of the requirements for the degree of  
Master of Science (MSc)

Wien, 2021 / Vienna, 2021

Studienkennzahl lt. Studienblatt /  
degree programme code as it appears on  
the student record sheet:

A 066 862

Studienrichtung lt. Studienblatt /  
degree programme as it appears on  
the student record sheet:

Masterstudium Chemie

Betreut von / Supervisor:

Dr. Philipp Marquetand, Privatdoz.



To strive, to seek, to find, and not to yield

---

*Observation Hill, McMurdo Station, Antarctica*  
*Lord Alfred Tennyson, "Ulysses"*

# Abstract

Transition metal complexes are promising photoactivatable candidates for the controlled delivery of either carbon monoxide (CO) or nitric oxide (NO) to biological targets. Both gaseous molecules have important messenger and cytoprotective functions in the human body such that a controlled delivery to target tissue via transition metal complexes could be harnessed in biomedical research for in-vitro and in-vivo studies. Within this framework, the present thesis is part of a collaborative research project tackling the challenge of finding selective pathways to dissociate either messenger molecule from the coordination sphere of heteroleptic transition metal complexes in a controlled manner upon photoactivation. For this purpose, two molybdenum complexes, the neutral dicarbonyl- $\eta^5$ cyclopentadienylnitrosylmolybdenum(I) ( $[\text{CpMo}(\text{CO})_2(\text{NO})]$ ) and the cationic dicarbonylnitrosyl-1,4,7-triisopropyl-1,4,7-triazacyclononanemolybdenum(I) ( $[\text{Mo}(\text{CO})_2(\text{NO})(\text{iPr}_3\text{tacn})]^+$ ) complex, are studied with regard to their charge transfer composition and photodissociation capabilities. More specifically, analysis of excited states within the Franck-Condon region reveals that low-energy excitation predominantly leads to target-oriented charge transfer towards the NO-ligand for both complexes which provides opportunity to further explore NO-dissociative reaction pathways. Experimentally measured infrared spectra however show that both complexes most likely release one or two CO-ligands after continuous UV-irradiation of several minutes. Since not all signals have been assigned without ambiguity, these spectra serve as basis for a comprehensive photoproduct exploration conducted in this thesis to determine whether NO-dissociation is observed at all. Lastly, the photodissociation behaviour of both complexes is further explored in one-dimensional potential energy scans to determine selective dissociation-pathways for both ligands. For this end, different multi-reference methods are evaluated with respect to their performance and disadvantages for the simulation of both dissociation reactions at the same time. This discussion shows that the theoretical exploration of selective ligand dissociations is delicate and highly dependent on the approximations used along the way to make the calculations feasible. Lastly, a new type of ligand for the application of selective photo-induced CO/NO-dissociation is proposed in this thesis. The advantages of this ligand are highlighted and preliminary calculations exploring the dissociation capabilities when bound to a cobalt metal precursor equipped with one equivalent CO and NO are discussed.

# Kurzfassung

Übergangsmetallkomplexe sind vielversprechende photoaktivierbare Kandidaten für die kontrollierte Abgabe von entweder Kohlenmonoxid (CO) oder Stickstoffmonoxid (NO) an biologische Zellbereiche. Beide gasförmigen Moleküle haben wichtige Boten- und Zytoprotektionsfunktionen im menschlichen Körper, sodass eine kontrollierte Abgabe an das Zielgewebe in der biomedizinischen Forschung für in-vitro- und in-vivo-Studien genutzt werden kann. In diesem Rahmen ist die vorliegende Abschlussarbeit als Beitrag eines Verbundforschungsprojekts zu sehen, das sich mit der Herausforderung befasst, selektive Wege eines der beiden Botenstoffe aus der Koordinationssphäre von Übergangsmetallkomplexen auf kontrollierte Weise nach Photoaktivierung abzuspalten. Zu diesem Zweck werden zwei Molybdänkomplexe, der neutrale dicarbonyl- $\eta^5$ cyclopentadienylnitrosylmolybdenum(I) ( $[\text{CpMo}(\text{CO})_2(\text{NO})]$ ) und der kationische dicarbonylnitrosyl-1,4,7-triisopropyl-1,4,7-triazacyclononanemolybdenum(I) ( $[\text{Mo}(\text{CO})_2(\text{NO})(\text{iPr}_3\text{tacn})]^+$ ) Komplex, hinsichtlich ihrer Ladungsübertragungszusammensetzung und ihrer Photodissoziationsfähigkeit untersucht. Insbesondere zeigt die Analyse angeregter Zustände in der Franck-Condon-Region, dass eine Anregung mit niedriger Energie für beide Komplexe vorwiegend zu einem zielorientierten Ladungstransfer zum NO-Liganden führt, was die Möglichkeit bietet, NO-dissoziative Reaktionswege weiter zu untersuchen. Experimentell gemessene Infrarotspektren zeigen jedoch, dass beide Komplexe höchstwahrscheinlich einen oder zwei CO-Liganden nach kontinuierlicher UV-Bestrahlung von mehreren Minuten freisetzen. Da nicht alle Signale eindeutig zugeordnet wurden, dienen diese Spektren als Grundlage für eine umfassende Untersuchung möglicher Photoprodukte, die in dieser Arbeit durchgeführt wird, um festzustellen, ob überhaupt eine NO-Dissoziation beobachtet wird. Schließlich wird das Photodissoziationsverhalten beider Komplexe in eindimensionalen Potentialenergiescans weiter untersucht, um selektive Dissoziationswege für beide Liganden zu bestimmen. Zu diesem Zweck werden verschiedene Multi-Referenzmethoden hinsichtlich ihrer Leistung und Nachteile für die gleichzeitige Simulation beider Dissoziationsreaktionen erprobt. Diese Diskussion zeigt, dass die theoretische Untersuchung selektiver Ligandendissoziationen schwierig ist und stark von den Näherungen abhängt, die erforderlich sind, um die Berechnungen überhaupt erst durchführen zu können. Schließlich schlägt die vorliegende Arbeit einen neuen Ligandentyp für die Anwendung der selektiven photoinduzierten CO/NO-Dissoziation vor. Die Vorteile dieses Liganden werden gezeigt und vorläufige Berechnungen zur Untersuchung der Dissoziationsfähigkeit bei der Bindung des Liganden an ein Kobaltzentrum, das mit einem Äquivalent CO und NO jeweils ausgestattet ist, werden diskutiert.

# Acknowledgements

I have a ton of people to thank not only for this thesis, but for my experiences in the last couple of years that veraciously shaped my life. First of all, I want to thank my long-term supervisor Priv.-Doz. Dr. Philipp Marquetand for taking me on as one of his Master students and supporting, encouraging and advising me throughout this time. Next, I want to thank Univ.-Prof. Dr. Dr. h.c. Leticia González for giving me many learning opportunities in the past and for being a true inspiration for so many years. Thank you both for all the time and knowledge you share with your students. The internships in the González group were certainly the highlights of my Bachelor and Master study and I am grateful for these experiences. While I have still a long way ahead of me, I feel well equipped and above all motivated for what lies ahead. Furthermore, I want to thank Prof. Dr. Patrick Nürnberger, Niklas Gessner BSc MSc, Prof. Dr. Ulrich Schatzschneider and Dr. Patrick (actually Jan!) Zobel for all the meetings and discussions on this exciting topic.

I also want to thank all members of the González research group. Dr. Boris Maryasin is the one I need to mention first. You were a supervisor to me early on and encouraged me in times I really needed support, thank you for that. Next, I want to thank Dr. Sebastian Mai for all the information I was able to absorb around you and for the scripting advice even on a Saturday (sorry Katrin...!). Equally important is Dr. Leon Freitag. Thank you for converting me to DMRG and for your annoyance of any process that cannot be automated by a script. Very amusing at times but I get it now. Space is limited, so to all former and current members of the González group which I got to know in the past years, I thank you.

Most importantly, I want to thank my family and friends for being firmly in my corner. My life companions and sisters Julia Bäck BA BSc, Christina Bäck BA MA and Mag. Katharina Bäck deserve my biggest appreciation. No matter how dark life gets, no mountain is too high for you, or in our case the A2 too long. I will never be able to express how thankful I am for your unconditional support. I also need to thank my roommate Sophie Haselsteiner, my fellow Kolar-fan Stefan Glatzl and my Yoga buddies Lukás and Jem Mamet. While it is safe to say that we are pretty far from being Zen, life gets really complicated balancing all seven chakras, the right coffee-to-sleep ratio and parallel-ish parking (and lately a global pandemic with an ever-extended lockdown period that transforms any home to a prison cell). So, I thank you for struggling with me. I know that none of you will ever bother to read anything below this chapter. Therefore, this goes directly to you so that you can stop reading sooner than you've thought and way passed you've hoped: I cannot wait to celebrate this thesis with you at Café Paris (when it opens again) with nothing else but San Franciscos and us tossing the small umbrellas while losing the big, discovering true magic and an app without phone uniting us again (inside

jokes). At last, Mag. Johannes Breger BA, the love of my life, you shall be mentioned as well. You introduced me to the world of science, instigated and accompanied me to so many countries and showed me what true companionship looks like for the greater part of a decade. Without you, I would not be on my way to become a scientist. You will never be forgotten and I wish you would be here to share this important moment with me.

My deepest gratitude also goes to Thomas Sigmund M.A., Wilfred Wimmer and Dr. Magdalena Kujawa. As my bosses in the past, you helped me keeping me afloat and accommodated me with the right work shifts that helped me navigate student obligations and work while allowing me to catch much-needed breath in many different travel periods during off-season. Working part-time while studying full-time is hands-down just hard and I will never forget the role you played in helping me realize my dream. Thank you.

# Acronyms

**1TDM** one-electron transition density matrix.

**AO** atomic orbital.

**B3LYP** Becke three-parameter exchange and LeeYangParr correlation.

**BDE** bond dissociation energy.

**BOA** Born-Oppenheimer approximation.

**CASPT2** second-order complete active space perturbation theory.

**CASSCF** complete active space self-consistent field.

**CDS** cavity-dispersion solvent-structure.

**CI** configuration interaction.

**CONORM** CO-NO-releasing molecule.

**CORM** CO-releasing molecule.

**CPCM** conductor-like polarizable continuum model.

**D3(BJ)** dispersion correction with the Becke-Johnson damping scheme.

**DFT** density functional theory.

**DMRG** density matrix renormalization group.

**ECP** effective core potential.

**GTO** Gaussian-type orbitals.

**HF** Hartree-Fock.

**HOMO** highest occupied molecular orbital.

**hybrid GGA** hybrid generalized-gradient approximation.

**IC** internal conversion.

## *Acronyms*

- IPEA** ionization potential and electron affinity.
- ISC** intersystem crossing.
- LCAO** linear combination of atomic orbitals.
- LUMO** lowest unoccupied molecular orbital.
- MCH** molecular coulomb Hamiltonian.
- MCSCF** multi-configurational self-consistent field.
- MO** molecular orbital.
- MPS** matrix product state.
- MS-CASPT2** multi-state CASPT2.
- NAC** non-adiabatic coupling.
- NORM** NO-releasing molecule.
- NTO** natural transition orbitals.
- PES** potential energy surface.
- RDM** reduced density matrix.
- SA-CASSCF** state-averaged CASSCF.
- SCF** self-consistent field.
- SOC** spin-orbit coupling.
- SS-CASSCF** state-specific CASSCF.
- TD-DFT** time-dependent density functional theory.
- TDA** Tamm-Dancoff approximation.
- TDSE** time-dependent Schrödinger equation.
- TISE** time-independent Schrödinger equation.
- TMC** transition metal complex.

# Contents

<b>1. Introduction</b>	<b>1</b>
<b>2. Theoretical Background and Methodology</b>	<b>4</b>
2.1. Fundamental Quantum Mechanics and Methods of Approximation . . . . .	4
2.1.1. The Schrödinger Equation . . . . .	4
2.1.2. The Born-Oppenheimer Approximation . . . . .	6
2.1.3. MCH, Diagonal and Diabatic State Representation . . . . .	7
2.1.4. Electronic Structure Methods . . . . .	8
2.2. Quantitative Wave Function and Electron Density Analysis . . . . .	24
2.3. Density Matrix Renormalization Group Algorithm . . . . .	26
<b>3. Computational Details</b>	<b>30</b>
<b>4. Results and Discussion</b>	<b>33</b>
4.1. Vertical Excitation and Charge Transfer Analysis . . . . .	33
4.1.1. Geometry Optimization and Structural Peculiarities . . . . .	33
4.1.2. UV/Vis Absorption Spectra . . . . .	35
4.1.3. Qualitative Wave Function Analysis . . . . .	38
4.1.4. Quantitative Charge Transfer Analysis . . . . .	40
4.2. Exploration of Potential Photodissociation Products . . . . .	47
4.2.1. FTIR Spectroscopic Analysis of CpMo and TacnMo . . . . .	47
4.2.2. Simulated IR-Spectra of Potential Photoproducts . . . . .	49
4.3. Photodissociation Behaviour of CpMo . . . . .	54
4.3.1. The Active Space Challenge . . . . .	54
4.3.2. Triplets States and Spin-orbit Couplings . . . . .	63
4.4. Photodissociation Behaviour of TacnMo . . . . .	70
4.5. DabCo: A New PhotoCONORM Proposed . . . . .	75
<b>5. Conclusion</b>	<b>81</b>
<b>Bibliography</b>	<b>84</b>
<b>A. Appendices</b>	<b>91</b>

# 1. Introduction

A research topic gaining traction in recent years is the development of strategies for the controlled photo-induced release of biologically active small molecules such as carbon monoxide (CO) and nitric oxide (NO). Both molecules have important messenger functions in the human body and exhibit cytoprotective activity.<sup>[1,2]</sup> In order to exploit these qualities for either therapeutic applications such as photo-dynamic therapy in cancer treatment<sup>[3]</sup> or to investigate control mechanisms of biological activity within tissue cells,<sup>[4]</sup> it is imperative to develop efficient molecular systems equipped with CO and/or NO capable of releasing either or both messenger molecules as a safe-to-handle, in-situ source. Hence, key for the development of such molecules is the dissociation mechanism upon activation that must be selective and controlled in order to cause no harm when applied in a biomedical environment. Although some metal-free organic compounds have been developed for this context,<sup>[5]</sup> the majority of already investigated systems or systems currently in development are transition metal complexes (TMCs) which are commonly differentiated depending on the uncaged molecule and the trigger mechanism initiating the release. For instance, CO-releasing molecules (CORMs) upon enzyme-triggered activation are termed ET-CORMs, upon ligand exchange reactions are called LE-CORMs and upon photoactivation are named photo-CORMs. In analogy, NO-releasing molecules (NORMs) are classified as ET-NORMs, LE-NORMs, photo-NORMs, although these types of systems have so far not been as extensively studied as CORMs.<sup>[6-9]</sup> This thesis is part of an on-going research project developing and investigating potential selective dissociation pathways of heteroleptic photo-CO-NO-releasing molecules (photo-CONORMs) containing transition metals.

The development and investigation of these systems is certainly not an easy task and constitutes a challenge from three different perspectives. First, in order to utilize the molecular systems as prodrug within a biomedical context, air and water stability, solubility within a biological buffer and accumulation within the targeted area must be achieved which constitutes the synthetic challenge. For these hurdles, important features to target are functionalizability of ligands bound to the coordination center and a stable metal center that does not undergo rapid oxidation processes.<sup>[10]</sup> Secondly, activation must occur with spatial and temporal precision via for the system specially designed focused laser-pulses which thus summarizes the experimental spectroscopic challenge. In this regard, different pulsed radiation sources with the tunability to target electronic transitions selectively and with the ability to follow photochemical dynamics on nano-, pico- and also femtosecond time scale in real time are being explored.<sup>[11]</sup> Thirdly, the theoretical challenge constitutes accurate and feasible modeling of trigger mechanisms that initiate a controlled release from a metal center which accounts not only for relativistic heavy atom effects, but also for the electronic flexibility within the system. Generally,

## 1. Introduction

large molecules such as TMCs require approximations to computational methods so that accuracy is least affected and experimentally measured optical signals can be understood and interpreted. Methodological obstacles in this regard are not only relativistic effects of atoms of higher nuclear charge, but also a high density of low-lying electronic states, possible open-shell configurations and the inclusion of environmental effects.<sup>[12,13]</sup>

In an joint effort to address these issues, this thesis emerged from a collaboration of the group of Leticia González, University of Vienna, specializing in theoretical chemistry with an organic synthesis group under the lead of Ulrich Schatzschneider, University of Würzburg, and an experimental physical chemistry group specializing in ultrafast spectroscopy under the lead of Patrick Nürnberger, University of Regensburg. In experimental pre-studies<sup>[14]</sup> conducted in both experimental groups, two potential photo-CONORMs containing molybdenum were synthesized and analyzed regarding their capability of dissociating either CO or NO upon ultraviolet (UV) light irradiation. Both the neutral dicarbonyl- $\eta^5$ cyclopentadienylnitrosylmolybdenum(I) complex ( $[\text{CpMo}(\text{CO})_2(\text{NO})]$ ; in the following denoted as **CpMo**) and the cationic dicarbonylnitrosyl-1,4,7-triisopropyl-1,4,7-triazacyclononanemolybdenum(I) complex ( $[\text{Mo}(\text{CO})_2(\text{NO})(\text{iPr}_3\text{tacn})]^+$ ; in the following abbreviated as **TacnMo**) are depicted in Figure 1.1. One goal is to perform reference calculations to gain a deeper understanding of the experimentally determined ultraviolet–visible (UV-Vis) and infrared (IR) absorption spectra regarding the nature of the charge transfer and potential photodissociation products. Furthermore, potential energy scans were performed to investigate potential relaxation pathways after UV irradiation and to determine whether it is possible to dissociate NO from the coordination sphere of the molybdenum center. The larger objective of this project is to find a way to selectively dissociate CO and NO under different conditions ideally applicable within a biomedical context. For this reason, a close investigation of the potential energy landscape is essential to find potential routes. Particular attention was directed towards **CpMo**, which, due to

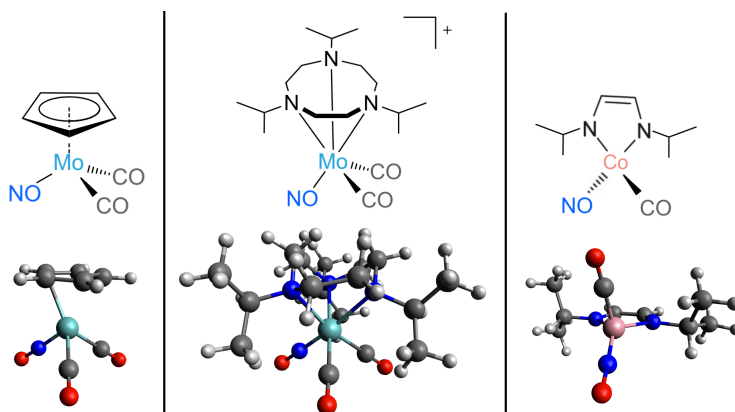


Figure 1.1.: Three in this thesis investigated potential photo-CONORMs, **CpMo** (*left*), **TacnMo** (*middle*), **DabCo** (*right*).

## 1. Introduction

the smaller system size compared to **TacnMo**, was deemed potentially suitable for dynamics calculations if an appropriate level of theory is found. Regarding the non-innocent NO-ligand, a potential photo-dissociation and photoisomerization of **CpMo** was explored, as well as a close examination of the incorporation of triplet states on the calculation outcome was performed.

Furthermore, during many discussions with both experimental groups, the importance of a small system size was emphasized, which is why I proposed a new and more versatile type of ligand to the project based on the knowledge gained from stationary calculations on both molybdenum complexes. Preliminary calculations were performed on one of many possible and already published<sup>[15]</sup> substructures of this ligand coordinated to a cobalt metal precursor, carbonyl-1,4-diazadiisopropyl-1,3-butadiene-nitrosylcobalt(II) ( $[(^i\text{PrNCH})_2\text{Co}(\text{NO})(\text{CO})]$ ), in the following referred to as **DabCo**.

The remainder of this thesis is organised as follows. First, key concepts of the theoretical and methodological background important for all calculations conducted in this thesis will be explained. Then, a summary of all computational parameters and methodologies will be given. The subsequent chapter presents the results and can be subdivided into two parts. In chapter 4.1 and 4.2, a detailed charge transfer analysis and possible photodissociation products will be discussed based on computations using single-reference methods. The remaining three chapters 4.3, 4.4 and 4.5 will deal with the photodissociation behaviour of each complex individually based on multi-reference calculations. Overall, this thesis will demonstrate that the simulation of ligand dissociations is delicate and highly dependent on the level of theory and the corresponding approximations along the way. Furthermore, it will be shown that a comparison to experimentally measured reference values, especially the bond dissociation energy (BDE), is desirable for the evaluation of the computational outcome. Moreover, two relatively new analysis schemes were employed to determine the charge transfer character of a multitude of excited states and to deduce an appropriate level of theory for the computation of potential energy surfaces during dissociation whose advantages and disadvantages will be emphasized throughout the discussion.

## 2. Theoretical Background and Methodology

In this chapter, the theoretical formalism of all methods employed in this thesis is described. In section 2.1, general quantum mechanical concepts and approximations used in theoretical chemistry are introduced. Sections 2.2 and 2.3 present the conceptual framework of two different algorithms utilized in the following, namely a quantitative wave function analysis tool and an automated active orbital space selection algorithm.

### 2.1. Fundamental Quantum Mechanics and Methods of Approximation

#### 2.1.1. The Schrödinger Equation

In quantum mechanics, the fundamental equation of motion is the time-dependent Schrödinger equation (TDSE), which describes the temporal evolution of any quantum mechanical system in a non-relativistic fashion. The equation reads as follows

$$\hat{\mathcal{H}}(\mathbf{R}, \mathbf{r}, t)|\Psi(\mathbf{R}, \mathbf{r}, t)\rangle = i\hbar\frac{\partial}{\partial t}|\Psi(\mathbf{R}, \mathbf{r}, t)\rangle \quad (2.1)$$

and consists of two main components, the Hamiltonian operator  $\hat{\mathcal{H}}(\mathbf{R}, \mathbf{r}, t)$  and the wave function  $|\Psi(\mathbf{R}, \mathbf{r}, t)\rangle$  with both being dependent on the coordinates of all nuclei  $\mathbf{R}$  and all electrons  $\mathbf{r}$  as well as on time  $t$ . The molecular  $\hat{\mathcal{H}}(\mathbf{R}, \mathbf{r}, t)$  denotes all energies and interactions between the particles of a system and  $|\Psi(\mathbf{R}, \mathbf{r}, t)\rangle$  encodes all information about a quantum-mechanical state of the complete system. The absolute square  $|\langle\Psi(\mathbf{R}, \mathbf{r}, t)|\Psi(\mathbf{R}, \mathbf{r}, t)\rangle|^2$  gives the probability distribution of all particles of the system by which the wave function gets physical meaning, namely finding a particular particle at a given coordinate at a specific time. In the partial differential TDSE,  $\hat{\mathcal{H}}$  acts upon  $|\Psi\rangle$  by which the wave function is propagated in time. In order to obtain properties of the molecular system at any given time, such as excitation energies, transition moments, electric dipole moments etc., this equation has to be solved. Solving the TDSE for any real molecular system is an extremely challenging endeavour due to the high dimensionality of the wave function by which the mathematical problem quickly becomes too complex to solve exactly. Consequently, approximations were introduced with the central goal of approximating  $|\Psi\rangle$  as accurately as possible.<sup>[16–19]</sup>

Before diving into the formalism of some approximations proposed in the past, it is important to introduce the time-independent Schrödinger equation (TISE) which describes stationary systems and contains a Hamiltonian that includes only time-independent

## 2. Theoretical Background and Methodology

potential energy operators. Inserting this time-independent Hamiltonian  $\hat{\mathcal{H}}(\mathbf{R}, \mathbf{r})$  into the TDSE, time-independency of the wave function is achieved by solving the first-order differential equation with respect to time. Doing so shows that the time-dependent wave function can be rewritten as a product of a spatial, time-independent wave function and a time-dependent complex phase factor that oscillates in time depending on the energy

$$|\Psi(\mathbf{R}, \mathbf{r}, t)\rangle = |\Psi(\mathbf{R}, \mathbf{r})\rangle e^{-i(E/\hbar)t} \quad (2.2)$$

with the latter usually being neglected for time-independent problems.<sup>[20]</sup>

This separation of space and time variables ultimately leads to the TISE which constitutes an eigenvalue problem and is formulated as

$$\hat{\mathcal{H}}(\mathbf{R}, \mathbf{r})|\Psi(\mathbf{R}, \mathbf{r})\rangle = E_{tot}|\Psi(\mathbf{R}, \mathbf{r})\rangle. \quad (2.3)$$

In this context, the wave function  $|\Psi(\mathbf{R}, \mathbf{r})\rangle$  represents a stationary quantum-mechanical state and is an eigenfunction of  $\hat{\mathcal{H}}(\mathbf{R}, \mathbf{r})$ . Solving this equation yields  $|\Psi(\mathbf{R}, \mathbf{r})\rangle$  as well as the eigenvalue of  $\hat{\mathcal{H}}(\mathbf{R}, \mathbf{r})$ , namely the total energy of the molecular system in this respective state  $E_{tot}$ . For a system of  $N$  electrons (index  $i$  and  $j$ , mass  $m_e$ , coordinates  $\mathbf{r}$ ) and  $K$  nuclei (index  $A$  and  $B$ , mass  $M$ , coordinates  $\mathbf{R}$ , charge  $Z$ ),  $\hat{\mathcal{H}}(\mathbf{R}, \mathbf{r})$  can be written as

$$\begin{aligned} \hat{\mathcal{H}}(\mathbf{R}, \mathbf{r}) = & - \underbrace{\sum_{i=1}^N \frac{\hbar^2}{2m_e} \nabla_i^2}_{\hat{\mathcal{T}}^e(\mathbf{r})} - \underbrace{\sum_{A=1}^K \frac{\hbar^2}{2M_A} \nabla_A^2}_{\hat{\mathcal{T}}^n(\mathbf{R})} + \underbrace{\sum_{i=1}^N \sum_{j>i}^N \frac{e^2}{4\pi\epsilon_0 |\mathbf{r}_i - \mathbf{r}_j|}}_{\hat{\mathcal{V}}^{ee}(\mathbf{r})} \\ & + \underbrace{\sum_{A=1}^K \sum_{B>A}^K \frac{Z_A Z_B}{4\pi\epsilon_0 |\mathbf{R}_A - \mathbf{R}_B|}}_{\hat{\mathcal{V}}^{nn}(\mathbf{R})} - \underbrace{\sum_{i=1}^N \sum_{A=1}^K \frac{e Z_A}{4\pi\epsilon_0 |\mathbf{r}_i - \mathbf{R}_A|}}_{\hat{\mathcal{V}}^{en}(\mathbf{r}, \mathbf{R})} \end{aligned} \quad (2.4)$$

and encompasses five energy contributions to the total energy of the system: the kinetic energy of the electrons  $\hat{\mathcal{T}}^e(\mathbf{r})$  and the nuclei  $\hat{\mathcal{T}}^n(\mathbf{R})$ , the Coulomb repulsion among electrons  $\hat{\mathcal{V}}^{ee}(\mathbf{r})$  and among nuclei  $\hat{\mathcal{V}}^{nn}(\mathbf{R})$  and the Coulomb attraction between electrons and nuclei  $\hat{\mathcal{V}}^{en}(\mathbf{r}, \mathbf{R})$ .<sup>[18]</sup> The Hamiltonian operator includes further terms not mentioned in equation 2.4 in the presence of external electric or magnetic fields or when taking into account relativistic effects such as spin-orbit coupling.<sup>[21]</sup>

Both variants of the Schrödinger equation are so-called many-body problems as explained above and analytical solutions exist only for very small molecules with the most famous, still debated example being  $\text{H}_2^+$ .<sup>[22]</sup> Thus, the need for approximate solutions gave birth to the broad research field of quantum chemistry which will be introduced in the following.

### 2.1.2. The Born-Oppenheimer Approximation

In order to simplify the complexity of the TISE, Born and Oppenheimer<sup>[23]</sup> showed that it is a reasonable approximation to treat nuclei and electrons separately due to their considerable mass difference which conditions significantly different velocities. Precisely because electrons are much lighter and move much faster, nuclei can be considered stationary and electrons to be moving in a field of fixed nuclei. Mathematically, this approximation known as the Born-Oppenheimer approximation (BOA) splits the Schrödinger equation into an electronic and a nuclear equation by considering the wave function of the system as product of an electronic and a nuclear wave function

$$|\Psi(\mathbf{R}, \mathbf{r})\rangle = |\Psi^e(\mathbf{r}; \bar{\mathbf{R}})\rangle |\Psi^n(\mathbf{R})\rangle \quad (2.5)$$

with  $\bar{\mathbf{R}}$  denoting a parametrized dependency of the electronic motion on the stationary nuclear coordinates. Assuming the positions of all nuclei fixed, the nuclear kinetic energy is neglected ( $\hat{T}^n(\mathbf{R}) = 0$ ) and the Coulomb interaction between the nuclei becomes constant. Inserting these assumptions into the TISE, one derives the electronic Schrödinger equation

$$\hat{\mathcal{H}}^e(\mathbf{r}; \bar{\mathbf{R}})\Psi^e(\mathbf{r}; \bar{\mathbf{R}}) = E^e(\bar{\mathbf{R}})\Psi^e(\mathbf{r}; \bar{\mathbf{R}}) \quad (2.6)$$

where  $\hat{\mathcal{H}}^e(\mathbf{r}; \bar{\mathbf{R}}) = \hat{\mathcal{H}}(\mathbf{R}, \mathbf{r}) - \hat{T}^n(\mathbf{R})$ . The solutions of the electronic Schrödinger equation are the electronic wave function  $\Psi^e(\mathbf{r}; \bar{\mathbf{R}})$ , which describes the electronic configuration, and the respective electronic energy of the system  $E^e(\bar{\mathbf{R}})$  with both being dependent on a fixed nuclear arrangement. Consequently, varying the nuclear arrangement yields different electronic energies and by subsequently adding the Coulomb repulsion between the nuclei of each conformation ( $\hat{V}^{nn}(\mathbf{R})$ ) to its respective  $E^e(\bar{\mathbf{R}})$ , one obtains the total energy of the system for each electronic state as a hypersurface of  $3N-6$  dimensions ( $N$  being number of nuclei) known as potential energy surface (PES).<sup>[24,25]</sup>

The power of this approximation, which essentially proposes only a decoupling of the electronic and nuclear motion, is that molecules get a depictable 3D-shape based on the stationary coordinates of their nuclei and the complex mathematical object of a PES becomes conceptually accessible. The energetically lowest state is called the ground state, while all others are known as excited states.

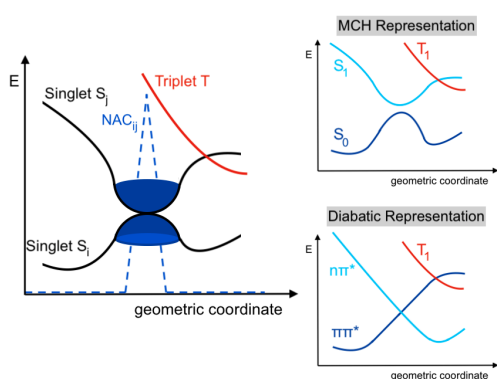


Figure 2.1.: Schematic representation of the avoided crossing between two 1D-PESs.<sup>[26]</sup>

Within a PES, it is possible to locate stationary points such as global minima (known as geometry optimization) and saddle points which correspond to transition states. However, the BOA has severe limitations and applies only to energetically well separated PESs where coupling effects, such as non-adiabatic coupling (NAC) or spin-orbit coupling (SOC), do not play a significant role. The BOA famously breaks down when two or more solutions to the electronic Schrödinger equation yield similar energies. In these regions, two electronic

## 2. Theoretical Background and Methodology

states come close in energy within a narrow nuclear coordinate space. These crossing points represented by the double cone in Figure 2.1 are called avoided crossings in one-dimensional PESs and conical intersections in two or higher dimensional PESs and are of utmost importance in the understanding of photo-induced processes because this is where electronic states intersect and photo-relaxation pathways can be determined.<sup>[21,27]</sup>

### 2.1.3. MCH, Diagonal and Diabatic State Representation

Essentially, in these crucial regions of the PES, the electronic wave function changes fast with the nuclear coordinates so that the coupling between electronic and nuclear motion can no longer be neglected. Mathematically, coupling can be accounted for by first constructing the total, exact wave function as a linear combination of all electronic eigenstates with equation 2.5, which is known as *Born-Huang expansion*,<sup>[28]</sup>

$$|\Psi(\mathbf{R}, \mathbf{r})\rangle = \sum_{\alpha} |\Psi_{\alpha}^e(\mathbf{r}; \overline{\mathbf{R}})\rangle \Psi_{\alpha}^n(\mathbf{R}) \quad (2.7)$$

and by inserting equation 2.7 into the TISE and subsequently projecting it onto a specific electronic state  $\langle \Psi_{\beta}^e(\mathbf{r}, \overline{\mathbf{R}}) |$  one arrives at

$$(\hat{\mathcal{T}}^n + E_{\alpha}^e) |\Psi_{\alpha}^n(\mathbf{R})\rangle + \sum_{\alpha} \hat{\mathcal{T}}_{\beta\alpha}^{NAC} |\Psi_{\beta}^n(\mathbf{R})\rangle = E |\Psi_{\alpha}^n(\mathbf{R})\rangle \quad (2.8)$$

with the kinetic operator  $\hat{\mathcal{T}}_{\beta\alpha}^{NAC}$  being

$$\hat{\mathcal{T}}_{\beta\alpha}^{NAC} = - \sum_A \frac{\hbar^2}{2M_A} \left[ \langle \Psi_{\alpha}^e | \nabla_A^2 | \Psi_{\beta}^e \rangle + \langle \Psi_{\alpha}^e | \nabla_A | \Psi_{\beta}^e \rangle \nabla_A \right]. \quad (2.9)$$

The first coupling term of  $\hat{\mathcal{T}}_{\beta\alpha}^{NAC}$  is termed BO diagonal coupling and is usually neglected. However, the second term is what is known as NAC and a large value signifies a high probability for a non-adiabatic transition between two states of equal multiplicity as depicted on the left-hand side of Figure 2.1. Such a relaxation path is termed internal conversion (IC). It is important to emphasize, that this depiction is still within the *adiabatic* picture, where two states of same multiplicity only approach one another but do not cross, hence the term non-adiabatic crossing if population transfer "goes through" this region from an upper to a lower PES. Here, we consider the molecular coulomb Hamiltonian (MCH) that contains terms for the kinetic energy of the electrons, the Coulombic interactions and NAC. The electronic basis spanned by the eigenstates of this Hamiltonian is called MCH representation (see *upper right* Figure 2.1).<sup>[18,20,27]</sup>

Instead of using the eigenstates of the MCH Hamiltonian as basis, one could define a basis so that the electronic states do not depend on nuclear coordinates, but rather on the eigenstates of the MCH Hamiltonian at one particular geometry. Choosing such a basis gives the *diabatic* representation in which each PES preserves the character it had at the chosen basis (see *lower right* Figure 2.1). Effectively, the NAC terms are ideally

## 2. Theoretical Background and Methodology

fully absorbed into the off-diagonal elements of the potential energy matrix, however, in practice, it is usually not possible to find strictly diabatic states, so the NACs are minimized as good as possible. The diabatic representation is usually preferred in wave packet dynamics.<sup>[18]</sup>

There is an important relativistic effect to consider when investigating transitions between triplet and singlet states which is termed intersystem crossing (ISC). Analogously to IC, ISC depends on several factors including the energy difference of the two electronic states with different multiplicity in this context and on a relativistic effect between both states called SOC. Relativistic within this context means fast electronic motion almost at the speed of light which results from an coupled interaction between the magnetic moment of electron spin and the orbital angular momentum. When SOC is sufficiently large, the electron spin is inverted which facilitates a crossing between two states of different multiplicity. For **CpMo**, SOCs were computed and for their depiction, a third representation needs to be mentioned, namely the diagonal representation. To obtain diagonal states, a unitary transformation

$$\hat{H}^{diag} = U^\dagger \hat{H}^{MCH} U \quad (2.10)$$

is necessary to diagonalize the MCH Hamiltonian because the SOC terms are included in the off-diagonal elements. By definition, the Hamiltonian of the diagonal representation is diagonal, ergo the NAC and SOC terms are absorbed into the matrix diagonal and the formerly delocalized couplings become fully localized. The important peculiarities of this representation is that one triplet state splits threefold due to the intrinsic spin angular momentum of electrons and all singlet and triplet states merely approach one another, but never cross. Due to this reason, this representation is also often referred to as fully-adiabatic representation.<sup>[25,27]</sup>

### 2.1.4. Electronic Structure Methods

Even though the complexity of the TISE is drastically reduced by the decoupling of the nuclear and electronic motion, one is left with the problem of solving the electronic Schrödinger equation which in itself is still too complex to solve analytically for any real molecular systems. The reason for this is the Coulomb repulsion between electrons ( $\hat{V}^{ee}(\mathbf{r})$ ) which emerges from the fact that electrons do not move independently from one another. Due to this correlated motion, it is not possible to simply solve the electronic Schrödinger equation one electron at a time. As a consequence, many methods have been proposed in the past to account for electronic correlation which are classified as either wavefunction-based (*ab initio*) methods or density-based methods.

#### Hartree-Fock Method

The simplest *ab initio* method is the Hartree-Fock (HF) approach where electrons are treated as independently moving within an average field of all other electrons and nuclei. By treating the electron-electron repulsion in an average fashion, this method essentially neglects most electronic correlation which is however regained in more accurate

## 2. Theoretical Background and Methodology

methods that use HF as a starting point. In this approximation, the multi-electron wave function is constructed by the product of multiple single-electron wave functions called spin orbitals. Each spin orbital  $\chi(\mathbf{r}, \omega)$  consists of a spatial orbital  $\phi(\mathbf{r})$  depending on the position of the electron  $\mathbf{r}$  and a spin function  $\xi(\omega)$  with  $\omega$  denoting either spin-up ( $\alpha$  or  $\uparrow$ ) or spin-down ( $\beta$  or  $\downarrow$ ) so that  $\chi(\mathbf{r}, \omega) = \phi(\mathbf{r})\xi(\omega)$ . Hence, two electrons can occupy the same spatial orbit, but then need to differ in their spin component to satisfy the *Pauli exclusion principle* which states that fermions (particles with half-integer spin) cannot occupy the same quantum state.<sup>[20]</sup> In further consequence, it is not sufficient to just take the product of all single-electron wave functions to approximate the total wave function  $|\Psi_{HF}\rangle$  of the N-electron system because the total wave function must be antisymmetric and change its sign upon the simultaneous exchange of two electrons. The latter is achieved by arranging all spin orbitals in a so-called *Slater determinant* which for an N-electron wave function has the generalized form of

$$|\Psi_{HF}\rangle = |\chi_1\chi_2\cdots\chi_N\rangle = \frac{1}{\sqrt{N!}} \begin{vmatrix} \chi_i(\mathbf{r}_1) & \chi_j(\mathbf{r}_1) & \cdots & \chi_z(\mathbf{r}_1) \\ \chi_i(\mathbf{r}_2) & \chi_j(\mathbf{r}_2) & \cdots & \chi_z(\mathbf{r}_2) \\ \vdots & \vdots & \ddots & \vdots \\ \chi_i(\mathbf{r}_N) & \chi_j(\mathbf{r}_N) & \cdots & \chi_z(\mathbf{r}_N) \end{vmatrix} \quad (2.11)$$

where ultimately no electron is tied to a specific orbital. Hence, the antisymmetry requirement is fulfilled because the determinant changes its sign upon interchanging either two columns or two rows which translates to an exchange of either two orbitals or two electrons within the wave function. Additionally, the Slater determinant complies with the Pauli exclusion principle, because having two electrons occupy the same spin orbital mathematically corresponds to having two identical columns which equates to a determinant value of zero. Due to the inclusion of this exchange effect of two electrons, the Slater determinant incorporates *exchange correlation* which accounts for the correlated motion of two electrons with parallel spin. However, the motion of two electrons exhibiting opposite spin remains uncorrelated.<sup>[24]</sup>

With this simplest antisymmetric wave function, it is possible to describe the ground state of a molecule by applying the *variational principle*. The variational principle states that the constructed wave function of the total system exhibits variational flexibility and yields an energy greater or equal to the energy obtained with the exact wave function. The variational flexibility of the wave function lies in the choice of spin orbitals and, in order to obtain the best set of spin orbitals,  $|\Psi_{HF}\rangle$  is inserted into the TISE and the HF equations are derived and iteratively solved so that the electronic energy is systematically minimized in each round. The HF equations minimize the energy by systematically varying the spin orbitals utilizing the optimization method of Lagrange multipliers with the only condition that the orbitals have to remain orthonormal ( $\langle\chi_i|\chi_j\rangle = \delta_{ij}$ ). The resulting HF equations read as follows

$$\hat{f}(\mathbf{r}_m)|\chi_i(\mathbf{r}_m)\rangle = \epsilon_i|\chi_i(\mathbf{r}_m)\rangle \quad (2.12)$$

where  $\epsilon_i$  is the energy of spin orbital  $\chi_i(\mathbf{r}_m)$  of electron  $m$  and  $\hat{f}(\mathbf{r}_m)$  is the so-called *Fock*

## 2. Theoretical Background and Methodology

operator which is an effective one-electron operator acting only on the coordinates of one electron  $\mathbf{r}_m$  of the form

$$\hat{f}(\mathbf{r}_m) = \overbrace{\hat{\mathcal{T}}_{e_m}(\mathbf{r}_m) + \hat{\mathcal{V}}_{e_m n}(\mathbf{r}_m, \bar{\mathbf{R}})}^{\hat{h}(\mathbf{r}_m)} + \hat{v}^{HF} = \hat{h}(\mathbf{r}_m) + \sum_{x=1}^{N/2} (2\hat{\mathcal{J}}_x - \hat{\mathcal{K}}_x). \quad (2.13)$$

$\hat{f}(\mathbf{r}_m)$  has three components, namely the kinetic energy of electron  $m$ ,  $\hat{\mathcal{T}}_{e_m}(\mathbf{r}_m)$ , the sum of the Coulomb attraction of electron  $m$  to each nuclei,  $\hat{\mathcal{V}}_{e_m n}(\mathbf{r}_m, \bar{\mathbf{R}})$ , and a term for the average interaction electron  $m$  experiences in the presence of all other  $N - 1$  electrons,  $\hat{v}^{HF}$ . The HF potential  $\hat{v}^{HF}$  is the sum over all  $N/2$  two-electron spacial orbitals and includes the Coulomb operator  $\hat{\mathcal{J}}_x$  defining the electron-electron repulsion in a two-electron orbital and the exchange operator  $\hat{\mathcal{K}}_x$  denoting the electron exchange energy due to the antisymmetry of the total wave function. Equation 2.12 is solved iteratively until self-consistency is achieved, meaning until the newly constructed  $\hat{f}(\mathbf{r}_m)$  yields the same  $|\chi_i(\mathbf{r}_m)\rangle$  that was used to construct the Fock operator. For this reason, HF is also labelled as self-consistent field (SCF) method.<sup>[20,24]</sup>

In order to apply HF in practice,  $\chi_i(\mathbf{r}_m)$  needs to be explicitly expressed which is typically done via a linear combination of atomic basis functions  $\phi_a(\mathbf{r}_m)$ ,

$$|\chi_i(\mathbf{r}_m)\rangle = \sum_a c_{ai} |\phi_a(\mathbf{r}_m)\rangle. \quad (2.14)$$

The expansion coefficients  $c_{ai}$  are optimized with respect to the ground state energy via a SCF calculation as outlined below. This ansatz is called linear combination of atomic orbitals (LCAO) and typically Gaussian-type functions are used for mathematical convenience since they are easier to integrate both analytically and numerically. Unfortunately, Gaussian-type functions are not optimal to mimic the functional behavior of spacial orbitals called molecular orbitals (MOs) from now on. In order to approximate the functional form of the spherical harmonic solutions of an H-atom which represent the optimal basis functions for MOs, a number of primitive Gaussian functions are combined in a particular contraction scheme resulting in Gaussian-type orbitals (GTOs). Depending on the contraction scheme, there are many different pre-defined so-called *basis sets* to choose from which typically vary in size, meaning in the number and type of function for each element. The choice of basis set strongly depends on the chosen quantum chemical methods, because the performance of the method and thus the accuracy of the results as well as the duration of the calculation is directly affected by the basis set. Furthermore, depending on the chemical problem at hand, more specialized basis set may be selected, such as polarized or diffuse basis sets where additional functions better describe the polarization of electron density or charge density far away from the nucleus and therefore aid the simulation of bond dissociation or anionic species.<sup>[20,29]</sup>

The LCAO ansatz reduces the problem of finding the best set of orbitals to the problem of finding the best expansion coefficients  $c_{ai}$  for the basis functions. This effectively converts the integro-differential HF equations into a matrix eigenvalue problem known as

## 2. Theoretical Background and Methodology

Roothaan equations of the following form

$$\mathbf{FC} = \mathbf{SC}\epsilon \quad (2.15)$$

where  $\mathbf{F}$  is the Fock matrix containing the Fock operators,  $\mathbf{C}$  is the coefficient matrix and  $\mathbf{S}$  is the overlap matrix between basis functions. Equivalent to the HF equations, the Roothaan equations are also solved in an iterative fashion because  $\mathbf{F}$  depend on the orbitals which are unknown and iteratively improved in this calculation.

With HF, the wave function and energy of the ground state can be calculated but only with low accuracy. Even with an infinitely large basis set, the exact energy will never be obtained due to the mean-field approximation that does not account for the explicit electron-electron interactions. The energy difference is termed *correlation energy*<sup>[30]</sup>

$$E^{corr} = E^{HF} - E^{exact} \quad (2.16)$$

and stems from two types of correlation, *dynamical* correlation caused by the instantaneous repulsion of electrons while in motion and *non-dynamical* or *static* correlation which has a large effect when orbitals are near-degenerate and more than one Slater determinant is necessary to describe the ground state wave function. The latter is of particular significance when dealing with excited states, transition metals, non-innocent ligands and dissociations or bond-breaking situations that are not compatible with a continuous orbital occupation.<sup>[20]</sup>

### Configuration Interaction

Post-HF methods attempt to retrieve the missing electron correlation energy by adding more electronic configurations to the wave function. One of these approaches is called configuration interaction (CI) where the HF ground state wave function  $|\Psi_{HF}\rangle$  serves as a reference to improve upon by adding additional excited configurations in which electrons have been promoted from occupied ( $a, b \dots$ ) to unoccupied ( $r, s \dots$ ) orbitals. In this way, not only a single Slater determinant is used to construct the wave function, but rather a linear combination of as many orthogonal Slater determinants as one can afford. The CI wave function has the general form

$$\Psi_{CI} = c_0|\Psi_{HF}\rangle + \underbrace{\left(\frac{1}{1!}\right)^2 \sum_{ra} c_a^r |\Phi_a^r\rangle}_{\sum_S c_S |\Phi_S\rangle} + \underbrace{\left(\frac{1}{2!}\right)^2 \sum_{\substack{ab \\ rs}} c_{ab}^{rs} |\Phi_{ab}^{rs}\rangle}_{\sum_D c_D |\Phi_D\rangle} + \underbrace{\left(\frac{1}{3!}\right)^2 \sum_{\substack{abc \\ rst}} c_{abc}^{rst} |\Phi_{abc}^{rst}\rangle}_{\sum_T c_T |\Phi_T\rangle} + \dots = \sum_{i=0} c_i |\Phi_i\rangle \quad (2.17)$$

where a single excitation is described by the substitution of one spin orbital  $a$  in  $|\Psi_{HF}\rangle$  with another spin orbital  $r$  giving the single-excited Slater determinant  $|\Phi_a^r\rangle$  or  $|\Phi_S\rangle$ . In analogy, double, triple up to the  $i^{th}$  excitation are denoted with the index  $D, T, i$  in

## 2. Theoretical Background and Methodology

equation 2.17. Including a factor of  $(n!)^{-2}$  ensures that each n-tuply excited determinant is counted only once. Following the variational theorem, the expansion coefficients  $c_i$  are optimized with respect to a minimization in energy while the molecular orbitals are not optimized during the CI procedure.

In order to obtain the CI coefficients and thus the energy of the system, equation

$$E_{CI} = \langle \Psi_{CI} | \hat{\mathcal{H}} | \Psi_{CI} \rangle = \sum_{i=0} \sum_{j=0} c_i c_j \langle \Phi_i | \hat{\mathcal{H}} | \Phi_j \rangle \quad (2.18)$$

must be solved. For this aim, all individual elements of the CI matrix,  $\hat{\mathcal{H}}_{ij} = \langle \Phi_i | \hat{\mathcal{H}} | \Phi_j \rangle$ , need to be solved, which is usually done by diagonalizing the matrix within the determinant basis. Before diagonalization, the CI matrix has the form

$$\begin{pmatrix} \langle 0 | \hat{\mathcal{H}} | 0 \rangle & \langle 0 | \hat{\mathcal{H}} | S \rangle & \langle 0 | \hat{\mathcal{H}} | D \rangle & \langle 0 | \hat{\mathcal{H}} | T \rangle & \langle 0 | \hat{\mathcal{H}} | Q \rangle & \dots \\ \langle S | \hat{\mathcal{H}} | 0 \rangle & \langle S | \hat{\mathcal{H}} | S \rangle & \langle S | \hat{\mathcal{H}} | D \rangle & \langle S | \hat{\mathcal{H}} | T \rangle & \langle S | \hat{\mathcal{H}} | Q \rangle & \dots \\ \langle D | \hat{\mathcal{H}} | 0 \rangle & \langle D | \hat{\mathcal{H}} | S \rangle & \langle D | \hat{\mathcal{H}} | D \rangle & \langle D | \hat{\mathcal{H}} | T \rangle & \langle D | \hat{\mathcal{H}} | Q \rangle & \dots \\ \langle T | \hat{\mathcal{H}} | 0 \rangle & \langle T | \hat{\mathcal{H}} | S \rangle & \langle T | \hat{\mathcal{H}} | D \rangle & \langle T | \hat{\mathcal{H}} | T \rangle & \langle T | \hat{\mathcal{H}} | Q \rangle & \dots \\ \langle Q | \hat{\mathcal{H}} | 0 \rangle & \langle Q | \hat{\mathcal{H}} | S \rangle & \langle Q | \hat{\mathcal{H}} | D \rangle & \langle Q | \hat{\mathcal{H}} | T \rangle & \langle Q | \hat{\mathcal{H}} | Q \rangle & \dots \\ \vdots & \vdots & \vdots & \vdots & \ddots & \ddots \end{pmatrix} \quad (2.19)$$

with the  $\Psi_{HF}$  denoted in short-hand notation as  $|0\rangle$  and all other excited determinant following the same scheme. Crucially, not all matrix elements need to be calculated and the matrix can be greatly simplified when considering the nature of the determinants and a few mathematical principles. First,  $\hat{\mathcal{H}}$  is Hermitian and - assuming only real orbitals are used - also symmetric. It follows directly from the eigenvalue problem introduced in equation 2.6 that the eigenvalues of the Hamiltonian are real and its eigenvectors form a unitary basis that diagonalize  $\hat{\mathcal{H}}$ . Secondly, according to *Brillouin's Theorem*,<sup>[31]</sup>  $|1\rangle$  will not couple with  $|0\rangle$  so that  $\langle 0 | \hat{\mathcal{H}} | S \rangle = \langle S | \hat{\mathcal{H}} | 0 \rangle = 0$ . Thirdly, according to the *Slater-Condon rules*,<sup>[32,33]</sup> all matrix elements between Slater determinants which differ in more than two spin orbitals are zero, which has two practical implications: On the one hand, this means that  $\langle 0 | \hat{\mathcal{H}} | T \rangle = \langle T | \hat{\mathcal{H}} | 0 \rangle = 0$  and  $\langle S | \hat{\mathcal{H}} | Q \rangle = \langle Q | \hat{\mathcal{H}} | S \rangle = 0$ . On the other hand, taking the example of  $\langle D | \hat{\mathcal{H}} | T \rangle$ , some matrix elements will be zero if they differ in two spin orbitals so that  $\langle \Phi_{ab}^{rs} | \hat{\mathcal{H}} | \Phi_{cde}^{tuv} \rangle = 0$  but  $\langle \Phi_{ab}^{rs} | \hat{\mathcal{H}} | \Phi_{abc}^{rst} \rangle \neq 0$ . These auxiliaries effectively diagonalize the CI matrix and greatly reduce the amount of integrals needed to be solved so that 2.18 can be rewritten as

$$\begin{pmatrix} \langle 0 | \hat{\mathcal{H}} | 0 \rangle & 0 & \langle 0 | \hat{\mathcal{H}} | D \rangle & 0 & 0 & \dots \\ & \langle S | \hat{\mathcal{H}} | S \rangle & \langle S | \hat{\mathcal{H}} | D \rangle & \langle S | \hat{\mathcal{H}} | T \rangle & 0 & \dots \\ & & \langle D | \hat{\mathcal{H}} | D \rangle & \langle D | \hat{\mathcal{H}} | T \rangle & \langle D | \hat{\mathcal{H}} | Q \rangle & \dots \\ & & & \langle T | \hat{\mathcal{H}} | T \rangle & \langle T | \hat{\mathcal{H}} | Q \rangle & \dots \\ & & & & \langle Q | \hat{\mathcal{H}} | Q \rangle & \dots \\ \vdots & \vdots & \vdots & \vdots & \ddots & \ddots \end{pmatrix} \quad (2.20)$$

where some matrix elements may still be zero (see third principle) and the property of  $\hat{\mathcal{H}}$

## 2. Theoretical Background and Methodology

being Hermitian is considered, so only the upper triangle is shown (see first principle). The coefficients are then determined from the eigenvector of the CI matrix given in 2.20 yielding the lowest eigenvalue, whereas in principle also excited states (far away from conical intersections and near-degeneracy) can be constructed from eigenvectors corresponding to higher energies.<sup>[21,24]</sup>

Using all possible excitations to construct the CI wave function is called *Full CI* which would together with a reasonable infinite basis set yield the exact solution to the TISE. However, in practice this is not feasible because of the method’s factorial scaling with system size and extremely high computational duration and cost already for smaller molecules.<sup>[34]</sup> For this reason, the linear expansion can be restricted to a chosen number of excitations giving truncated CI methods starting from CID or the slightly better CISD (truncation after doubly excitations; CIS would yield the same result as HF see second principle), CISDT (truncation after triple excitations) etc. Important to note is that while Full CI is size consistent, truncated CI methods are not which bears the problem that the regained correlation energy does not scale with system size. For this reason, the latter methods are not well suited for larger molecules. For these systems and for computation of excited states, other single-reference methods following perturbation theory, e.g. *Møller-Plesset perturbation theory* or *algebraic diagrammatic construction*, or following *coupled cluster theory* are more adequate.<sup>[20]</sup>

### Complete Active Space Self-consistent Field

In the previous section, only single-reference methods have been considered which use the HF wave function as a single reference to improve upon. However, when describing excited states, transition metal complexes or dissociation where near degeneracy is prevailing, the HF wave function alone is usually not a good reference because not enough static correlation is regained to achieve a good qualitative description. For these chemical problems, multi-reference methods are better suited. One important approach in this regard is multi-configurational self-consistent field (MCSCF) where the total wave function is built from a linear combination of multiple Slater determinants analogous to the CI approach (see equation 2.17) so that

$$\Psi_{MCSCF} = \sum_{i=0} c_i |\Phi_i\rangle. \quad (2.21)$$

In contrast to CI, both the expansion coefficients  $c_i$  as well as the coefficients of the orthonormal orbitals  $|\Phi_i\rangle$  (which are the coefficients given in equation 2.14 of the LCAO expansion) are optimized following the variational procedure. This takes the effect of the excitation on the orbitals into account, such as orbital relaxation, and the wave function becomes more flexible.<sup>[20,35]</sup> By doing so, the computational demand increases dramatically compared to CI which necessitates a limit on how many determinants enter equation 2.21. In principle, using more and more configurations, also more and more dynamical correlation is gained until - at Full CI level - the exact energy is obtained.

The major problem with MCSCF is to decide which and how many configurations are necessary to describe the property of interest properly within a reasonable computation

## 2. Theoretical Background and Methodology

time. In principle, one has to include only a small amount of meaningful determinants which involve excitations only within the near-degenerate orbitals causing static correlation. However, selecting this set of meaningful determinants is certainly not trivial and is an important topic of this thesis. One of the most widely used MCSCF approaches to tackle this problem is complete active space self-consistent field (CASSCF).<sup>[36,37]</sup> In this method, the molecular spin orbitals are computed first using a SCF method such as HF and then partitioned into *inactive* and *active* orbitals with the latter being usually selected from the energetically highest occupied and lowest unoccupied MOs. All active orbitals are designated as *active space* in which a Full CI is performed. A common notation for a CASSCF calculation is *CASSCF*( $e,o$ ) with  $e$  denoting the amount of electrons and  $o$  the amount of orbitals chosen for the active space. The accuracy and duration of a CASSCF computation strongly depends on the size of the active space. Presently, CASSCF is limited to around 10-12 electrons/orbitals for practical applications, but larger active spaces up to a maximum of approximately 16 electrons/orbitals are also used occasionally.<sup>[20]</sup> In order to increase the practical size of active spaces, other approaches are used such *restricted active space SCF method* or *generalized active space SCF method* which both impose more restrictions on the active space so that, instead of a Full CI, certain excited Slater determinants are neglected within smaller subspaces of the active space. A relatively new algorithm which is conceptually radically different to any electronic structure method presented in this chapter is density matrix renormalization group (DMRG). This algorithm has the advantage that it also constructs CAS-CI-wave functions but scales computational time polynomial not factorial.<sup>[38]</sup> This algorithm will be discussed in section 2.3.

For the computation of excited states, two CASSCF methods are differentiated. In state-specific CASSCF (SS-CASSCF), the orbital basis is optimized regarding both coefficients for each targeted state individually (equation 2.14 and 2.21) so that the energy of each state is minimized individually. This produces well-optimized, but non-orthogonal states and orbitals which necessitates a subsequent diagonalization of the Hamiltonian in the basis of all optimized states in order to compute any property of two coupled states. To circumvent this complication, usually state-averaged CASSCF (SA-CASSCF) is favoured where only a single set of orthogonal orbitals is used to compute all states. Each state has an own set of CI coefficients which are optimized with respect to a minimization of the average energy weighting each respective state energy with a factor so that

$$E_{average} = \sum_{i=1}^K w_i E_i \quad \text{with} \quad \sum_{i=1}^K w_i = 1. \quad (2.22)$$

The state-specific factor  $w_i$  is by default assumed equal for all states and generally designates the impact of the state on the orbital relaxation within the complete system. However, the shared orbital set assembling the complete system is not optimal for any state and a large number of states badly affects the quality of the predicted energy which can be partially counterbalanced by a modulation of  $w_i$  for some states.<sup>[34]</sup>

### Complete Active Space Second-order Perturbation Theory

A CASSCF computation successfully accounts for the multi-configurational character of the wave function and, hence, for static correlation energy. Furthermore, all electron correlation within the active space is accounted for, however not within the inactive space or between the active and inactive space. Therefore, the calculated energy can be even further improved in cases where dynamical correlation energy is important to obtain a good description of the investigated system by applying for instance perturbation theory on top of the CASSCF wave function. Generally, perturbation theory is used in many scientific fields<sup>[39]</sup> by assuming that the given problem has been solved to a large extent with a small deviation to the exact solution. Mathematically, this perturbative deviation is expanded in a Taylor series so that the approximate solution is systematically improved. Contrary to CI which aims to systematically improve the wave function, perturbation theory refines the Hamiltonian. More specifically, the approximated wave function is inserted into the TISE as zeroth-order reference wave function  $|\Psi_i(0)\rangle$ , and the Hamiltonian is partitioned into a non-perturbative  $\hat{\mathcal{H}}_0$  and a perturbative  $\hat{\mathcal{H}}'$  with  $\lambda$  giving the strength of the perturbation so that

$$\hat{\mathcal{H}}|\Psi_i\rangle = (\hat{\mathcal{H}}_0 + \lambda\hat{\mathcal{H}}')|\Psi_i\rangle = E_i|\Psi_i\rangle. \quad (2.23)$$

The eigenfunctions and eigenvalues of the zeroth-order  $\lambda = 0$  is known from the CASSCF computation and a solution to

$$\hat{\mathcal{H}}_0|\Psi_i^{(0)}\rangle = E_i^{(0)}|\Psi_i^{(0)}\rangle \quad (2.24)$$

thus already exists.  $\lim_{\lambda \approx 0} E_i^{(0)} \approx E_i$  describes a case where the CASSCF wave function already gives a reasonable good description of the system. However, in cases where dynamical correlation is still missing,  $\lambda \neq 0$  and the perturbation corresponds to the correlation that is not yet accounted for. Since  $\hat{\mathcal{H}}$  depends on  $\lambda$ , its eigenfunctions and eigenvalues also depend on it. Furthermore, because the perturbation is generally small compared to the non-perturbative part and an increase in  $\lambda$  yields a continuous change in the observable, perturbation theory is applicable and both  $|\Psi_i\rangle$  and  $E_i$  can be expanded in a Taylor series:

$$\begin{aligned} |\Psi_i\rangle &= |\Psi_i^{(0)}\rangle + \lambda^1|\Psi_i^{(1)}\rangle + \lambda^2|\Psi_i^{(2)}\rangle + \dots + \lambda^n|\Psi_i^{(n)}\rangle \\ E_i &= E_i^{(0)} + \lambda^1 E_i^{(1)} + \lambda^2 E_i^{(2)} + \dots + \lambda^n E_i^{(n)} \end{aligned} \quad (2.25)$$

with index  $i$  denoting a set of targeted states and the numbers given in parenthesis indicating the correction order. Hence, for instance,  $|\Psi_i^{(1)}\rangle$  and  $E_i^{(1)}$  are termed first-order wave function and energy correction.

The unperturbed total wave function,  $|\Psi_i\rangle$  and the perturbed wave functions,  $|\Psi_i^{(1,2,\dots,n)}\rangle$ , are spanned in the same Hilbert space which requires a normalization that is later used to solve the mathematical problem. First, the wave function of  $\hat{\mathcal{H}}_0$  is normalized so that  $\langle\Psi_i^{(0)}|\Psi_i^{(0)}\rangle = 1$ . Then, the normalization of the total wave function is chosen so that

## 2. Theoretical Background and Methodology

$\langle \Psi_i^{(0)} | \Psi_i \rangle = 1$ , which can be made because  $\Psi_i^{(0)}$  and  $\Psi_i$  are orthogonal. Inserting the to the power of  $\lambda$  expanded wave function (second equation in 2.25) into the second normalization condition yields

$$\langle \Psi_i^{(0)} | \Psi_i \rangle = \langle \Psi_i^{(0)} | \Psi_i^{(0)} \rangle + \langle \Psi_i^{(0)} | \Psi_i^{(1)} \rangle + \langle \Psi_i^{(0)} | \Psi_i^{(2)} \rangle + \dots + \langle \Psi_i^{(0)} | \Psi_i^{(n)} \rangle = 1 \quad (2.26)$$

which - due to the first normalization step - only holds if  $\langle \Psi_i^{(0)} | \Psi_i^{(1,2,\dots,n)} \rangle = 0$ . This normalization technique is termed *intermediate normalization*<sup>[24]</sup> and can be summarized by

$$\langle \Psi_i^{(0)} | \Psi_i \rangle = 1 \quad \text{and} \quad \langle \Psi_i^{(0)} | \Psi_i^{(n)} \rangle = \delta_{0n}. \quad (2.27)$$

Inserting the expanded equations of 2.25 into 2.23 and clustering by order gives the following equations for each perturbation order:

$$\begin{aligned} \lambda^0 : \quad & \hat{\mathcal{H}}_0 | \Psi_i^{(0)} \rangle = E_i^{(0)} | \Psi_i^{(0)} \rangle \\ \lambda^1 : \quad & \hat{\mathcal{H}}_0 | \Psi_i^{(1)} \rangle + \hat{\mathcal{H}}' | \Psi_i^{(0)} \rangle = E_i^{(0)} | \Psi_i^{(1)} \rangle + E_i^{(1)} | \Psi_i^{(0)} \rangle \\ \lambda^2 : \quad & \hat{\mathcal{H}}_0 | \Psi_i^{(2)} \rangle + \hat{\mathcal{H}}' | \Psi_i^{(1)} \rangle = E_i^{(0)} | \Psi_i^{(2)} \rangle + E_i^{(1)} | \Psi_i^{(1)} \rangle + E_i^{(2)} | \Psi_i^{(0)} \rangle \\ & \vdots \\ \lambda^n : \quad & \hat{\mathcal{H}}_0 | \Psi_i^{(n)} \rangle + \hat{\mathcal{H}}' | \Psi_i^{(n-1)} \rangle = \sum_{m=0}^n E_i^m | \Psi_i^{n-m} \rangle. \end{aligned} \quad (2.28)$$

The solutions to the zeroth-order equation exist and generated a complete set of functions. The first-order equation already contains two unknown terms, namely the first-order correction term to the wave function and the energy. The first order energy correction can be solved by utilizing 2.27 and projecting onto  $\langle \Psi_i^{(0)} |$  whereas all higher orders require the knowledge of the  $(n - 1)$ -order wave functions:

$$\begin{aligned} E_i^{(0)} &= \langle \Psi_i^{(0)} | \hat{\mathcal{H}}_0 | \Psi_i^{(0)} \rangle \\ E_i^{(1)} &= \langle \Psi_i^{(0)} | \hat{\mathcal{H}}' | \Psi_i^{(0)} \rangle \\ E_i^{(2)} &= \langle \Psi_i^{(0)} | \hat{\mathcal{H}}' | \Psi_i^{(1)} \rangle \\ & \vdots \\ E_i^{(n)} &= \langle \Psi_i^{(0)} | \hat{\mathcal{H}}' | \Psi_i^{(n-1)} \rangle. \end{aligned} \quad (2.29)$$

In order to obtain the  $(n - 1)$ -order wave functions, knowledge of the  $(n - 2)$ -order eigenfunctions must be at hand, which makes the solution to 2.28 a strictly hierarchical problem. The hierarchically first unknown wave function correction term is located in the second-order energy correction equation, namely the first order  $|\Psi_i^{(1)}\rangle$  which can be

## 2. Theoretical Background and Methodology

solved by expanding it in the known eigenfunctions of  $\hat{\mathcal{H}}_0$  (indicated by index  $z$ ) so that

$$|\Psi_i^{(1)}\rangle = \sum_z c_z^{(1)} |\Psi_{i,z}^{(0)}\rangle = - \sum_z \frac{\langle \Psi_{i,z}^{(0)} | \hat{\mathcal{H}}' | \Psi_i^{(0)} \rangle}{E_{i,z}^{(0)} - E_i^{(0)}} |\Psi_{i,z}^{(0)}\rangle. \quad (2.30)$$

This is known as the *Rayleigh-Schrödinger perturbation ansatz*.<sup>[20]</sup> Following this ansatz, the second-order correction term of the energy in equation 2.29 can be calculated by

$$E_i^{(2)} = \sum_z c_z \langle \Psi_i^{(0)} | \hat{\mathcal{H}}' | \Psi_{i,z}^{(0)} \rangle = - \sum_z \frac{|\langle \Psi_i^{(0)} | \hat{\mathcal{H}}' | \Psi_{i,z}^{(0)} \rangle|^2}{E_{i,z}^{(0)} - E_i^{(0)}} \quad (2.31)$$

Although higher order energy corrections become accessible with this ansatz, corrections after the second-order are usually omitted. This is due to the typical oscillating behaviour of the calculated energy requiring a computation of forth order to improve the second-order outcome, which dramatically increases computational effort.<sup>[20]</sup>

The question remaining is how to define the zeroth-order Hamiltonian  $\hat{\mathcal{H}}_0$  when using a CASSCF wave function  $|\Psi_i^{(0)}\rangle$  ( $|0\rangle$  in the following) as a reference. Different approaches exist with one being second-order complete active space perturbation theory (CASPT2) which - as the name implies - includes energy corrections up to the second order and uses a projection operator technique to built  $\hat{\mathcal{H}}_0$ . Essentially, a combination of projection operators  $\hat{\mathcal{P}}$  and an effective one-electron operator, the generalized Fock operator  $\hat{\mathcal{F}}$ , give the zeroth-order Hamiltonian as

$$\hat{\mathcal{H}}_0 = \hat{\mathcal{P}}_0 \hat{\mathcal{F}} \hat{\mathcal{P}}_0 + \hat{\mathcal{P}}_K \hat{\mathcal{F}} \hat{\mathcal{P}}_K + \hat{\mathcal{P}}_{SD} \hat{\mathcal{F}} \hat{\mathcal{P}}_{SD}. \quad (2.32)$$

The projection operators act on different configurational spaces, namely  $\hat{\mathcal{P}}_0$  projects onto  $|0\rangle$ , whereas  $\hat{\mathcal{P}}_K$  and  $\hat{\mathcal{P}}_{SD}$  project onto the single and double replacement states within and outside the active space respectively. The generalized Fock operator  $\hat{\mathcal{F}}$  is given as

$$\hat{\mathcal{F}} = \sum_{pq} f_{pq} \hat{\mathcal{A}}_{pq} \quad \text{with} \quad \hat{\mathcal{A}}_{pq} = \sum_{\sigma} \hat{a}_{p\sigma}^{\dagger} \hat{a}_{q\sigma} \quad (2.33)$$

$$f_{pq} = h_{pq} + \sum_{rs} D_{rs} [\langle pq|rs\rangle - \frac{1}{2} \langle pr|qs\rangle].$$

Here,  $\hat{\mathcal{A}}_{pq}$  denotes spin-averaged excitation operators each consisting of a creation ( $\hat{a}^{\dagger}$ ) and an annihilation ( $\hat{a}$ ) operator where one electron of average spin  $\sigma$  is excited from orbital  $q$  to  $p$ .<sup>[40]</sup> Moreover,  $D_{rs}$  stands for an one-particle density matrix. The overall generalized Fock matrix  $f_{pq}$  consists of 3x3 blocks corresponding to the three orbital spaces, inactive (doubly occupied;  $D_{pp} = 2$ ), active (variable occupation number;  $0 \leq D_{pp} \leq 2$ ) and secondary (unoccupied;  $D_{pp} = 0$ ). According to the *generalized Brillouin theorem*,<sup>[41]</sup> the complexity of  $f_{pq}$  can be reduced, for instance  $f_{pq}$  is zero if  $p$  or  $p$  corresponds to a inactive and the other to a secondary orbital; in other words, there is no coupling between inactive and secondary orbitals. The other blocks comprised of orbitals of the

## 2. Theoretical Background and Methodology

same subspace (corresponding to inactive-inactive, active-active and secondary-secondary coupling) are then diagonalized one by one to determine a unique set of orbitals which are used in the computation of the first-order wave function correction, equation 2.30, and subsequently in the second-order energy correction, equation 2.31.<sup>[42–44]</sup>

On a more practical note regarding CASPT2 calculations, three additions employed in this thesis need further introduction. First, multi-state CASPT2 (MS-CASPT2) constitutes an extension to CASPT2 and addresses two important issues that manifest in inadequate potential energy surfaces. One being apparent in the region of avoided crossings, where the CASSCF wave function is not a good zeroth-order reference state for the perturbation calculation due to the strong mixing with other secondary-space states. Hence, these states do not contribute to the second-order treatment since by definition they do not interact with the reference state via the total Hamiltonian. The other issue arises when valence and Rydberg states mix. Also in this instance, the single CASSCF wave function is not a good zeroth-order description. Hence, MS-CASPT2 uses a multi-dimensional reference space spanned by two or more SA-CASSCF wave functions. These wave functions are allowed to interact by computing an effective Hamiltonian perturbatively which was diagonalized within this reference space.<sup>[45]</sup>

Second, in order to address the intruder state problem, different shift techniques are available for CASPT2 computations. Intruder states are states that exhibit a quasi-degeneracy with the reference state so that their zeroth-order energies come very close ( $E_{i,z}^{(0)} - E_i^{(0)} \approx 0$ ) resulting in a small denominator in equation 2.30 and 2.31 respectively and thus in an unphysically large (positive or negative) value of  $E_i^{(2)}$ . In such an instance, the PESs lose their smoothness and exhibit discontinuities. In order to remove the localized coupling between such an intruder state and the reference state, one can adopt a level-shift technique affecting the first-order wave function correction so that equation 2.31 becomes

$$E_i^{(2)} = - \sum_z \frac{|\langle \Psi_i^{(0)} | \hat{\mathcal{H}}' | \Psi_{i,z}^{(0)} \rangle|^2}{E_{i,z}^{(0)} - E_i^{(0)} + \Delta} \quad (2.34)$$

where  $\Delta$  is a real or an imaginary shift parameter counterbalancing the denominator decrease. Adopting shift parameters per default is not advisable and should be used with caution since a substantial amount of dynamical correlation may be lost in the process. Furthermore, the presence of intruder states also means that these configurations are important to consider for the total wave functions, which means that the orbitals of the active space should be critically evaluated and appropriately adjusted.<sup>[46,47]</sup>

Third, a very different shift technique constitutes the ionization potential and electron affinity (IPEA) shift which essentially modifies the zeroth-order partition of the Hamiltonian to correct errors observed in systems with open-shell electronic states. This shift technique can be understood by knowing that the diagonal elements of the generalized Fock matrix  $f$  (see equation 2.33) for the inactive (doubly occupied) and the secondary (unoccupied) orbital block can be associated with negative ionization potentials (IP) and negative electron affinities (EA) respectively assuming inactive/active and active/secondary coupling zero. For the active orbital block, the diagonal elements correspond to a

## 2. Theoretical Background and Methodology

by the occupation number weighted average of both the negative IP and the negative EA. Crucially, this feature of the matrix results in a systematically undervalued denominator of equation 2.31 for excitations from or into partially occupied active orbitals. Hence, a modification of the zeroth-order Hamiltonian was suggested that yields diagonal elements of  $f_{pp}^{active}$  which are closer to the negative IP and EA for singly occupied active orbitals so that the denominator increases slightly. This effect only corrects systematic errors obtained for open-shell electronic states so that equation 2.31 can be reformulated as

$$E_i^{(2)} = - \sum_z^{closed-shell\ config.} \frac{|\langle \Psi_i^{(0)} | \hat{\mathcal{H}}' | \Psi_{i,z}^{(0)} \rangle|^2}{E_{i,z}^{(0)} - E_i^{(0)}} - \sum_z^{open-shell\ config.} \frac{|\langle \Psi_i^{(0)} | \hat{\mathcal{H}}' | \Psi_{i,z}^{(0)} \rangle|^2}{E_{i,z}^{(0)} - E_i^{(0)} + \frac{1}{2}\kappa\epsilon} \quad (2.35)$$

where  $\epsilon$  denotes the IPEA shift value and its prefactor  $\kappa$  ensures that  $\epsilon$  only applies for electronic states that are mainly composed of open-shell configurations.<sup>[44]</sup> Originally, 49 diatomic molecules were tested in gas phase calculations and an optimal IPEA shift of 0.25 a.u. was determined which is implemented as the default value in the MOLCAS program package utilized in this thesis. The authors additionally estimate that  $\epsilon$  for transition metals may have their optimum between 0.25 and 0.30 a.u., however TMCs were not investigated.<sup>[48]</sup> Chapter 4.3.1 in the following critically evaluates the effect of different IPEA shift values for the BDE of **CpMo**.

### Density Functional Theory Method

In the methods introduced so far, the crucial component is the molecular wave function which is used to calculate molecular properties with the help of suitable operators. However, a wave function is not what scientists call an "observable"; it is not a measurable property and, in fact, there is not even general consensus on what, if anything, a wave function is.<sup>[49,50]</sup> On top or precisely because a molecular wave function is too complex to compute accurately, approximations are necessary each having their own drawbacks as discussed above. An alternative was found in the electron (probability) density function, commonly called electron density  $\rho(\mathbf{r})$ , which is a physical observable that integrated over all space gives the total number of electrons. Furthermore, the cusps in the density define the position of the nuclei and the height of the cusps define the respective nuclear charges.<sup>[51]</sup> Crucially, the Hamiltonian depends on the number of electrons and the positions and atomic numbers of nuclei rendering electron density a viable alternative for a wave function. This realization gave birth to the density functional theory (DFT) method which radically differs from *ab initio* methods by exploiting instead of the complicated 3N-dimensional wave function (including spin 4N-dimensional), the simpler three-dimensional electron density (including spin four-dimensional) to fully describe the ground state of a molecular system and to determine its energy. The proof for this assumption was given by Hohenberg and Kohn<sup>[52]</sup> who formalized what is now known as the *Hohenberg-Kohn Theorems* and thus provided a necessary framework to solve the

## 2. Theoretical Background and Methodology

TISE based on  $\rho(\mathbf{r})$ .<sup>a</sup>

As established above, the essential property for DFT is the electron density which is the integral over the probability density and reads for an N-electron system excluding spin

$$\rho(\mathbf{r}) = N \cdot \int |\Psi(\mathbf{r}, \mathbf{r}_2, \dots, \mathbf{r}_N)|^2 d\mathbf{r}_2 \dots d\mathbf{r}_N. \quad (2.36)$$

Argued in the language of DFT, electrons interact with one another and with an external potential that is the attraction to the nuclei. The first Hohenberg-Kohn Theorem called the *Existence Theorem* establishes via a groundbreaking *reductio ad absurdum* argument that the ground-state electron density for a non-degenerate system uniquely defines the external potential and therefore not only the Hamiltonian, but also the electronic wave function. As a further consequence, the wave function can be defined as a unique functional of the electron density

$$\Psi(\mathbf{r}, \mathbf{r}_2, \dots, \mathbf{r}_N) = \Psi[\rho(\mathbf{r})](\mathbf{r}, \mathbf{r}_2, \dots, \mathbf{r}_N) \quad (2.37)$$

which allows us to reformulate the energy - being a functional of a wave function - as a functional of electron density:

$$E[\rho(\mathbf{r})] = T[\rho(\mathbf{r})] + V_{ee}[\rho(\mathbf{r})] + V_{en}[\rho(\mathbf{r})] \geq E_0. \quad (2.38)$$

Already included in equation 2.38 is the second Hohenberg-Kohn Theorem which provides a means to *predict* the electron density of a system. Namely, Hohenberg and Kohn postulated that the electron density is an optimizable fundamental quantity obeying the variational principle. Hence, every trial density that integrates to the proper number of electrons for the system can be evaluated with regard to a minimization of its energy expectation value. This implies that minimising the energy will lead to the exact energy and electron density of the ground state. However, this is only achieved if the exact energy functional  $E[\rho(\mathbf{r})]$  is obtained, which is not a trivial task as explained in the following.

The DFT formalism introduced so far is an orbital-free ansatz which, although simple, suffers from the drawback that the computation of the kinetic energy term  $T[\rho(\mathbf{r})]$ , which has the largest contribution to the energy and should be calculated as accurately as possible, is challenging. Even though methods such as the *Thomas-Fermi* approximation<sup>[53,54]</sup> together with the *Weizsäcker* gradient correction<sup>[55]</sup> on top have been used in an attempt to resolve this difficulty, their success is still limited.<sup>[56]</sup> Instead the orbital-ansatz introduced by Kohn and Sham<sup>[57]</sup> is preferred which made DFT one of the most widely used methods in theoretical chemistry.<sup>[21]</sup>

Two realizations are decisive for the Kohn-Sham formalism. First, the Hamiltonian is significantly simpler for a system of non-interacting electrons given as a sum of one-electron

---

<sup>a</sup>Semantically, there is an important distinction between a *function*  $f(\mathbf{r})$ , which depends on coordinates and produces a number, and a *functional*  $F[f]$ , which produces a number from a function. While for instance a wave function or electron density constitutes a function, the energy depending on either descriptor exemplifies a functional. The notation to differentiate both in the present discussion was adopted from Jensen.<sup>[20]</sup>

## 2. Theoretical Background and Methodology

operators,  $\hat{\mathcal{H}}^{ni} = \hat{\mathcal{T}}^{ni} + \hat{\mathcal{V}}_{ne}$ , accounting for the kinetic energy of the non-interacting electrons and their repulsion to the nuclei. The eigenfunction of  $\hat{\mathcal{H}}^{ni}$  is simply a Slater determinant of individual one-electron eigenfunctions  $|\phi_i^{KS}\rangle$ , called the *Kohn-Sham orbitals*, and its eigenvalues are a sum of one-electron eigenvalues. Second and perhaps most crucial, the ground state density of the system is the same for this fictitious, non-interacting system and the real, interacting system and can be written for an N-electron system as

$$\rho(\mathbf{r}) = \sum_{i=1}^N \langle \phi_i^{KS} | \phi_i^{KS} \rangle. \quad (2.39)$$

Thus, it is convenient to refine the energy contributing terms in equation 2.38 with regard to the latter rationale, so that  $T$  is split into  $T^{ni} + \Delta T$ , for the non-interacting system and the correction to the kinetic energy deriving from the interaction respectively, and  $V_{ee}$  into  $V_{ee} + \Delta V_{ee}$ , separating the classical Coulomb repulsion from the non-classical correction. With the orbital expression of the electron density, the energy of the real interacting system is then given in atomic units by

$$\begin{aligned} E[\rho(\mathbf{r})] = & - \overbrace{\sum_{i=1}^N \left\langle \phi_i^{KS} \left| \frac{1}{2} \nabla_i^2 \right| \phi_i^{KS} \right\rangle}^{T^{ni}} - \overbrace{\sum_{i=1}^N \sum_{A=1}^K \left\langle \phi_i^{KS} \left| \frac{Z_A}{|\mathbf{r}_i - \mathbf{R}_A|} \right| \phi_i^{KS} \right\rangle}^{V_{ne}} \\ & + \underbrace{\sum_{i=1}^N \left\langle \phi_i^{KS} \left| \frac{1}{2} \int \frac{\rho(\mathbf{r}')}{|\mathbf{r}_i - \mathbf{r}'|} d\mathbf{r}' \right| \phi_i^{KS} \right\rangle}_{V_{ee}} + E_{xc}[\rho(\mathbf{r})]. \end{aligned} \quad (2.40)$$

The two correction terms  $\Delta T + \Delta V_{ee}$  are subsumed in  $E_{xc}[\rho(\mathbf{r})]$  which is known as the *exchange-correlation functional*. Similarly to HF, one can find a set of Kohn-Sham orbitals that systematically minimize the energy in a self-consistent manner satisfying the pseudo-eigenvalue equation using the one-electron Kohn-Sham operator  $\hat{h}^{KS}$ :

$$\hat{h}_i^{KS} |\phi_i\rangle = \left( -\frac{1}{2} \nabla_i^2 - \sum_{A=1}^K \frac{Z_A}{|\mathbf{r}_i - \mathbf{R}_A|} + \int \frac{\rho(\mathbf{r}')}{|\mathbf{r}_i - \mathbf{r}'|} d\mathbf{r}' + V_{xc}[\rho(\mathbf{r})] \right) |\phi_i\rangle = \epsilon_i |\phi_i\rangle. \quad (2.41)$$

Here,  $V_{xc}[\rho(\mathbf{r})]$  is the functional derivative,  $V_{xc} = \frac{\partial E_{xc}}{\partial \rho}$ , also called *exchange-correlation potential*. Importantly, the exact exchange-correlation functional  $E_{xc}[\rho(\mathbf{r})]$  that defines  $V_{xc}[\rho(\mathbf{r})]$  is unknown.<sup>[51]</sup> For decades, great effort has been put into constructing one that performs well for all systems resulting in many different approximated functionals that need careful evaluation and testing for each targeted molecular system. For the present thesis, a hybrid generalized-gradient approximation (hybrid GGA) functional called Becke three-parameter exchange and LeeYangParr correlation (B3LYP) functional was chosen. This type of functional depends on the local electron density, the gradient of the density, in order to account for the non-homogeneous nature and the exact asymptotic

## 2. Theoretical Background and Methodology

behavior of the exchange-energy density, the Laplacian which is the second derivative of the gradient, as well as the exact exchange energy for the non-interacting system composed of Kohn-Sham orbitals computed on HF level of theory.<sup>[20,58-61]</sup>

Thus far, DFT was limited to the ground-state energy and density. In order to calculate excited states, a time-dependent variant of the three pillars of DFT, existence theorem, applicability of the variational principle and an orbital ansatz, needed to be formulated. First, the *Runge-Gross theorem*<sup>[62]</sup> constitutes a time-dependent analogue of the first Hohenberg-Kohn theorem and essentially proves a dependency of the time-dependent wave function on the time-dependent electron density. In their argumentation, they show via *reductio ad absurdum* that two time-dependent potentials, such as two time-dependent electric fields, differing only in a purely time-dependent function  $C(t)$ , correspond to two different time-dependent densities, and vice versa. Subsequently, they prove through induction that the electron density determines a unique wave function at each given time step

$$\rho(\mathbf{r}, t) \leftrightarrow v[\rho](\mathbf{r}, t) + C(t) \leftrightarrow \Psi[\rho](\mathbf{r}, t)e^{-i\alpha(t)} \quad \text{with} \quad \frac{\partial\alpha}{\partial t} = C(t). \quad (2.42)$$

Here, the time propagation is given by the TDSE (see equation 2.1). The second requirement is to establish a means to obtain the exact time-dependent density in a self-consistent manner. This is done by applying the variational principle to the action integral using the wave function as a solution to the TDSE and extract the time-dependent electron density as the stationary point of the action integral via the Euler equation:

$$A[\rho] = \int_{t_0}^{t_1} dt \left\langle \Psi(\mathbf{r}, t) \left| i \frac{\partial}{\partial t} - H(t) \right| \Psi(\mathbf{r}, t) \right\rangle \implies \frac{\partial A[\rho]}{\partial \rho(\mathbf{r}, t)} = 0. \quad (2.43)$$

Next, this stationary action principle can be applied to derive the time-dependent variant of the Kohn-Sham equation similarly to how it was established for the time-independent case. Namely, the existence of a time-dependent non-interacting system is assumed whose electron density is equal to the electron density of the real interacting system and which can be determined via the Euler equation. The non-interacting system is represented by a single Slater determinant consisting of single-electron orbitals  $\phi(\mathbf{r}, t)$  so that the electron density of both the fictitious and the real system is given by

$$\rho(\mathbf{r}, t) = \sum_{i=1}^N |\phi_i^{KS}(\mathbf{r}, t)|^2. \quad (2.44)$$

These single-electron wave functions are used to solve the time-dependent Kohn-Sham equations

$$\hat{h}^{KS}[\rho(\mathbf{r}, t)]|\phi(\mathbf{r}, t)\rangle = i \frac{\partial}{\partial t} \phi(\mathbf{r}, t) \quad (2.45)$$

## 2. Theoretical Background and Methodology

where the time-dependent Kohn-Sham operator reads

$$\hat{h}^{KS}[\rho(\mathbf{r}, t)] = -\frac{1}{2}\nabla_i^2 - \sum_{A=1}^K \frac{Z_A}{|\mathbf{r}_i - \mathbf{R}_A|} + \int \frac{\rho(\mathbf{r}', t)}{|\mathbf{r}_i - \mathbf{r}'|} d\mathbf{r}' + V_{xc}[\rho(\mathbf{r}, t)]. \quad (2.46)$$

Again, the exact exchange-correlation potential is not known. One possible approximation to this problem is the so-called *adiabatic approximation* where the exchange-correlation functional is assumed to be local in time and formulated as a functional of the electron density that parametrically depends on time,  $V_{xc}[\rho(\mathbf{r}, t)] = V_{xc}[\rho(\mathbf{r}; \bar{t})]$  adhering to the assumption that each time step corresponds to a different density function. Following this premise, one can simply use the time-independent approximations to the exchange-correlation functional.<sup>[63,64]</sup> Solving the time-dependent Kohn-Sham equation given in equation 2.45 and 2.46 is called *real-time* time-dependent density functional theory (TD-DFT) and constitutes only one possible avenue for a time-propagation within the DFT method. It is mainly applied for investigating matter-external field radiation interactions including laser fields where the electric field strengths exceed the attractive Coulomb field of the nuclei.<sup>[65]</sup>

However, when the interaction with the field are much smaller than the intramolecular interactions and the field induces only a weak excitation and thus a much smaller perturbation from the ground state, *linear-response* TD-DFT is a more common approach.<sup>[66]</sup> In this method, the response of the electron density to a small time-dependent perturbation truncated after the first-order term is considered. To compute the excitation energy for an excited-state  $\Psi_I$  relative to the ground state  $\Psi_0$ ,  $E_I$ , one has to find frequencies of the time-dependent perturbation where the density response function has a pole,  $\omega_I = E_I - E_0$ . This linear density response problem can be formulated as a matrix pseudo-eigenvalue problem whose solution are the poles of the response function.<sup>[67]</sup>

$$\begin{bmatrix} \mathbf{A} & \mathbf{B} \\ \mathbf{B} & \mathbf{A} \end{bmatrix} \begin{pmatrix} \mathbf{X}_I \\ \mathbf{Y}_I \end{pmatrix} = \omega_I \begin{bmatrix} \mathbf{1} & \mathbf{0} \\ \mathbf{0} & -\mathbf{1} \end{bmatrix} \begin{pmatrix} \mathbf{X}_I \\ \mathbf{Y}_I \end{pmatrix}. \quad (2.47)$$

Here,  $\mathbf{A}$  and  $\mathbf{B}$  are sometimes referred to as *orbital rotation Hessians*<sup>[68]</sup> and depend on the energy differences of the Kohn-Sham orbitals, integral over the two-electron Coulomb operator and the exchange-correlation kernel which includes all non-trivial many body effects. Essentially, this matrix can be understood as describing a system of independent electrons where one electron is excited between two orbitals and their orbital energy difference together with correlation effects with other electrons gives the excitation energy upon solving equation 2.47.<sup>[63]</sup> When a solution to 2.47 was found, also the response vector  $(\mathbf{X}_I, \mathbf{Y}_I)$  is obtained which represents particle-hole and hole-particle excitations of the system. The eigenvector element  $\mathbf{X}_I$  corresponds to an excitation from an occupied to an unoccupied virtual orbital, whereas  $\mathbf{Y}_I$  denotes de-excitations from an virtual to an occupied orbital which does not possess clear physical meaning. Dismissing the latter transforms equation 2.47 to

$$\mathbf{A}\mathbf{X}_I = E_I\mathbf{X}_I \quad (2.48)$$

which is called the Tamm-Dancoff approximation (TDA) and has several advantages. Namely, it replaces the non-Hermitian eigenvalue problem by a Hermitian version, it reduces the size of the problem by half and is thus computationally more efficient and has some system- and method-dependent benefits such as reducing triplet instabilities for long-range corrected hybrid functionals.<sup>[69–71]</sup>

## 2.2. Quantitative Wave Function and Electron Density Analysis

Once a number of excited-states were computed with a method of choice, the subsequent accurate description of all calculated states is indispensable to determine state characters, transition energies or other electronic structure properties of the molecular system. However, the analysis of excited states is challenging because a state is usually a linear combination of many different configurations composed of different, often delocalized orbitals so that the assignment of an overall state character upon visual inspection is tedious and not free of personal bias. This is especially true for TMCs which, in addition, often exhibit a high density of states so that a large number of states needs to be considered and subsequently evaluated which is often time consuming and incomplete. In order to provide remedy for this hurdle, the toolbox TheoDORE<sup>[72–74]</sup> was developed to facilitate an unambiguous, reproducible and detailed wave function and electron density analysis both qualitatively and quantitatively and independent of the quantum chemical method employed to compute the states.

The main idea and formalism behind this program is a fragment-based analysis scheme in which the system is divided into different units where excited states are deconstructed by creating electron-hole pair assignments. This enables a characterization of an electron transfer with respect to its origin and destination and hence allows a localization on individual fragments. The theoretical basis for this single-excitation description is given by the one-electron transition density matrix (1TDM). For a transition between the ground state  $|\Psi_0\rangle$  and an excited state  $|\Psi_I\rangle$ , the 1TDM can be written in the second quantization formalism as

$$\gamma_{0I}(r_h, r_e) = \sum_{pq} \phi_p^*(r_h) \underbrace{\langle \Psi_0 | \hat{a}_p^\dagger \hat{a}_q | \Psi_I \rangle}_{\mathbf{T}_{pq}^{0I}(r_h, r_e)} \phi_q^*(r_e) \quad (2.49)$$

with  $r_h$  and  $r_e$  denoting the coordinates of the hole and the electron on  $|\Psi_0\rangle$  and  $|\Psi_I\rangle$  respectively.  $\hat{a}_p^\dagger$  is again the creation operator for orbital  $\phi_p$  and  $\hat{a}_q$  is the annihilation operator for orbital  $\phi_q$ . In less abstract terms, this equation translates to a hole being created in orbital  $\phi_p$  and an electron transition that is annihilated in orbital  $\phi_q$  as destination resulting in the configuration of excited state  $|\Psi_I\rangle$ . Generally, 1TDM has no intuitive interpretation, but it is closely related to the physical observable of the transition dipole moment, which signposts the 1TDM as a suitable basis for a physically meaningful description of excited states. Furthermore, 1TDM is directly related to the response vector  $\mathbf{X}_I$  when using TD-DFT coupled with TDA so that  $T_{ov}^I = X_{ov}^I$ , where the indices

## 2. Theoretical Background and Methodology

$o$  and  $v$  signify all occupied and virtual orbitals respectively.<sup>[70]</sup>

The most important quantitative descriptor in this framework is the *charge transfer number* which allows a quantification of the charge transfer localization in the fragmented molecular system. Taking the 1TDM  $T_{pq}^{0I}$ , if orbitals  $p$  and  $q$  are located on the same fragment, the charge transfer is local and the weight of this excitation is the matrix element  $\Omega_{AA}$  of the charge transfer number matrix. If orbitals  $p$  and  $q$  belong to two different fragments  $A$  and  $B$ , then the weight corresponds to the matrix element  $\Omega_{AB}$ . The charge transfer numbers are a direct result of a two-dimensional population analysis of which the *Löwdin* analysis scheme was chosen for the present thesis. This crucial step precedes a transformation of the 1TDM from a MO to a atomic orbital (AO) basis

$$\tilde{\mathbf{T}}^{0I} = \mathbf{C}\mathbf{T}^{0I}\mathbf{C}^T \quad (2.50)$$

where  $\mathbf{C}$  is the MO-coefficient matrix and the square of each matrix element,  $(\tilde{\mathbf{T}}_{pq}^{0I})^2 = \gamma_{pq}^{0I}$ , measures the contribution of an excitation from the AO  $p$  to  $q$ . The charge transfer number  $\Omega_{AB}$  quantifying over all contributions of excitations originating from any AO located on fragment  $A$  going to any AO located on fragment  $B$ . Because AOs are not orthogonal, a direct sum of the squared matrix elements is not possible and a population analysis has to be performed. For this reason, a *Löwdin orthogonalization* as implemented in TheoDORÉ is applied onto  $\tilde{\mathbf{T}}^{0I}$  so that

$$\bar{\mathbf{T}}^{0I} = \mathbf{S}^{1/2}\tilde{\mathbf{T}}^{0I}\mathbf{S}^{1/2} = (\mathbf{P}\mathbf{Q}^T)\mathbf{T}^{0I}(\mathbf{P}\mathbf{Q}^T)^T \quad (2.51)$$

with  $\mathbf{S}$  denoting the overlap matrix between AOs and  $\mathbf{P}$  and  $\mathbf{Q}$  are matrices comprised of the left and right singular vectors of the MO-coefficient matrix  $\mathbf{C}$ . The matrix elements of the orthogonalized  $\bar{\mathbf{T}}^{0I}$  can be used for summation to calculate the charge transfer number accordingly, e.g.

$$\Omega_{AB}^{0I} = \sum_{p \in A} \sum_{q \in B} (\bar{\mathbf{T}}_{pq}^{0I})^2 = \sum_{i=1} (\gamma_i^{0I})^2. \quad (2.52)$$

If an excited state is a pure singly excited state,  $\Omega_{AB}^{0I} = \Omega^{0I} = 1$ . In states, where double and triple excitations contribute,  $\Omega^{0I} < 1$  and more charge transfer number other than  $\Omega_{AB}^{0I}$  characterize the transition from the ground to this excited state and thus define the state character of  $\Psi_I$ . In a system that is divided into  $n_{frag}$  fragments, the charge transfer analysis produces an  $n_{frag} \times n_{frag}$  matrix including all charge transfer contributions. If more configurations define a particular state which is usually the case, this analysis scheme provides a reproducible and bias-free way to quantify the contributions of each configuration.<sup>[70,73]</sup> Moreover, the qualitative description of excited-states in this framework is not based on canonical orbitals, but rather on more compact natural transition orbitals (NTOs). The latter are obtained by a single value decomposition of 1TDM which is necessary because a transition density is not symmetric and therefore a

## 2. Theoretical Background and Methodology

diagonalization is not possible. The single value decomposition scheme is

$$\mathbf{T}^{0I} = \mathbf{V} \times \text{diag}(\sqrt{\gamma_1}, \sqrt{\gamma_2}, \dots, \sqrt{\gamma_i}) \times \mathbf{W}^T \quad (2.53)$$

where the unitary matrix  $V$  denotes a set of initial orbitals containing holes and  $W$  the final orbitals containing the electrons after the transition and  $\gamma_i$  correspond to the weights of each transition. Typically, the advantage of the NTO transformation is that only a few weights are significantly larger than zero. By considering only these transitions, a very compact representation of an excited state is obtained and effectively reduces the number of configurations that needs to be evaluated. The number of significant NTOs to consider for a given state is defined by the *NTO participation ratio*

$$PR_{NTO} = \frac{(\sum_i \gamma_i)^2}{\sum_i \gamma_i^2} = \frac{4\Omega^2}{\sum_i \gamma_i^2} \quad (2.54)$$

which quantifies how many single-electron excitations are needed to describe the state and is always greater or equal to one.<sup>[72,75]</sup>

### 2.3. Density Matrix Renormalization Group Algorithm

Another key challenge in computational chemistry is the manual selection of active space orbitals when dealing with multi-configurational methods. To remedy this difficulty, the numerical DMRG algorithm offers an appealing automated selection routine to include up to one hundred active space orbitals initially and iteratively reduce to a set of the most important active orbitals based on entanglement descriptors. Hence, this method offers the advantage to design an adequate active space for the chemical problem at hand and essentially turns multi-configurational models into black-box approaches. Additionally, the method enables benchmark calculations on strongly correlated, large molecular systems, which were previously inaccessible due to its favourable polynomial scaling.<sup>[76]</sup> The algorithm was originally introduced in the field of solid state physics for interacting quantum lattice systems<sup>[77,78]</sup> and has made its way into quantum chemistry only fairly recently.<sup>[38,79,80]</sup> Currently, the QCMAquis software suite<sup>[81]</sup> and its graphical user interface SCINE autoCAS<sup>[82]</sup> is in development and already facilitates a routine applicability of DMRG for the investigation of molecular systems exhibiting strong static correlation and slowly also for the investigation of excited states.

Generally, strongly correlated, multi-configurational states arise when several underlying orbitals are near degenerate and a number of Slater determinants significantly contribute to the wave function of the system. Multiple determinants are necessary to consider in order to account for the static correlation energy inaccessible with single reference methods as explained in previous chapters. This situation often occurs in TMCs where several  $d$ - and  $f$ -orbitals exhibit near-degeneracy with often little overlaps to neighboring orbitals. A careful selection of the underlying orbitals considered as active space is mandatory to regain as much static correlation as possible. In this regard, DMRG offers a solution

## 2. Theoretical Background and Methodology

whose theoretical formalism rests upon the *locality principle* of quantum states. It states that, although the overall property of the position of a particle is non-local, the response of the system to an external perturbation is inherently local regardless of the complexity of a system.<sup>[79,83]</sup> This principle is perhaps best conceptualized in a quantum lattice system where a perturbation on one side does not effect the other side of the lattice and remains local. As a consequence of locality, a state described by a large number of determinants must exhibit highly structured expansion coefficients that reflect locality.

Mathematically, locality can be encoded in the wave function by reformulating the expansion as a tensor network. To do so, we start at the Full CI wave function expansion for a given state spanned by  $k$  orbitals in Hilbert space

$$|\Psi_{CI}\rangle = \sum_{\{\sigma\}} c_{\sigma_1\sigma_2\dots\sigma_k} |\sigma_1\sigma_2\dots\sigma_k\rangle = \sum_{\{\sigma\}} c_{\sigma} |\sigma\rangle \quad \text{with } \{\sigma\} = \{|0\rangle, |\uparrow\rangle, |\downarrow\rangle, |\uparrow\downarrow\rangle\} \quad (2.55)$$

$$\sum_i \sigma_i = N$$

where  $|\sigma\rangle$  is the occupation-number representation of the determinant composed of individual occupation number vectors for each orbital,  $\sigma_i$  is the occupation of orbital  $i$  and  $N$  is the total number of electrons. The dimension of the coefficient tensor  $c_{\sigma}$  is  $4^k$  which is unfeasible for  $k > \approx 10$  (which is the reason why commonly only up to a particular excitation order is considered giving rise to truncated CI methods as described in chapter 2.1.4). In strongly correlated systems, a large amount of these coefficients is non-zero and earlier truncation is not possible. One solution is to reformulate the high-dimensional coefficient tensor as a product of  $k$  matrices, namely  $k$  so-called *occupancy matrices* each reflecting the different occupancies of an orbital, which can be explicitly written as

$$|\Psi_{CI}\rangle = \sum_{\{\sigma\}} \sum_{\{j\}} C_{j_1}^{\sigma_1} C_{j_1j_2}^{\sigma_2} \dots C_{j_{k-1}j_k}^{\sigma_k} |\sigma\rangle = \sum_{\{\sigma\}} \mathbf{C}^{\sigma_1} \mathbf{C}^{\sigma_2} \dots \mathbf{C}^{\sigma_k} |\sigma\rangle. \quad (2.56)$$

This solution ansatz contains  $4k$  parameters with the dimension of each matrix tensor being limited to a maximum dimension of  $m$  termed the *maximum number of renormalized block states* or *bond dimension*.<sup>[84]</sup> As a direct result of this dimensional restriction, a significant improvement of computational scaling from factorial to polynomial is achieved. Increasing  $m$  arbitrarily improves the accuracy of the result but also prolongs the computational time which requires careful consideration a priori.<sup>[85]</sup> The DMRG wave function given in equation 2.56 encodes locality through the crucial auxiliary indices  $j_i$  which are omitted in the compact notation of the matrix product state (MPS). The number of elements typically contained in an auxiliary index  $j_i$  is truncated via single-value decomposition and is limited to  $m$  significant values. Considering for instance  $j_1$ , this auxiliary index is associated with the occupancy of  $\sigma_1$  and  $\sigma_2$  and accounts for the correlation between both orbitals via contraction during the DMRG optimization procedure.<sup>[81]</sup>

Hence, DMRG encodes a sequential structure to correlations produced by locality via a one-dimensional orbital topology as visualized in Figure 2.2. Each active space

## 2. Theoretical Background and Methodology

orbital is assigned to a  $\sigma_i$  index called *site* whereby the MPSs are constructed in an one-dimensional lattice. Because of the single-value decomposition, the order of the active space orbitals along this lattice matters and can have an effect on the DMRG outcome.<sup>[85]</sup> The lattice is partitioned into two blocks called *system* and *environment* with two orbitals inbetween in the so-called *two-sided DMRG formalism*.<sup>[84]</sup> During optimization, two adjacent sites are optimized simultaneously by contraction to a *superblock* along their shared auxiliary index to give a two-sided MPS tensor. The superblock Hamiltonian is constructed thereof and diagonalized yielding variationally optimized coefficients

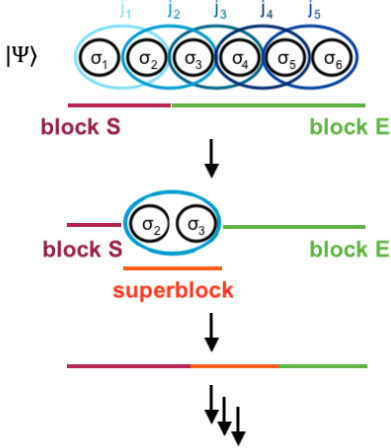


Figure 2.2.: Illustration of the DMRG orbital topology and partitioning scheme of a micro-iteration during optimization.

that result in the lowest ground state energy. The optimized two-site tensor is again split into two MPS tensors via truncated single-value decomposition which concludes a micro-iteration. In the subsequent micro-iteration, the system block increases and the environment block shrinks by one orbital. This procedure is continued until the environmental block only consists of one orbital. Then, the optimization series changes direction so that the system block is consecutively increased until all MPS tensors have been optimized and a macro-iteration termed *sweep* is concluded. Generally, it is advisable to perform multiple sweeps because the optimization process is improved during each sweep until convergence is achieved. The third parameter that needs some consideration and can have an effect on the DMRG outcome is the choice of the initial environment guess in the first warm-up sweep. While only the parameter  $m$  strongly affects the accuracy of the DMRG outcome, the orbital ordering and the initial environment guess together with the size of

the active space mainly influences how fast convergence is reached.<sup>[85]</sup>

Crucially, DMRG provides a means for determining the contribution of each orbital to the static correlation energy gain of the active space. Conceptually, let's consider the last step of a macro-iteration when the system contains one orbital and all other orbitals belong to the environment block. In this case, the optimized CI coefficients obtained in this micro-optimization step can be used to form the *one-orbital* reduced density matrix (1o-RDM) whose eigenvalues  $\omega_{\alpha,i}$  for orbital  $i$  after diagonalization lead to the most important descriptor of the DMRG diagnostic, the *single-orbital von Neumann entropy*  $s(1)_i$  for orbital  $i$ :

$$s(1)_i = - \sum_{\alpha=1}^4 \omega_{\alpha,i} \ln \omega_{\alpha,i} \quad (2.57)$$

where  $|i\rangle$  constitutes a spatial orbital which requires a 1o-RDM dimension of  $4 \times 4$  corresponding to the four different single-orbital basis states  $\{\sigma\}$  (see equation 2.55) and  $\alpha$  therefore runs over the four eigenvalues of the 1o-RDM. Because only two orbitals occupy

## 2. Theoretical Background and Methodology

the lateral lattice sites, in practice, the 1o-RDM is determined from the many-particle reduced density matrix by integrating out all other orbital-degrees of freedom except those of orbital  $i$ .<sup>[86]</sup> The  $s(1)_i$  value of this one-orbital system quantifies the entanglement to the environment it is embedded in, namely all other active space orbitals. It is a measure for how strongly the orbital interacts with all other orbitals, or in other words, how strongly the orbital occupation number deviates from two or zero.<sup>[76,87]</sup> The maximum entanglement is achieved when all four occupation types  $\{\sigma\}$  are equally likely ( $\omega_{\alpha,i} = 0.25$  for all  $\alpha$ ) which corresponds to  $\ln 4 \approx 1.39$ . Due to this theoretical maximum, a multi-configurational diagnostic  $Z_{s(1)}$  was introduced and implemented in autoCAS<sup>[82]</sup> which reads for a total of  $k$  orbitals

$$Z_{s(1)} = \frac{1}{k \ln 4} \sum_i^k s(1)_i \quad (2.58)$$

and allows for numbers between 0, corresponding to no entanglement, and 1, denoting maximum entanglement. With this scaling, different active spaces can be compared to one another and a threshold value can be defined to discard orbitals based on their degree of entanglement. Moreover, maximum entanglement can only be achieved if the number of electrons equals to the number of spacial orbitals over which they are distributed together with an even number of orbitals. If the number of orbitals is not restricted, the four possible electronic occupations cannot be realized in the large number of virtual orbitals which artificially lowers  $Z_{s(1)}$ .<sup>[80]</sup>

The second important descriptor of the DMRG diagnostic is the *mutual information*  $I_{ij}$ , to measure the information exchange between two pairs of orbitals.<sup>[88]</sup>  $I_{ij}$  is calculated from the two-orbital entropy  $s_{ij}(2)$  of two orbitals  $i$  and  $j$

$$s(2)_{ij} = - \sum_{\alpha=1}^{16} \omega_{\alpha,ij} \ln \omega_{\alpha,ij} \quad (2.59)$$

obtained from the 16 eigenvalues  $\omega_{\alpha,ij}$  of the *two-orbital* RDM (2o-RDM). Analogous to above, the latter is computed from the many-particle density matrix by tracing out all other orbital-degrees of freedom except those of orbital  $i$  and  $j$  and has a dimension of  $16 \times 16$ .<sup>[86]</sup> In the formalism introduced by Rissler et al.,<sup>[88]</sup>  $I_{ij}$  is derived by subtracting the two-orbital entropy from both single-orbital entropies

$$I_{ij} = \frac{1}{2}(s(1)_i + s(1)_j - s(2)_{ij})(1 - \delta_{ij}). \quad (2.60)$$

More specifically,  $I_{ij}$  quantifies how statically correlated two orbital pairs are within the environment they are embedded in. Both entropy-based entanglement descriptors,  $s(1)_i$  or  $Z_{s(1)}$  and  $I_{ij}$ , need to be taken into account when evaluating the active space. Based on published studies, it can be concluded that the orbital selection based on the single-orbital entropy rather than the mutual information yields more accurate and faster converged results.<sup>[89,90]</sup>

## 3. Computational Details

This thesis can be partitioned into two sets of static calculation types. On the one hand, excitations within the Frank-Condon region of the ground state structures in solvent were performed on TD-DFT level of theory and subsequently analyzed regarding absorption properties and charge transfer types as discussed in chapter 4.1 and 4.2. On the other hand, multi-reference methods, namely CASSCF and MS-CASPT2, were employed to model and investigate the photorelease of both CO and NO from the coordination sphere of the metal center. For this task, an extensive active space testing was performed using DMRG as well as the traditional trail-and-error routine as summarized in chapter 4.3 to 4.5.

### Single-reference methodology

All structures were first optimized with the semi-empirical method HF-3c<sup>[91]</sup> and afterwards using DFT coupled with the hybrid functional B3LYP and two different Karlsruhe basis sets def2-SVP and def2-TZVP whose performance will be briefly compared in the following. All geometry optimizations and frequency calculations were carried out with the Gaussian 16<sup>[92]</sup> program package and all vertical TD-DFT excitations were performed with the program ORCA.<sup>[93,94]</sup> In these calculations, an effective core potential (ECP) for both central heavy metal atoms was employed in order to reduce computational cost which means that a valence-only basis is assumed by excluding the highly contracted and chemically inert core basis functions.<sup>[95]</sup> Through this approximation, ultimately 28 electrons of molybdenum were considered as frozen core and thus excluded from all computations and 14 electrons were included as valence electrons. For cobalt, 10 electrons constitute the excluded frozen core and 17 electrons were considered as valence. Another approximation utilized to accelerate the DFT and TD-DFT computations is the RIJCOSX approximation in which the Coulomb part of the Fock matrix is computed with the Split-RI-J method with additional assistance of an automatically generated larger auxiliary basis set (AutoAux) and the exchange part with a semi-numerical integration technique (COSX).<sup>[96,97]</sup> Furthermore, an atom-pairwise dispersion correction with the Becke-Johnson damping scheme (D3(BJ)) was included which is necessary in DFT and TD-DFT to account for long-ranging effects such as London dispersion interactions.<sup>[98,99]</sup> Furthermore, solvent effects were considered by assuming both molybdenum molecules in solution with acetonitrile (dielectric constant  $\epsilon=35.6$  a.u.) and the cobalt complex in toluene ( $\epsilon=2.4$  a.u.). The choice on both solvents was guided by two pre-studies<sup>[14,15]</sup> which provided experimental reference spectra. For this purpose, Gaussians's C-PCM solvation model and ORCA's SMD solvation model was utilized which both include electrostatic interactions via the conductor-like polarizable continuum model (CPCM)

### 3. Computational Details

with a cavity-dispersion solvent-structure (CDS) correction.<sup>[100–103]</sup>

For the excited-state calculations, the TDA approximation to TD-DFT was considered as explained in the previous chapter. In total, 60 singlet and 60 triplet states were computed including SOCs by using quasi-degenerate perturbation theory.<sup>[104]</sup> The performance of both levels of theory, TD-DFT B3LYP-D3(BJ)/def2-SVP and TD-DFT B3LYP-D3(BJ)/def2-TZVP, were compared to experimental UV-Vis and IR absorption spectra extracted from unpublished work by Nürnberger et al.<sup>[14]</sup> and the published work by Kaim et al.<sup>[15]</sup> For this aim, the excitation energies and oscillator strengths of all states were convoluted with Gaussian functions of FWHM 0.7 eV if not stated otherwise. The multi-configurational character of each state was decomposed into different charge transfer characters using the wave function analysis package TheoDORE.<sup>[72–74]</sup>

Following the optimization and frequency calculation of the ground state of both molybdenum systems, a set of 100 geometries distributed around the equilibrium geometry of each system was generated via harmonic Wigner-sampling<sup>[105]</sup> using the program package SHARC 2.1.<sup>[106–108]</sup> On each geometry, a single point calculation was performed considering - in analogy to the Frank-Condon excitation - 60 singlet and 60 triplet states. From this ensemble data, an absorption spectrum was simulated via the nuclear ensemble method<sup>[109]</sup> in which pairs of excitation energies and oscillator strengths were convoluted by Gaussian functions using a FWHM of 0.15 eV. Additionally, an absorption spectrum of the Wigner ensemble was generated and subsequently decomposed into different charge transfer contributions obtained with TheoDORE.

## Multi-reference methodology

For the second part of this thesis investigating the dissociation behaviour of ligands, all structures were re-optimized using the def2-TZVPP basis set and gas phase setting with otherwise equivalent conditions as described above. The new basis set was chosen because the additional second set of polarized functions adds flexibility to the basis set and therefore aids bond breaking simulations. In order to obtain a suitable set of active space orbitals, the DMRG algorithm was first performed on the equilibrium geometry as well as on the respective CO- and NO-dissociated geometries where the bond length was set to 4 Å. The initial HF orbitals of each geometry were calculated using the SCF program of the Molcas<sup>[110,111]</sup> suite of programs and subsequently utilized in the matrix product operator based DMRG program QCMAquis<sup>[81]</sup> to obtain the entanglement measures. For these calculations, Cholesky decomposition<sup>[112]</sup> with the standard Molcas settings was adopted for the two-electron integrals and an energy threshold of  $10^{-8}$  was chosen. Additional DMRG-SCF parameters include a bond dimension  $m$  of 250, maximum of 5 sweep iterations, optimization on CI-only basis and a total of 30 electrons in 26 orbitals for **CpMo**, 46 electrons in 33 orbitals for **TacnMo** and 38 electrons in 26 orbitals for **DabCo**. The latter was determined by excluding all atom-centered inner-core orbitals (e.g. incl. 1s, 2s, 2p, 3s, 3p, 4s, 4p for Mo and 1s, 2s for C, N, O, Co etc.) and energetically low-lying  $\sigma$  and  $\sigma^*$  MOs, which is similar to the ECP rationale. Orbital ordering for the DMRG algorithm corresponds to the natural order by increasing energy. Hence, the

### 3. Computational Details

DMRG methodologies can be summarized by the common notation<sup>[89]</sup> DMRG[250](30,26)-SCF for **CpMo**, DMRG[250](46,33)-SCF for **TacnMo** and DMRG[250](38,26)-SCF for **DabCo**. Moreover, 8 states were included resulting in 24 entanglement diagrams (8 states of every geometry) for each complex. A final entanglement diagram of each geometry was computed by selecting out of all states (indicated by index  $v$ ) the maximum state-specific single orbital entropy per orbital and the maximum state-specific mutual information per pair of orbitals so that

$$s(1)_i = \max_v (s(1)_i^v) \quad \text{and} \quad I_{ij} = \max_v (I_{ij}^v). \quad (3.1)$$

Compared to the alternative route of averaging the entanglement descriptors over all computed states, this procedure ensures that after defining a threshold, all orbitals contributing most to the static correlation energy gain are included and do not perish within the average.<sup>[113]</sup>

Thereafter, different smaller active spaces were selected and their performance in simulating one-dimensional potential energy scans for a CO and NO dissociation was investigated including both singlet and triplet states. For this purpose, CASSCF and MS-CASPT2 calculations were performed using the program Molcas with an ANO-RCC-VDZP basis set. Additionally, the scalar relativistic Douglas-Kroll-Hess correction<sup>[114]</sup> to the one-electron Hamiltonian and Cholesky decomposition for the computation of the two-electron integrals was employed.<sup>[112]</sup> For MS-CASPT2, different level shifts were tested in benchmark calculations prior to the potential scans which yielded an imaginary shift of 0.1 a.u. to be optimal. However, the final IPEA shift value remains controversial and the corresponding testing thereof will be discussed in detail in chapter 4.3.1.

Additionally, the potential energy scans of **CpMo** on CASSCF(6,10) level of theory was calculated on basis of an adiabatic and a diabatic Hamiltonian. For this aim, the overlap matrices between wave functions of subsequent steps in the potential energy scans were computed using SHARC 2.1<sup>[115]</sup> and the diabatization of the Hamiltonian and the dipole matrices were subsequently calculated by hand.

## 4. Results and Discussion

### 4.1. Vertical Excitation and Charge Transfer Analysis

#### 4.1.1. Geometry Optimization and Structural Peculiarities

For the DFT and TD-DFT calculations, the hybrid functional B3LYP was selected upon literature review based on the performance of different functionals for the computation of TMCs. According to published studies, between B3LYP, BP86, B98, PBE0 and PBE, B3LYP exhibits low mean absolute errors and performs well for first and second row transition metal systems, in particular involving cobalt.<sup>[116–118]</sup> Regarding the basis set, the performance of def2-SVP and def2-TZVP was compared in the initial optimization of **CpMo** and **TacnCo** with both yielding very similar results. The superimposed structures are depicted in Figure 4.1 and visually supports the equality of both optimization outcomes. More specifically, a RMSD of 0.016 Å for **CpMo** and a RMSD of 0.025 Å for **TacnMo** was determined. Comparing selected bond lengths and angles, given in table A.1 and A.2 of Appendix A, shows that the Mo-N<sub>NO</sub> bond is slightly longer and the Mo-Cp distance is marginally shorter in the optimized structure using def2-SVP. Due to this irrefutable similarity, further calculations were performed using only the def2-SVP basis set because computation times are about 8.7 times higher for the def2-TZVP basis set which is of particular consequence for the 58 atom heavy **TacnMo**.

Independent of the basis set, several structural peculiarities need to be mentioned. First, **CpMo** possesses two different conformers - staggered and eclipsed - with respect

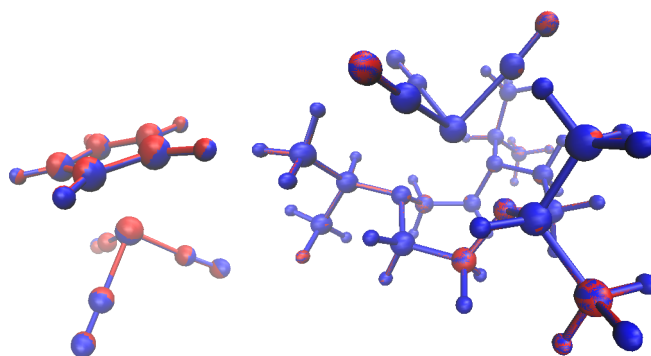


Figure 4.1.: Superimposed structures of **CpMo** (*left*) and **TacnMo** (*right*) computed with DFT B3LYP-D3(BJ)/def2-SVP implicit acetonitrile (*blue*) und DFT B3LYP-D3/def2-TZVP implicit acetonitrile (*red*).

#### 4. Results and Discussion

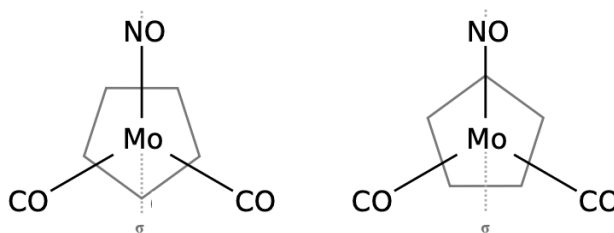


Figure 4.2.: Staggered (*left*) and eclipsed (*right*) conformer of **CpMo** depending on the dihedral angle being either  $180^\circ$  or  $0^\circ$  between NO and the  $\text{CH}_{\text{Cp}}$  in the same mirror plane  $\sigma$ .

to the dihedral angle of either  $180^\circ$  or  $0^\circ$  between NO and  $\text{CH}_{\text{Cp}}$  with both lying in the same mirror plane  $\sigma$  as shown in Figure 4.2. The two conformers are very close in energy which renders the optimization procedure rather difficult because the wrong conformer is easily obtained yielding an imaginary frequency of  $9.92 \text{ cm}^{-1}$  in mode 6 which constitutes a rotational movement of the Cp-ring as well as a slight umbrella-type motion of the  $\text{Mo}(\text{CO})_2\text{NO}$  fragment in relation to the Cp-plane. Convergence to the right conformer was only achieved by using Gaussian instead of Orca and enforcing particularly tight cutoffs on forces and step sizes, as well as by computing force constants and the Hessian matrix (second derivative of the energy with respect to coordinates) at every point. Furthermore, it is important to mention that this problem only occurred during the optimization of the structure in implicit solvent. Hence, one could also contemplate that the solvent model of Orca might be the reason why convergence without imaginary frequency was only achieved using Gaussian. In the end, the staggered conformer was determined to be the energetically lowest ground state structure of **CpMo** in gas phase and the eclipsed conformer (dihedral angle  $\text{HCMoN} = 0.847^\circ$ ) in implicit acetonitrile for the def2-SVP computation. Both superimposed structures are depicted in Figure 4.3.

Furthermore, the NO-ligand when coordinated to a metal center in a terminal fashion

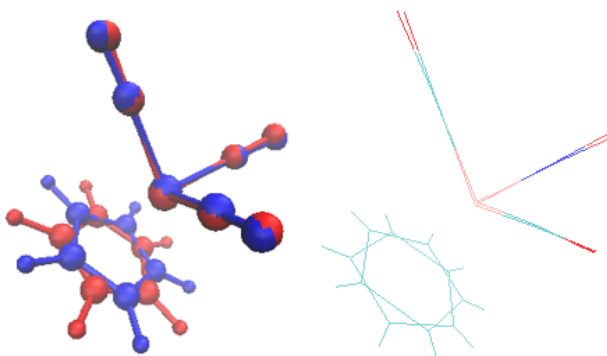


Figure 4.3.: Superimposed structures of the ground state geometry of **CpMo** in gas phase (*blue*) and in implicit solvent in (*red*) (DFT B3LYP-D3(BJ)/def2-SVP).

can have either a linear or bend binding mode. For both molybdenum complexes, the binding mode clearly is linear with an Mo-N-O bond angle of  $178^\circ$ . In this mode, according to the neutral ligand method, NO exhibits a synergistic three-electron  $\sigma$ -donor and  $\pi$ -acceptor binding scheme.<sup>[119]</sup> Determining the NO ligand as three electron donor, both molybdenum complexes obey the 18-electron rule.

A closer look at the **TacnMo** complex reveals that the Tacn-ligand, as well as the Cp-ligand, coordinate *facial* to Mo. Moreover, the three *i*Pr-groups are turned towards the Mo(CO)<sub>2</sub>NO-fragment and thereby enclose the central atom. Lastly, the three Mo-N<sub>Tacn</sub> bonds are with 2.34, 2.39 and 2.32 Å almost equivalent.

#### 4.1.2. UV/Vis Absorption Spectra

For the generation of a UV/Vis absorption spectrum, the in implicit acetonitrile optimized ground state structures of both molybdenum complexes were vertically excited within the Frank-Condon region including 60 singlet and 60 triplet states. Based on excitation energies and oscillator strengths, an absorption spectrum was computed via convolution with Gaussian functions. In addition, a harmonic Wigner sampling procedure was performed generating 100 geometries around the ground state equilibrium structure. Analogously, each of the 100 geometries was vertically excited and an absorption spectrum was calculated thereof. The outcome of these calculations is depicted in Figure 4.4 for **CpMo** and in Figure 4.5 for **TacnMo** together with the experimentally measured absorption spectra.<sup>[14]</sup> The experimentally measured UV/Vis spectra during photoexcitation at 285 nm or 4.35 eV for several exposure times is given in Figure A.4 and A.5.

Generally, good agreement between the experimental and simulated spectrum is found for **CpMo**. Nürnberger et al.<sup>[14]</sup> have previously identified three distinct absorption bands, namely an absorption peak around 194 nm, a smaller peak at 219 nm and a weak shoulder at 255 nm (indicated by black arrows in Figure 4.4). Moreover, upon continuous illumination for about 10 min, they found an uprising signal between 310 to 320 nm and an isosbestic point at 268 nm (see Figure A.4). Both simulated spectra generated via excitation of the equilibrium geometry clearly exhibit the characteristic absorption bands at 194 and 255 nm. However, the peak at 219 nm is only discernible in the B3LYP/def2-SVP simulation using a convolution of 0.7 eV FWHM. The spectrum of the Wigner distribution, whose superimposed structures are also depicted in Figure 4.4, shows all three distinct absorption bands. The signals at 219 and 255 nm are slightly red-shifted for about 15 nm and 20 nm respectively in the simulated spectra.

A closer inspection of the state distributions plotted at the bottom of the spectrum, with the colored Gaussians representing the distribution of each computed singlet state of 100 excited geometries, reveals that four states are particularly highly absorbing. Singlet state S<sub>60</sub> (with an excitation energy of 7.82 eV and an oscillator strength of 0.056 a.u. for the ground state geometry) and S<sub>55</sub> (with an excitation energy of 7.48 eV and an oscillator strength of 0.018 a.u. for the ground state geometry) fall within the main peak region of 194 nm, state S<sub>33</sub> (with an excitation energy of 6.39 eV and an oscillator strength of 0.007 a.u. for the ground state geometry) contributes to the band at 219 nm and state S<sub>7</sub> (with an excitation energy of 4.30 eV and an oscillator strength of 0.007 a.u. for the

## 4. Results and Discussion

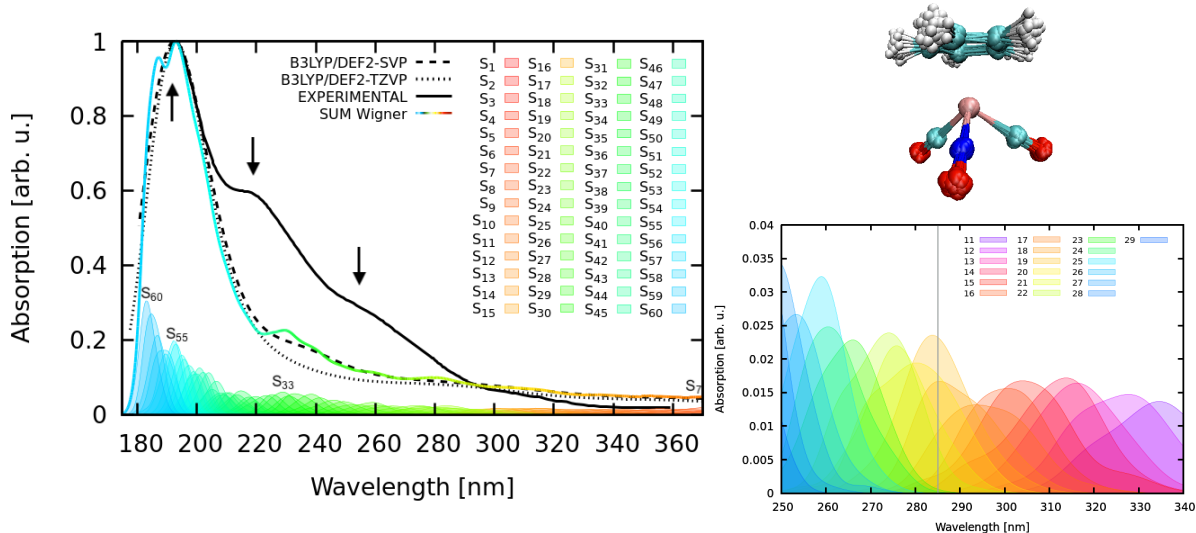


Figure 4.4.: Absorption spectra of **CpMo** with the experimental spectrum<sup>[14]</sup> given in black, the simulated spectra based on the equilibrium geometry excitation in dashed black (convolution with FWHM = 0.7 eV, blue-shift correction of the B3LYP/def2-SVP spectrum is 1.12 eV and of the B3LYP/def2-TZVP spectrum is 1.00 eV) and the simulated spectrum based on the excitation of the 100 Wigner-sampled geometries (superimposed structures *upper right*) given in color (B3LYP/def2-SVP, convolution with FWHM = 0.15 eV, blue-shift correction 1.00 eV); colored Gaussians represent the state distribution of the excited Wigner geometries; grey line indicates experimental setup for photoexcitation using a 285 nm diode with the corresponding measured absorption spectra for different exposure times given in Figure A.4 (CASSCF spectra for reference in Figure A.6) (implicit acetonitrile).

ground state geometry) represents the highest absorbing state at higher wave lengths. With the experimentally chosen excitation energy of 285 nm or 4.35 eV, one can reach up to state  $S_{23}$  with only a few of the sampled geometries of **CpMo** and up to state  $S_{19}$  with a majority of sampled structures as evidenced in the spectrum extract given in Figure 4.4 (*bottom right*).

For **TacnMo**, similar conclusions can be drawn. Experimentally, two strong absorption bands have been found at 265 nm and 208 nm with the latter being accompanied by a weak shoulder at 235 nm (indicated by black arrows in Figure 4.5). In addition, a weak band mound has been identified at 330 nm rising within 15 min UV-light exposure which is not discernible at the beginning of the UV-light excitation and an isosbestic point at 308 nm (see Figure A.5).<sup>[14]</sup> The simulated spectra generated via equilibrium geometry excitation both clearly reproduce the two main peaks at 265 and 208 nm, whereas the weak shoulder at 235 nm is not well-defined in either of the two spectra using Gaussians with FWHM of 0.7 eV for convolution. The Wigner distribution, whose superimposed structures are also depicted in Figure 4.5, exhibits all three experimentally determined peaks and again agrees best with the experimental spectrum. The broad signal at 265 nm is clearly red-shifted in all three simulated spectra, more specifically

## 4. Results and Discussion

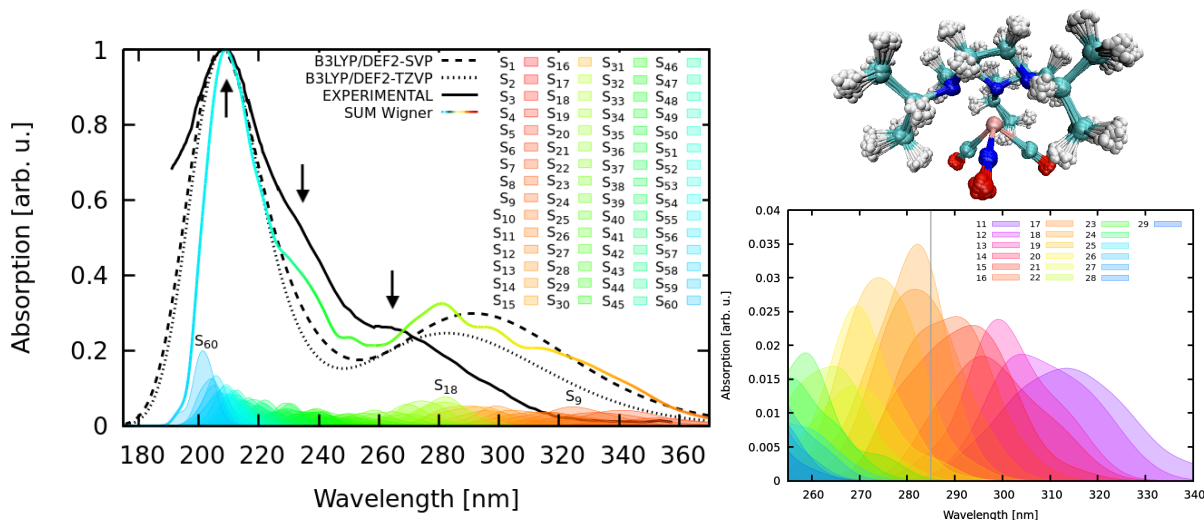


Figure 4.5.: Absorption spectra of **TacnMo** with the experimental spectrum<sup>[14]</sup> given in black, the simulated spectra based on the equilibrium geometry excitation in dashed black (convolution with FWHM = 0.7 eV, blue-shift correction of the B3LYP/def2-SVP spectrum is 0.93 eV and of the B3LYP/def2-TZVP spectrum is 0.80 eV) and the simulated spectrum based on the excitation of the 100 Wigner-sampled geometries (superimposed structures *upper right*) given in color (B3LYP/def2-SVP, convolution with FWHM = 0.15 eV, blue-shift correction 0.80 eV); colored Gaussians represent the state distribution of the excited Wigner geometries; grey line indicates experimental setup for photoexcitation using a 285 nm diode with the corresponding measured absorption spectra for different exposure times given in Figure A.5 (CASSCF spectra for reference in Figure A.7) (implicit acetonitrile).

30 nm in the B3LYP-D3(BJ)/def2-SVP simulation of the equilibrium geometry excitation and 15 nm for the other two computations.

The state distributions show that there are three distinct high-absorbing states in the excitation of the Wigner ensemble: Singlet state  $S_{60}$  (with an excitation energy of 7.17 eV and an oscillator strength of 0.003 a.u. for the ground state geometry) falling within the main peak region of 208 nm, as well as state  $S_{18}$  (with an excitation energy of 5.28 eV and an oscillator strength of 0.000 a.u. for the ground state geometry) and state  $S_9$  (with an excitation energy of 4.87 eV and an oscillator strength of 0.005 a.u. for the ground state geometry) contributing to the broad peak at 265 nm. All three states exhibit relatively low oscillator strengths in the excitation of the ground state geometry where the neighboring state  $S_{58}$  (with an excitation energy of 7.03 eV and an oscillator strength of 0.007 a.u.),  $S_{17}$  (with an excitation energy of 5.25 eV and an oscillator strength of 0.011 a.u.) and  $S_8$  (with an excitation energy of 4.77 eV and an oscillator strength of 0.016 a.u.) have higher oscillator strengths in the corresponding energy regions. Hence, states  $S_{60}$ ,  $S_{18}$  and  $S_9$  become more significant in the excitation of 100 geometries as an ensemble. With an illumination at 285 nm or 4.35 eV, singlet state  $S_{21}$  can be reached with a small fraction and singlet state  $S_{18}$  with the majority of 100 Wigner-sampled geometries (see Figure 4.5 *bottom right*).

## 4.1.3. Qualitative Wave Function Analysis

In order to describe excited states, determining the state character is important. A state character is assigned by close inspection of MOs involved in the electronic transition which is often not free of personal bias as explained in chapter 2. It is important to emphasize the fact that MOs have no physical meaning per se and are mere mathematical functions describing the location and wave-like behavior of electrons. For many TMCs, as is the case of **CpMo** and **TacnMo**, MOs are often delocalized and excited states exhibit significant multi-configurational composition which complicates the character assignments.<sup>[70]</sup> Nonetheless, in order to gain deeper insight into the excited states, two of the brightest singlet states for each complex will be discussed in detail regarding possible character assignments based on the visual inspection of frontier MOs. This qualitative discussion will be followed by a quantitative wave function analysis in the next section.

Generally, the MOs of **CpMo** in canonical form are rather delocalized as depicted in Figure 4.6 (*left*). The three highest-occupied MOs (abbreviated as H, H-1, H-2 in decreasing energy) are either  $\pi(\text{d}(\text{Mo})+\pi^*(\text{NO}))$  or  $\pi(\text{d}(\text{Mo})+\pi^*(\text{CO}))$  with the highest occupied molecular orbital (HOMO), abbreviated as H, and the energetically lower orbital H-1 exhibiting minor contributions from p-orbitals located on the Cp-ligand. The energetically lowest-unoccupied MOs are either  $\pi$ - or  $\pi^*$ -MOs (abbreviation scheme L, L+1, L+2 etc. with increasing energy) exhibiting stronger delocalization compared to the occupied MOs. Two of the brightest states are  $S_6$  with an oscillator strength of 0.023 a.u. and  $S_7$  with an oscillator strength of 0.007 a.u. and are of multi-configurational character. While  $S_6$  consists of 58 % electronic excitations from H to L+2 ( $\pi(\text{MoCO})\pi(\text{MoCO})$ ), 23 % of H to L+4 ( $\pi(\text{MoCO})\pi(\text{MoCp})$ ) and 4 % of H-2 to L+2 charge transitions

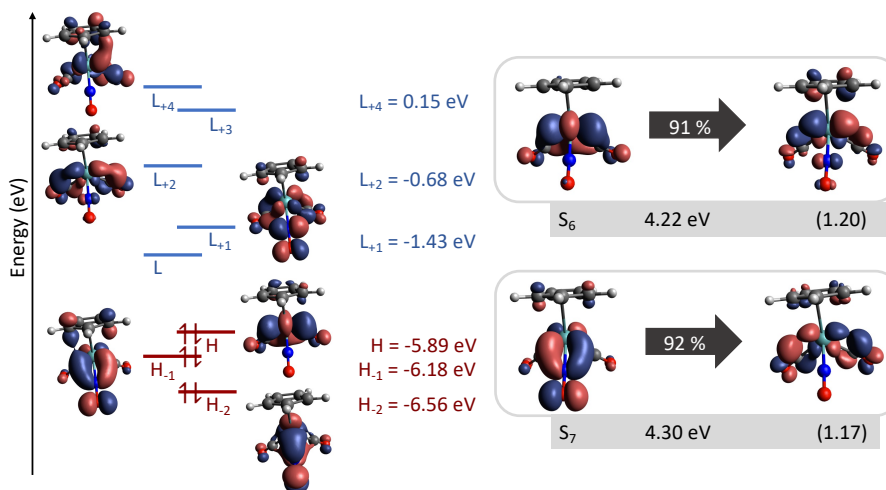


Figure 4.6.: Frontier canonical orbitals of **CpMo** (*left*) and main leading NTOs of the two brightest states including label for state number, excitation energy and PR<sub>NTO</sub> in parenthesis (*right*) (TD-DFT B3LYP-D3(BJ)/def2-SVP implicit acetonitrile).

## 4. Results and Discussion

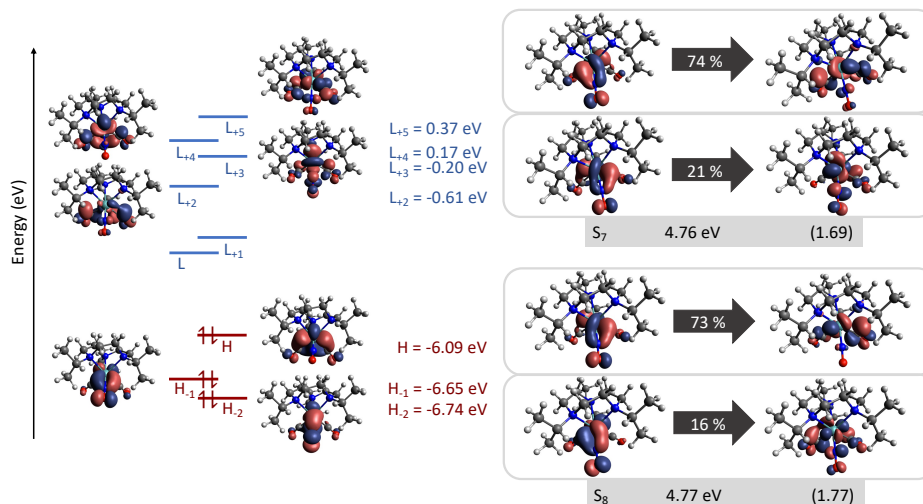


Figure 4.7.: Frontier canonical orbitals of **TacnMo** (left) and main leading NTOs of the two brightest states including label for state number, excitation energy and in parenthesis (right) (TD-DFT B3LYP-D3(BJ)/def2-SVP implicit acetonitrile).

( $\pi(\text{MoNO})\pi(\text{MoCO})$ ), S<sub>7</sub> includes 86 % H-1 to L+2 ( $\pi(\text{MoNO})\pi(\text{MoCO})$ ) and 4 % H-1 to L+1 ( $\pi(\text{MoNO})\pi^*(\pi(\text{MoCO})\text{NO})$ ) electronic transitions. Hence, an overall state character assignment is difficult, also due to the delocalization of the MOs. A more compact description is achieved on basis of NTOs depicted for both bright states in Figure 4.6 (right). The PR<sub>NTO</sub> for both states show that only one transition is necessary to fully describe both states on basis of NTOs. Namely, the main character of state S<sub>6</sub> is  $\pi(\text{MoCO})n(\text{MoCO})$  with a weight of 91 %, whereas S<sub>7</sub> is described with a state character of  $\pi(\text{MoNO})\pi(\text{MoCO})$  with a weight of 92 %.

Similarly, the canonical orbital basis hampers the state character assignment for selected states of **TacnMo** due to an even more pronounced multi-configurationality. In Figure 4.7 on the left hand side, the frontier orbitals in canonical form important for the description of the two brightest states are shown. The three lowest HOMOs are all three binding MOs between a d-orbital of the metal and either a  $\pi^*$  located on the NO- or both CO-ligands. Similarly to **CpMo**, the LUMOs exhibit a slightly higher delocalization compared to the HOMOs. The two brightest states of **TacnMo** are S<sub>7</sub> and S<sub>8</sub> having an oscillator strength of 0.014 a.u. and 0.016 a.u. respectively. S<sub>7</sub> consists of multiple configurations, namely 29 % H-1 to L+2 ( $\pi(\text{MoNO})\pi(\text{MoCO})$ ), 23 % H to L+2 ( $\pi(\text{MoCO})\pi(\text{MoCO})$ ), 14 % H to L+5 ( $\pi(\text{MoCO})\pi^*(\text{MoCO})$ ), 12 % H-1 to L+3 ( $\pi(\text{MoNO})\pi^*(\text{MoNO})$ ) and 5 % H-2 to L+2 ( $\pi(\text{MoNO})\pi(\text{MoCO})$ ), whereas S<sub>8</sub> is characterized by seven transitions of weight >5 % including 34 % H-1 to L+2 ( $\pi(\text{MoNO})\pi(\text{MoCO})$ ), 13 % H to L+4 ( $\pi(\text{MoCO})\pi^*(\text{MoCO})$ ) and 12 % H to L+5 ( $\pi(\text{MoCO})\pi^*(\text{MoCO})$ ). Transformation into NTOs proves again beneficial because it significantly reduces the amount of transitions to consider for the state character appointment. As shown in Figure 4.7 on the right hand side, S<sub>7</sub> can be

## 4. Results and Discussion

described with two configurations, namely  $\pi(\text{MoNO})\pi(\text{MoCO})$  with a weight of 74 % and  $\pi(\text{MoNO})\pi^*(\text{MoNOCO})$  with a weight of 21 %. Also  $S_8$ , can be described by two transition types, namely as having a character of  $\pi(\text{MoNO})\pi(\text{MoCO})$  with a weight of 73 % and  $\pi(\text{MoNO})\pi^*(\pi(\text{MoCO})\text{NO})$  with a weight of 16 %.

### 4.1.4. Quantitative Charge Transfer Analysis

The manual inspection of the frontier orbitals as performed above is quite tedious for more than two states. However, qualitative state characterization is primarily dependent on determining where an excitation originated and where it goes to. In the quantitative wave function analysis procedure as described in chapter 2.2, charge transfer numbers allow an automatization of this assignment. In order to determine the charge transfer numbers for each state, the molecule under investigation needs to be partitioned into fragments to localize electronic transitions. For this purpose, a hierarchical clustering algorithm introduced by Mai et al.<sup>[70]</sup> was used to evaluate meaningful clustering schemes. Intuitively, we decided beforehand to define four clusters for both complexes: one containing the metal center, one including the NO-ligand, one combining both CO-ligands and either Cp or Tacn as one large cluster within the complex. For **CpMo**, the decision to subsume both CO-ligands as one cluster was due to symmetry. Because **CpMo** belongs to the  $C_S$  point group with a central mirror plane, both CO ligands should be equivalent due to symmetry. Contrary, **TacnMo** belongs to the  $C_1$  point group and essentially has no symmetry. Therefore, two questions arose which were aimed to resolve by the hierarchical clustering algorithm: First, because of the absence of higher symmetry elements (other than identity), do the two CO-ligands behave differently when considered as separate fragments? Secondly, due to the large size of the Tacn-ligand containing a total of 51 atoms, how - if at all - should this ligand be partitioned for the charge transfer analysis? Before answering both questions, the diagnostic concept is first described with the outcome of the hierarchical clustering analysis performed on **CpMo**.

Important for the hierarchical clustering algorithm are two concepts. The first concept is the correlation coefficient that measures how each pair of fragment is correlated. Hence, it describes, for instance, whether an excitation from the CO-ligands to the Mo-center is simultaneously occurring as an excitation from the NO-ligand to the same destination. Based on these coefficients a correlation matrix is assembled with perfect correlation being indicated by a coefficient value of 1 or color *black* and no correlation by a coefficient value of 0 or color *white* (as can be seen from Figure 4.8 or 4.9). The algorithm further differentiates between a hole correlation, measuring if two fragments are likely to release electron density simultaneously (see Figure 4.8 *lower left triangular matrix*), and an electron correlation, quantifying whether two fragments are likely to receive electron density at the same time (*upper left triangular matrix*). With the correlation matrices, it becomes evident that not all clustering schemes lead to information gain because fragments that behave equally can be subsumed to one fragment. The latter information is perhaps more easily extracted from the dendrogram computed from the matrix. More specifically, the dendrogram is obtained from the agglomerative algorithm that enables

## 4. Results and Discussion

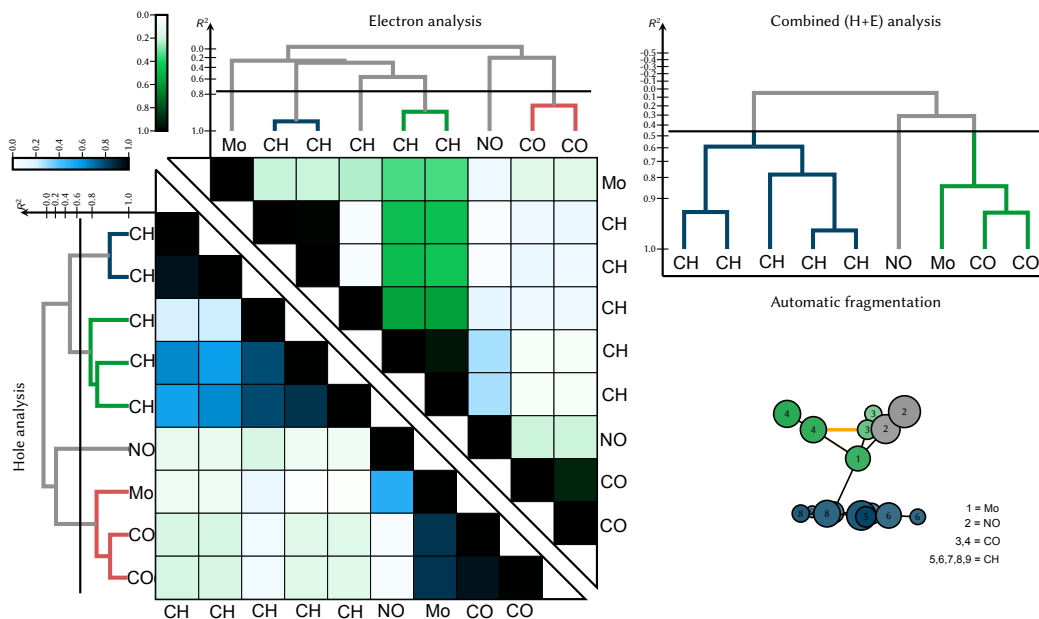


Figure 4.8.: Hierarchical clustering analysis of **CpMo** with (*left*) the correlation matrices of the excitation hole (*lower left triangular matrix*) and the excited electron (*upper left triangular matrix*) with the respective dendrograms showing the clustering scheme to each correlation matrix and (*right*) the combined dendrogram with the threshold of 0.45 as indicated by the black vertical line, as well as the to this threshold corresponding clustering scheme depicted on the molecular geometry (TD-DFT B3LYP-D3(BJ)/def2-SVP implicit acetonitrile).

hierarchical clustering where all fragments are separate clusters at the beginning and sequentially merged until only one cluster - the complete molecule - remains. In a final step, both dendrograms of the hole and electron correlation matrix are combined to a single dendrogram with a minimum function in order to infer a meaningful clustering scheme by defining a threshold (see black vertical line in dendrograms shown in Figure 4.8).<sup>[70,74]</sup> For the hierarchical clustering analysis outcome of **CpMo** given in Figure 4.8, it can be concluded that indeed both CO-ligands show strong correlation which was previously assumed due to symmetry. Moreover, both CO-ligands show tighter correlation to Mo than the NO-ligand. Remarkably, equal correlation prevails among the two symmetrical  $\text{CH}_{\text{Cp}}$ -groups (labeled as 5 and 7 in Figure 4.8 *bottom right*) on opposite side of the mirror plane, as well as the other two symmetry-equivalent  $\text{CH}_{\text{Cp}}$ -groups (labeled as 8 and 9 in Figure 4.8 *bottom right*) located closer on either side of the mirror plane and opposite to the NO-ligand. The latter two show further a higher correlation to the  $\text{CH}_{\text{Cp}}$ -group (labeled as 6 in Figure 4.8 *bottom right*) located on the mirror plane. Consequently, the correlation matrices capture the symmetry of the molecular system which is quite

## 4. Results and Discussion

remarkable. Also, a possible alternative fragmentation scheme is detected at a threshold of 0.9 by partitioning the Cp-ligand into its three different CH-groups in addition to an NO, (CO)<sub>2</sub> and Mo fragment. However, a generally meaningful clustering scheme contains fragments whose charge transfer numbers do not necessarily correlate in a significant way (which translates to mid-level threshold cut) so that maximum information gain is achieved in the charge transfer analysis and whose partitioning should still be reasonable from a chemical intuition point of view. For this reason and for the chemical problem at hand, it was decided to use the initially proposed fourfold clustering scheme for the quantitative charge transfer analysis and treat the Cp-ligand as one fragment.

Contrary to **CpMo**, the hierarchical clustering outcome of **TacnMo** given in Figure 4.9 does not necessarily corroborate the initial fourfold clustering scheme and thus provided two interesting answers to the question posed above. Namely, the complex is comprised of two general subunits (threshold cut at 0.45), namely the carbon backbone of the Tacn-

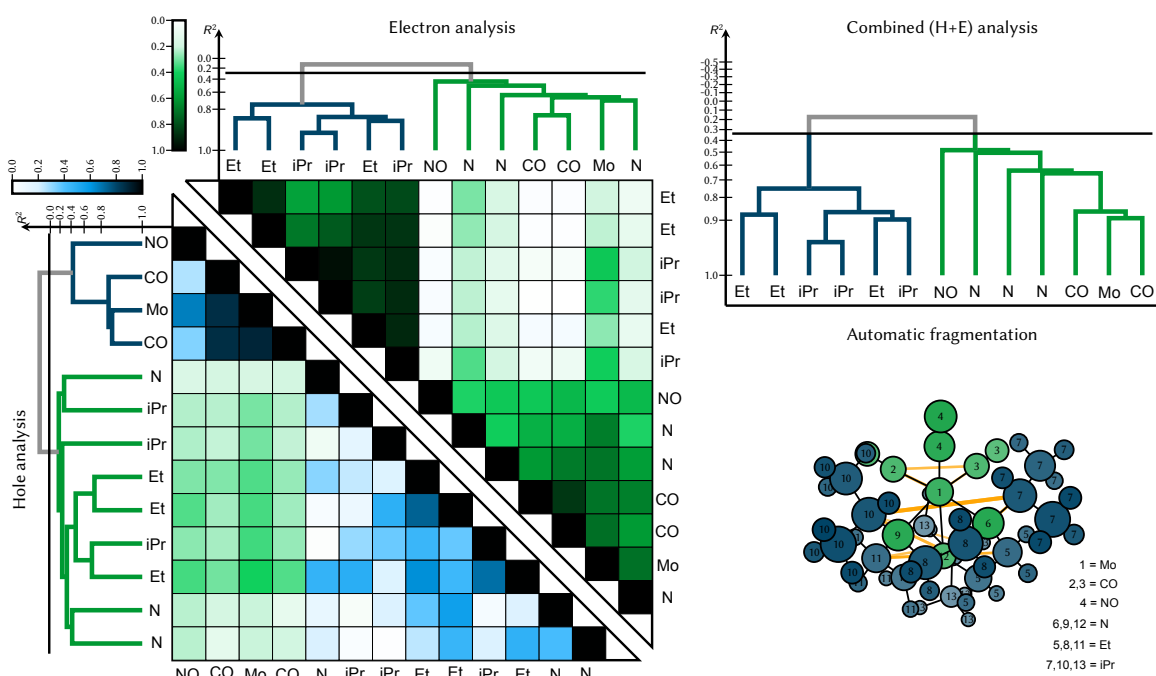


Figure 4.9.: Hierarchical clustering analysis of **TacnMo** with (left) the correlation matrices of the excitation hole (lower left triangular matrix) and the excited electron (upper left triangular matrix) with the respective dendrograms showing the clustering scheme to each correlation matrix and (right) the combined dendrogram with the threshold of 0.45 as indicated by the black vertical line, as well as the to this threshold corresponding clustering scheme depicted on the molecular geometry (TD-DFT B3LYP-D3(BJ)/def2-SVP implicit acetonitrile).

#### 4. Results and Discussion

ligand on the one hand and the remaining complex which mainly consists of hetero atoms and the central Mo on the other hand. Looking at larger correlation values within the latter subunit, one can see that indeed both CO-ligands correlate stronger with Mo than the NO-ligand (as was the case for **CpMo**), however not equally. One CO-ligand (labeled as 2 in Figure 4.9 *bottom right*) shows tighter correlation to Mo than the other. Furthermore, the clustering algorithm is not able to retrieve the Tacn-ligand as one subunit. This is due to the fact that the nitrogen atoms of Tacn correlate stronger with the other hetero atoms than with the carbon backbone of the Tacn-ligand. Moreover, all three nitrogen are not subsumed as one cluster at any threshold value of the cluster hierarchy and are not equal in the sense that they do exhibit different correlations to other fragments, which could be due to the molecule being of  $C_1$ -symmetry. Taking all together, strictly speaking the CO ligands are not equivalent and the Tacn-ligand seems best to partition at least in heteroatoms and non-heteroatoms. However, it was decided to also use a fourfold fragmentation scheme for **TacnMo** in order to ensure better comparability to the charge transfer analysis of **CpMo** so that the role of both ligands, Cp and Tacn, on the electronic structure of  $\text{Mo}(\text{CO})_2\text{NO}$  can be determined.

Based on this fragmentation scheme for both molybdenum complexes, 16 different charge transfer characters can be formulated for the charge transfer analysis. Each excitation type is determined with regard to where the hole and the electron population, hence the excitation origin and destination, are located. For instance, excitations from the central metal atom can remain local within the metal fragment, which is characterized as metal centered charge transfer (MC), or can go to another fragment such as a metal

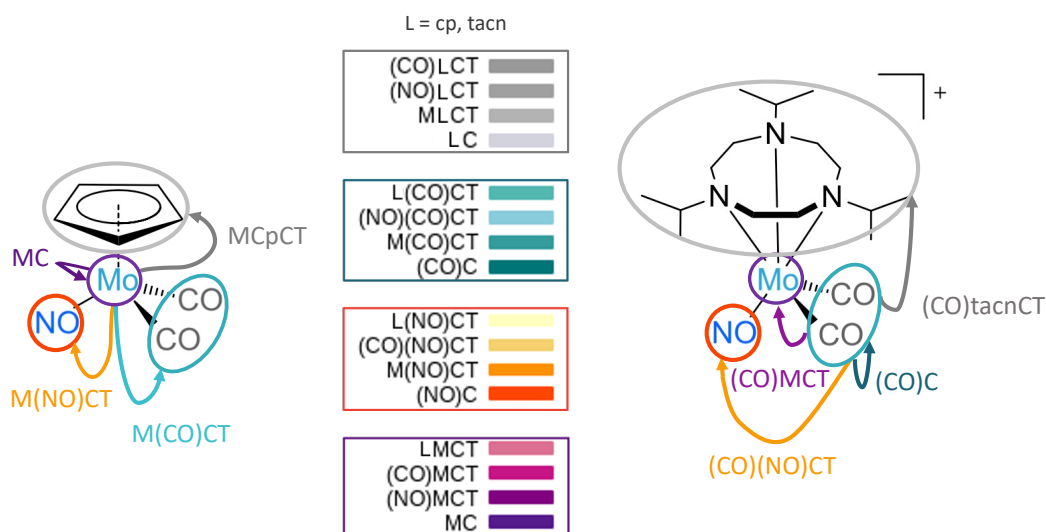


Figure 4.10.: Color scheme of the decomposed charge flow based on a fourfold fragmentation scheme resulting in a total of 16 different charge transfer characters; origin of arrows corresponds to the excitation hole and arrow head to the electron population.

#### 4. Results and Discussion

to CO charge transfer (M(CO)CT) or a metal to NO charge transfer (M(NO)CT). This scheme gives rise to 16 different characters which are henceforward color coded depending on the excitation destination. As depicted in Figure 4.10, excitations within or towards the metal center are shown in purple, towards the NO-ligand in orange, towards either CO-ligand in cyan and towards either Cp- or Tacn-ligand in gray. The comprehensive quantitative charge flow analysis for all computed singlet and triplet states including excitation energies, oscillator strengths, the  $PR_{NTO}$  value utilized above and the most important charge transfer characters are given in table A.4 and A.5 for **CpMo** and table A.6 and A.7 for **TacnMo**. Certainly, visually more revealing is the charge transfer analysis translated into bar plots in the aforementioned color code as displayed in Figure 4.11 for **CpMo** and Figure 4.12 for **TacnMo**. The bar plots are further subdivided into a diagram depicting energy and oscillator strength (*upper panel*) and the state characters with the respective weight for each state (*lower panel*).

From the charge transfer analysis of **CpMo**, four general observations can be made upon inspection of Figure 4.11. First, charge transfer towards the NO-ligand clearly dominants within an excitation energy  $< 4$  eV with charge flow being primarily directed towards the NO-ligand or transferred from the metal center. Secondly, charge flow towards the CO-ligands occurs in minor contributions throughout the complete excitation window up to 8 eV, but prevails within an excitation range of 4 to 6 eV. Thirdly, inner-metal charge transfer is conspicuously strong in all computed 120 states and charge flow directed towards molybdenum from either Cp or NO is particularly strong within an excitation

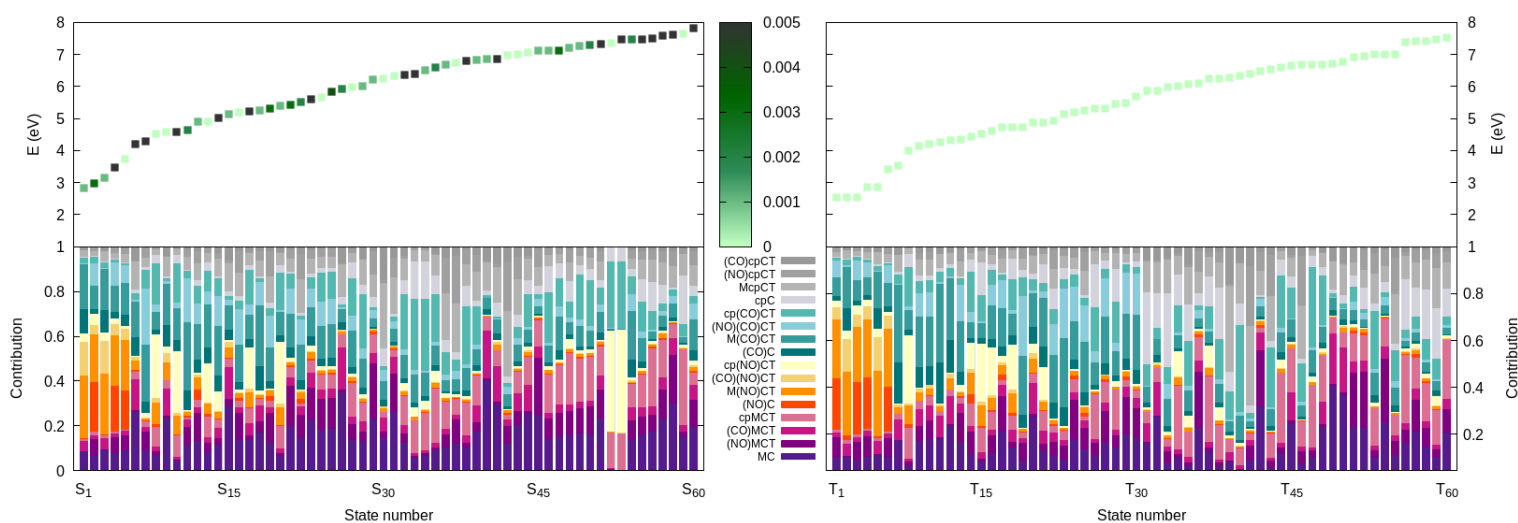


Figure 4.11.: Color-coded decomposition of the charge transfer number matrix (*lower panel*) for each computed singlet (*left*) and triplet state (*right*) of **CpMo** with excitation energies and oscillator strengths (*upper panel*) (TD-DFT B3LYP-D3(BJ)/def2-SVP implicit acetonitrile).

#### 4. Results and Discussion

window of 6 to 8 eV. Lastly, electronic excitations towards the Cp-ligand increase with an excitation energy of 6 eV or higher and are generally stronger in triplet states compared to singlet states. Overall, singlet and triplet states exhibit roughly the same trends with the notable exception of singlet state  $S_{52}$  and  $S_{53}$  (excitation energy of 7.37 and 7.46 eV and oscillator strength of 0.000 and 0.006 a.u. respectively) where charge flow exclusively originates from Cp going to NO, CO and Mo in descending order. Hence, both states deviate from the common trend abided by all states of both multiplicities in the respective energy regions. Furthermore, the quantitative analysis scheme validates the outcome of the previous qualitative, visual assessment of the two brightest states having the highest oscillator strength in the excitation of the ground state geometry,  $S_6$  and  $S_7$ . Based on the NTO basis, it was concluded that  $S_6$  has mainly a  $\pi(\text{MoCO})_n(\text{MoCO})$  state character which corresponds nicely to the three main characters determined with this analysis scheme, namely MC (26 %), M(CO)CT (16 %) and (CO)MCT (13 %). Also, the previously defined state character of  $S_7$ ,  $\pi(\text{MoNO})\pi(\text{MoCO})$ , is in accordance with the state-specific character types from this analysis, namely (NO)(CO)CT (25 %) and M(CO)CT (25 %).

The result of this charge transfer analysis is significant for the chemical problem at hand that is finding selective ways for a dissociation of either NO or CO. Since the charge transfer to the NO-ligand is consolidated in a lower excitation energy window, it can be rationalized that by exciting the molecule within this energy range, a directed electron transfer towards the NO ligands can be achieved. Consequently, if  $\pi^*(\text{MoNO})$ -orbitals are occupied in the process, the bond between Mo and N is selectively weakened such that a dissociation is achieved. Furthermore, because a charge transfer towards and from the CO-ligand increases after this excitation window, irradiation must occur at an energy smaller than 4.22 eV. Due to the computed oscillator strengths of the energetically lowest singlet states, it can be hypothesized that a targeted excitation into the bright  $S_4$  (excitation energy of 3.46 eV and oscillator strength 0.006 a.u.) constitutes the so-far best way to selectively dissociate NO and an excitation in either of the energetically higher-lying and bright states,  $S_6$  or  $S_7$  (excitation energy of 4.22 and 4.30 eV and oscillator strength of 0.023 and 0.007 a.u. respectively), could lead to a selective dissociation of CO. This conclusion is verified by the multi-reference CASSCF calculations. Since triplet states show the same trend, also an excitation into triplet states is conceivable and will be evaluated when discussing the 1D-potential energy scans on CASSCF level of theory in the following.

In comparison to **CpMo**, the charge transfer analysis of **TacnMo** given in Figure 4.12 shows similarities, but also major differences. The most important similarity is that also for **TacnMo**, charge transfer towards the NO-fragment dominates at lower excitation energies of  $< 4$  eV. Furthermore, singlets and triplets show again similar trends within the same energy regions with differences primarily occurring in  $T_{57}$  to  $T_{60}$  which are located at higher excitation energies of 6.63 to 6.89 eV and are thus neglectable. The most important difference is that the Tacn-ligand is much more involved in the charge flow than the Cp-ligand. Already from excitation energies of 5 eV or higher, excitations from the Tacn-ligand play a major role in the state characters. This becomes also evident in the main state characters of each state given in table A.6 and A.7 where electronic transitions

#### 4. Results and Discussion

from Tacn towards either CO or NO prevail. Another difference is that inner-metal localized charge fluctuations are only occurring at lower excitation energies below 6 eV. At higher energies, charge transfer from Tacn towards the metal center clearly predominates which is less pronounced in **CpMo** with the Cp-ligand.

Another further similarity to the **CpMo** analysis can be mentioned for **TacnMo**. Namely, the charge transfer analysis also validates the qualitative assessment of the state character of the two brightest singlet states of low excitation energy performed in the previous chapter. On the one hand,  $S_7$  (excitation energy of 4.76 eV and oscillator strength of 0.014 a.u.) was determined to have a  $\pi(\text{MoNO})\pi(\text{MoCO})$  (74 %) and  $\pi(\text{MoNO})\pi^*(\text{MoNOCO})$  (21 %) character which nicely corresponds to the three main characters of  $\text{M}(\text{CO})\text{CT}$  (25 %),  $\text{MC}$  (19 %) and  $(\text{NO})(\text{CO})\text{CT}$  (12 %). On the other hand,  $S_8$  (excitation energy of 4.77 eV and oscillator strength of 0.016 a.u.) has a state character of  $\pi(\text{MoNO})\pi(\text{MoCO})$  (73 %) and  $\pi(\text{MoNO})\pi^*(\pi(\text{MoCO})\text{NO})$  (16 %) according to the qualitative analysis which agrees well with the three main characters determined in the quantitative wave function analysis,  $\text{M}(\text{CO})\text{CT}$  (30 %),  $(\text{NO})(\text{CO})\text{CT}$  (17 %) and  $\text{MC}$  (16 %).

Overall, for **TacnMo**, it can be concluded that an excitation to  $S_5$  (excitation energy 3.67 eV and oscillator strength of 0.006 a.u.) could potentially lead to a selective dissociation of NO, whereas a slightly higher excitation to  $S_7$  to  $S_8$  (excitation energy 4.76 and 4.77 eV and oscillator strength of 0.014 and 0.016 a.u. respectively) could achieve a CO-dissociation for the same reasons elaborated previously for **CpMo**.

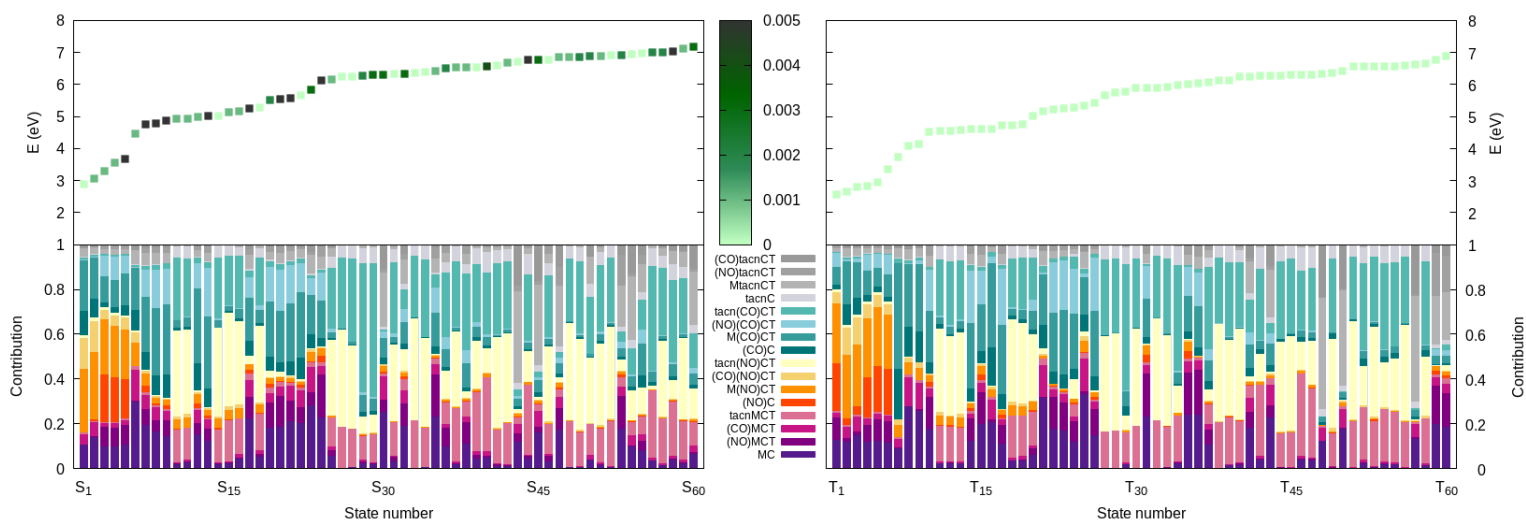


Figure 4.12.: Color-coded decomposition of the charge transfer number matrix (*lower panel*) for each computed singlet (*left*) and triplet state (*right*) of **TacnMo** with excitation energies and oscillator strengths (*upper panel*) (TD-DFT B3LYP-D3(BJ)/def2-SVP implicit acetonitrile).

## 4.2. Exploration of Potential Photodissociation Products

### 4.2.1. FTIR Spectroscopic Analysis of CpMo and TacnMo

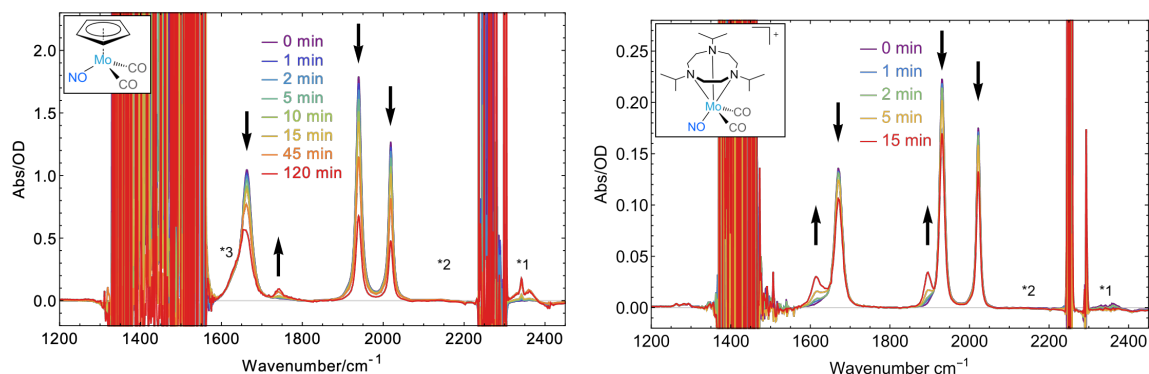


Figure 4.13.: Experimentally measured mid-infrared (MIR) spectra of **CpMo** (left) and **TacnMo** (right) in acetonitrile under continuous illumination with a 285 nm diode for different exposure times; arrows indicate absorption increase and decrease during UV-light exposure<sup>[14]</sup> (printed with permission).

In experimental pre-studies,<sup>[14]</sup> the IR absorption spectra during photoexcitation of both complexes were measured as depicted in Figure 4.13. For **CpMo**, three main peaks were determined for the photosubstrate (exposure time 0 min), namely an asymmetric N-O stretching band at  $1664\text{ cm}^{-1}$  and an asymmetric and symmetric vibration for the CO-ligands at  $1940$  and  $2019\text{ cm}^{-1}$  respectively. During continuous excitation at  $298\text{ nm}$  for 120 min, all three bands decrease whereas one peak clearly emerges at  $1743\text{ cm}^{-1}$ , as well as three additional minor peaks: a peak at  $2342\text{ cm}^{-1}$  (labelled as \*1 in Figure 4.13) which could be associated to  $\text{CO}_2$  and an additional peak of an unknown species due to the characteristic double-peak shape of  $\text{CO}_2$ , a very weak band at  $2137\text{ cm}^{-1}$  (labelled as \*2 in Figure 4.13) that is only clearly discernible in differential spectra and could stem from free CO in solution and a weak shoulder at  $1663\text{ cm}^{-1}$  (labelled as \*3 in Figure 4.13) which overlaps with the NO-band. Upon further investigation, it was determined that the uprising peak at  $1743\text{ cm}^{-1}$  exhibits approximately the same time constant as the decay time of the decreasing signals. However, a more detailed kinetic evaluation of the spectrum is hampered by the fact that not enough data points were measured so that a proper kinetic fit can be achieved. Additionally, the spectrum of the photoproduct (exposure time 120 min) suffers from a notable baseline drift so that a baseline correction was necessary which is significant for the evaluation of all three weak bands. Nonetheless, with the information obtained in the experiment, it was concluded that **CpMo** most likely loses both CO-ligands during UV-light exposure because there are no rising signals in the CO-region.

The experimentally measured IR spectra of **TacnMo** are also shown in Figure 4.13 up to an UV-light irradiation of 15 min. The spectra after 15 min were not included

#### 4. Results and Discussion

because of visible water vapor absorption distorting the spectrum within the wavenumber region of 1500 to 1570  $\text{cm}^{-1}$ . Also for this complex, three main peaks were determined for the photosubstrate (exposure time 0 min), namely an asymmetric N-O stretching band at 1671  $\text{cm}^{-1}$  and an asymmetric and symmetric vibration for the CO-ligands at 1932 and 2023  $\text{cm}^{-1}$  respectively. During continuous photoexcitation, all three main peaks decrease and two distinct peaks emerge. One peak at 1615  $\text{cm}^{-1}$  which is red-shifted with respect to the NO-band and one peak at 1896  $\text{cm}^{-1}$  red-shifted to the asymmetrical CO-peak. Hence, both peaks were rationalized to belong to the photoproduct whereby a single CO-dissociation is assumed to occur within 15 min UV-light exposure. Furthermore, in accordance to the **CpMo** spectrum, two additional very weak, rising signals are discernible, one at 2343  $\text{cm}^{-1}$  (labelled as \*1 in Figure 4.13) which could be assigned to free  $\text{CO}_2$  with a signal inbetween and one at 2140  $\text{cm}^{-1}$  (labelled as \*2 in Figure 4.13) which could stem from an unbound CO in solution.

In order to validate the conclusion that the photoproduct of **CpMo** is  $[\text{CpMo}(\text{NO})]$  and thus contains no CO-ligands whereas the photoproduct of **TacnMo** retains one CO-ligand, DFT calculations were performed. The results of this endeavour are discussed in the next section. For this purpose, two important additional findings need to be mentioned. On the one hand, the isosbestic point measured in the static UV/Vis absorption measurements on **CpMo** is observed at 268 nm for different exposure times (see Figure A.4). However, for longer exposure times, the isosbestic point gets blurred which could be an indicator of another photoproduct.<sup>[14]</sup> On the other hand, the determination of a **CpMo**-photoproduct proved particularly difficult on basis of the experimental spectrum given in Figure 4.13, which will be discussed in detail below. In order to uncover overlapping signals, an additional fit using Voigt functions was performed, whose line profile is a convolution of both Gaussian and Lorentzian profiles. While Gaussian distributions are sharper and narrower compared to Lorentzian distributions, Voigt line profiles are inbetween as depicted in Figure 4.14 and thereby achieve a better fit of the spectroscopic signals by allowing more flexibility.

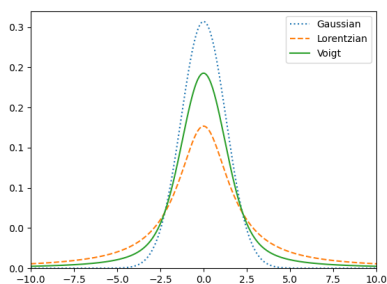


Figure 4.14.: Schematic representation of a Gaussian, Voigt and Lorentzian function.

Upon fitting the IR spectrum of **CpMo** (exposure time 0 min), two additional hidden signals under both CO-peaks became evident at 1911 and 2013  $\text{cm}^{-1}$  which are therefore slightly red-shifted compared to the two main CO stretching vibrations (see Figure 4.15). As to which species causes these signals in the photosubstrate solution remains unclear. Possible explanations include water or air contamination resulting in an oxidation of Mo, potential low-energy isomerization with respect to a Mo-NO-bend, or other contaminations or storage difficulties that resulted in complex decomposition (also due to the fact that the measured sample was several years old when used in the experiment).

## 4. Results and Discussion

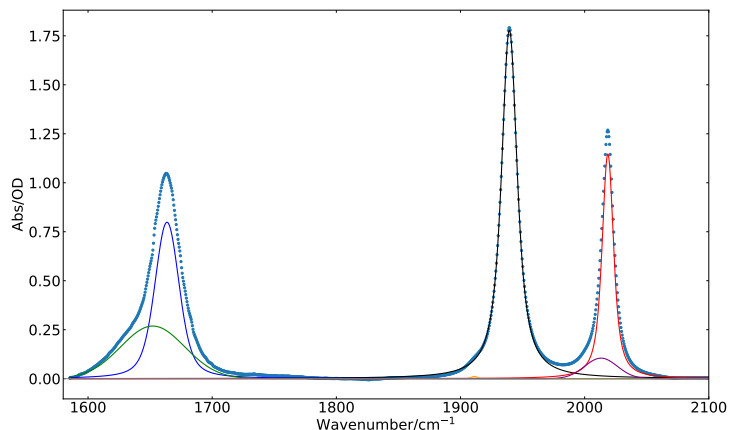


Figure 4.15.: Experimental IR spectrum of **CpMo** *dashed blue* fitted with six Voigt functions whose peak are located at  $1652\text{ cm}^{-1}$  (*green*),  $1664\text{ cm}^{-1}$  (*blue*),  $1911\text{ cm}^{-1}$  (*yellow*),  $1939\text{ cm}^{-1}$  (*black*),  $2013\text{ cm}^{-1}$  (*purple*),  $2019\text{ cm}^{-1}$  (*red*).

### 4.2.2. Simulated IR-Spectra of Potential Photoproducts

For the photoproduct exploration, four different scenarios were considered. First, a dissociation event occurred where either one or two ligands dissociated and were replaced by an acetonitrile solvent molecule. Secondly, a dimerization took place upon dissociation of one or two ligands and subsequent replacement by a solvent molecule. Thirdly, water contamination caused water to coordinate to the metal center after dissociation of one or two ligands. Lastly, an NO-isomerization occurred instigated by UV-light irradiation before or after one or two ligands dissociated. In Figure 4.16, all considered structures optimized on DFT B3LYP/def2-SVP level of theory in implicit acetonitrile are shown. In order to compare the simulated IR spectra of these structures with the experimental spectrum, a shift parameter was determined by comparing the simulated and experimental IR spectrum of the intact **CpMo** complex before photoexcitation henceforward termed photosubstrate. Perfect agreement among both spectra was only achieved by a separate shift parameter for the NO- and CO-stretching modes. Therefore, all vibrational modes around the NO stretching mode with a wavenumber smaller than  $1905\text{ cm}^{-1}$  were red-shifted by  $110\text{ cm}^{-1}$  and all modes of higher wavenumbers were red-shifted by  $56.5\text{ cm}^{-1}$ . The calculated raw peak data before applying the shift correction is listed in table A.10 in Appendix A and includes wavenumbers, peak intensities and vibrational modes for reference. Only peaks exhibiting an intensity of 180 a.u. or higher were included in the analysis whereby a few minor molecular vibrations of acetonitrile were not included. The calculated spectra are plotted in Figure 4.17 together with the experimental spectrum measured before UV light exposure, labeled as experimental photosubstrate, and after continuous excitation for 120 min, labeled as experimental photoproduct.

Aim of the photoproduct exploration for **CpMo** is to find an explanation for several signals visible in the experimental spectra. The first task is to determine the species that causes the rising signal at  $1743\text{ cm}^{-1}$ . The second task is to identify the species

#### 4. Results and Discussion

that gives rise to the increasing peak shoulder at  $1663\text{ cm}^{-1}$ . The third task is to find an explanation for the two red-shifted peak signals in the photosubstrate solution at  $1911$  and  $2013\text{ cm}^{-1}$ . On basis of the simulated spectra none of the three signals can be assigned with absolute certainty to a single species. Which could suggest that either we have not considered the correct photoproduct or two or three separate events take place during photoexcitation which yield different photoproducts. Nonetheless, some hypothesis can be formulated that need further validation by additional experiments.

The best explanation for the peak at  $1743\text{ cm}^{-1}$  is a dissociation of the NO-ligand which is replaced by acetonitrile. As can be seen from the orange colored peaks in Figure 4.17 (*upper left spectrum*), the asymmetric and symmetric stretching modes are significantly red-shifted upon the replacement of NO with ACN in **CpMo**. The asymmetric C-O vibration of the  $\text{Mo}(\text{CO})_2$ -group approaches the region of the unidentified peak and the symmetric counterpart could overlaps with and thus perish under the broad peak located at  $1940\text{ cm}^{-1}$ . Repeating the experiment and measuring more data points during photoexcitation could clarify whether there is a hidden signal of the same time constant at around  $1908\text{ cm}^{-1}$ . At first glance, another species approaches the wave number region of this unidentified peak, namely the dimer formed after dissociation of two CO and one NO and CO given in sepia (*upper right spectrum*). However, this species can be ruled out by the asymmetrical NO stretching mode at  $1589\text{ cm}^{-1}$  exhibiting an even higher intensity than the unknown peak shoulder. The close proximity of both peaks characterizing this dimerized species to the two unknown rising signals could hint to a possible dimer formation which was perhaps not considered in the analysis. Repeating the experiment with different initial photosubstrate concentrations is key to clarify whether an dimerization event occurred or not.

For the peak shoulder located at  $1663\text{ cm}^{-1}$ , four species come close alluding to either an isomerization of the NO ligand in an otherwise intact complex or a single CO-

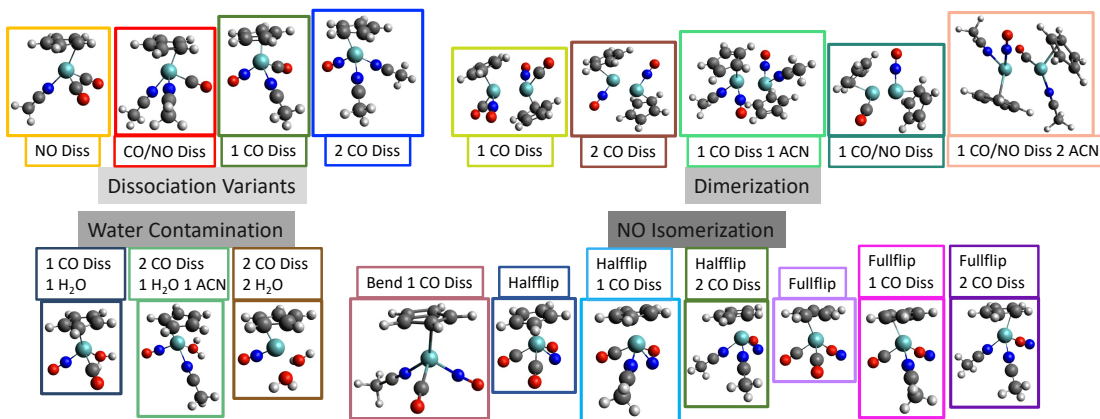


Figure 4.16.: Optimized structures of all **CpMo** variants considered during photoproduct exploration; empty coordination sites are assumed by either acetonitrile or water (DFT B3LYP-D3(BJ)/def2-SVP implicit acetonitrile).

#### 4. Results and Discussion

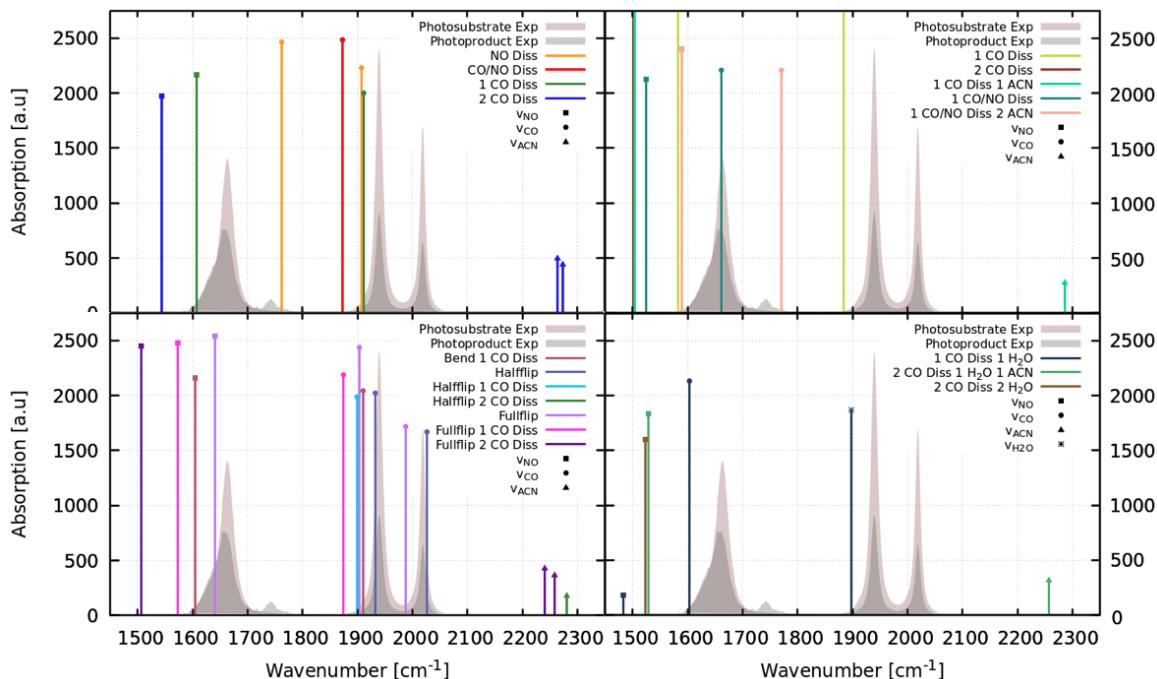


Figure 4.17.: Calculated IR spectra of all considered potential products of the photoexcitation of **CpMo** plotted with the experimental spectrum of the photosubstrate (exposure time 0 min) and photoproduct (exposure time 120 min); all simulated IR-spectra are plotted with a shift correction of  $110\text{ cm}^{-1}$  for peaks below  $1905\text{ cm}^{-1}$  and  $56.5\text{ cm}^{-1}$  for peaks at higher wavenumbers; color scheme corresponds to Figure 4.16 with the solvated dissociation variants and the dimerized species given in the *upper panel* and water contaminated and isomerized species in the *lower panel* (DFT B3LYP-D3(BJ)/def2-SVP implicit acetonitrile).

dissociation. The isomerized species where the NO-ligand is fully flipped such that the oxygen is coordinated to the metal center shown in light purple (*lower left spectrum* in Figure 4.17) comes close to the peak shoulder position with an asymmetrical stretching mode of the flipped NO-ligand. In order to rule out a possible NO-isomerization of **CpMo**, a CASSCF(8,13) potential energy scan was performed which is shown in Figure 4.18. Based on this rotational scan, it can be concluded that a linkage isomerization cannot occur with a photoexcitation at  $285\text{ nm}$  due to the large potential barrier of  $10.94\text{ eV}$  at an  $45^\circ$ -angle. The other three species indicate a single CO-dissociation, namely the species given in dark green (*upper left spectrum* in Figure 4.17) which represents the solvated complex after single CO dissociation, the NO-isomerized variant of this species with a bent NO-ligand encoded in plum purple color (*lower left spectrum* in Figure 4.17) and a water-contaminated variant of this species where the dissociated CO is replaced by a water molecule shown in dark blue (*lower right spectrum*). All four species could be validated by a distinct peak between  $1880\text{ to }1910\text{ cm}^{-1}$  of slightly lower intensity which is absent or also hidden under the broad peak located at  $1940\text{ cm}^{-1}$ , which is not very

#### 4. Results and Discussion

likely because also the peak positions at lower wave numbers do not exactly match the signal. With certainty, it can only be concluded that the peak belongs to an NO-bond vibration whose bond strengths is weakened such that less energy is needed to excite this motion because no other bond vibration - other than NO - was found in the region.

Lastly, based on the IR spectrum computation, a possible explanation for the two red-shifted signals in the photosubstrate solution at  $1911$  and  $2013\text{ cm}^{-1}$  could weakly support the aforementioned possibilities of a low-energy NO-isomer of the intact complex with the MoNO-angle being slightly decreased. This hypothesis was formulated based on a geometry that converged during the NO-flip conformer search (not depicted in Figure 4.17, but enumerated in table A.10 under "NO-bend"). Compared to the equilibrium geometry of **CpMo**, this geometry exhibits a slightly decreased Mo-N-O angle by only  $2^\circ$  and exhibits red-shifted peaks of around  $4\text{ cm}^{-1}$  compared to the photosubstrate, which is negligibly small. However, for the half-flipped structure with an Mo-N-O angle of around  $90^\circ$ , the peaks are further red-shifted by  $400\text{ cm}^{-1}$  for NO and  $5\text{ cm}^{-1}$  for the asymmetrical CO vibration. Both observations together could hint to a potential low-energy conformation of the **CpMo** with a slightly bent NO-ligand that is obtained upon dissolving the complex in acetonitrile. Nevertheless, repeating the experiment is inevitable for finding a definitive answer to this and the other two unsolved peak instances.

For **TacnMo**, an equivalent photoproduct exploration was conducted. In order to achieve the best agreement between the experimental and the simulated photosubstrate IR spectrum of this complex, two separate red-shift parameters were also introduced, namely  $101\text{ cm}^{-1}$  for the wavenumber region up to  $1905\text{ cm}^{-1}$  and  $67\text{ cm}^{-1}$  for peaks at

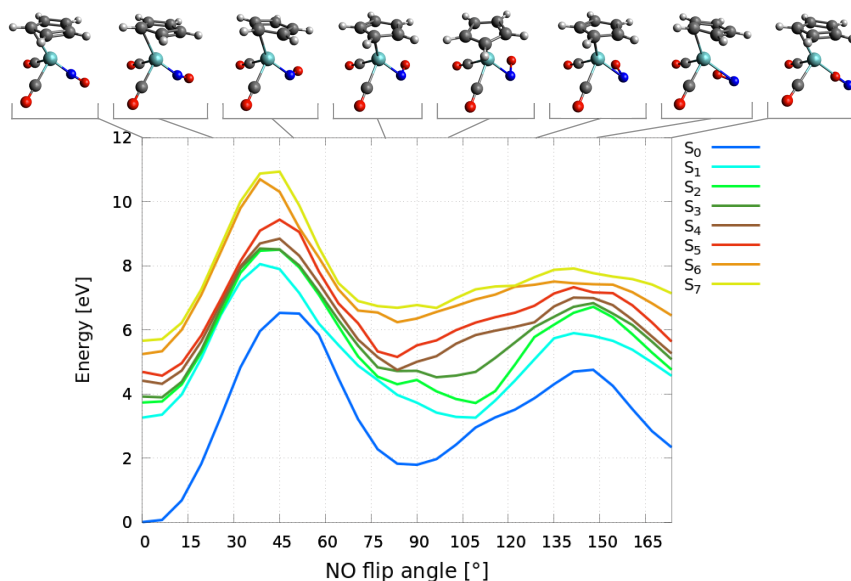


Figure 4.18.: Potential energy scan of a linkage isomerization of NO in **CpMo**. (CASSCF(8,13) gas phase).

#### 4. Results and Discussion

higher wave numbers. The comprehensive list of all peaks obtained in the IR simulations including intensity, wavenumber and corresponding vibrational mode are given in table A.11. Analogously to **CpMo**, from all simulated spectra, only peaks with an intensity higher or equal to 180 a.u. were considered in the analysis which therefore excludes minor vibrations of the carbon backbone of the Tacn-ligand and of coordinated acetonitrile molecules. For the analysis, the dimerization event was not considered for **TacnMo** due to possible steric effects conditioned by the bulky Tacn-ligand and its <sup>i</sup>Pr-groups enclosing the central atom. The optimized structures for this analysis are shown in Figure 4.19 with the respective calculated IR spectra being summarized in Figure 4.20.

The main task of the IR spectrum simulation was to determine the species causing the two rising signals at 1615 and 1896 cm<sup>-1</sup>. Perfect agreement was found for the species formed after a single CO-dissociation event occurred where the dissociated CO is replaced by a solvent molecule (red spectrum *upper panel*). Consequently, this outcome supports the experimental conclusion of a **TacnMo** photoproduct retaining one CO-ligand.

With that, only the remaining two weak, rising peaks need to be discussed which is valid for both complexes. The underlying peak under both signals labeled as \*1 in Figure 4.13 is presumably repatriatable to a coordinated acetonitrile as evidenced by multiple simulated spectra shown in Figure 4.17 and 4.20 which validates our approach of assuming empty coordination sites being taken by a solvent molecule. The second weak signal at this position could indeed be assigned to the asymmetrical stretching mode of CO<sub>2</sub> which usually occurs at 2349 cm<sup>-1</sup> as free, uncoordinated molecule in gas phase. As previously experimentally observed, the signal is expected to blue-shift to around 2385 cm<sup>-1</sup> if CO<sub>2</sub> forms a cluster with cationic metal species and/or solvent molecules where interactions to the environment cause the increase in energy and frequency of this molecular motion..<sup>[120]</sup> The other weak band located at 2140 and 2137 cm<sup>-1</sup> for the **TacnMo**- and **CpMo**-spectrum respectively (labeled as \*2 in Figure 4.13) could arise

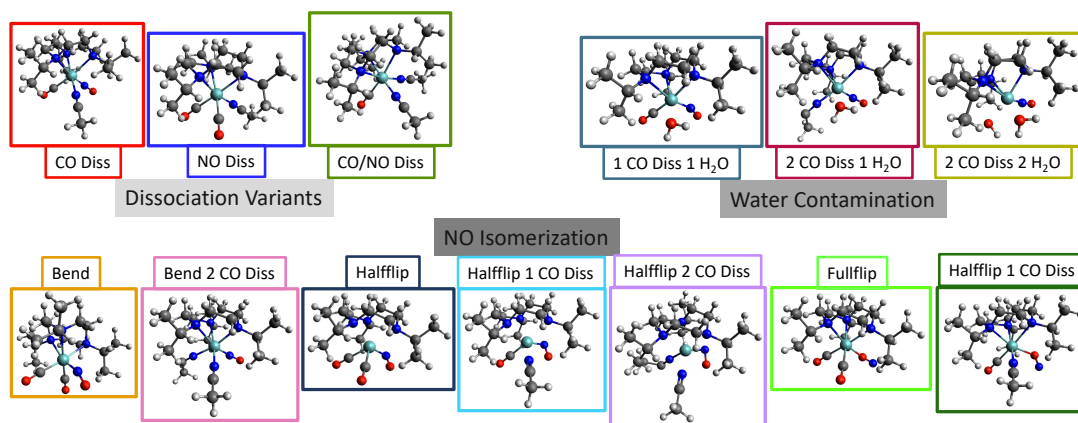


Figure 4.19.: Optimized structures of all **TacnMo** variants considered during photoproduct exploration; empty coordination sites are assumed by either acetonitrile or water (DFT B3LYP-D3(BJ)/def2-SVP implicit acetonitrile).

## 4. Results and Discussion

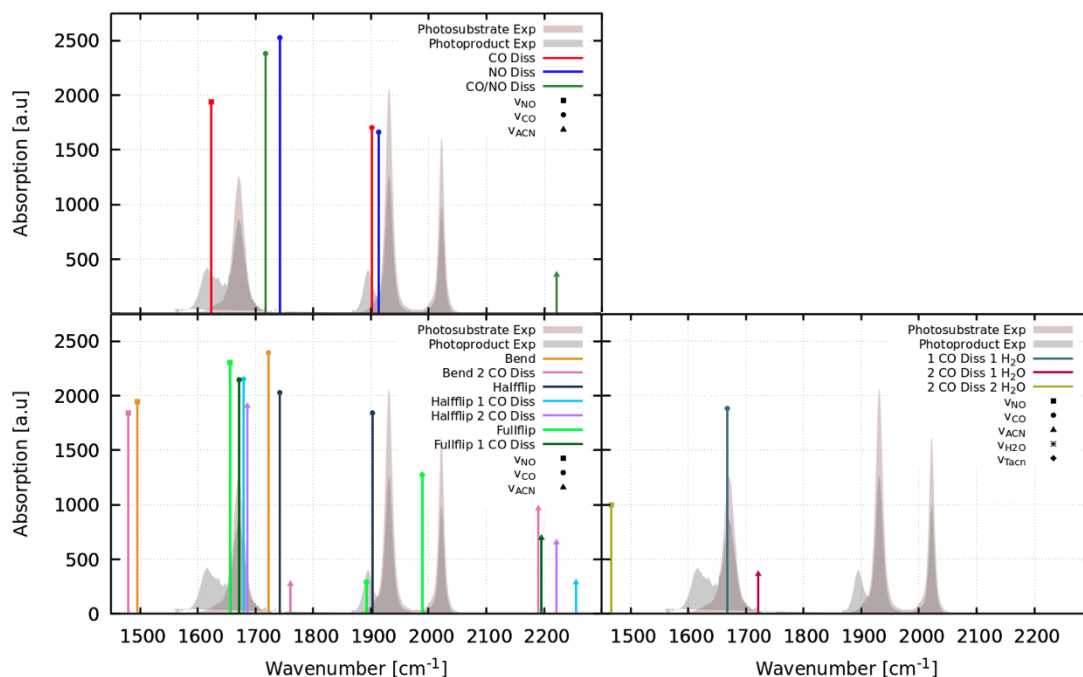


Figure 4.20.: Calculated IR spectra of all considered potential products of the photoexcitation of **TacnMo** plotted with the experimental spectrum of the photosubstrate (exposure time 0 min) and photoproduct (exposure time 15 min); all simulated IR-spectra are plotted with a shift correction of  $101\text{ cm}^{-1}$  for peaks below  $1905\text{ cm}^{-1}$  and  $67\text{ cm}^{-1}$  for peaks at higher wavenumbers; color scheme corresponds to Figure 4.19 with the solvated dissociation variants given in the *upper panel* and the isomerized and water contaminated species in the *lower panel* (DFT B3LYP-D3(BJ)/def2-SVP implicit acetonitrile).

from uncoordinated, free CO whose C-O stretch occurs in a frequency region which is isolated from many other vibrations, namely at  $2143\text{ cm}^{-1}$ .<sup>[121]</sup> The peak displacement between experiment and reference values are explained by solvent effects. In further consequence, this also indicates that the peak displacements of the potential photoproducts of **CpMo** discussed above who do not correspond in one-to-one agreement with the experimental spectrum could arise from solvent effect which would be better approximated by using explicit solvent models in the simulation. In order to validate this conclusion, additional calculations on selected structures considering explicit acetonitrile would be necessary to gain a better understanding of the solvent influence on the IR peak positions.

### 4.3. Photodissociation Behaviour of CpMo

#### 4.3.1. The Active Space Challenge

In order to investigate the photodissociation behaviour of **CpMo**, potential energy scans were performed using CASSCF and CASPT2. As already explained in chapter 2,

#### 4. Results and Discussion

multi-reference methods are computationally very demanding and only feasible when restricting the amount of active orbitals for the calculation of the CASSCF wave function and by limiting the amount of states. The latter was assessed based on the vertical excitation on TD-DFT level of theory where singlet state  $S_6$  with an oscillator strength of 0.023 a.u. was determined to be the brightest state among the energetically lowest

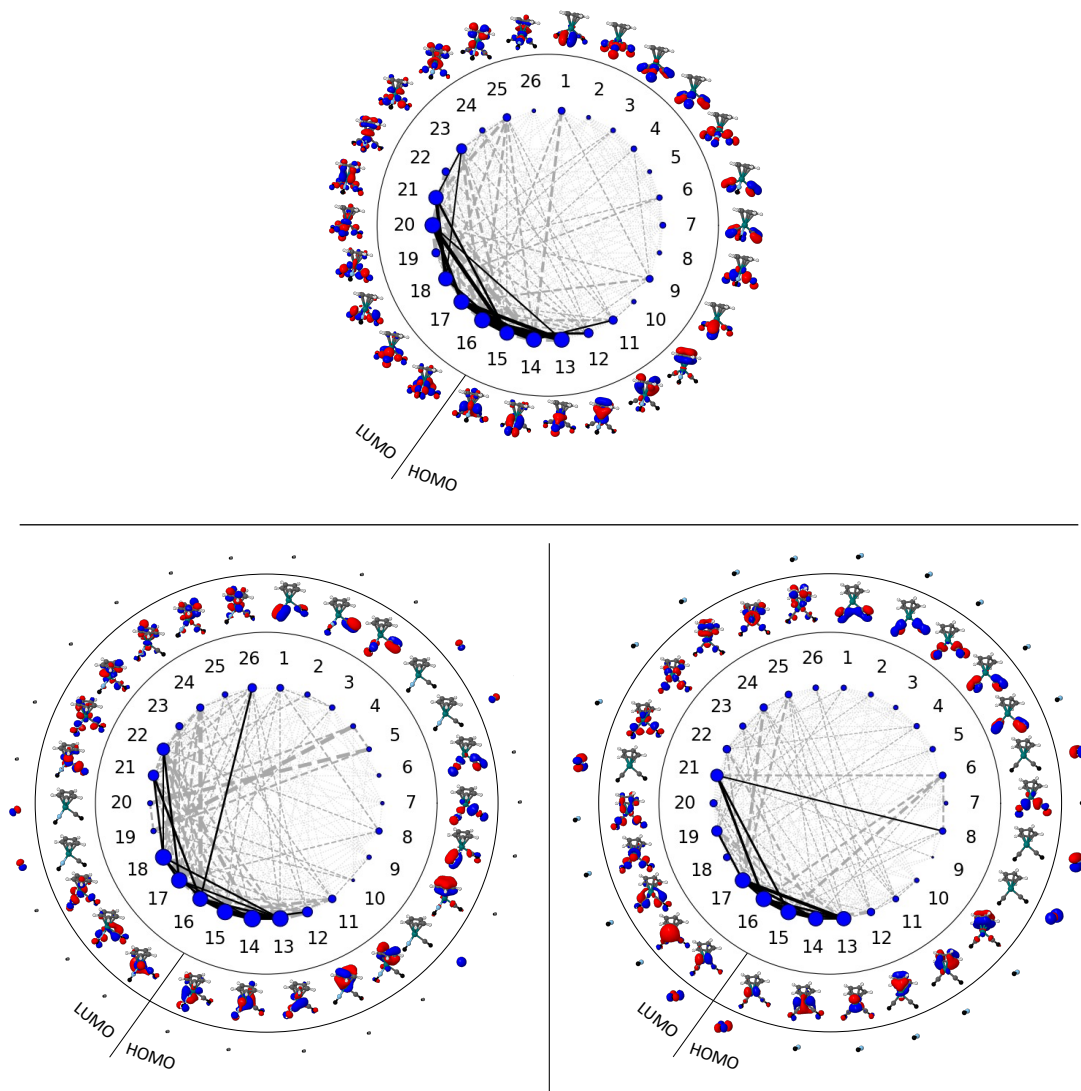


Figure 4.21.: Multi-state entanglement diagrams of **CpMo** (*upper panel*) and **CpMo**<sub>COdiss</sub> and **CpMo**<sub>NOdiss</sub> (*lower panel left to right*); single orbital entropy,  $Z_{s(1)}$ , for each orbital is encoded in the node size given in blue and the mutual information of each orbital pair,  $I_{ij}$ , is represented by the connecting lines of different thickness and color intensity depending on the value. (DMRG[250](30,26)-SCF/ANO-RCC-MB gas phase, natural orbitals).

## 4. Results and Discussion

states. Due to the asymptotic behaviour of NO-dissociation curves exhibiting degeneracy among pairs of singlet states due to the unpaired electron, an even number of singlet states was chosen, namely 8 singlet states in total. For the selection of the best set of orbitals, the DMRG algorithm and diagnostics was employed and is discussed first.

The outcome of the DMRG computation applied to **CpMo** is given in Figure 4.21 in form of entanglement diagrams. To arrive at this figure, a total of 15 occupied and 11 virtual MOs were considered as active space for the calculation of the DMRG wave function by excluding 41 energetically low-lying, inner-core orbitals based on the rationale explained in chapter 3. Because the overall objective is to find selective routes for the dissociation of CO and NO under different conditions, the active space needs to describe both photo-induced reactions equally well. For this reason, the algorithm was applied to all three border-line structures, the intact complex **CpMo**, the complex immediately after CO-dissociation **CpMo**<sub>COdiss</sub> and after NO-dissociation **CpMo**<sub>NOdiss</sub>, to assess the importance of each orbital for both reactions. A full orbital classification with the respective state-specific single-orbital entropies,  $Z_{s(1)}$ , can be found in table A.12 with the corresponding 8 state-specific entanglement diagrams for each geometry given in A.8 to A.10 of the Appendix A. Thereof, multi-state entanglement diagrams were computed by the chosen scheme elaborated in chapter 3.

Generally, **CpMo** has a relatively complicated electronic structure especially for the investigation of selective dissociations which will be shown in the course of this chapter. A first important indicator for this conclusion is shown in Figure 4.21 where almost all active orbitals of **CpMo** exhibit large or moderate entanglement which translates to almost all orbitals being statically correlated and should be included in the active space for the CASSCF computation. This is problematic for CASSCF active spaces that are composed of around 10 orbitals and 6 to 8 electrons, because many sets of orbitals can be selected from the large set of possibilities and their performance must be evaluated manually. However, all orbitals composed of  $\sigma$ - or  $\sigma^*$ -type orbital contributions along either the Mo-C<sub>CO</sub>- or the Mo-N<sub>NO</sub>-bond have only small contributions to the static correlation, indicated by thin, light-grey colored connecting lines, among themselves and to other active orbitals. Therefore, the correlation of these orbitals is primarily dynamical. Coincidentally, these types of orbitals also have a small single-orbital entropy, which means that their orbital occupation does not strongly deviate from two. Consequently, they can be excluded in a smaller active space to simulate dissociation curves where static correlation is key to obtain a qualitatively good result. This assessment is also valid for the energetically lowest  $\pi$ (Cp)-orbital (DMRG index 10) and the energetically highest virtual  $n$ -orbital which is a hodgepodge of different orbital contributions (DMRG index 26). All other orbitals are either  $\pi$ ,  $\pi^*$  or  $\delta^*$ -type orbitals and exhibit significant static correlation as well as a strong deviations from their original occupation number which renders them potential candidates for a final truncated active space.

Regarding **CpMo**<sub>COdiss</sub> and **CpMo**<sub>NOdiss</sub>, the same observation can be made for the  $\sigma$ - or  $\sigma^*$ -type orbitals. Particularly interesting in this regard is the high static correlation between the  $\pi$ -orbitals of the dissociation ligands (**CpMo**<sub>COdiss</sub>: DMRG index 4, 5, 19, 20; **CpMo**<sub>NOdiss</sub>: DMRG index 6, 8, 15, 16, 21) as opposed to the  $\sigma^*$ (CO)-orbitals of the same fragment (**CpMo**<sub>COdiss</sub>: DMRG index 10; **CpMo**<sub>NOdiss</sub>: DMRG index 9)

#### 4. Results and Discussion

which thus primarily feature dynamical correlation. The entanglement diagrams of both dissociated structures show highest values for  $Z_{s(1)}$  and  $I_{ij}$  in  $\pi$ - or  $\pi^*$ -type orbitals which are exclusively localized on Mo, NO or CO. This observation was later utilized to find an even smaller active space than initially considered, namely the CASSCF(6,10) active space. However, one  $\pi(\text{Cp})$ -orbital, which coincidentally has a DMRG index of 12 in all three diagrams, constitutes an exception to this rule and has high entanglement in the diagrams of both dissociated structures even though it is primarily located on the Cp-ligand. Interestingly, upon inclusion of this orbital in the initial CASSCF(8,13) active space for the computation of trial potential energy scans along the bond dissociation of both reactions, the performance was improved which shows that a comparison of all three geometries is indeed beneficial for the construction of an active space.

Based on these observations, multiple initial active spaces were assembled from the orbitals which possess high entanglement (DMRG index for **CpMo** of 1, 4, 6, 9, 11-23, 25) and trial potential energy scans were calculated to assess their performance. In these benchmark calculations, an active space comprised of 13 orbitals and 8 electrons was selected which produced the lowest absolute energies and the smoothest energy curves. The active space is shown in Figure 4.22 and includes three Cp-centered MOs. In the single point calculation of the equilibrium geometry including 8 singlet states, the occupation number of the last three orbitals is relatively small with 0.0160, 0.0281 and 0.0266 for the three energetically highest active orbitals (*bottom row* in Figure 4.22) which provides opportunity to further reduce the active space.

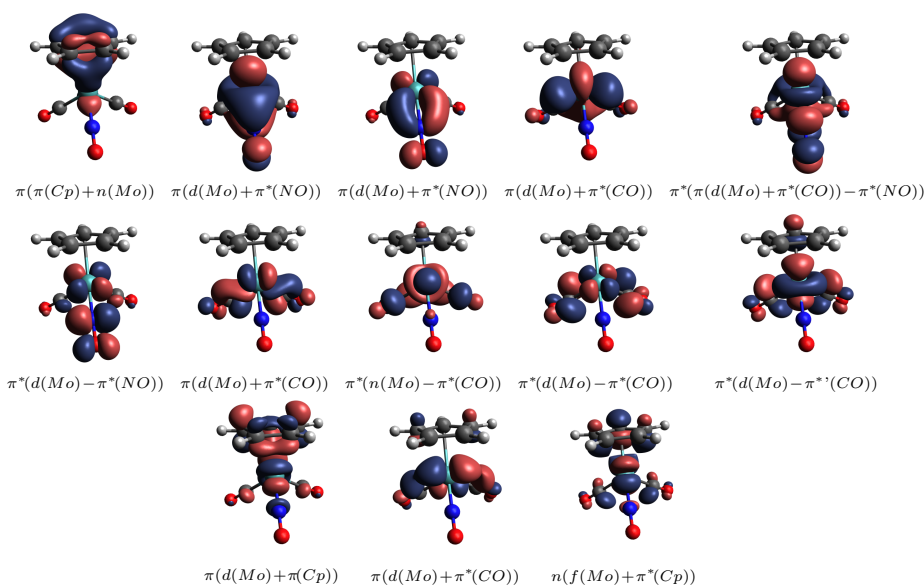


Figure 4.22.: CASSCF(8,13) active space from *left to right*; first four MOs ( $\pi(\text{CpMo})$ ,  $\pi(\text{MoNO})$ ,  $\pi(\text{MoNO})$ ,  $\pi(\text{MoCO})$ ) are occupied, the remaining orbitals ( $\pi^*(\text{MoNO})$ ,  $\pi^*(\text{MoNO})$ ,  $\pi(\text{MoCO})$ ,  $\pi^*(\text{MoCO})$ ,  $\pi^*(\text{MoCO})$ ,  $\pi^*(\text{MoCO})$ ,  $\pi(\text{MoCp})$ ,  $\pi(\text{MoCO})$ ,  $n(\text{MoCp})$ ) are unoccupied (CASSCF(8,13)/ANO-RCC-VDZP gas phase, natural orbitals).

## 4. Results and Discussion

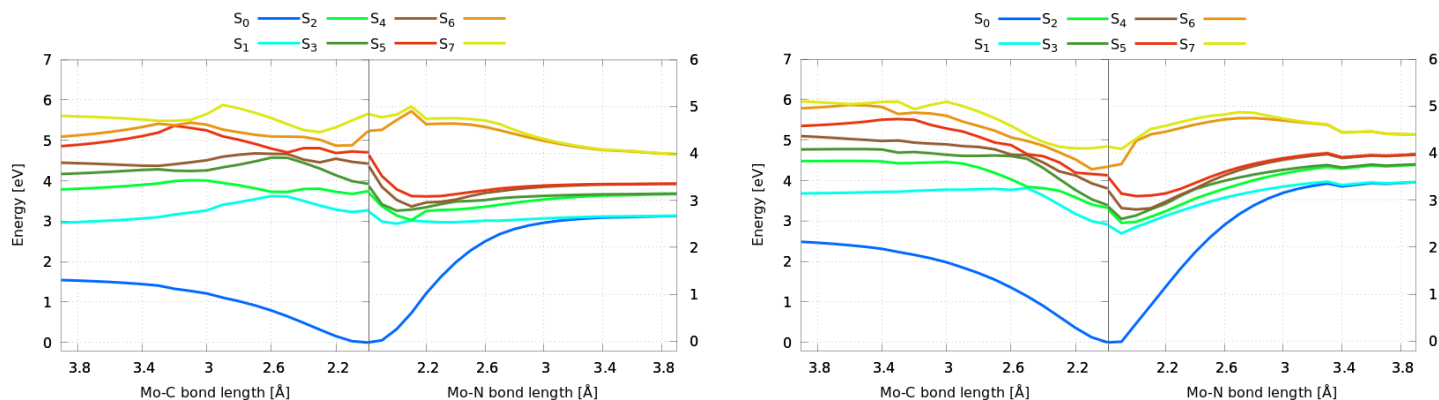


Figure 4.23.: 1D-Potential energy scans along the Mo-C<sub>CO</sub> and Mo-N<sub>NO</sub> bond dissociation of **CpMo** calculated with CASSCF(8,13) (*left*) and MS-CASPT2(8,13) with IPEA of 0.25 a.u. and imaginary shift of 0.1 a.u. (*right*); energies plotted relative to the ground state of the equilibrium structure (ANO-RCC-VDZP gas phase).

The CASSCF and MS-CASPT2 potential energy scans along one degree of freedom for both dissociation reactions computed with this active space are given in Figure 4.23. Qualitatively, both calculations significantly differ especially for the NO-dissociation. While the scans along the Mo-C<sub>CO</sub> bond on both levels of theory clearly indicate a successful CO-dissociation. Even though both simulations show the correct asymptotic behaviour of the NO-dissociation, an NO-dissociation seems only achievable in the CASSCF computation if excited to singlet state S<sub>5</sub> or S<sub>4</sub> due to the flat potential energy curve of S<sub>1</sub>. In the MS-CASPT2 computation, the potential energy well is too steep so that - based on this potential energy scan - no NO-dissociation can be accomplished. Furthermore, the calculated BDEs differ considerably. For the Mo-C-bond, a BDE of 1.56 eV was calculated with CASSCF whereas MS-CASPT2 predicts 2.25 eV. For the Mo-N-bond, CASSCF produced a BDE of 3.14 eV, while MS-CASPT2 yields 3.96 eV.

In order to determine which method is qualitatively more accurate, the calculated BDEs were compared to experimentally measured values found in literature. Generally, not many BDEs are published for molybdenum, especially for the Mo-N bond. In addition, no experimental studies on either of the three complexes investigated in this thesis were found that report a BDE which is problematic because different molecules have their own electronic structure and bond strengths differ often significantly depending on other ligands coordinated to the metal center. Moreover, different experimental methods require different setups with differing temperatures, pressures, solvents, etc. being used. Consequently, a comparison with reported reference values is difficult. Nonetheless, the results of this literature search are summarized in table 4.1 which identifies CASSCF as the more accurate method. This conclusion is evident when comparing the Mo-C<sub>CO</sub>-BDEs, where the latter two entries are closest to the simulation setup because measurements were also performed in gas phase. For the Mo-N<sub>NO</sub>-BDEs, essentially no reliable reference

## 4. Results and Discussion

Table 4.1.: Summary of reported BDEs found in literature with the corresponding in this thesis calculated values for comparison.

BDE [eV]	Molecule	Mo-C Method	Reference	BDE [eV]	Molecule	Mo-N Method	Reference
1.56	CpMo	CASSCF(8,13), gas phase	this thesis	3.14	CpMo	CASSCF(8,13), gas phase	this thesis
2.25	CpMo	MS-CASPT2(8,13)*, gas phase	this thesis	3.96	CpMo	MS-CASPT2(8,13)* <sup>o</sup> , gas phase	this thesis
1.74	Mo(CO) <sub>6</sub>	photoacoustic calorimetry, Hpt	[122]	0.85	Mo(CO) <sub>5</sub> N <sub>2</sub>	photoacoustic cali- metry, 130 bar, Hpt	[122]
1.39	Mo(CO) <sub>6</sub>	photoacoustic calorimetry, Hpt	[123]	0.39	Mo(CO) <sub>3</sub> (P(Cy) <sub>3</sub> ) <sub>2</sub> N <sub>2</sub>	solution calorimetry, THF	[124]
1.29	Mo(CO) <sub>6</sub>	photoacoustic calorimetry, THF	[125]	0.85	NO on Mo(100)	thermal desorption spectroscopy, 360 K	[126]
1.78	Mo(CO) <sub>6</sub>	molecular beam photo- fragment spectroscopy, 248 nm, gas phase	[127]				
1.76	Mo(CO) <sub>6</sub>	laser pyrolysis, gas phase	[128]				

\* IPEA shift of 0.25 a.u.  
<sup>o</sup> 3.77 eV with IPEA shift of 0.0 a.u.

values were found that could validate either computation outcome due to the reasons mentioned above.

Although CASPT2 is known to overestimate BDEs,<sup>[129]</sup> one question that arises is as to why both potential scans differ so considerably. A reason was suspected in the IPEA shift value which, if included, typically increases excitation energies as explained in chapter 2. Therefore, the CASPT2 calculation was repeated for six different IPEA shift values ranging from 0.0 to 0.35 a.u. which is depicted in Figure 4.24 for the last geometry shown in the potential energy scan where the dissociated bond lengths are 4 Å. The recommended default value implemented in Molcas is 0.25 a.u. which is applied even if no IPEA-keyword is set. As evidenced in Figure 4.24, the IPEA shift affects the excitation energies of the CO-dissociation more strongly than for the NO-dissociation. The exact energy differences between the correction of 0.0 and 0.35 a.u. for each state are shown in the last column of table 4.2. Excitation energies are increased by up to 0.49 eV for the CO dissociation and up to 0.40 eV for the NO-dissociation. This constitutes a particularly interesting result because these values considerably exceed reported values from benchmark studies where an increase of 0.1 to 0.3 eV is observed.<sup>[130,131]</sup> Even though higher shift values have a large effect on the excitation energies especially for higher excited states, the effect on the ground state is small for the CO-dissociation so that the BDE is essentially not affected when using no IPEA shift correction. The situation changes for the Mo-N BDE which decreased to 3.77 eV when no IPEA shift is considered.

To conclude this analysis, it is important to emphasize the fact that the IPEA correction alone does not explain the qualitative differences. However, a more likely explanation for

## 4. Results and Discussion

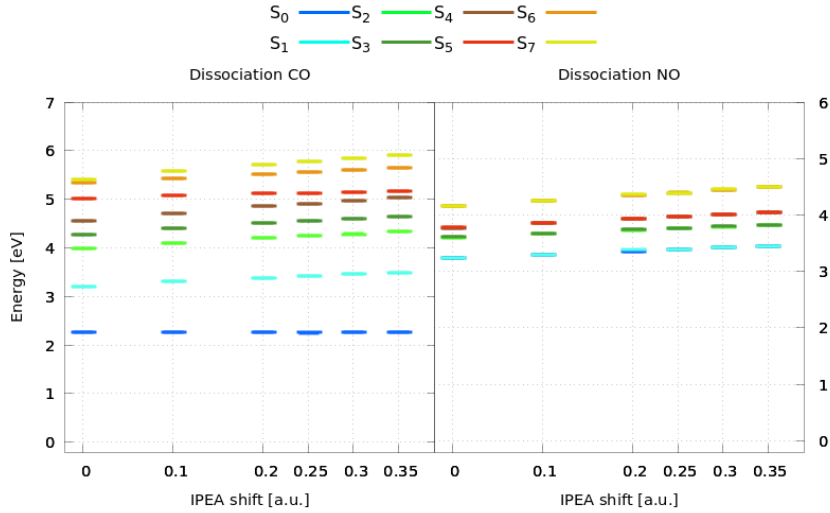


Figure 4.24.: Single state energies for different IPEA shift values at Mo-C<sub>CO</sub> and Mo-N<sub>NO</sub> bond length of 4 Å; energies plotted each relative to the ground state of the equilibrium structure calculated with the same IPEA shift value. (MS-CASPT2(8,13)/ANO-RCC-VDZP gas phase).

Table 4.2.: Single state energies for different IPEA shift values at Mo-C<sub>CO</sub> and Mo-N<sub>NO</sub> bond length of 4 Å; energies given each relative to the ground state of the equilibrium structure calculated with the same shift value; last column contains the energy difference obtained by employing a shift correction of 0.35 a.u. as opposed to none at all (MS-CASPT2(8,13)/ANO-RCC-VDZP gas phase).

State	Energy [eV]						$\Delta E$ [eV]
	0.00 a.u.	0.10 a.u.	0.20 a.u.	0.25 a.u.	0.30 a.u.	0.35 a.u.	
<b>Dissociation CO</b>							
S <sub>0</sub>	2.26	2.26	2.25	2.25	2.25	2.25	-0.01
S <sub>1</sub>	3.20	3.29	3.37	3.41	3.45	3.49	0.29
S <sub>2</sub>	3.97	4.09	4.19	4.23	4.28	4.32	0.35
S <sub>3</sub>	4.27	4.39	4.49	4.54	4.59	4.63	0.37
S <sub>4</sub>	4.54	4.71	4.84	4.90	4.96	5.02	0.47
S <sub>5</sub>	5.01	5.06	5.10	5.12	5.14	5.15	0.14
S <sub>6</sub>	5.33	5.42	5.51	5.55	5.59	5.63	0.30
S <sub>7</sub>	5.40	5.57	5.71	5.78	5.84	5.90	0.49
<b>Dissociation NO</b>							
S <sub>0</sub>	3.77	3.85	3.92	3.96	3.99	4.03	0.25
S <sub>1</sub>	3.78	3.86	3.93	3.96	4.00	4.03	0.25
S <sub>2</sub>	4.20	4.27	4.35	4.39	4.42	4.45	0.26
S <sub>3</sub>	4.21	4.29	4.36	4.40	4.43	4.47	0.26
S <sub>4</sub>	4.40	4.50	4.59	4.63	4.68	4.72	0.31
S <sub>5</sub>	4.41	4.50	4.60	4.64	4.68	4.72	0.31
S <sub>6</sub>	4.84	4.97	5.08	5.13	5.19	5.24	0.39
S <sub>7</sub>	4.84	4.97	5.08	5.14	5.19	5.24	0.40

#### 4. Results and Discussion

this outcome is the small basis set used for the computation. In several benchmark studies, it was shown that CASPT2 and higher levels of theory in general are more sensitive with regard to the size of the basis set, whereby a larger basis set is commonly recommended for these methods.<sup>[131–133]</sup> Therefore, taking all arguments into account, the potential energy curves and calculated BDEs computed with CASPT2 can be assumed to be qualitatively inaccurate compared to the CASSCF outcome, although the latter method is generally considered inferior because it does not capture enough dynamical correlation energy as CASPT2.

During this analysis, it became clear that finding another smaller active space is necessary also with regard to future dynamics calculation which are considerably accelerated in this way so that also a triple-zeta basis set is potentially feasible. For this aim, three observations mentioned above were utilized. The first is the fact that the highest entanglement for both dissociated geometries was found to occur only in orbitals localized on Mo, NO and CO. **CpMo** shows three major exception to this trend, orbital with index 21 which has high entanglement for both diagnostics, as well as orbitals 25 and 12 showing moderate entanglement. The second was the realization that the occupation number of orbital 21 and 25 is relatively small ( $\leq 0.026$ ) compared to all other active space orbitals. The third realization is the general rule of including typically orbitals located on the bond that is being broken during simulation in the active space because they are assumed to retrieve most static energy correlation upon inclusion. Since two different bond-breaking situations should be described with this active space, this means that orbitals primarily located on the Mo-C and Mo-N bond must be included for the chemical problem at hand. Taking all three observations into account, an active space was assembled with no Cp-centered MOs (only one active MO exhibits small delocalization involving Cp). The active space is shown in Figure 4.25 and produced qualitatively similar results to the CASSCF(8,13) active space as depicted in Figure 4.26. On a side note, at

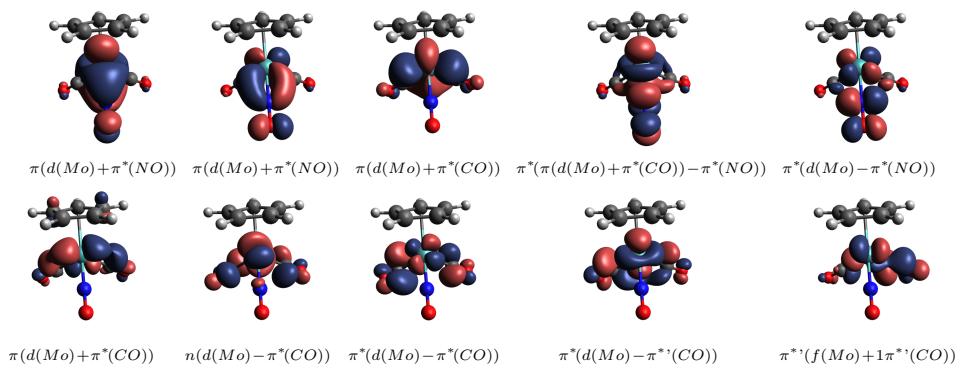


Figure 4.25.: CASSCF(6,10) active space from *left to right*; first three MOs ( $\pi(\text{MoNO})$ ,  $\pi(\text{MoNO})$ ,  $\pi(\text{MoCO})$ ) are occupied, the remaining orbitals ( $\pi^*(\text{MoNO})$ ,  $\pi^*(\text{MoNO})$ ,  $\pi(\text{MoCO})$ ,  $n(\text{MoCO})$ ,  $\pi^*(\text{MoCO})$ ,  $\pi^*(\text{MoCO})$ ,  $\pi^*(\text{MoCO})$ ) are unoccupied (CASSCF(8,13)/ANO-RCC-VDZP gas phase, natural orbitals).

#### 4. Results and Discussion

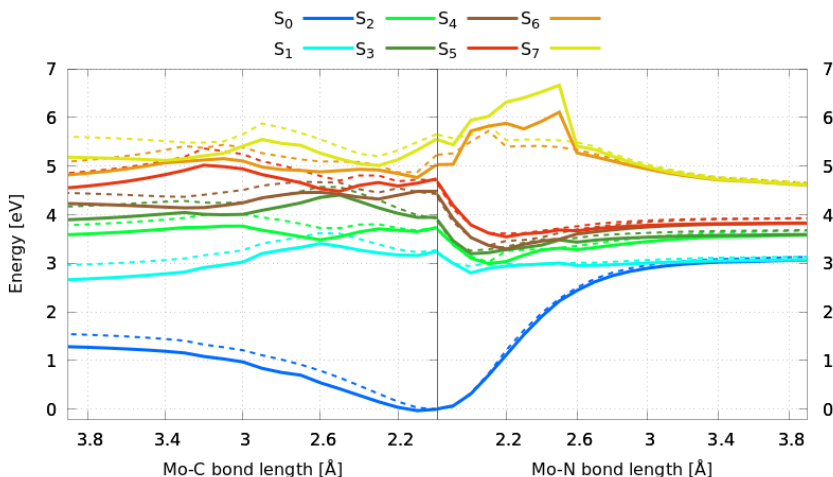


Figure 4.26.: 1D-Potential energy scans along the Mo-C<sub>CO</sub> and Mo-N<sub>NO</sub> bond dissociation of **CpMo** calculated with CASSCF(6,10) (*continuous lines*) and CASSCF(8,13) (*dashed lines*); energies plotted relative to the ground state of the equilibrium structure (ANO-RCC-VDZP gas phase).

this point many different active spaces were tested - also with one active Cp-centered MO - but none of them showed as much conformity to the potential scan produced by the larger active space. Conformance to the CASSCF(8,13) outcome was targeted because a larger active space usually leads to more accurate results. As evidenced in Figure 4.26, the smaller active space shows particularly good agreement to the potential energy curves of the NO-dissociation below 5 eV important for the NO-dissociation simulation. The two energetically highest singlet state are not as good described with the smaller basis set. The relative energies of the CO-dissociation show high agreement to the CASSCF(8,13) computation at lower excitation energies for a small bond elongation and decrease over the course of 2 Å bond elongation. However, the qualitative conclusions are equal for both active spaces, namely that a CO-dissociation is likely to occur in a simulation with this active space whereas an NO-dissociation could possibly occur. Furthermore, the BDE for Mo-N decreases from 3.14 eV (CASSCF(8,13)) to 3.07 eV (CASSCF(6,10)), which is essentially very similar, and, for Mo-C, from 1.56 eV (CASSCF(8,13)) to 1.30 eV (CASSCF(6,10)) which is still closer to the best experimental guess than the MS-CASPT2(8,13) computation. Hence, it can be concluded that the smaller active space is sufficient for the simulation of both reactions.

## 4.3.2. Triplets States and Spin-orbit Couplings

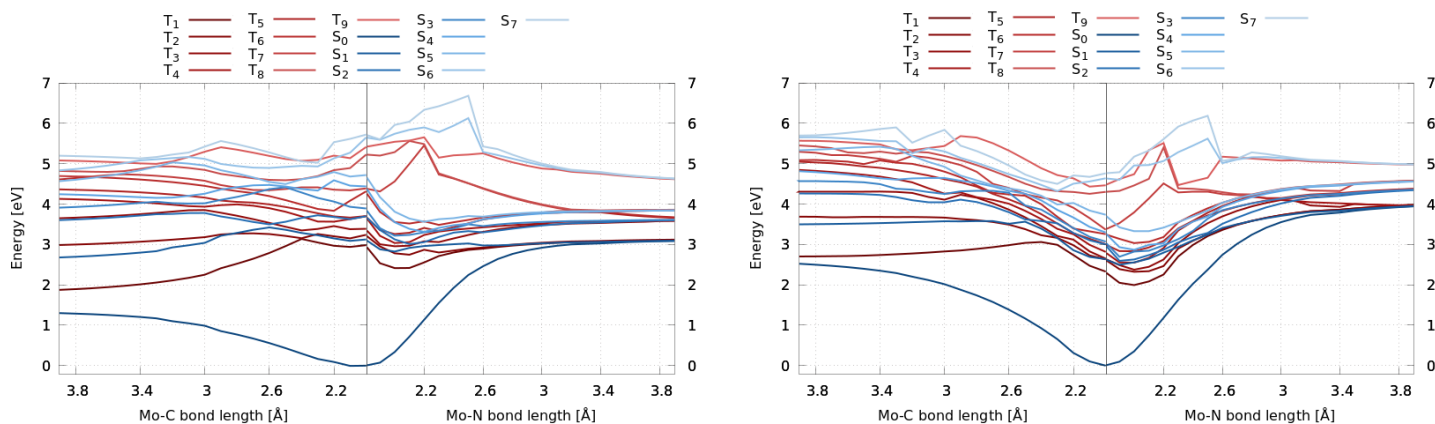


Figure 4.27.: 1D-Potential energy scans along the Mo-C<sub>CO</sub> and Mo-N<sub>NO</sub> bond dissociation of **CpMo** calculated with CASSCF(6,10) (*left*) and MS-CASPT2(6,10) with IPEA of 0.0 a.u. and imaginary shift of 0.1 a.u. (*right*); energies plotted relative to the ground state of the equilibrium structure (ANO-RCC-VDZP gas phase).

Since the selective dissociation of NO cannot be inferred with certainty from the one-dimensional potential energy scan including eight singlet states, two ideas were developed. The first idea involves an experimental setup that excites the molecule twice with two separate laser pulses. In this way, the molecule would be promoted into an excited state and via second laser pulse, the excited molecule can then be promoted into an even higher excited state to follow a different relaxation pathway as would have been the case using one single laser pulse. In order to assess the effectiveness of this experiment, an advanced insight into the multi-dimensional potential energy landscape of **CpMo** is indispensable and certainly difficult to validate on one-dimensional potential energy scans alone which simulate only one degree of freedom. The second idea is to use a triplet sensitizer to specifically target a triplet state in order to coerce the molecule to follow a different relaxation pathway and thereby achieve selective NO-dissociation (with one or two laser pulses). In order to justify such an elaborate and also costly experiment, the project proceeded by assessing both active spaces with regard to their performance of simulating both singlet and triplet states. Therefore, 1D-potential energy scans were calculated that include energetically low-lying triplet states as well. The outcome of this computation using the smaller active space is depicted in Figure 4.27 for CASSCF and CASPT2 level of theory. Based on these scans, it can be concluded that triplet states do not affect the qualitative conclusions drawn from the singlets-only potential scans shown.

Interestingly, the one-dimensional singlet-only potential scan of the NO-dissociation of the smaller active space showed that energetically highest singlet states, S<sub>6</sub> and S<sub>7</sub>, are not as well described with the smaller active space compared to the larger active space. This effect was found to have huge consequence in the scans including triplet states

## 4. Results and Discussion

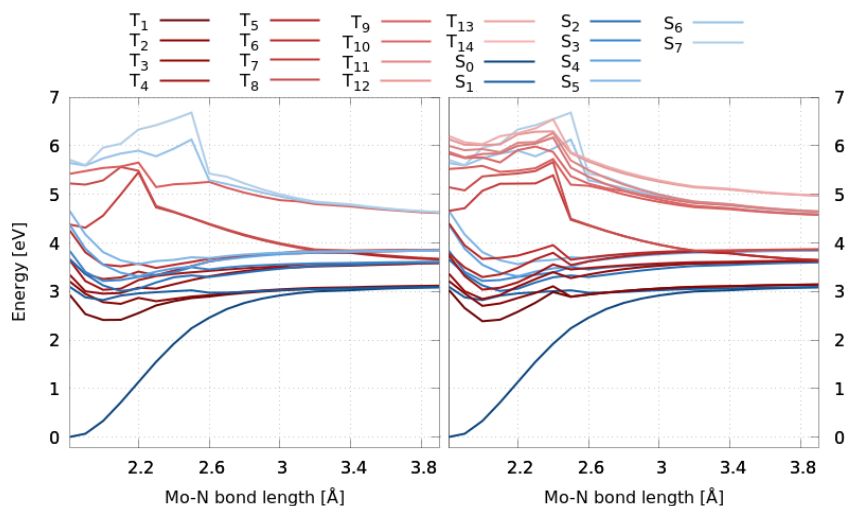


Figure 4.28.: 1D-Potential energy scans along the Mo-N<sub>NO</sub> bond dissociation including 8 singlet states and 9 triplet states (*left*) and 8 singlet states and 14 triplet states (*right*). (CASSCF(6,10)/ANO-RCC-VDZP gas phase).

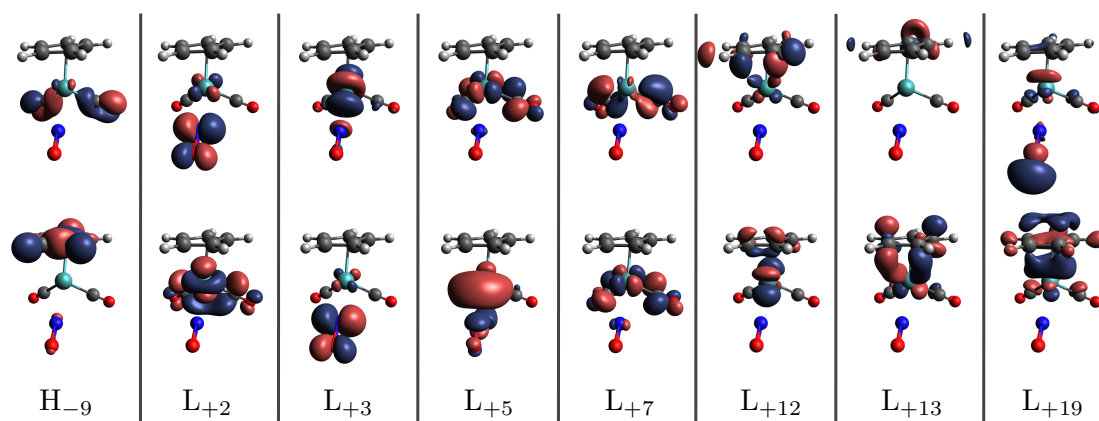


Figure 4.29.: Comparison of the state-averaged orbitals set used for the computation of 8 singlet states and 9 triplet states (*upper row*) and 8 singlet states and 14 triplet states (*bottom row*) at Mo-N<sub>NO</sub> bond length of 2.4 Å (CASSCF(6,10)/ANO-RCC-VDZP gas phase, natural orbitals).

also for energetically low-lying potential energy curves as evidenced in Figure 4.28 where two NO-dissociation simulations are contrasted (the CO-dissociations can be found in Figure A.17 of the Appendix A for reference). On the left hand side, 9 triplet states are included whereas 14 triplet states were included on the right hand side. Particularly conspicuous is the behaviour of the potential energy curves at a Mo-N bond distance of

## 4. Results and Discussion

2.4 Å where a kink in the low-lying potential energy curves compromises the smoothness of the curves also for singlet states. The reason for this outcome was found in the state-averaging protocol of the CASSCF computation. In SA-CASSCF, a single set of orbitals is used to compute all states so that orthogonal states are computed which can be used to calculate further properties as explained in chapter 2.1.4. Comparing the two potential scans of Figure 4.29, it becomes evident that including a larger amount of states badly affect the outcome for all states. In order to validate this explanation, the state-averaged natural orbitals of both simulations, which are used to compute all states, were compared for the critical geometry at Mo-N bond length of 2.4 Å where the kink is located. A summary of this comparison is shown in Figure 4.29, whereas a more detailed version is given in Figure A.18 of the Appendix A. The four orbitals  $L_{+2}$ ,  $L_{+3}$ ,  $L_{+5}$  and  $L_{+7}$  are of particular importance because they are part of the active state. As can be seen in Figure 4.29 (and Figure A.18), the nature and localisation of these MOs changes completely which ultimately causes these differences in the computation of state energies.

The larger active space was also utilized for the computation of triplet states which is shown in comparison to the smaller active space in Figure 4.30. Similarly to the singlet-only potential energy curves, both active spaces produce similar curves. The larger active space clearly describes energetically higher electronic states better than the smaller active space when comparing both computations with regard to lowest relative energies and smoothness of the curves. This also has an effect on the state characters which differ for both active spaces. As can be seen in table 4.3 for the equilibrium geometry, primarily impacted are the state characters of  $S_6$ ,  $S_7$ ,  $T_6$ ,  $T_8$  and  $T_9$ , ergo all higher electronic

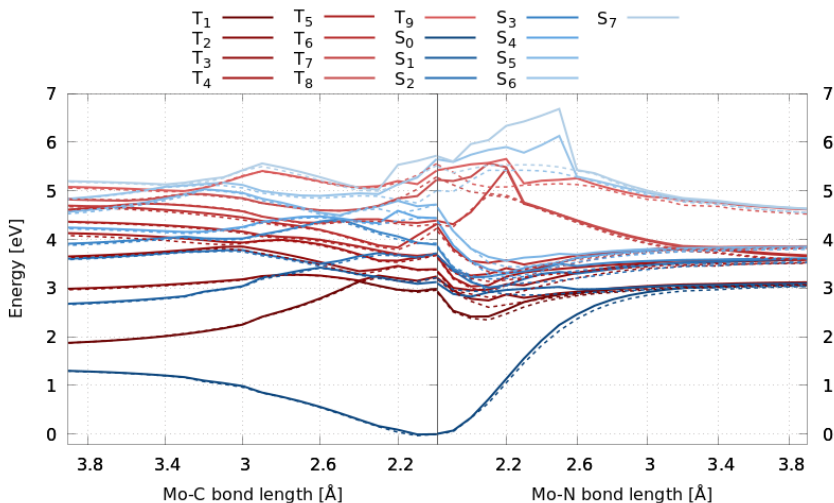


Figure 4.30.: 1D-Potential energy scans along the Mo-C<sub>CO</sub> and Mo-N<sub>NO</sub> bond dissociation of **CpMo** calculated with CASSCF(6,10) (*continuous lines*) and CASSCF(8,13) (*dashed lines*); energies plotted relative to the ground state of the equilibrium structure (ANO-RCC-VDZP gas phase).

## 4. Results and Discussion

Table 4.3.: State characters with a weight of  $> 5\%$ , excitation energies and oscillator strength for all computed states including 8 singlet and 9 triplet states in the calculation (CASSCF(6,10)/ANO-RCC-VDZP and CASSCF(8,13)/ANO-RCC-VDZP gas phase).

State	CAS(8,13)				CAS(6,10)			
	$\Delta E$ [eV]	Character	$w$ [%]	$f_{osc}$	$\Delta E$ [eV]	Character	$w$ [%]	$f_{osc}$
S <sub>1</sub>	3.22	$\pi_{MoCO}\pi^*_{MoNO}$	79	0.0010	3.13	$\pi_{MoCO}\pi^*_{MoNO}$	78	0.0003
S <sub>2</sub>	3.72	$\pi_{MoCO}\pi^*_{MoNO}$	78	$< 0.001$	3.70	$\pi_{MoNO}\pi^*_{MoNO}$	77	$< 0.0001$
S <sub>3</sub>	3.92	$\pi_{MoNO}\pi^*_{MoNO}$	81	0.0011	3.89	$\pi_{MoNO}\pi^*_{MoNO}$	83	0.0014
S <sub>4</sub>	4.44	$\pi_{MoNO}\pi^*_{MoNO}$	49	0.0106	4.44	$\pi_{MoNO}\pi^*_{MoNO}$	48	0.0118
		$\pi_{MoNO}\pi^*_{MoNO}$	37		$\pi_{MoNO}\pi^*_{MoNO}$	38		
S <sub>5</sub>	4.72	$\pi_{MoNO}\pi^*_{MoNO}$	76	$< 0.0001$	4.72	$\pi_{MoNO}\pi^*_{MoNO}$	80	$< 0.001$
		$\pi_{MoCO}\pi_{MoCO}$	7		$\pi_{MoCO}\pi_{MoCO}$	5		
S <sub>6</sub>	5.00	$\pi_{MoCO}\pi_{MoCO}$	70	0.0598	5.65	$\pi_{MoCO}\pi_{MoCO}$	73	0.0005
		$\pi_{MoNO}\pi^*_{MoNO}$	6					
S <sub>7</sub>	5.52	$\pi_{MoNO}\pi_{MoCO}$	65	0.0155	5.72	$\pi_{MoCO}\pi_{MoCO}$	50	0.1026
		$\pi^*_{MoNO}\pi_{MoCO}$	6		$\pi_{MoNO}\pi_{MoCO}$	13		
T <sub>1</sub>	2.96	$\pi_{MoNO}\pi^*_{MoNO}$	52	-	2.98	$\pi_{MoNO}\pi^*_{MoNO}$	52	-
		$\pi_{MoNO}\pi^*_{MoNO}$	34			$\pi_{MoNO}\pi^*_{MoNO}$	36	
T <sub>2</sub>	3.21	$\pi_{MoCO}\pi^*_{MoNO}$	77	-	3.24	$\pi_{MoCO}\pi^*_{MoNO}$	80	-
T <sub>3</sub>	3.38	$\pi_{MoNO}\pi^*_{MoNO}$	78	-	3.39	$\pi_{MoNO}\pi^*_{MoNO}$	79	-
		$\pi_{MoNO}\pi^*_{MoNO}$	10			$\pi_{MoNO}\pi^*_{MoNO}$	9	
T <sub>4</sub>	3.68	$\pi_{MoNO}\pi^*_{MoNO}$	53	-	3.70	$\pi_{MoNO}\pi^*_{MoNO}$	45	-
		$\pi_{MoNO}\pi^*_{MoNO}$	34			$\pi_{MoNO}\pi^*_{MoNO}$	33	
						$\pi_{MoCO}\pi^*_{MoNO}$	10	
T <sub>5</sub>	3.69	$\pi_{MoCO}\pi^*_{MoNO}$	76	-	3.71	$\pi_{MoCO}\pi^*_{MoNO}$	70	-
						$\pi_{MoNO}\pi^*_{MoNO}$	8	
T <sub>6</sub>	4.23	$\pi_{MoCO}\pi_{MoCO}$	60	-	4.32	$\pi_{MoCO}\pi_{MoCO}$	42	-
		$\pi_{MoNO}\pi_{MoCO}$	16			$\pi_{MoNO}\pi^*_{MoNO}$	38	
T <sub>7</sub>	4.32	$\pi_{MoNO}\pi^*_{MoNO}$	61	-	4.39	$\pi_{MoNO}\pi^*_{MoNO}$	41	-
		$\pi_{MoCO}\pi_{MoCO}$	16			$\pi_{MoCO}\pi_{MoCO}$	37	
		$\pi_{MoNO}\pi^*_{MoNO}$	8			$\pi_{MoNO}\pi^*_{MoNO}$	5	
T <sub>8</sub>	5.29	$\pi_{MoNO}\pi_{MoCO}$	73	-	5.23	$\pi_{MoCO}\pi^*_{MoCO}$	78	-
T <sub>9</sub>	5.56	$\pi_{MoNO}\pi_{MoCO}$	75	-	5.42	$\pi_{MoNO}\pi_{MoCO}$	73	-
						$\pi^*_{MoNO}\pi_{MoCO}$	5	
						$\pi_{MoNO}\pi_{MoCO}$	5	-

states, with one exception being S<sub>2</sub>. Furthermore, also the calculated oscillator strengths and SOCs are impacted by the active space. While S<sub>6</sub> constitutes the brightest state in the CASSCF(8,13) calculation, for CASSCF(6,10) it is S<sub>7</sub>. Regarding the SOC calculation, both active spaces tend to agree better for higher Mo-C<sub>CO</sub>- and Mo-N<sub>NO</sub>-bond elongations as evidenced in Figure A.19 to A.20 for all calculated steps for the CO-dissociation and Figure A.21 to A.22 for the NO-dissociation. Selected geometries along both dissociation reactions are given in Figure 4.31. The SOC components diverge in the CO-dissociation simulation with the two different active spaces of different size mainly in the first three calculated points and otherwise agree reasonably well. However, as already established above, the NO-dissociation is not as good described with the smaller active space especially for the energetically highest states. This also has an effect on the calculation of the SOCs which significantly diverge at smaller Mo-N<sub>NO</sub>-bond elongations, as well as higher

#### 4. Results and Discussion

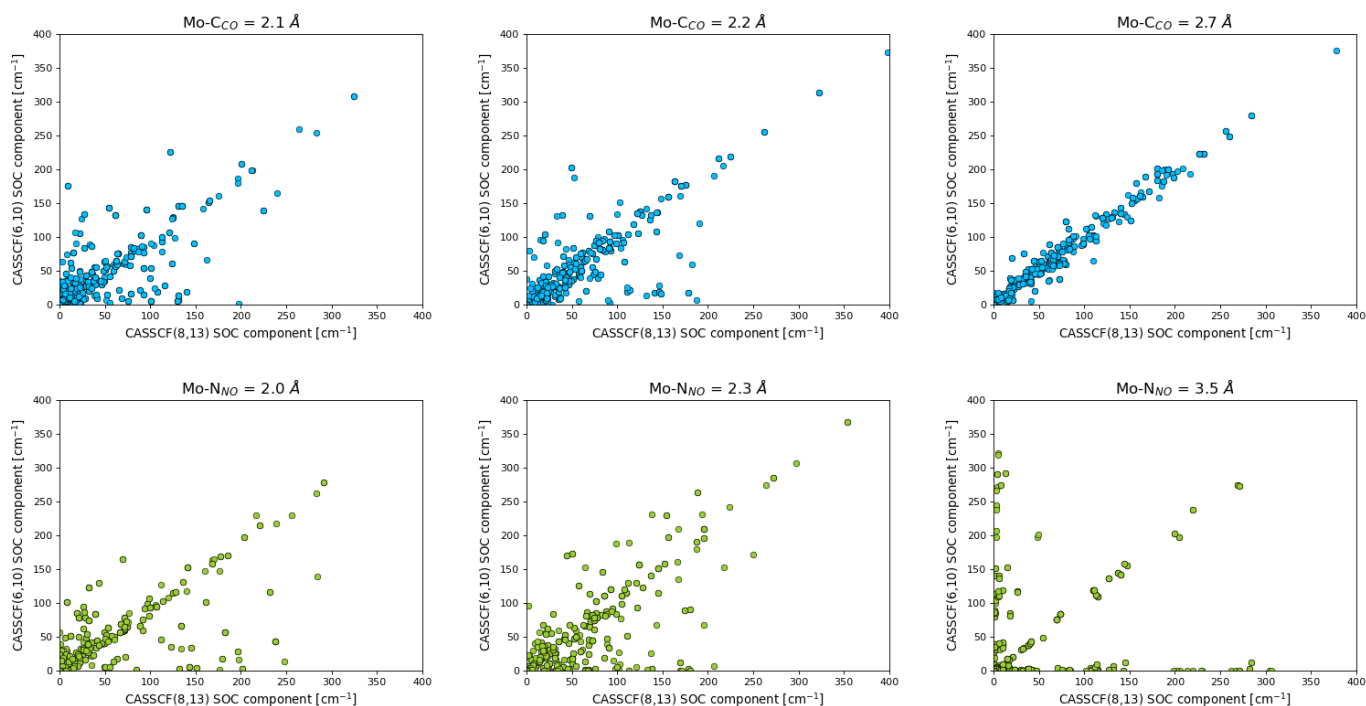


Figure 4.31.: SOC component comparison for the CO-dissociation (*upper panel*) and the NO-dissociation (*lower panel*) of **CpMo** computed on CASSCF(6,10) and CASSCF(8,13) level of theory (gas phase).

Mo-N<sub>NO</sub>-bond lengths even though the potential energy curves shown in Figure 4.30 agree well with one another.

Generally, based on the one-dimensional potential energy scans for both active spaces, it can be concluded that triplet states do not seem to provide opportunity to dissociate NO selectively by using a triplet sensitizer alone. However, the experimental setup of another laser pulse might do the trick. The potential energy scans discussed so far are all unrelaxed scans, where the Mo-C<sub>CO</sub> and Mo-N<sub>NO</sub> bond lengths were progressively elongated whereas the remaining geometrical parameters in the complex do not change. Obviously, this introduces artificiality to some extent. Therefore, an additional relaxed scan was performed with the large active space where the dissociated bond is frozen and the remaining complex is allowed to relax in order to assess how the one-dimensional potential energy curves change. Qualitatively, unrelaxed and relaxed scan agree well with one another, as can be seen from Figure 4.32. Based on the relaxed scan, a second laser pulse seems a valid option for the selective NO-dissociation which should be explored - theoretically and experimentally - in the future. This could be achieved by first promoting the complex into S<sub>5</sub> to accomplish a Mo-N bond elongation to around 2.2 or 2.3 Å. Before the complex is trapped in the potential well found at this geometry and relaxes back to the ground state, a second laser pulse could then promote the excited molecule further

## 4. Results and Discussion

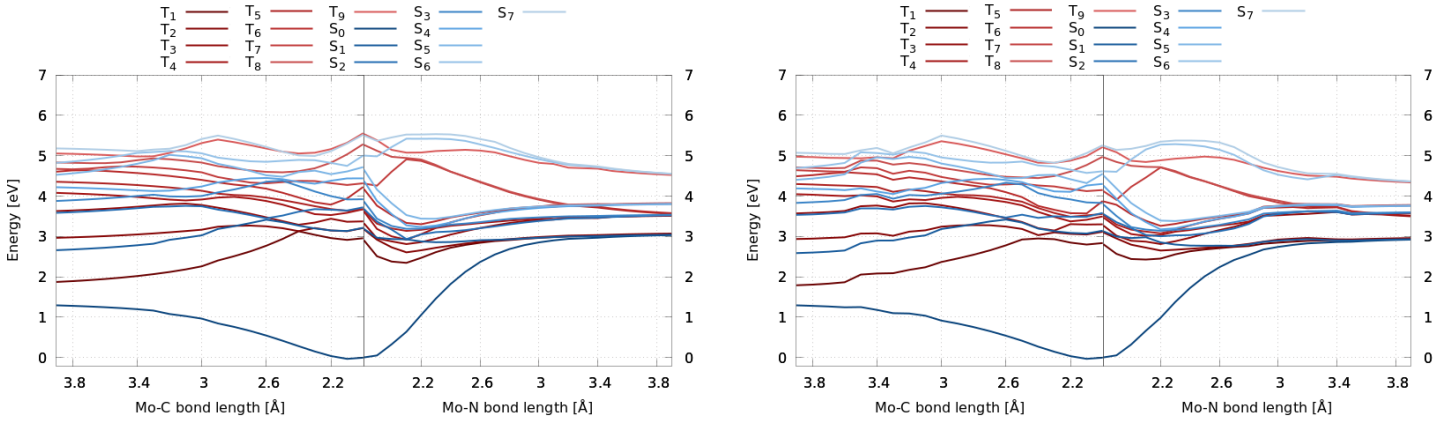


Figure 4.32.: 1D-Potential energy curves along the Mo-C<sub>CO</sub> and Mo-N<sub>NO</sub> bond dissociation of **CpMo** as unrelaxed (*left*) and relaxed (*right*) scan; energies plotted relative to the ground state of the equilibrium structure. (CASSCF(8,13)/ANO-RCC-VDZP gas phase).

Table 4.4.: Summary of calculated BDEs for **CpMo** in gas phase given in eV with the respective computational methodology.

Mo-C			Mo-N		
BDE [eV]	Molecule	Method	BDE [eV]	Molecule	Method
Including 8 singlets					
1.56	<b>CpMo</b>	CASSCF(8,13)	3.14	<b>CpMo</b>	CASSCF(8,13)
2.25	<b>CpMo</b>	MS-CASPT2(8,13), IPEA 0.25 a.u.	3.96	<b>CpMo</b>	MS-CASPT2(8,13), IPEA 0.25 a.u.
2.26	<b>CpMo</b>	MS-CASPT2(8,13), IPEA 0.0 a.u.	3.77	<b>CpMo</b>	MS-CASPT2(8,13), IPEA 0.0 a.u.
Including 8 singlets and 14 triplets					
1.34	<b>CpMo</b>	CASSCF(8,13)	3.08	<b>CpMo</b>	CASSCF(8,13)
1.31	<b>CpMo</b>	CASSCF(6,10)	3.09	<b>CpMo</b>	CASSCF(6,10)
Including 8 singlets and 9 triplets in unrelaxed scan					
1.31	<b>CpMo</b>	CASSCF(8,13)	3.04	<b>CpMo</b>	CASSCF(8,13)
1.31	<b>CpMo</b>	CASSCF(6,10)	3.09	<b>CpMo</b>	CASSCF(6,10)
2.54	<b>CpMo</b>	MS-CASPT2(6,10), IPEA 0.0 a.u.	3.94	<b>CpMo</b>	MS-CASPT2(6,10), IPEA 0.0 a.u.
Including 8 singlets and 9 triplets in relaxed scan					
1.31	<b>CpMo</b>	CASSCF(8,13)	2.92	<b>CpMo</b>	CASSCF(8,13)

into either S<sub>6</sub>, S<sub>7</sub>, T<sub>8</sub> or T<sub>9</sub> to successfully dissociate NO. The latter two triplet states can only be targeted in two instances. First, if energetically low-lying singlet states from which the re-excitation is planned to emanate from have high SOCs to these two triplet states, which is the case for instance for S<sub>1</sub>/T<sub>8</sub> and S<sub>2</sub>/T<sub>9</sub> (with 286 and 279 cm<sup>-1</sup> for unrelaxed and with 230 and 279 cm<sup>-1</sup> for relaxed CASSCF(8,13) scan) at Mo-N<sub>NO</sub>-bond length of 2.2 Å or with 300 cm<sup>-1</sup> S<sub>1</sub>/T<sub>8</sub> (with 300 cm<sup>-1</sup> for unrelaxed and with 207 cm<sup>-1</sup>

#### 4. Results and Discussion

for relaxed CASSCF(8,13) scan) and  $S_2/T_9$  (with  $280\text{ cm}^{-1}$  for relaxed CASSCF(8,13) scan, unrelaxed scan suggests no possible transition here with  $44\text{ cm}^{-1}$ ) at Mo-N<sub>NO</sub>-bond length of  $2.3\text{ \AA}$ . These transitions exhibit one of the highest SOC values calculated for all transitions at this geometry (all top 3% of all 72 possible transitions). Secondly, re-excitation can also be targeted to emanate from an energetically lower triplet state such as  $T_1$  which could be accomplished by the use of a triplet sensitizer. In further consequence, a closer look on excited structures sampled on the relaxed potential energy scan of the NO-dissociation, the Mo-N-O-bond angle changes so that - assuming the molecules follows such a path - the donor mode progressively switches from a three-electron to a one-electron donor mode. This means that a reaction mechanism can be proposed for the experimental setup of two laser pulses, namely an initial laser pulse excites the complex so that an elongated Mo-N bond and a decreased Mo-N-O bond angle is obtained in which the three-electron donation of NO is impaired. This excited structure is then re-excited by a second laser pulse that facilitates the bond dissociation. At last, comparing the relaxed and unrelaxed scan with regard to the calculated BDEs, the Mo-C<sub>CO</sub>-BDE is the same, whereas the Mo-N<sub>NO</sub>-BDE is lowered to  $2.92\text{ eV}$  in the relaxed scan. A final summary of all calculated BDEs is given in table 4.4.

As a concluding task, a diabaticization of the one-dimensional potential energy scans was conducted whose outcome is given in direct comparison to the MCH representation in Figure 4.33. The basis of these diabatic potentials does not depend on molecular coordinates at each step but rather on the eigenstates of the MCH Hamiltonian at the equilibrium geometry. Therefore, the character of each state listed in table 4.3 (*middle column*) is preserved throughout the whole scan. Overall, the topographical features of these diabatic potential energy curves show a bundling of several states along the Mo-C<sub>CO</sub>-elongation scan which is not discernible for the NO-dissociation. In order to obtain any more knowledge with regard to potential relaxation pathways, however, wave packet dynamics could be calculated using the diabatic potential energy curves. Overall, the calculated curves are found to be sufficiently smooth for such a dynamics calculation.

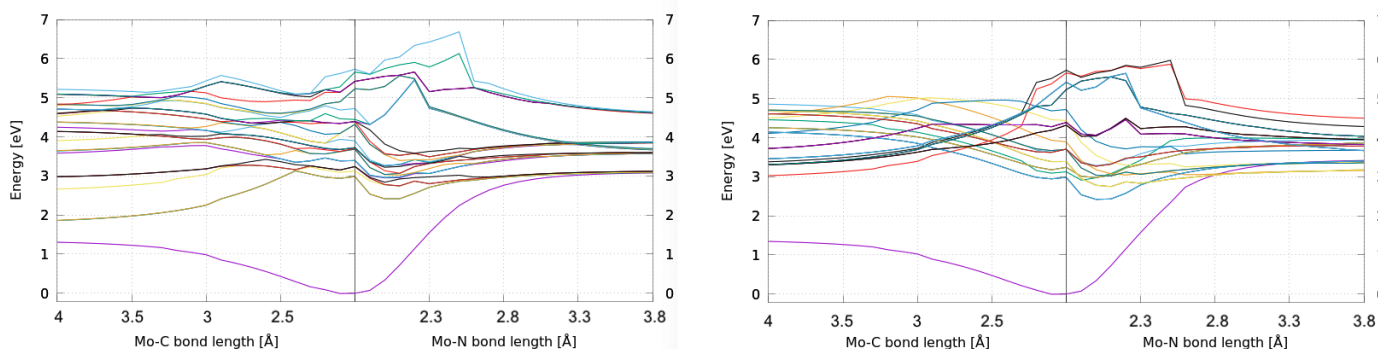


Figure 4.33.: MCH (*left*) and diabatic (*right*) representation of the 1D-Potential energy curves along the Mo-C<sub>CO</sub> and Mo-N<sub>NO</sub> bond dissociation of **CpMo**; energies plotted relative to the ground state of the equilibrium structure (CASSCF(6,10)/ANO-RCC-VDZP gas phase).

## 4.4. Photodissociation Behaviour of TacnMo

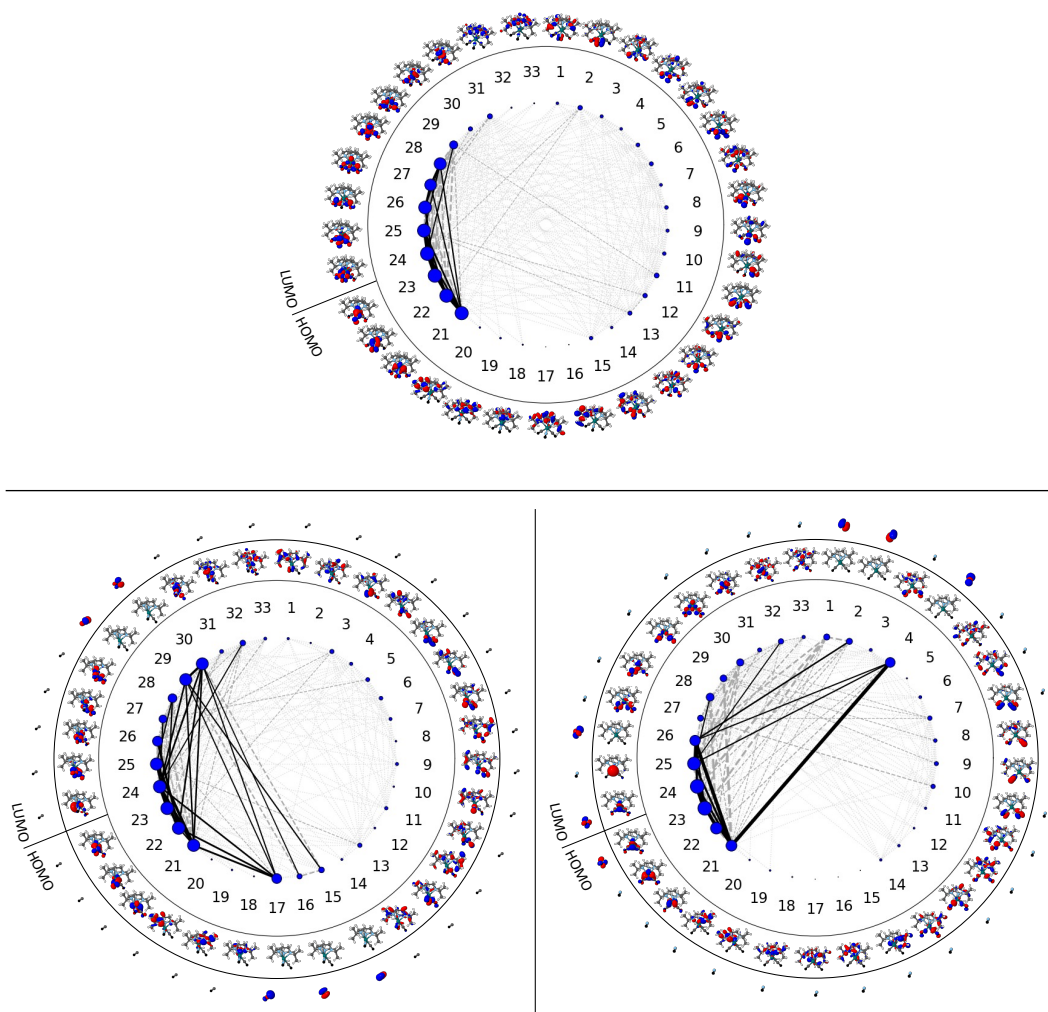


Figure 4.34.: Multi-state entanglement diagrams of **TacnMo** (*upper panel*) and **TacnMoCO<sub>diss</sub>** and **TacnMoNO<sub>diss</sub>** (*lower panel left to right*); single orbital entropy,  $Z_{s(1)}$ , for each orbital is encoded in the node size given in blue and the mutual information of each orbital pair,  $I_{ij}$ , is represented by the connecting lines of different thickness and color intensity depending on the value (DMRG[250](46,33)-SCF/ANO-RCC-MB gas phase, natural orbitals).

In order to assist in the design of a suitable active space for **TacnMo**, an analogous procedure to above was adopted. First, DMRG entanglement diagrams were generated on whose basis several active spaces were assembled. For each active space, one-dimensional potential energy scans for both dissociation reactions were performed to assess their performance. To avoid repetition, in this chapter, the outcome of the DMRG calculation is not discussed in detail and instead focus is given to notable differences compared to

#### 4. Results and Discussion

the entanglement diagrams of **CpMo**.

The multi-state entanglement diagrams for **TacnMo** are shown in Figure 4.34 for all three geometries whereas the respective orbital classification and single-orbital entropies are given in A.13 and the single-state diagrams in Figure A.8 to A.10 of the Appendix A. As can be seen from the multi-state entanglement diagrams, only a small orbital subset of the intact **TacnMo** shows large entanglement with regard to both diagnostics,  $Z_{s(1)}$  and  $I_{ij}$ . This subset (DMRG index 21 to 29) involves exclusively orbitals located on Mo, NO or CO and not on the Tacn-ligand. However, two orbitals involve p-orbitals located on the  $N_{\text{TACN}}$  that show moderate single orbital entropies in the intact Tacn (**TacnMo**: DMRG index 30 and 31) and in both dissociated complexes (**TacnMo**<sub>COdiss</sub> and **TacnMo**<sub>NOdiss</sub>: DMRG index 32 and 33). With the exception of these two orbitals, not many other MOs with contributions located on the Tacn-Ligand exhibit high entanglement. For this reason, contrary to the initial CASSCF(8,13)-active space and in line with the second active space for the CASSCF(6,10) computation of **CpMo**, no orbitals primarily located on the Tacn-ligand were included in the final active space of **TacnMo** with which the best result was achieved. An additional particularly interesting result visible in the entanglement diagram of both dissociated geometries is the high mutual information value of the

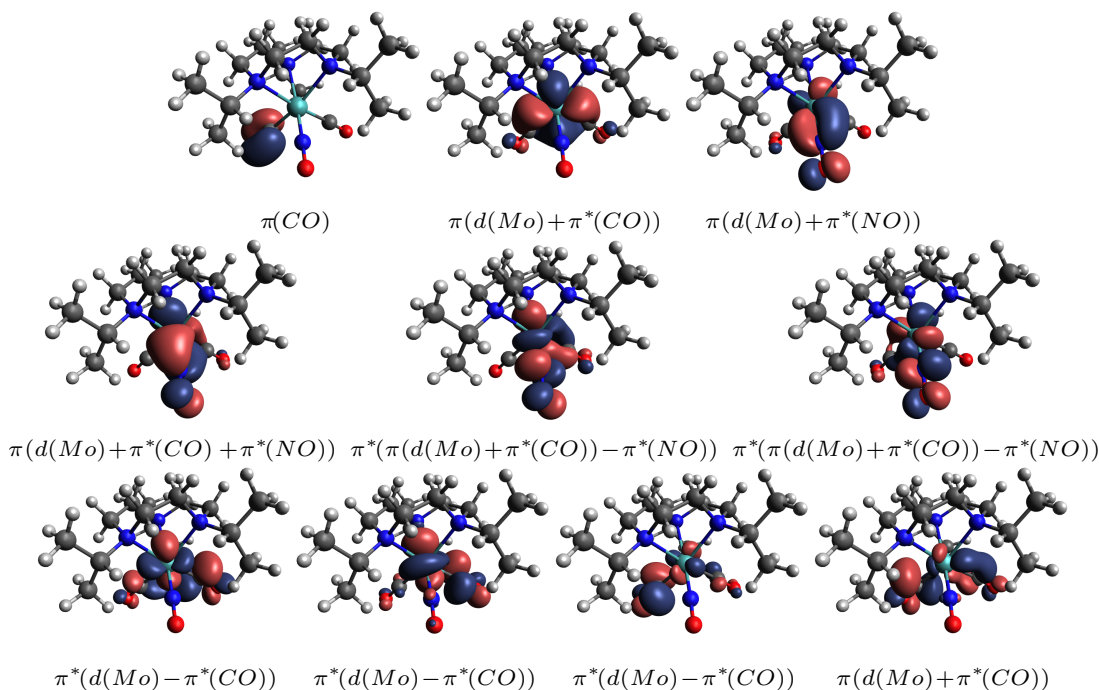


Figure 4.35.: CASSCF(8,10) active space from *left to right*; first four MOs ( $\pi(\text{CO})$ ,  $\pi(\text{MoCO})$ ,  $\pi(\text{MoNO})$ ,  $\pi(\text{MoCONO})$ ) are occupied, the remaining orbitals ( $\pi^*(\text{MoNO})$ ,  $\pi^*(\text{MoNO})$ ,  $\pi^*(\text{MoCO})$ ,  $\pi^*(\text{MoCO})$ ,  $\pi^*(\text{MoCO})$ ,  $\pi(\text{MoCO})$ ) are unoccupied (CASSCF(8,10)/ANO-RCC-VDZP gas phase, natural orbitals).

## 4. Results and Discussion

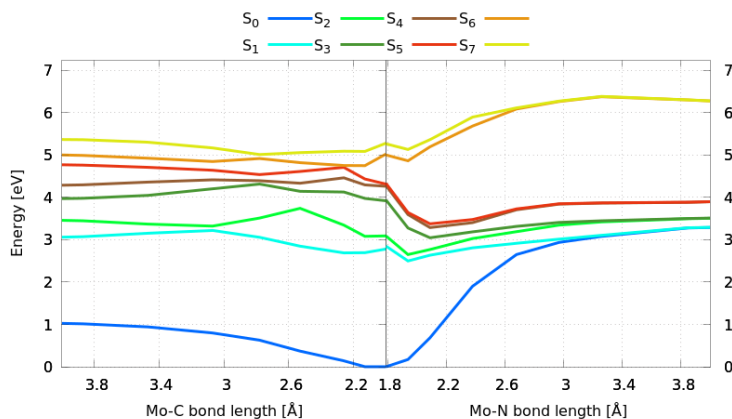


Figure 4.36.: 1D-Potential energy scans along the Mo-C<sub>CO</sub> and Mo-N<sub>NO</sub> bond dissociation of **TacnMo**; energies plotted relative to the ground state of the equilibrium structure (CASSCF(8,10)/ANO-RCC-MB gas phase).

$\sigma^*$ -orbital of the dissociated fragment. More specifically, for **TacnMoCO<sub>diss</sub>**, this involves  $\sigma^*(\text{CO})$  (DMRG index 17) and several other orbitals including  $\pi$ -orbitals involving the central atom and NO (DMRG index 21, 22 and 24) and  $\pi^*$ -orbitals located on the dissociating CO (DMRG index 29 and 30) which stems mainly from a high mutual information measured for singlet state  $S_0$ ,  $S_4$  and  $S_6$ . For **TacnMoNO<sub>diss</sub>**, a high static correlation is measured between  $\sigma^*(\text{NO})$  (DMRG index 4) and the  $\pi_1(\text{d}(\text{Mo})+\pi^*(\text{CO}))$  (DMRG index 21) which is particularly pronounced in singlet state  $S_1$  and  $S_3$  (see Figure A.10). In contrast, the corresponding  $\sigma^*(\text{CO})$  of **CpMoCO<sub>diss</sub>** (DMRG index 10) and  $\sigma^*(\text{NO})$  of **CpMoNO<sub>diss</sub>** (DMRG index 9) are statically uncorrelated in all calculated states.

Several active spaces involving the orbitals with highest entanglement were subsequently used to calculate one-dimensional potential energy curves for both dissociation reaction. The best result with respect to lowest absolute energies and smoothness of the curves was obtained with the active space given in Figure 4.35. The state-averaged active space orbitals are the same in composition and character for the optimization using ANO-RCC-MB and ANO-RCC-VDZP. The occupation numbers of the active space orbitals show that all orbitals are working to capacity with the smallest occupation value being observed in the second energetically highest orbital ( $\pi^*(\text{d}(\text{Mo})-\pi^*(\text{CO}))$ ) with 0.0546 for ANO-RCC-MB and the energetically fourth highest orbital ( $\pi^*(\text{d}(\text{Mo})-\pi^*(\text{CO}))$ ) with 0.1326 for ANO-RCC-VDZP which shows that further reduction would not necessarily lead to the same result. The initial potential energy scan including 8 singlet states (ground state and 7 excited states) is shown in Figure 4.36. Conspicuously, the potential energy scan looks very similar to the potential energy scan of **CpMo**. The curves are not as smooth as the curves obtained for **CpMo** which is presumably due to the fact that only 13 points were calculated within a bond elongation of 2 Å instead of the 21 points that were used for **CpMo**. Qualitatively, upon excitation into  $S_5$  or  $S_4$ , an NO-dissociation

## 4. Results and Discussion

Table 4.5.: State characters with a weight of  $> 5\%$ , excitation energies and oscillator strength for all computed states including 8 singlet states in the calculation (CASSCF(8,10)/ANO-RCC-MB gas phase).

State	$\Delta E$ [eV]	Character	$w$ [%]	$f_{osc}$
S <sub>1</sub>	2.78	$\pi_{\text{MoCO}}\pi^*_{\text{MoNO}}$	61	$<0.001$
		$\pi_{\text{MoCO}}\pi^*_{\text{MoNO}}$	15	
S <sub>2</sub>	3.09	$\pi_{\text{MoCO}}\pi^*_{\text{MoNO}}$	62	$<0.001$
		$\pi_{\text{MoCO}}\pi^*_{\text{MoNO}}$	14	
S <sub>3</sub>	3.92	$\pi_{\text{MoNO}}\pi^*_{\text{MoNO}}$	32	$<0.001$
		$\pi_{\text{MoCONO}}\pi^*_{\text{MoNO}}$	26	
		$\pi_{\text{MoCONO}}\pi^*_{\text{MoNO}}$	25	
S <sub>4</sub>	4.26	$\pi_{\text{MoCONO}}\pi^*_{\text{MoNO}}$	50	0.002
		$\pi_{\text{MoNO}}\pi^*_{\text{MoNO}}$	13	
		$\pi_{\text{MoNO}}\pi^*_{\text{MoNO}}$	10	
		$\pi_{\text{MoCO}}\pi^*_{\text{MoCO}}$	7	
S <sub>5</sub>	4.31	$\pi_{\text{MoNO}}\pi^*_{\text{MoNO}}$	34	0.002
		$\pi_{\text{MoNO}}\pi^*_{\text{MoNO}}$	31	
		$\pi_{\text{MoCONO}}\pi^*_{\text{MoNO}}$	16	
S <sub>6</sub>	5.03	$\pi_{\text{MoCO}}\pi_{\text{MoCO}}$	66	0.005
S <sub>7</sub>	5.28	$\pi_{\text{MoCO}}\pi^*_{\text{MoCO}}$	37	0.149
		$\pi_{\text{MoCONO}}\pi_{\text{MoCO}}$	17	
		$\pi_{\text{MoNO}}\pi^*_{\text{MoNO}}$	7	

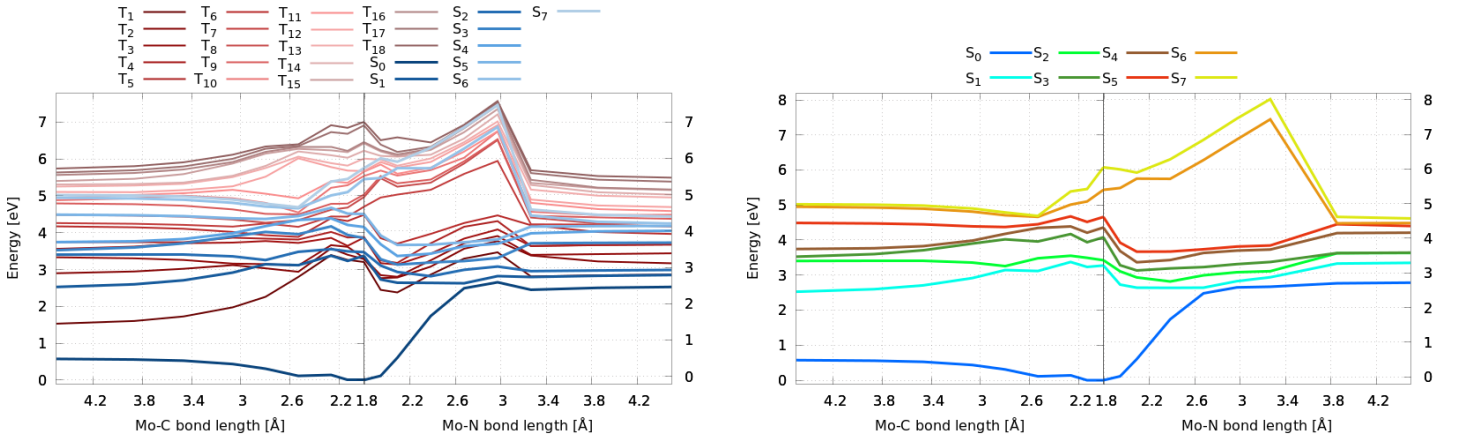


Figure 4.37.: 1D-Potential energy scans along the Mo-C<sub>CO</sub> and Mo-N<sub>NO</sub> bond dissociation of **TacnMo** including 8 singlet and 18 triplet states (*left*) and the same curves as singlet-only plot (*right*); energies plotted relative to the ground state of the equilibrium structure (CASSCF(8,10)/ANO-RCC-VDZP gas phase).

## 4. Results and Discussion

Table 4.6.: State characters with a weight of  $> 5\%$ , excitation energies and oscillator strength for all computed singlet states where 8 singlet and 18 triplet states were included in the calculation (CASSCF(8,10)/ANO-RCC-VDZP gas phase).

State	$\Delta E$ [eV]	Character	$w$ [%]	$f_{\text{osc}}$
S <sub>1</sub>	3.28	$\pi_{\text{MoCONO}}\pi^*_{\text{MoNO}}$	43	$<0.001$
		$\pi_{\text{MoCONO}}\pi^*_{\text{MoCO}}$	35	
S <sub>2</sub>	3.43	$\pi_{\text{MoCONO}}\pi^*_{\text{MoCO}}$	44	0.001
		$\pi_{\text{MoCONO}}\pi^*_{\text{MoCO}}$	35	
		$\pi_{\text{MoCONO}}\pi^*_{\text{MoCO}}$	11	
S <sub>3</sub>	4.08	$\pi_{\text{MoCO}}\pi^*_{\text{MoCO}}$	75	0.007
		$\pi_{\text{MoNO}}\pi^*_{\text{MoNO}}$	8	
S <sub>4</sub>	4.35	$\pi_{\text{MoCO}}\pi^*_{\text{MoNO}}$	48	0.024
		$\pi_{\text{MoNO}}\pi^*_{\text{MoCO}}$	31	
S <sub>5</sub>	4.66	$\pi_{\text{MoNO}}\pi^*_{\text{MoNO}}$	78	0.040
		$\pi_{\text{MoCO}}\pi^*_{\text{MoCO}}$	6	
S <sub>6</sub>	5.43	$\pi_{\text{MoCONO}}\pi^*_{\text{MoNO}}$	75	0.001
S <sub>7</sub>	6.08	$\pi_{\text{MoCO}}\pi_{\text{MoNO}}$	51	0.065
		$\pi_{\text{MoCONO}}\pi_{\text{MoCO}}$	13	
		$\pi^*_{\text{MoNO}}\pi^*_{\text{MoNO}}$	6	

cannot be excluded. Furthermore, the asymptotic behaviour of potential energy curves being degenerate in case of the NO-dissociation can be clearly observed. The respective excitation energies, oscillator strengths and state characters are listed in table 4.5 which shows that singlet state S<sub>7</sub> has the highest oscillator strength which was also expected from the vertical excitation on TD-DFT level of theory. The BDE for Mo-C<sub>CO</sub> is 1.12 eV and 3.38 eV for Mo-N<sub>NO</sub> based on this potential energy scan.

The same calculations have been repeated for the double-zeta basis set as well with triplet states being included from start to save time and computational resources. The outcome is depicted in Figure 4.37 where both singlet and triplet states are plotted on left hand side and only the singlets on right hand side. Already at first glance, it is noticeable that the active space is unsuitable for the simulation of energetically higher-lying states, which was already observed for the triplet computation of **CpMo**. The amount of triplet states to be included in the calculation was judged based on the outcome of the vertical excitation on TD-DFT level of theory which yielded different state energies compared to CASSCF. The effect is very significant for the calculation of the singlet states which in comparison to Figure 4.36 does not yield the qualitatively correct asymptotic behaviour of the NO-dissociation of S<sub>0</sub> and S<sub>1</sub>, as well as S<sub>4</sub> and S<sub>5</sub>. Although also S<sub>7</sub> has the highest oscillator strengths and the state characters do not change dramatically between the calculation using ANO-RCC-MB compared to ANO-RCC-VDZP, the two BDEs of 0.61 eV for Mo-C and 2.81 eV are nonetheless not to be trusted due to the wrong qualitative outcome of the NO-dissociation. Certainly, the calculations using ANO-RCC-VDZP should be repeated with a smaller amount of triplet states - 12 to be exact - or without any triplet states at all in the future to assess whether the active space is suitable for any further simulations on this molecule.

## 4.5. DabCo: A New PhotoCONORM Proposed

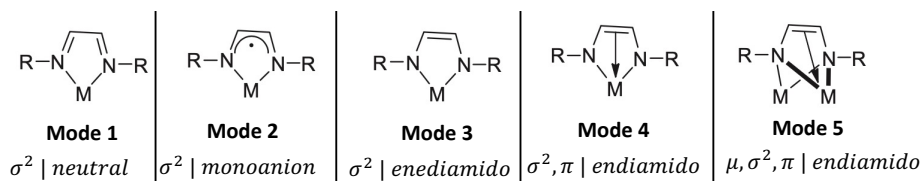


Figure 4.38.: Potential coordination modes of 1,4-diaza-1,3-butadiene when coordinated to a transition metal center.

As already elaborated in the introduction of this thesis, several key aspects for the design of an efficient photo-CONORM became evident in the discussions with both experimental groups collaborating on this project. On the one hand, functionalization of the ligand is desirable for the potential application in a biomedical context. On the other hand, in order to achieve selective CO-dissociation, having only one CO-ligand coordinated to the metal center is much more advantageous than two that could consecutively dissociate from the metal center as is believed to be the case for **CpMo**. Furthermore, the investigation of **TacnMo** showed that having a ligand with heteroatoms connecting to the metal center leads to a higher involvement of the ligand in the charge transfer upon photo-excitation. Inspired by the discussions with both experimental groups, a new ligand is proposed in this thesis that possesses these features, namely 1,4-diaza-1,3-butadiene (Dab). Depending on the metal center, several different coordination modes can be achieved as shown in Figure 4.38.<sup>[134]</sup> Interestingly, Dab constitutes a bidentate ligand coordinating tightly with two nitrogen atoms to the metal center. Thereby, different moieties of also larger size can attach to the coordinating Dab-ligand (abbreviated as R in Figure 4.38) with notable examples from literature being methyl,<sup>[135]</sup> isopropyl,<sup>[15]</sup> t-butyl,<sup>[136]</sup> phenylmethyl,<sup>[134]</sup> triphenylmethyl,<sup>[134]</sup> 2,6-diisopropylphenyl,<sup>[135]</sup> p-tolyl<sup>[135]</sup> as well as asymmetrical examples such as pyridinyl and t-butyl<sup>[136]</sup> among others.<sup>[135,137]</sup> Precisely these reasons make Dab an interesting choice to probe in the context of selective CO/NO-dissociation. Furthermore, by selecting a complex with smaller moieties attached to the Dab-ligand, dynamics calculations can become feasible which makes this ligand also interesting to explore in high-end theoretical calculations. One complex with the Dab-ligand, one CO and one NO attached to a cobalt metal center, **DabCo**, was selected and preliminary calculations were conducted in analogy to the two molybdenum complex. Because **DabCo** contains cobalt as central metal, the outcome of the TD-DFT, DMRG and CASSCF calculations for this complexes is separately discussed in this chapter.

For the calculation of the absorption spectrum, the experimental spectrum of Kaim et al.<sup>[15]</sup> was used as a reference. In order to achieve good alignment between the calculated and the experimental spectrum, a blue-shift-correction of 1.18 eV was considered for the simulated spectrum on TD-DFT level of theory in implicit toluene (see Figure 4.39). For the CASSCF computation in gas phase discussed below, the absorption spectrum is plotted as well. For this simulation, a significantly smaller blue-shift correction of

## 4. Results and Discussion

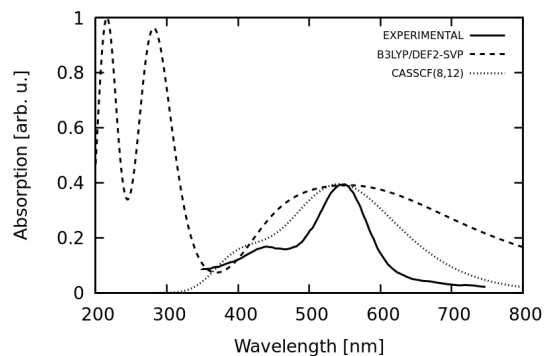


Figure 4.39.: Absorption spectrum of **DabCo** with the experimental spectrum<sup>[15]</sup> given in black and the simulated spectra based on the excitation of the ground state equilibrium geometry in dashed black with TD-DFT B3LYP-D3(BJ)/def2-SVP implicit toluene including a blue-shift-correction of 1.18 eV and CASSCF(8,12)/ANO-RCC-VDZP gas phase considering a blue-shift correction of 0.55 eV.

0.55 eV was needed compared to the TD-DFT calculation. The main absorption band measured at 550 nm or 2.25 eV was identified as MLCT from the authors of the paper published in 2002<sup>[15]</sup> which can be further refined by our charge transfer calculations depicted in Figure 4.40 with the corresponding excitation energies, oscillator strengths

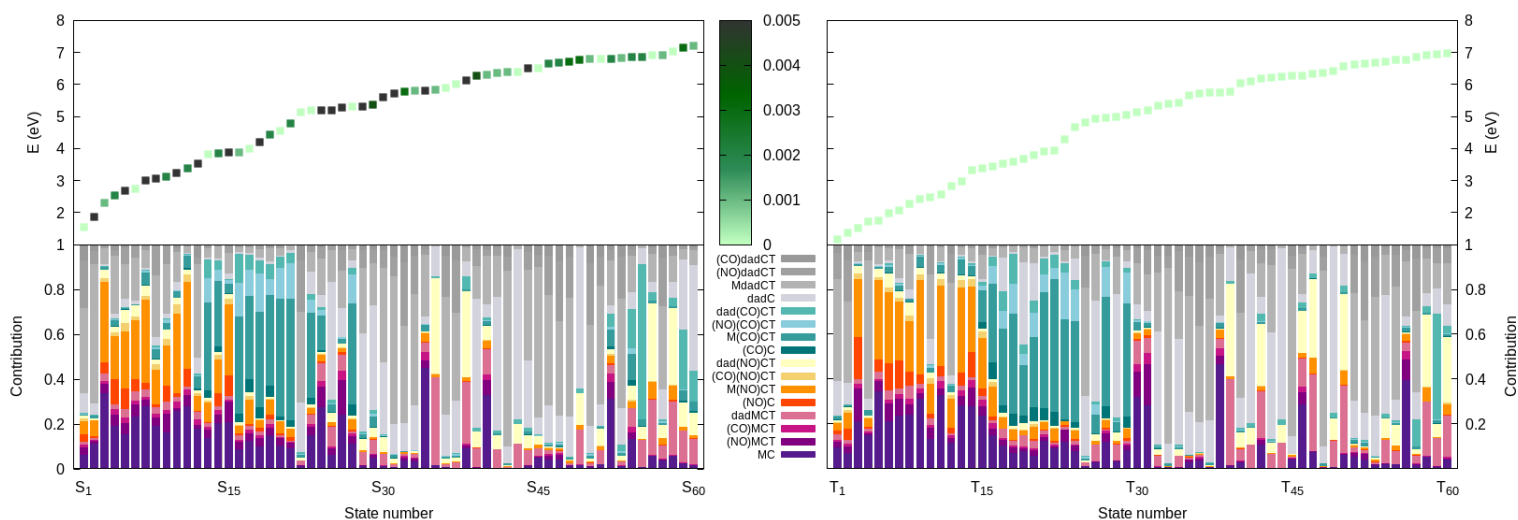


Figure 4.40.: Color-coded decomposition of the charge transfer number matrix (*lower panel*) for each computed singlet (*left*) and triplet state (*right*) of **DabCo** with excitation energies and oscillator strengths (*upper panel*) (TD-DFT B3LYP-D3(BJ)/def2-SVP implicit toluene).

## 4. Results and Discussion

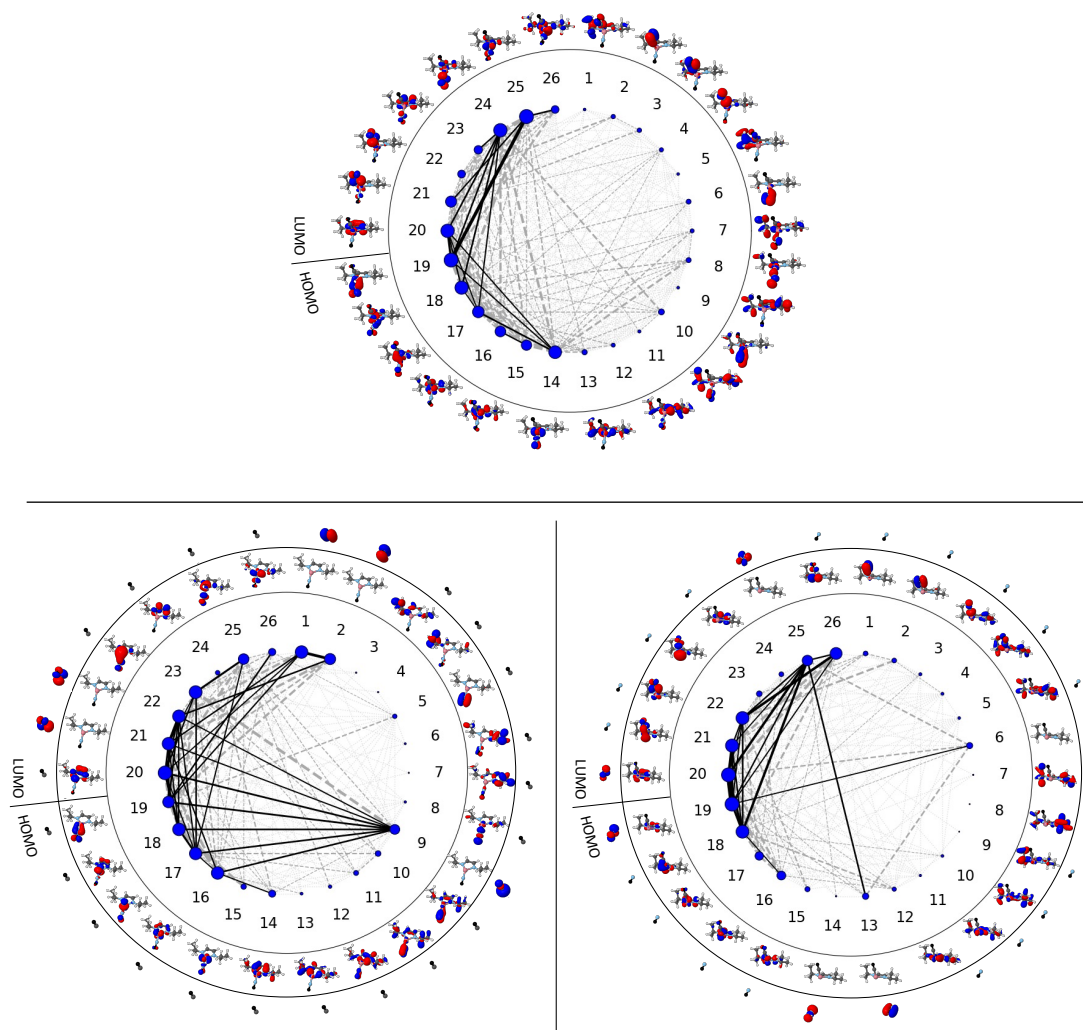


Figure 4.41.: Multi-state entanglement diagrams of **DabCo** (*upper panel*) and **DabCoCO<sub>diss</sub>** and **DabCoNO<sub>diss</sub>** (*lower panel left to right*); single orbital entropy,  $Z_{s(1)}$ , for each orbital is encoded in the node size given in blue and the mutual information of each orbital pair,  $I_{ij}$ , is represented by the connecting lines of different thickness and color intensity depending on the value (DMRG[250](38,26)-SCF/ANO-RCC-MB gas phase, natural orbitals).

and main charge transfer characters listed in table A.8 and A.9 of the Appendix A. The states at peak maximum including blue-shift correction are singlet state  $S_{10}$  and  $S_{11}$  which have a M(NO)CT character. Energetically immediately below and above those two states, a state character of MDabCT dominates. Overall, also for this complex, a charge transfer to the NO-ligand predominantly occurs bundled at lower energies followed by an energy regions where charge flow towards the CO is dominant. In contrast to both molybdenum complexes, a charge transfer towards the Dab-ligand strongly prevails at energies above

## 4. Results and Discussion

5 eV, as well as the first two excited states  $S_1$  and  $S_2$  and has larger contributions in the energy range of predominantly NO-directed character.

Before performing the charge transfer analysis, a hierarchical clustering analysis was also conducted on **DabCo** whose outcome is depicted in Figure A.23 for reference. Contrary to **TacnMo**, the algorithm is able to detect the complete Dab-ligand as one entity although hetero-atoms are coordinated to the metal center. The algorithm does suggest to separate the Dab-ligand into two entities containing both  $^iPr$ -groups in one fragment and the Dab-backbone in a second fragment when cut at a threshold between 0.47 to 0.71. However, in order to compare the charge transfer contributions to the other two complexes, an analogous fragmentation scheme to above was chosen such that the Dab-ligand remains one entity. However, if this complex is being further investigated, it would be interesting to explore in how far the charge flow to the Dab-backbone is influenced by different moieties attached to Dab.

The highest oscillator strength at lower energies was calculated on TD-DFT level of theory for  $S_5$  followed by  $S_2$  and  $S_7$ . Therefore, in analogy to above, 8 singlet states (ground state and 7 excited states) were considered in the DMRG and CASSCF calculations. The multi-state entanglement diagrams of **DabCo** is given in Figure 4.41 with the corresponding orbital characterization and single-orbital entropies being listed in A.14 and the single-state entanglement diagrams given in Figure A.14 to A.16 of Appendix A. Evidently, quite a large number of orbitals show static correlation with orbitals localized on the central metal and all coordinated ligands which is why a  $\pi$ -orbital localized

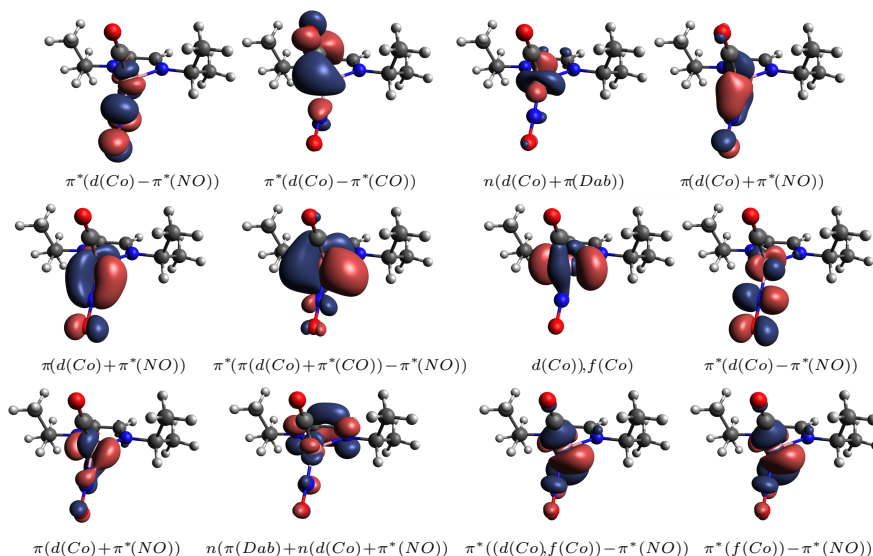


Figure 4.42.: CASSCF(8,12) active space from *left to right*; first four MOs ( $\pi^*(CoNO)$ ,  $\pi^*(CoCO)$ ,  $n(CoDab)$ ,  $\pi(CoNO)$ ) are occupied, the remaining orbitals ( $\pi(CoNO)$ ,  $\pi^*(CoNO)$ ,  $n(Co)$ ,  $\pi^*(CoNO)$ ,  $\pi(CoNO)$ ,  $n(CoNODab)$ ,  $\pi^*(CoNO)$ ,  $\pi^*(CoNO)$ ) are unoccupied (CASSCF(8,12)/ANO-RCC-VDZP gas phase, natural orbitals).

## 4. Results and Discussion

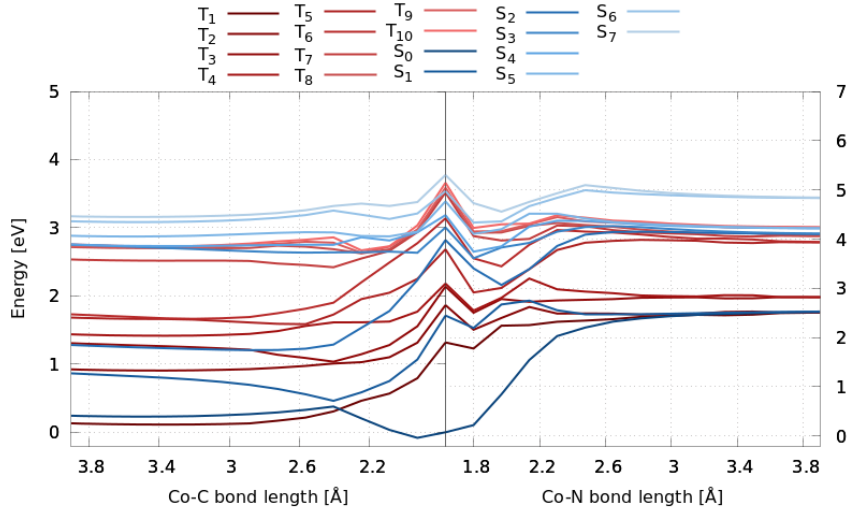


Figure 4.43.: 1D-Potential energy scans along the Co-C<sub>CO</sub> and Co-N<sub>NO</sub> bond dissociation of **DabCo** including 8 singlet and 10 triplet states; energies plotted relative to the ground state of the equilibrium structure (CASSCF(8,12)/ANO-RCC-VDZP gas phase).

Table 4.7.: State characters with a weight of > 5%, excitation energies and oscillator strength for all computed singlet states including 8 singlet and 10 triplet states in the calculation (CASSCF(8,12)/ANO-RCC-VDZP gas phase).

State	$\Delta E$ [eV]	Character	$w$ [%]	$f_{\text{osc}}$
S <sub>1</sub>	1.71	$n_{\text{CoDab}}n_{\text{Co}}$	63	< 0.001
S <sub>2</sub>	2.82	$\pi^*_{\text{CoNO}}n_{\text{Co}}$	46	0.328
S <sub>3</sub>	3.00	$\pi^*_{\text{CoCO}}n_{\text{Co}}, \pi^*_{\text{CoNO}}\pi_{\text{CoNO}}$	5	0.001
		$\pi^*_{\text{CoCO}}\pi_{\text{CoNO}}, \pi^*_{\text{CoNO}}\pi_{\text{CoNO}}$	51	
		$\pi^*_{\text{CoNO}}\pi^*_{\text{CoNO}}, \pi^*_{\text{CoCO}}\pi^*_{\text{CoNO}}, n_{\text{CoDab}}\pi^*_{\text{CoNO}}$	6	
		$\pi^*_{\text{CoNO}}\pi^*_{\text{CoNO}}, \pi^*_{\text{CoNO}}n_{\text{Co}}$	5	
S <sub>4</sub>	3.19	$\pi^*_{\text{CoNO}}\pi^*_{\text{CoNO}}, \pi^*_{\text{CoNO}}n_{\text{Co}}$	58	< 0.001
		$n_{\text{CoDab}}\pi^*_{\text{CoNO}}, \pi^*_{\text{CoNO}}\pi^*_{\text{CoNO}}$	33	0.015
S <sub>5</sub>	3.39	$\pi^*_{\text{CoNO}}\pi^*_{\text{CoNO}}, \pi^*_{\text{CoNO}}n_{\text{Co}}$	24	0.094
		$\pi^*_{\text{CoNO}}\pi^*_{\text{CoNO}}, \pi^*_{\text{CoCO}}\pi^*_{\text{CoNO}}$	5	
		$\pi^*_{\text{CoNO}}\pi^*_{\text{CoNO}}, \pi^*_{\text{CoNO}}n_{\text{Co}}, \pi^*_{\text{CoCO}}\pi^*_{\text{CoNO}}$	13	
S <sub>6</sub>	3.54	$\pi^*_{\text{CoNO}}\pi^*_{\text{CoNO}}, \pi^*_{\text{CoNO}}n_{\text{Co}}$	32	0.032
		$\pi^*_{\text{CoNO}}\pi^*_{\text{CoNO}}, \pi^*_{\text{CoCO}}\pi^*_{\text{CoNO}}$	13	
		$\pi^*_{\text{CoNO}}\pi^*_{\text{CoNO}}, \pi^*_{\text{CoNO}}n_{\text{Co}}, \pi^*_{\text{CoCO}}\pi^*_{\text{CoNO}}$	9	
		$\pi^*_{\text{CoNO}}n_{\text{CoNO}}, \pi^*_{\text{CoNO}}\pi^*_{\text{CoNO}}$	7	
S <sub>7</sub>	3.77	$\pi^*_{\text{CoCO}}\pi^*_{\text{CoNO}}, \pi^*_{\text{CoNO}}\pi^*_{\text{CoNO}}$	29	0.032
		$\pi^*_{\text{CoNO}}\pi^*_{\text{CoNO}}, n_{\text{CoDab}}\pi^*_{\text{CoNO}}$	15	
		$\pi^*_{\text{CoNO}}\pi^*_{\text{CoNO}}$	10	
		$\pi^*_{\text{CoNO}}\pi^*_{\text{CoNO}}n_{\text{CoDab}}$	5	

#### 4. Results and Discussion

mainly on Dab was included in the active space for the potential scan. Furthermore, the  $\sigma^*$ -orbital of the dissociating CO-ligand in **DabCo**<sub>COdiss</sub> exhibits a significantly high mutual information value with 8 other orbitals even more so than the  $\pi$ -orbitals of CO, which is characteristic for all calculated states except S<sub>5</sub>. Possibly, this could be explained by the fact that the  $\sigma^*$ -orbital is energetically much closer to the HOMO than the two  $\pi$ -orbitals. However, this observation is not valid for **DabCo**<sub>NOdiss</sub> where, even though the  $\sigma^*$ -orbital is energetically higher than the two  $\pi$ -orbitals of the dissociating NO-ligand, it is found to have almost no static correlation.

The active space which qualitatively achieved the best potential energy curves is depicted in Figure 4.42. As mentioned above, one  $\pi$ -orbital localized primarily on Dab was included in the active space and is found to have the fourth highest occupation number of all active orbitals. A particularly low occupation number of 0.0068 and 0.0025 have the two energetically highest orbitals within the active space which provides opportunity to truncate the active space for future calculations. The potential energy curves calculated with this active space are given in Figure 4.43. The curves are not particularly smooth which could be amended by simply calculating more points because only 11 points were calculated in 2 Å compared to the 21 points used for the **CpMo** potentials. Based on these two potential energy scans, both dissociation reactions could be a possibility. However, contrary to the two molybdenum complexes, a selective path for either of the two reaction cannot be inferred from the curves. To determine which reaction does occur predominantly, further calculations and experiments are necessary.

Another important result is that, in all states, multiple electrons are excited such that each state is characterized by a multitude of different state characters with the same weight, as well as with different weight (see table 4.7). This suggests together with the air-instability hinted at in literature<sup>[14]</sup> that the structural composition of **DabCo** probably must be altered with regard to the metal center for future studies to achieve tighter electronic control. Nonetheless, as was shown in this chapter, Dab constitutes an interesting ligand to further explore in the context of a selective CO/NO-dissociation.

## 5. Conclusion

The main objective of this thesis is to make a contribution towards understanding the photodissociation capabilities of two molybdenum complexes for a selective dissociation of either NO or CO. As previously known and confirmed in this project, TMCs are notoriously difficult to simulate especially within the framework of selective ligand dissociation of heteroleptic complexes. This is due to the fact that a large system size conditions long computational times and a sufficiently advanced multi-reference level of theory needs to be chosen in order to perform meaningful simulations for both chemical problems at hand. Additionally, a synergistic approach between experimental chemists and theoreticians is essential because experimental measurements need to provide a sufficient basis to validate theoretical computations. Overall, several findings were presented which will hopefully aid the project in the long run.

First, simulated UV/Vis spectra and charge transfer decomposition of the energetically lowest-excited states indicate that a target-oriented charge transfer towards the NO-ligand is achievable at excitation energies below 4 eV. This provides opportunity to further investigate potential NO-dissociative pathways for **CpMo** and **TacnMo** because if excited electrons populate  $\pi^*$ -orbitals located on the Mo-N<sub>NO</sub>-bond, this bond is selectively weakened which in turn facilitates NO-dissociation. Directed charge transfer towards the CO-ligand is found to occur at excitation energies greater than 4 eV, which thus provides opportunity for a selected CO-dissociation.

From experimentally measured IR spectra, it was prior to this thesis concluded that continuous illumination at 285 nm or 4.35 eV most likely results in CO-cleavage for both complexes with **CpMo** releasing both CO-ligands and **TacnMo** retaining one CO-ligand. To validate this conclusion, an extensive photoproduct exploration has been conducted in the second part of this thesis which verifies the dissociation of one CO-ligand for **TacnMo**. However, the exact photoproduct for **CpMo** remains undetermined on basis of the experimental reference data available at the time of writing this thesis. Nonetheless, several possible photoproducts have been identified including species formed after the dissociation and subsequent replacement of NO with ACN, as well as the dissociation of a single CO-ligand and subsequent replacement with either ACN or H<sub>2</sub>O. In this process, linkage isomerization of the NO-ligand has been ruled out to occur in **CpMo** because at least 10.94 eV is necessary in order to overcome the potential barrier found for a flip of NO. Consequently, to determine hidden signals and rule out dimerization processes, repeating the experiment with more data points and initial photosubstrate concentrations is essential. More data points would certainly achieve better spectroscopic and kinetic fits which in turn could repudiate the hypothesis of several photo-induced processes happening at the same time.

Furthermore, in the third part of this thesis, the photodissociation behaviour of both

## 5. Conclusion

molybdenum complexes was investigated using multi-reference methods. To assist in the tedious active space selection, DMRG generally offers low-cost assistance. However, as shown in this thesis, a feasible active space necessitates the radical reduction to only very few essential orbitals while describing both NO and CO dissociation equally well for which DMRG does not compensate for chemical intuition informed trial-and-error calculations to decide which orbitals, how many and in what order yield the best results. Originally, DMRG calculations were supposed to circumvent this computational time and resource lavish testing phase of different active orbitals. However, in the end, this process was still necessary to produce qualitatively meaningful potential energy curves. Nonetheless, DMRG diagnostics showed that MOs located on either Cp or Tacn primarily exhibit dynamical correlation which aided in the assembly of smaller active spaces.

As a further consequence, one-dimensional potential energy scans for both dissociation reactions have been calculated in order to infer some useful conclusions regarding the overall selective dissociation objective and to formulate future research stages. Firstly, **CpMo** does not seem to be a suitable complex for a selective laser-induced NO-release under continuous illumination. Both the IR-peak analysis of the simulated potential photoproduct as well as the potential energy scans on CASSCF and CASPT2 level of theory suggests this conclusion. To achieve NO-cleavage, an elaborate experimental setup must be employed which, for instance, features two subsequent laser pulses with a short time interval of a few pico- or femto-seconds in between to excite the molecule effectively twice. Another potential route is to make use of a triplet sensitizer while exciting with a first laser pulse to specifically target the energetically lowest triplet state of **CpMo** followed by a second laser-pulse to excite into higher-lying triplet states. For both scenarios, structurally, one can imagine a Mo-N<sub>NO</sub>-bond elongation and weakening achieved by the first laser pulse followed by a re-excitation from this excited state to accomplish the NO-dissociation. Secondly, **TacnMo** and **CpMo** exhibit striking similarities between their respective potential energy curves of both ligand dissociations. For both complexes, similar photochemical relaxation pathways can be hypothesised which could be due to a similar relaxation pathway or due to the active space being very similar because no active orbital is located on the the Tacn- or Cp-ligand. However, the potential energy scan of **TacnMo** shows that the NO-dissociation seems to be more hindered than for **CpMo** so that both two-pulsed experimental set-ups likely seem to fail here. Thirdly, the testing of different active spaces for each complex was done based on their performance for the computation of the energetically lowest singlet states. Upon inclusion of triplet states, the performance of the best active space decreased due to inaccurate computational modeling of the energetically highest triplet states. This is found to have great effect on the qualitative curve shape of the singlet states at lower energies as shown for **CpMo** and **TacnMo** because of the state-averaging procedure of CASSCF.

For **CpMo**, two different active spaces as well as multi-reference methods have been further critically evaluated. On the hand, a close comparison of two different active space sizes, CAS(6,10) and CAS(8,13), reveals that the smaller CAS(6,10) is less accurate for the description of energetically higher states which has an effect on the computation of state characters, oscillator strengths and SOCs for all states. However, both active spaces produced qualitatively similar potential energy curves and comparable values for

## 5. Conclusion

BDEs. The CAS(6,10) has the additional advantage of a three times faster computational time compared to CAS(8,13) and would therefore be more suitable for future dynamics calculations. On the other hand, a comparison of the computational outcome of CASSCF and CASPT2 calculations shows that CASSCF produced Mo-C and Mo-N BDE values closer to the experimental values of similar complexes reported in literature which was contemplated to be an effect of the rather small basis set which makes the outcome of the CASPT2 less reliable. Furthermore, the CASPT2 energy values can be artificially modulated by around 0.5 eV based on the considered IPEA shift value. Because the IPEA shift was shown to be controversial[44], the choice on which value to consider in the computations was aggravated by the fact that no published reference values for TMCs were found. Hence, another important finding of this thesis constitutes the fact that including no IPEA shift value yielded BDEs closest to reported reference values. However, using a higher basis set would be a more reliable strategy to improve the CASPT2 results.

Due to the close collaboration with experimentalists specializing in organic synthesis and laser spectroscopy and discussing the project's objective and progress from three different research perspectives - synthetic, spectroscopic and theoretical - on multiple occasions, it was concluded that a sufficiently small complex comprised of at least one ligand that can be postfunctionalized and a metal center that is equipped with only one equivalent of CO- and NO-ligand is key for future studies. Therefore, a new heteroleptic complex has been proposed and investigated with regard to its potential capability of dissociating either CO or NO from the coordination sphere. One of many possible substructures, namely, a cobalt complex containing two lateral isopropyl moieties on a Dab-ligand, has been selected and calculations analogous to the two molybdenum complexes were performed. Excitation within the Franck-Condon region followed by a charge transfer decomposition evince that also for **DabCo**, directed charge transfer towards the NO-ligand occurs in multiple energetically low-lying states, whereas the CO-ligand can be targeted at slightly higher energies. Overall, the Dab-ligand is more involved in the electronic configurations upon excitation within the calculated energy range of 0 to 7 eV. This result has been utilized in the subsequent CASSCF calculations by including an orbital localized on the Dab-ligand in contrast to both molybdenum complexes where the final active orbitals are only located on Mo, CO and NO. Based on the one-dimensional potential energy curves of this complex, a cleavage of CO and NO are equally likely such that further calculations and experiments are necessary to determine which dissociation occurs more likely.

In conclusion, none of the three complexes can be ruled out with certainty for selective CO- and NO-photodissociation thus far. In this thesis, the theoretical challenge of achieving this objective has been elucidated and tackled with regard to the selection of an appropriate level of theory for the simulation of both reactions. Furthermore, contributions have been made to the organic synthesis group by suggesting a new ligand type and to the experimental spectroscopic group by providing evidence for the justification of different experimental set-ups. As further consequence, the synergistic development of CONORMs can now enter a new research circuit equipped with new ideas and an improved understanding.

# Bibliography

- [1] C. A. Piantadosi, *Free Radical Biology and Medicine* **2008**, *45*, 562–569.
- [2] L. J. Ignarro, G. Cirino, A. Casini, C. Napoli, *Journal of Cardiovascular Pharmacology* **1999**, *34*, 879–86.
- [3] M. Kourti, W. G. Jiang, J. Cai, *Oxidative Medicine and Cellular Longevity* **2017**, *17*, 1942–0900.
- [4] U. Schatzschneider, *Inorganica Chimica Acta* **2011**, *374*, Special Volume: Protagonists in Chemistry Dedicated to Professor Wolfgang Kaim, 19–23.
- [5] M. Popova, L. S. Lazarus, S. Ayad, A. D. Benninghoff, L. M. Berreau, *Journal of the American Chemical Society* **2018**, *140*, 9721–9729.
- [6] S. Pordel, B. R. Schrage, C. J. Ziegler, J. K. White, *Inorganica Chimica Acta* **2020**, *511*, 119845.
- [7] E. Stamellou, D. Storz, S. Botov, E. Ntasis, J. Wedel, S. Sollazzo, B. Krämer, W. van Son, M. Seelen, H. Schmalz, A. Schmidt, M. Hafner, B. Yard, *Redox Biology* **2014**, *2*, 739–748.
- [8] W.-Q. Zhang, A. J. Atkin, I. J. S. Fairlamb, A. C. Whitwood, J. M. Lynam, *Organometallics* **2011**, *30*, 4643–4654.
- [9] P.-J. Huang, J. V. Garcia, A. Fenwick, G. Wu, P. C. Ford, *ACS Omega* **2019**, *4*, 9181–9187.
- [10] N. A. Smith, P. J. Sadler, *Philosophical Transactions of the Royal Society A: Mathematical Physical and Engineering Sciences* **2013**, *371*, 20120519.
- [11] P. Rudolf, F. Kanal, J. Knorr, C. Nagel, J. Niesel, T. Brixner, U. Schatzschneider, P. Nuernberger, *The Journal of Physical Chemistry Letters* **2013**, *4*, 596–602.
- [12] C. Daniel, L. González, F. Neese, *Physical Chemistry Chemical Physics* **2021**, *23*, 2533–2534.
- [13] M. Reiher, *Chimia* **2009**, *63*, 140–145.
- [14] J. Knorr, S. Schott, J. Riefer, C. Nagel, U. Schatzschneider, P. Nürnberger, **2021**, *unpublished manuscript*.
- [15] M. Sieger, K. Hübler, T. Scheiring, T. Sixt, S. Zalis, W. Kaim, *Zeitschrift für anorganische und allgemeine Chemie* **2002**, *628*, 2360–2364.
- [16] E. Schrödinger, *Annalen der Physik* **1926**, *384*, 361–376.
- [17] E. Schrödinger, *Physical Review* **1926**, *28*, 1049–1070.

## Bibliography

- [18] S. Gómez, I. F. Galván, R. Lindh, L. González in *Quantum Chemistry and Dynamics of Excited States*, John Wiley & Sons, Ltd, **2020**, Chapter 1, pp. 1–12.
- [19] D. J. Griffiths, 2nd Edition, Pearson Prentice Hall, **2004**.
- [20] F. Jensen, *Introduction to computational chemistry*, 3rd edition., John Wiley & Sons, Chichester, UK; **2017**.
- [21] C. J. Cramer, 2nd edition, John Wiley & Sons, **2005**.
- [22] D. R. Bates, K. Ledsham, A. L. Stewart, H. S. W. Massey, *Philosophical Transactions of the Royal Society of London. Series A Mathematical and Physical Sciences* **1953**, *246*, 215–240.
- [23] M. Born, R. Oppenheimer, *Annalen der Physik* **1927**, *389*, 457–484.
- [24] A. Szabo, N. S. Ostlund, *Modern Quantum Chemistry: Introduction to Advanced Electronic Structure Theory*, First, Dover Publications, Inc., Mineola, **1996**.
- [25] L. Piela, *Ideas of Quantum Chemistry*, 1st ed., Elsevier Science, **2007**.
- [26] J. Westermayr, PhD thesis, University of Vienna, **2020**.
- [27] S. Mai, P. Marquetand, L. González, *International Journal of Quantum Chemistry* **2015**, *115*, 1215–1231.
- [28] M. Born, K. Huang, *Dynamical Theory of Crystal Lattices*, Clarendon Press, **1954**.
- [29] J. P. Zobel, P.-O. Widmark, V. Veryazov, *Journal of Chemical Theory and Computation* **2020**, *16*, 278–294.
- [30] P.-O. Löwdin, *Physical Review* **1955**, *97*, 1509–1520.
- [31] L. Brillouin, *Journal de Physique et Le Radium* **1932**, *3*, 373–389.
- [32] J. C. Slater, *Physical Review* **1929**, *34*, 1293–1322.
- [33] E. U. Condon, *Physical Review* **1930**, *36*, 1121–1133.
- [34] G. Li Manni, K. Guther, D. Ma, W. Dobrautz in *Quantum Chemistry and Dynamics of Excited States*, John Wiley & Sons, Ltd, **2020**, Chapter 6, pp. 133–203.
- [35] E. Lewars, *Computational Chemistry: Introduction to the Theory and Applications of Molecular and Quantum Mechanics*, Kluwer Academic Publishers, **2003**.
- [36] B. O. Roos, P. R. Taylor, P. E. Siegbahn, *Chemical Physics* **1980**, *48*, 157–173.
- [37] P. E. M. Siegbahn, J. Almlöf, A. Heiberg, B. O. Roos, *The Journal of Chemical Physics* **1981**, *74*, 2384–2396.
- [38] S. Wouters, D. Van Neck, *The European Physical Journal* **2014**, *68*, 1434–6079.
- [39] S. M. Omohundro, *Geometric Perturbation Theory in Physics*, World Scientific, **1986**.
- [40] D. R. Alcoba, A. Torre, L. Lain, G. E. Massaccesi, O. B. Oña, P. Capuzzi, *The Journal of Chemical Physics* **2016**, *145*, 014109.
- [41] B. Levy, G. Berthier, *International Journal of Quantum Chemistry* **1968**, *2*, 307–319.

## Bibliography

- [42] K. Andersson, P. A. Malmqvist, B. O. Roos, A. J. Sadlej, K. Wolinski, *The Journal of Physical Chemistry* **1990**, *94*, 5483–5488.
- [43] K. Andersson, P.-Å. Malmqvist, B. O. Roos, *The Journal of Chemical Physics* **1992**, *96*, 1218–1226.
- [44] J. P. Zobel, J. J. Nogueira, L. González, *Chemical Science* **2017**, *8*, 1482–1499.
- [45] J. Finley, P.-Å. Malmqvist, B. O. Roos, L. Serrano-Andrés, *Chemical Physics Letters* **1998**, *288*, 299–306.
- [46] B. O. Roos, K. Andersson, M. P. Fülcher, L. Serrano-Andrés, K. Pierloot, M. Merchán, V. Molina, *Journal of Molecular Structure: THEOCHEM* **1996**, *388*, 257–276.
- [47] C. Camacho, H. A. Witek, S. Yamamoto, *Journal of Computational Chemistry* **2009**, *30*, 468–478.
- [48] G. Ghigo, B. O. Roos, P.-Å. Malmqvist, *Chemical Physics Letters* **2004**, *396*, 142–149.
- [49] M. F. Pusey, J. Barrett, T. Rudolph, *Nature Physics* **2012**, *8*, 475–478.
- [50] A. Whitaker, 2nd ed., Cambridge University Press, **2006**.
- [51] 2nd Edition, John Wiley Sons, Ltd, Weinheim, New York, **2001**.
- [52] P. Hohenberg, W. Kohn, *Physical Review* **1964**, *136*, B864–B871.
- [53] L. H. Thomas, *Mathematical Proceedings of the Cambridge Philosophical Society* **1927**, *23*, 542–548.
- [54] E. Fermi, *Zeitschrift für Physik* **1928**, *48*, 73–79.
- [55] C. F. V. Weizsäcker, *Zeitschrift für Physik* **1935**, *96*, 431–458.
- [56] G. K.-L. Chan, A. J. Cohen, N. C. Handy, *The Journal of Chemical Physics* **2001**, *114*, 631–638.
- [57] W. Kohn, L. J. Sham, *Physical Review* **1965**, *140*, A1133–A1138.
- [58] A. D. Becke, *The Journal of Chemical Physics* **1993**, *98*, 5648–5652.
- [59] C. Lee, W. Yang, R. G. Parr, *Physical Review B* **1988**, *37*, 785–789.
- [60] R. Colle, O. Salvetti, *Theoretica chimica acta* **1975**, *37*, 329–334.
- [61] A. D. Becke, *Physical Review A* **1988**, *38*, 3098–3100.
- [62] E. Runge, E. K. U. Gross, *Physical Review Letters* **1984**, *52*, 997–1000.
- [63] A. Dreuw, M. Head-Gordon, *Chemical Reviews* **2005**, *105*, 4009–4037.
- [64] E. K. U. Gross, N. T. Maitra in *Fundamentals of Time-Dependent Density Functional Theory*, (Eds.: M. A. Marques, N. T. Maitra, F. M. Nogueira, E. Gross, A. Rubio), Springer Berlin Heidelberg, Berlin, Heidelberg, **2012**, pp. 53–99.
- [65] K. Lopata, N. Govind, *Journal of Chemical Theory and Computation* **2011**, *7*, 1344–1355.

## Bibliography

- [66] K. Burke, J. Werschnik, E. K. U. Gross, *The Journal of Chemical Physics* **2005**, *123*, 062206.
- [67] M. E. Casida in *Recent Advances in Density Functional Methods*, pp. 155–192.
- [68] F. Furche, R. Ahlrichs, *The Journal of Chemical Physics* **2002**, *117*, 7433–7447.
- [69] S. Hirata, M. Head-Gordon, *Chemical Physics Letters* **1999**, *314*, 291–299.
- [70] S. Mai, F. Plasser, J. Dorn, M. Fumanal, C. Daniel, L. González, *Coordination Chemistry Reviews* **2018**, *361*, 74–97.
- [71] M. J. G. Peach, D. J. Tozer, *The Journal of Physical Chemistry A* **2012**, *116*, 9783–9789.
- [72] F. Plasser, H. Lischka, *Journal of Chemical Theory and Computation* **2012**, *8*, 2777–2789.
- [73] F. Plasser, M. Wormit, A. Dreuw, *The Journal of Chemical Physics* **2014**, *141*, 024106.
- [74] F. Plasser, *The Journal of Chemical Physics* **2020**, *152*, 084108.
- [75] R. L. Martin, *The Journal of Chemical Physics* **2003**, *118*, 4775–4777.
- [76] S. Mai, L. González, *Angewandte Chemie International Edition* **2020**, *59*, 16832–16846.
- [77] S. R. White, *Physical Review Letters* **1992**, *69*, 2863–2866.
- [78] S. R. White, *Physical Review B* **1993**, *48*, 10345–10356.
- [79] G. K.-L. Chan, S. Sharma, *Annual Review of Physical Chemistry* **2011**, *62*, 465–481.
- [80] C. J. Stein, M. Reiher, *Molecular Physics* **2017**, *115*, 2110–2119.
- [81] S. Keller, M. Dolfi, M. Troyer, M. Reiher, *The Journal of Chemical Physics* **2015**, *143*, 244118.
- [82] C. J. Stein, M. Reiher, *Journal of Computational Chemistry* **2019**, *40*, 2216–2226.
- [83] W. Unruh, *Philosophical Transactions of the Royal Society A: Mathematical Physical and Engineering Sciences* **2018**, *376*, 20170320.
- [84] L. Freitag, M. Reiher in *Quantum Chemistry and Dynamics of Excited States*, John Wiley Sons, Ltd, **2020**, Chapter 7, pp. 205–245.
- [85] S. F. Keller, M. Reiher, *Chimia* **2014**, *68*, 200–203.
- [86] K. Boguslawski, P. Tecmer, Ö. Legeza, M. Reiher, *The Journal of Physical Chemistry Letters* **2012**, *3*, 3129–3135.
- [87] Ö. Legeza, J. Sólyom, *Physical Review B* **2003**, *68*, 195116.
- [88] J. Rissler, R. M. Noack, S. R. White, *Chemical Physics* **2006**, *323*, 519–531.
- [89] C. J. Stein, M. Reiher, *Journal of Chemical Theory and Computation* **2016**, *12*, 1760–1771.

## Bibliography

- [90] C. J. Stein, V. von Burg, M. Reiher, *Journal of Chemical Theory and Computation* **2016**, *12*, 3764–3773.
- [91] R. Sure, S. Grimme, *Journal of Computational Chemistry* **2013**, *34*, 1672–1685.
- [92] M. J. Frisch, G. W. Trucks, H. B. Schlegel, G. E. Scuseria, M. A. Robb, J. R. Cheeseman, G. Scalmani, V. Barone, G. A. Petersson, H. Nakatsuji, X. Li, M. Caricato, A. V. Marenich, J. Bloino, B. G. Janesko, R. Gomperts, B. Mennucci, H. P. Hratchian, J. V. Ortiz, A. F. Izmaylov, J. L. Sonnenberg, D. Williams-Young, F. Ding, F. Lipparini, F. Egidi, J. Goings, B. Peng, A. Petrone, T. Henderson, D. Ranasinghe, V. G. Zakrzewski, J. Gao, N. Rega, G. Zheng, W. Liang, M. Hada, M. Ehara, K. Toyota, R. Fukuda, J. Hasegawa, M. Ishida, T. Nakajima, Y. Honda, O. Kitao, H. Nakai, T. Vreven, K. Throssell, J. A. Montgomery, Jr., J. E. Peralta, F. Ogliaro, M. J. Bearpark, J. J. Heyd, E. N. Brothers, K. N. Kudin, V. N. Staroverov, T. A. Keith, R. Kobayashi, J. Normand, K. Raghavachari, A. P. Rendell, J. C. Burant, S. S. Iyengar, J. Tomasi, M. Cossi, J. M. Millam, M. Klene, C. Adamo, R. Cammi, J. W. Ochterski, R. L. Martin, K. Morokuma, O. Farkas, J. B. Foresman, D. J. Fox, Gaussian 16 Revision C.01, Gaussian Inc. Wallingford CT, **2016**.
- [93] F. Neese, *Wiley interdisciplinary reviews. Computational molecular science* **2012**, *2*, 73–78.
- [94] F. Neese, *Wiley interdisciplinary reviews. Computational molecular science* **2018**, *8*, e1327.
- [95] M. Dolg, H. Stoll, H. Preuss, *The Journal of Chemical Physics* **1989**, *90*, 1730–1734.
- [96] G. L. Stoychev, A. A. Auer, F. Neese, *Journal of Chemical Theory and Computation* **2017**, *13*, 554–562.
- [97] F. Neese, F. Wennmohs, A. Hansen, U. Becker, *Chemical Physics* **2009**, *356*, 98–109.
- [98] S. Grimme, J. Antony, S. Ehrlich, H. Krieg, *The Journal of Chemical Physics* **2010**, *132*, 154104.
- [99] S. Grimme, S. Ehrlich, L. Goerigk, *Journal of Computational Chemistry* **2011**, *32*, 1456–1465.
- [100] A. V. Marenich, C. J. Cramer, D. G. Truhlar, *The Journal of Physical Chemistry B* **2009**, *113*, 6378–6396.
- [101] M. Cossi, N. Rega, G. Scalmani, V. Barone, *Journal of Computational Chemistry* **2003**, *24*, 669–681.
- [102] V. Barone, M. Cossi, *The Journal of Physical Chemistry A* **1998**, *102*, 1995–2001.
- [103] G. Scalmani, M. J. Frisch, *The Journal of Chemical Physics* **2010**, *132*, 114110.
- [104] B. de Souza, G. Farias, F. Neese, R. Izsák, *Journal of Chemical Theory and Computation* **2019**, *15*, 1896–1904.

## Bibliography

- [105] M. Barbatti, K. Sen, *International Journal of Quantum Chemistry* **2016**, *116*, 762–771.
- [106] S. Mai, M. Richter, M. Heindl, M. F. S. J. Menger, A. Atkins, M. Ruckebauer, F. Plasser, L. M. Ibele, S. Kropf, M. Oppel, P. Marquetand, L. Gonzalez, SHARC 2.1: Surface Hopping Including Arbitrary Couplings — Program Package for Non-Adiabatic Dynamics, [sharc-md.org](http://sharc-md.org), **2019**.
- [107] M. Richter, P. Marquetand, J. González-Vázquez, I. Sola, L. González, *Journal of Chemical Theory and Computation* **2011**, *7*, 1253–1258.
- [108] S. Mai, P. Marquetand, L. Gonzalez, *Wiley interdisciplinary reviews. Computational molecular science* **2018**, *8*, e1370.
- [109] R. Crespo-Otero, M. Barbatti, *Theoretical Chemistry Accounts* **2012**, *131*, 1237.
- [110] F. Aquilante, J. Autschbach, A. Baiardi, S. Battaglia, V. A. Borin, L. F. Chibotaru, I. Conti, L. De Vico, M. Delcey, I. Fdez. Galván, N. Ferré, L. Freitag, M. Garavelli, X. Gong, S. Knecht, E. D. Larsson, R. Lindh, M. Lundberg, P. Å. Malmqvist, A. Nenov, J. Norell, M. Odellius, M. Olivucci, T. B. Pedersen, L. Pedraza-González, Q. M. Phung, K. Pierloot, M. Reiher, I. Schapiro, J. Segarra-Martí, F. Segatta, L. Seijo, S. Sen, D.-C. Sergentu, C. J. Stein, L. Ungur, M. Vacher, A. Valentini, V. Veryazov, *The Journal of Chemical Physics* **2020**, *152*, 214117.
- [111] V. Veryazov, P.-O. Widmark, L. Serrano-Andrés, R. Lindh, B. O. Roos, *International Journal of Quantum Chemistry* **2004**, *100*, 626–635.
- [112] F. Aquilante, R. Lindh, T. B. Pedersen, *The Journal of Chemical Physics* **2008**, *129*, 034106.
- [113] L. Lindenbauer, M. Oppel, L. González, *Molecules* **2020**, *submitted*.
- [114] M. Reiher, D. Peng, *Theoretical Chemistry Accounts* **2012**, *131*, 1432–2234.
- [115] F. Plasser, M. Ruckebauer, S. Mai, M. Oppel, P. Marquetand, L. González, *Journal of Chemical Theory and Computation* **2016**, *12*, 1207–1219.
- [116] K. A. Moltved, K. P. Kepp, *ChemPhysChem* **2019**, *20*, 3210–3220.
- [117] K. P. Jensen, B. O. Roos, U. Ryde, *The Journal of Chemical Physics* **2007**, *126*, 014103.
- [118] M. Lundberg, P. E. M. Siegbahn, *Journal of Computational Chemistry* **2005**, *26*, 661–667.
- [119] G. O. Spessard, G. L. Miessler, Oxford University Press, **2010**.
- [120] A. Iskra, A. S. Gentleman, A. Kartouzian, M. J. Kent, A. P. Sharp, S. R. Mackenzie, *The Journal of Physical Chemistry A* **2017**, *121*, 133–140.
- [121] A. M. Ricks, J. M. Bakker, G. E. Douberly, M. A. Duncan, *The Journal of Physical Chemistry A* **2009**, *113*, 4701–4708.
- [122] E. F. Walsh, V. K. Popov, M. W. George, M. Poliakoff, *The Journal of Physical Chemistry* **1995**, *99*, 12016–12020.

## Bibliography

- [123] J. M. Morse, G. H. Parker, T. J. Burkey, *Organometallics* **1989**, *8*, 2471–2474.
- [124] K. Zhang, A. A. Gonzalez, S. L. Mukerjee, S. J. Chou, C. D. Hoff, K. A. Kubat-Martin, D. Barnhart, G. J. Kubas, *Journal of the American Chemical Society* **1991**, *113*, 9170–9176.
- [125] S. M. Gittermann, T. J. Burkey, *Chemical Physics* **2018**, *512*, 122–127.
- [126] J. Fulmer, W. Tysoe, *Surface Science* **1990**, *233*, 35–43.
- [127] B. Venkataraman, H.-q. Hou, Z. Zhang, S. Chen, G. Bandukwalla, M. Vernon, *The Journal of Chemical Physics* **1990**, *92*, 5338–5362.
- [128] K. E. Lewis, D. M. Golden, G. P. Smith, *Journal of the American Chemical Society* **1984**, *106*, 3905–3912.
- [129] S. Chattopadhyay, *The Journal of Physical Chemistry A* **2020**, *124*, 1444–1463.
- [130] J. L. Bao, S. O. Odoh, L. Gagliardi, D. G. Truhlar, *Journal of Chemical Theory and Computation* **2017**, *13*, 616–626.
- [131] M. Schreiber, M. R. Silva-Junior, S. P. A. Sauer, W. Thiel, *The Journal of Chemical Physics* **2008**, *128*, 134110.
- [132] J. Wen, B. Han, Z. Havlas, J. Michl, *Journal of Chemical Theory and Computation* **2018**, *14*, 4291–4297.
- [133] M. Kepenekian, V. Robert, B. Le Guennic, C. De Graaf, *Journal of Computational Chemistry* **2009**, *30*, 2327–2333.
- [134] S. Anga, R. K. Kottalanka, T. Pal, T. K. Panda, *Journal of Molecular Structure* **2013**, *1040*, 129–138.
- [135] M. Sieger, M. Wanner, W. Kaim, D. J. Stufkens, T. L. Snoeck, S. Zálíš, *Inorganic Chemistry* **2003**, *42*, 3340–3346.
- [136] v. K. Gerad, J. Jastrzebski, K. Vrieze, *Journal of Organometallic Chemistry* **1983**, *250*, 46–61.
- [137] J. P. Neu, P. Di Martino-Fumo, B. Oelkers, Y. Sun, A. Neuba, M. Gerhards, W. R. Thiel, *Dalton Transactions* **2018**, *47*, 9643–9656.

# A. Appendices

## Appendix A1: Geometry comparison

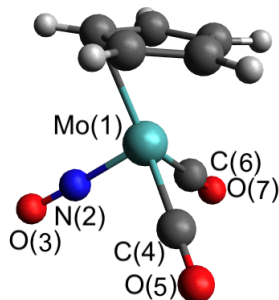


Figure A.1.: Three-dimensional representation of **CpMo** with atom labeling corresponding to table A.1.

Table A.1.: Selected bond lengths and angles of **CpMo** computed on different levels of theory.

	DFT B3LYP-D3(BJ)			CASSCF(8,13)
	def2-SVP*	def2-TZVP*	def2-TZVPP**	ANO-RCC-VDZP**
<b>Distance [Å]</b>				
Mo-C <sup>4</sup>	1.99	1.99	2.00	2.00
Mo-C <sup>6</sup>	2.00	1.99	2.00	2.00
Mo-N <sup>2</sup>	1.82	1.81	1.81	1.85
C <sup>4</sup> -O <sup>5</sup>	1.16	1.15	1.15	1.13
C <sup>6</sup> -O <sup>7</sup>	1.16	1.15	1.15	1.12
N <sup>2</sup> -O <sup>3</sup>	1.18	1.18	1.17	1.14
<b>Angle [°]</b>				
Mo-C <sup>4</sup> -O <sup>5</sup>	178	178	178	178
Mo-C <sup>6</sup> -O <sup>7</sup>	178	178	178	178
Mo-N <sup>2</sup> -O <sup>3</sup>	178	177	176	176
conformer	eclipsed	eclipsed	staggered	staggered
<b>RMSD [Å]</b>	0.016			

\* *implicit solvent acetonitile*; \*\* *gasphase*

## A. Appendices

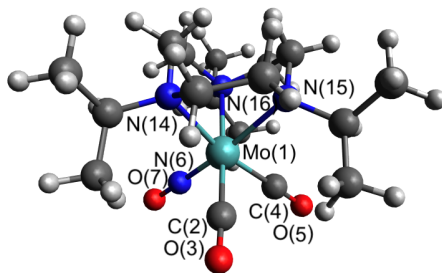


Figure A.2.: Three-dimensional representation of **TacnMo** with atom labeling corresponding to table A.2.

Table A.2.: Selected bond lengths and angles of **TacnMo** computed on different levels of theory.

	DFT B3LYP-D3(BJ)		
	def2-SVP*	def2-TZVP*	def2-TZVPP**
<b>Distance [Å]</b>			
Mo-C <sup>2</sup>	2.01	2.01	2.01
Mo-C <sup>4</sup>	2.00	2.00	2.00
Mo-N <sup>6</sup>	1.80	1.79	1.79
Mo-N <sup>14</sup>	2.34	2.34	2.34
Mo-N <sup>15</sup>	2.39	2.39	2.39
Mo-N <sup>16</sup>	2.32	2.31	2.32
C <sup>2</sup> -O <sup>3</sup>	1.15	1.15	1.15
C <sup>4</sup> -O <sup>5</sup>	1.15	1.15	1.15
N <sup>6</sup> -O <sup>7</sup>	1.18	1.18	1.18
<b>Angle [°]</b>			
Mo-C <sup>2</sup> -O <sup>3</sup>	176	175	176
Mo-C <sup>4</sup> -O <sup>5</sup>	178	177	178
Mo-N <sup>6</sup> -O <sup>7</sup>	178	179	178
N <sup>14</sup> -Mo-N <sup>15</sup>	75	75	75
N <sup>15</sup> -Mo-N <sup>16</sup>	80	80	80
N <sup>16</sup> -Mo-N <sup>14</sup>	80	80	80
<b>RMSD [Å]</b>	0.016		

\* *implicit solvent acetonitile*; \*\* *gasphase*

## A. Appendices

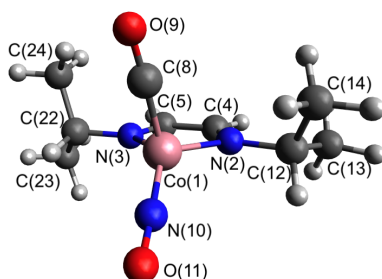


Figure A.3.: Three-dimensional representation of **DabCo** with atom labeling corresponding to table A.3.

Table A.3.: Selected bond lengths and angles of **DadMo** computed on different levels of theory.

	DFT B3LYP-D3(BJ)			
	def2-SVP*	def2-TZVP*	def2-SVP**	def2-TZVP**
<b>Distance [Å]</b>				
Co-C <sup>8</sup>	1.76	1.76	1.76	1.77
Co-N <sup>10</sup>	1.62	1.63	1.63	1.63
Co-N <sup>2</sup>	1.97	1.98	1.96	1.97
Co-N <sup>3</sup>	1.97	1.98	1.95	1.97
C <sup>8</sup> -O <sup>9</sup>	1.15	1.15	1.15	1.15
N <sup>10</sup> -O <sup>11</sup>	1.18	1.18	1.17	1.17
<b>Angle [°]</b>				
Co-N <sup>10</sup> -O <sup>11</sup>	171	171	172	173
Co-C <sup>8</sup> -O <sup>9</sup>	178	177	178	177
C <sup>8</sup> -Co-N <sup>10</sup>	109	109	107	108
N <sup>2</sup> -Co-N <sup>3</sup>	81	81	81	81
C <sup>12</sup> -N <sup>2</sup> -C <sup>4</sup> -C <sup>5</sup>	177	179	179	180
C <sup>22</sup> -N <sup>2</sup> -C <sup>4</sup> -C <sup>5</sup>	177	179	177	179

\* *implicit solvent toluene*; \*\* *gasphase*

## Appendix A2: Experimentally Measured UV/Vis Absorption Spectra

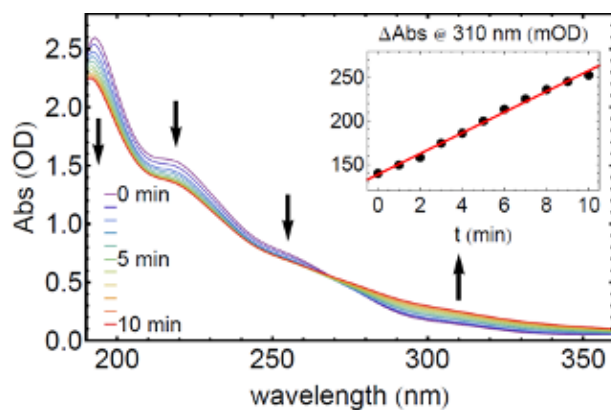


Figure A.4.: Experimentally measured UV/Vis absorption spectra of **CpMo** under continuous illumination with a 285 nm diode for various exposure times between 0 and 10 minutes obtained from [14]; arrows indicate rising or falling signals during photoexcitation (*printed with permission*).

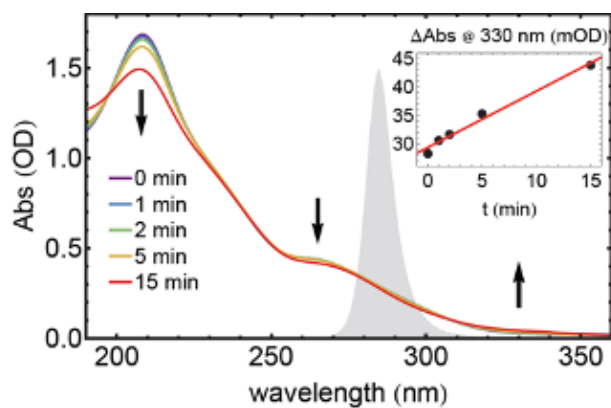


Figure A.5.: Experimentally measured UV/Vis absorption spectra of **TacnMo** under continuous illumination with a 285 nm diode for various exposure times between 0 and 15 minutes obtained from [14]; arrows indicate rising or falling signals during photoexcitation (*printed with permission*).

## Appendix A3: Absorption Spectra on CASSCF level of theory

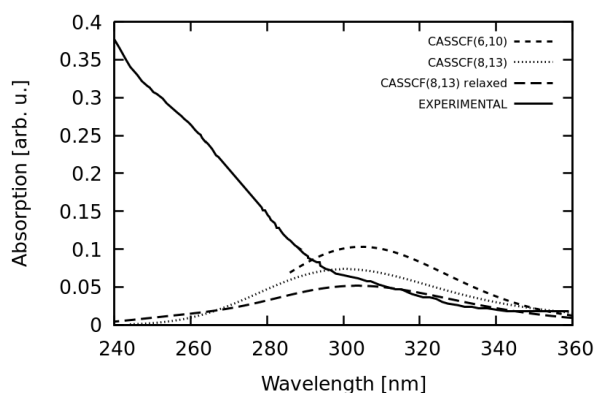


Figure A.6.: Experimental UV/Vis absorption spectra of **CpMo**<sup>[14]</sup> given in black and simulated CASSCF spectra in gas phase given in dashed black; blue-shift correction of CASSCF(6,10) is 1.65 eV, of CASSCF(8,13) in unrelaxed version is 0.9 eV and of CASSCF(8,13) in relaxed version is 0.5 eV. As expected, the larger the active space and the less constraints are included in the simulation, the more accurate are the results which need a smaller blue-shift correction.

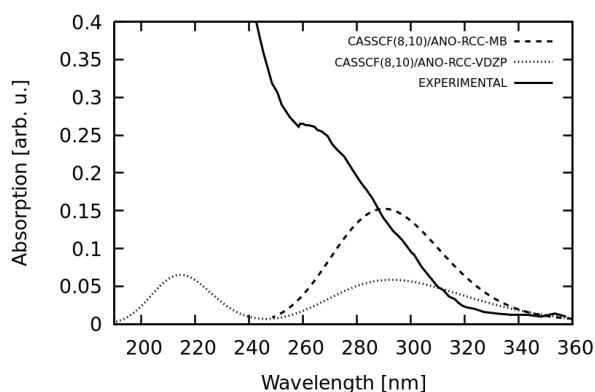


Figure A.7.: Experimental UV/Vis absorption spectra of **TacnMo**<sup>[14]</sup> given in black and simulated CASSCF(8,10) spectra in gas phase given in dashed black; blue-shift correction of the simulation using ANO-RCC-MB is 1.00 eV and of the simulation using ANO-RCC-VDZP is 0.3 eV. Due to the impact of the great number of energetically higher-lying triplet states on the outcome of the singlet states, the CASSCF(8,10)/ANO-RCC-VDZP can be assumed to be less accurate as discussed in chapter 4.4.

## Appendix A3: Quantitative Wave Function Analysis

Table A.4.: Singlet state character analysis of CpMo (DFT B3LYP-D3(BJ)/def2-SVP implicit acetonitrile).

State	$\Delta E$ [eV]	$f_{\text{osc}}$	State Character Analysis						$\sum_{i=1}^3 w_i$ [%]	PR <sub>NTO</sub>
			$w_1$ [%]	$\Omega$	$w_2$ [%]	$\Omega$	$w_3$ [%]	$\Omega$		
S <sub>1</sub>	2.82	0.001	28	M(NO)CT	20	M(CO)CT	15	(CO)(NO)CT	63	1.01
S <sub>2</sub>	2.97	0.003	22	(NO)C	21	M(NO)CT	10	M(CO)CT	53	1.09
S <sub>3</sub>	3.14	0.001	27	M(NO)CT	18	M(CO)CT	14	(CO)(NO)CT	59	1.03
S <sub>4</sub>	3.46	0.006	23	M(NO)CT	20	(NO)C	12	M(CO)CT	55	2.04
S <sub>5</sub>	3.74	0.000	23	M(NO)CT	17	(NO)C	14	M(CO)CT	54	1.26
S <sub>6</sub>	4.22	0.023	26	MC	16	M(CO)CT	13	(CO)MCT	55	1.20
S <sub>7</sub>	4.30	0.007	25	(NO)(CO)CT	25	M(CO)CT			50	1.17
S <sub>8</sub>	4.51	0.000	28	cp(NO)CT	18	cp(CO)CT	10	M(NO)CT	56	1.35
S <sub>9</sub>	4.58	0.000	24	MC	19	M(CO)CT	12	(CO)MCT	55	1.07
S <sub>10</sub>	4.59	0.006	27	cp(NO)CT	18	cp(CO)CT	14	M(CO)CT	59	1.80
S <sub>11</sub>	4.65	0.002	30	M(CO)CT	20	(NO)(CO)CT	12	MC	62	1.54
S <sub>12</sub>	4.89	0.001	16	M(CO)CT	13	MC	12	(NO)MCT	41	1.37
S <sub>13</sub>	4.91	0.000	19	M(CO)CT	18	cp(NO)CT	9	cpMCT	46	1.63
S <sub>14</sub>	5.02	0.006	22	M(CO)CT	13	(NO)(CO)CT	11	MC	46	3.63
S <sub>15</sub>	5.14	0.001	29	MC	14	(CO)MCT	13	McpCT	56	2.55
S <sub>16</sub>	5.21	0.000	17	M(CO)CT	16	(NO)(CO)CT	13	MC	46	2.63
S <sub>17</sub>	5.22	0.007	18	cp(NO)CT	16	cp(CO)CT	14	MC	48	1.79
S <sub>18</sub>	5.24	0.001	27	M(CO)CT	17	MC	11	(CO)C	55	1.60
S <sub>19</sub>	5.32	0.003	15	M(CO)CT	14	(NO)(CO)CT	13	MC	42	2.96
S <sub>20</sub>	5.41	0.001	27	cp(NO)CT	16	cp(CO)CT	10	M(CO)CT	53	2.88
S <sub>21</sub>	5.44	0.003	20	MC	18	(NO)MCT	15	M(CO)CT	53	1.88
S <sub>22</sub>	5.52	0.002	16	M(CO)CT	15	McpCT	15	MC	46	1.75
S <sub>23</sub>	5.61	0.005	23	MC	14	(NO)MCT	13	M(CO)CT	50	1.95
S <sub>24</sub>	5.68	0.000	18	MC	15	M(CO)CT	14	(NO)MCT	47	2.21
S <sub>25</sub>	5.84	0.004	18	MC	15	M(CO)CT	14	(NO)MCT	47	2.38
S <sub>26</sub>	5.93	0.002	35	MC	19	(CO)MCT			54	1.64
S <sub>27</sub>	5.97	0.000	16	cp(CO)CT	16	M(CO)CT	15	cpMCT	47	2.68
S <sub>28</sub>	6.00	0.001	24	cp(CO)CT	13	M(CO)CT	13	MC	50	3.19
S <sub>29</sub>	6.21	0.001	25	(NO)MCT	23	MC	10	(NO)cpCT	58	1.08
S <sub>30</sub>	6.23	0.000	29	McpCT	15	(CO)cpCT	14	MC	58	1.65
S <sub>31</sub>	6.33	0.000	26	MC	17	(NO)MCT	16	McpCT	59	1.44
S <sub>32</sub>	6.38	0.006	25	cp(CO)CT	13	cpMCT	12	MC	50	3.84
S <sub>33</sub>	6.39	0.007	32	cp(CO)CT	17	cpC	15	cpMCT	64	2.39
S <sub>34</sub>	6.50	0.001	32	cp(CO)CT	17	cpC	17	cpMCT	66	1.91
S <sub>35</sub>	6.58	0.002	24	cpMCT	21	cp(CO)CT	9	MC	54	1.79
S <sub>36</sub>	6.69	0.001	21	McpCT	16	(NO)cpCT	12	cpMCT	49	3.63
S <sub>37</sub>	6.74	0.000	22	McpCT	21	(NO)cpCT	12	MC	55	2.65
S <sub>38</sub>	6.79	0.010	26	cp(CO)CT	15	cpMCT	10	M(CO)CT	51	2.58
S <sub>39</sub>	6.82	0.001	17	MC	17	cp(CO)CT	13	cpMCT	47	3.15
S <sub>40</sub>	6.85	0.001	40	MC	21	(CO)MCT			61	1.76
S <sub>41</sub>	6.87	0.006	30	MC	16	McpCT	15	(CO)MCT	61	2.95
S <sub>42</sub>	6.99	0.000	29	McpCT	22	(NO)cpCT			51	1.99
S <sub>43</sub>	7.02	0.000	20	MC	16	McpCT	10	(NO)cpCT	46	1.47
S <sub>44</sub>	7.05	0.000	25	MC	15	cp(CO)CT	13	cpMCT	53	3.38
S <sub>45</sub>	7.12	0.001	26	(NO)MCT	25	MC			51	1.58
S <sub>46</sub>	7.13	0.001	22	cp(CO)CT	17	cpMCT	14	MC	53	3.15
S <sub>47</sub>	7.13	0.003	18	cpMCT	15	MC	15	M(CO)CT	48	2.91
S <sub>48</sub>	7.20	0.001	23	cpMCT	16	MC	10	(NO)MCT	49	2.35
S <sub>49</sub>	7.27	0.001	20	cp(CO)CT	19	cpMCT	16	MC	55	2.25
S <sub>50</sub>	7.30	0.002	21	cp(CO)CT	19	cpMCT	16	MC	56	3.29
S <sub>51</sub>	7.32	0.007	23	MC	13	(NO)MCT	13	cpMCT	49	3.03
S <sub>52</sub>	7.37	0.000	45	cp(NO)CT	29	cp(CO)CT			74	1.00
S <sub>53</sub>	7.46	0.006	46	cp(NO)CT	30	cp(CO)CT			76	1.20
S <sub>54</sub>	7.48	0.002	22	M(CO)CT	14	MC	11	cpMCT	47	3.17
S <sub>55</sub>	7.48	0.018	16	MC	14	cpMCT	14	cp(CO)CT	44	3.94
S <sub>56</sub>	7.51	0.009	26	cpMCT	17	MC	13	cpC	56	2.03
S <sub>57</sub>	7.59	0.028	23	MC	17	cpMCT	13	(NO)MCT	53	2.69
S <sub>58</sub>	7.63	0.006	30	MC	21	(NO)MCT			51	1.41
S <sub>59</sub>	7.64	0.000	34	cpMCT	22	cpC			56	1.27
S <sub>60</sub>	7.82	0.056	19	MC	14	M(CO)CT	12	(NO)MCT	45	2.19

## A. Appendices

Table A.5.: Triplet state character analysis of **CpMo** (DFT B3LYP-D3(BJ)/def2-SVP implicit acetonitrile).

State	$\Delta E$ [eV]	$f_{osc}$	State Character Analysis							PR <sub>NTO</sub>
			$w_1$ [%]	$\Omega$	$w_2$ [%]	$\Omega$	$w_3$ [%]	$\Omega$	$ \sum_{i=1}^3 w_i $ [%]	
T <sub>1</sub>	2.52	-	25	M(NO)CT	22	(NO)C	10	MC	57	1.55
T <sub>2</sub>	2.53	-	27	M(NO)CT	18	M(CO)CT	14	(CO)(NO)CT	59	1.02
T <sub>3</sub>	2.55	-	23	M(NO)CT	22	(NO)C	9	M(CO)CT	54	1.08
T <sub>4</sub>	2.85	-	25	M(NO)CT	22	(NO)C	10	MC	57	2.01
T <sub>5</sub>	2.87	-	28	M(NO)CT	16	M(CO)CT	14	(CO)(NO)CT	58	1.01
T <sub>6</sub>	3.42	-	25	M(NO)CT	19	(NO)C	10	MC	54	1.19
T <sub>7</sub>	3.52	-	33	M(CO)CT	18	(CO)C			51	1.03
T <sub>8</sub>	4.01	-	29	cp(NO)CT	17	cp(CO)CT	13	cpMCT	59	1.30
T <sub>9</sub>	4.13	-	22	M(CO)CT	17	MC	10	(NO)(CO)CT	49	2.02
T <sub>10</sub>	4.20	-	21	M(CO)CT	18	MC	10	(NO)(CO)CT	49	2.09
T <sub>11</sub>	4.25	-	33	M(CO)CT	18	MC			51	1.06
T <sub>12</sub>	4.32	-	26	M(CO)CT	24	MC			50	1.11
T <sub>13</sub>	4.36	-	22	M(CO)CT	17	MC	15	(NO)(CO)CT	54	1.52
T <sub>14</sub>	4.43	-	17	cp(CO)CT	12	MC	11	cp(NO)CT	40	2.17
T <sub>15</sub>	4.53	-	25	cp(NO)CT	14	cpC	11	cp(CO)CT	50	1.54
T <sub>16</sub>	4.62	-	20	cp(NO)CT	14	M(CO)CT	11	MC	45	2.65
T <sub>17</sub>	4.72	-	21	MC	16	M(CO)CT	15	(NO)MCT	52	1.47
T <sub>18</sub>	4.73	-	19	cp(NO)CT	14	MC	13	cp(CO)CT	46	2.23
T <sub>19</sub>	4.73	-	25	(NO)(CO)CT	25	M(CO)CT			50	1.25
T <sub>20</sub>	4.86	-	28	MC	14	M(CO)CT	13	(CO)MCT	55	1.43
T <sub>21</sub>	4.88	-	21	M(CO)CT	14	cp(NO)CT	13	MC	48	2.84
T <sub>22</sub>	4.92	-	20	M(CO)CT	13	(NO)(CO)CT	11	MC	44	1.67
T <sub>23</sub>	5.13	-	30	M(CO)CT	21	(NO)(CO)CT			51	1.68
T <sub>24</sub>	5.19	-	18	MC	17	M(CO)CT	17	(NO)MCT	52	2.01
T <sub>25</sub>	5.26	-	21	M(CO)CT	16	(NO)(CO)CT	13	MC	50	1.28
T <sub>26</sub>	5.31	-	19	cpMCT	19	cp(CO)CT	18	cpC	56	1.85
T <sub>27</sub>	5.31	-	20	M(CO)CT	17	MC	17	(NO)(CO)CT	54	2.62
T <sub>28</sub>	5.45	-	18	cp(CO)CT	17	cpMCT	14	MC	49	1.65
T <sub>29</sub>	5.48	-	20	MC	19	M(CO)CT	17	(NO)(CO)CT	56	2.07
T <sub>30</sub>	5.70	-	23	M(CO)CT	18	MC	18	(NO)(CO)CT	59	1.40
T <sub>31</sub>	5.86	-	30	cpC	16	MC	13	McpCT	59	1.94
T <sub>32</sub>	5.87	-	27	MC	15	cpC	14	(CO)MCT	56	1.57
T <sub>33</sub>	5.98	-	32	cpC	14	McpCT	12	M(CO)CT	58	2.63
T <sub>34</sub>	6.01	-	27	cpMCT	13	cpC	12	cp(CO)CT	52	2.15
T <sub>35</sub>	6.06	-	19	cp(CO)CT	16	McpCT	15	cpC	50	2.31
T <sub>36</sub>	6.11	-	24	(NO)MCT	23	MC	10	cpMCT	57	1.12
T <sub>37</sub>	6.24	-	28	cpMCT	13	cpC	12	MC	53	1.53
T <sub>38</sub>	6.25	-	22	cpC	17	cp(CO)CT	15	cpMCT	54	2.44
T <sub>39</sub>	6.27	-	37	McpCT	16	(CO)cpCT			53	2.07
T <sub>40</sub>	6.33	-	37	cp(CO)CT	17	McpCT			54	1.73
T <sub>41</sub>	6.40	-	34	McpCT	25	(NO)cpCT			59	1.13
T <sub>42</sub>	6.49	-	32	MC	24	(NO)MCT			56	1.04
T <sub>43</sub>	6.53	-	26	cp(CO)CT	19	McpCT	18	(NO)cpCT	63	2.24
T <sub>44</sub>	6.59	-	30	cpMCT	23	cp(CO)CT			53	1.75
T <sub>45</sub>	6.64	-	25	MC	19	cpMCT	13	cp(CO)CT	57	2.05
T <sub>46</sub>	6.68	-	23	McpCT	21	(NO)cpCT	16	cp(CO)CT	60	1.84
T <sub>47</sub>	6.68	-	34	cp(CO)CT	27	cpMCT			61	1.71
T <sub>48</sub>	6.69	-	23	MC	21	cp(CO)CT	19	cpMCT	63	2.26
T <sub>49</sub>	6.71	-	40	MC	21	(CO)MCT			61	1.09
T <sub>50</sub>	6.77	-	37	MC	19	(CO)MCT			56	1.11
T <sub>51</sub>	6.93	-	23	(NO)MCT	23	MC	12	cpMCT	58	1.40
T <sub>52</sub>	6.94	-	24	(NO)MCT	23	MC	11	cpMCT	58	1.17
T <sub>53</sub>	7.00	-	25	cp(CO)CT	16	cpMCT	13	McpCT	54	2.27
T <sub>54</sub>	7.01	-	27	(NO)MCT	25	MC			52	1.09
T <sub>55</sub>	7.02	-	21	McpCT	16	(NO)cpCT	13	cp(CO)CT	50	2.02
T <sub>56</sub>	7.39	-	29	cpMCT	22	cpC			51	1.77
T <sub>57</sub>	7.41	-	21	MC	14	(NO)MCT	13	cpMCT	48	2.30
T <sub>58</sub>	7.42	-	21	cpC	16	cpMCT	15	MC	52	1.82
T <sub>59</sub>	7.49	-	22	cpC	17	McpCT	15	cpMCT	54	1.65
T <sub>60</sub>	7.54	-	25	cpMCT	21	MC	12	cpC	58	1.97

## A. Appendices

Table A.6.: Singlet state character analysis of **TacnMo** (DFT B3LYP-D3(BJ)/def2-SVP implicit acetonitrile).

State	$\Delta E$ [eV]	$f_{osc}$	State Character Analysis							PR <sub>NTO</sub>
			$w_1$ [%]	$\Omega$	$w_2$ [%]	$\Omega$	$w_3$ [%]	$\Omega$	$ \sum_{i=1}^3 w_i $ [%]	
S <sub>1</sub>	2.88	0.000	29	M(NO)CT	23	M(CO)CT			52	1.01
S <sub>2</sub>	3.06	0.001	30	M(NO)CT	18	M(CO)CT			62	1.05
S <sub>3</sub>	3.29	0.001	24	M(NO)CT	21	(NO)C	14	(CO)(NO)CT	56	1.46
S <sub>4</sub>	3.56	0.001	23	M(NO)CT	20	(NO)C	12	M(CO)CT	55	2.02
S <sub>5</sub>	3.67	0.006	22	M(NO)CT	18	(NO)C	14	M(CO)CT	54	1.55
S <sub>6</sub>	4.46	0.001	30	MC	19	M(CO)CT	14	(CO)MCT	63	1.04
S <sub>7</sub>	4.76	0.014	25	M(CO)CT	19	MC	12	(NO)(CO)CT	56	1.69
S <sub>8</sub>	4.77	0.016	30	M(CO)CT	17	(NO)(CO)CT	16	MC	63	1.77
S <sub>9</sub>	4.87	0.005	31	M(CO)CT	16	(NO)(CO)CT	14	MC	61	1.80
S <sub>10</sub>	4.94	0.001	38	tacn(NO)CT	28	tacn(CO)CT			66	1.35
S <sub>11</sub>	4.94	0.001	37	tacn(NO)CT	26	tacn(CO)CT			63	1.22
S <sub>12</sub>	4.99	0.001	34	M(CO)CT	15	MC	12	(CO)C	61	2.55
S <sub>13</sub>	5.02	0.006	32	M(CO)CT	22	(NO)(CO)CT			54	1.60
S <sub>14</sub>	5.02	0.000	40	tacn(NO)CT	27	tacn(CO)CT			67	1.40
S <sub>15</sub>	5.12	0.001	42	tacn(NO)CT	22	tacn(CO)CT			64	1.41
S <sub>16</sub>	5.16	0.001	37	tacn(NO)CT	23	tacn(CO)CT			60	1.30
S <sub>17</sub>	5.25	0.011	22	MC	19	M(CO)CT	10	(NO)MCT	51	2.66
S <sub>18</sub>	5.28	0.000	34	tacn(NO)CT	21	tacn(CO)CT			55	1.40
S <sub>19</sub>	5.51	0.002	25	M(CO)CT	18	MC	16	(NO)(CO)CT	59	2.31
S <sub>20</sub>	5.54	0.005	23	M(CO)CT	19	MC	18	(NO)(CO)CT	60	1.35
S <sub>21</sub>	5.58	0.005	26	M(CO)CT	21	MC	17	(NO)(CO)CT	64	1.80
S <sub>22</sub>	5.66	0.000	29	M(CO)CT	20	MC	13	(NO)(CO)CT	62	2.15
S <sub>23</sub>	5.83	0.003	28	MC	17	M(CO)CT	11	(CO)MCT	56	2.00
S <sub>24</sub>	6.14	0.006	23	MC	19	(NO)MCT	17	M(CO)CT	59	1.61
S <sub>25</sub>	6.16	0.001	34	tacn(NO)CT	27	tacn(CO)CT			61	1.60
S <sub>26</sub>	6.25	0.000	44	tacn(NO)CT	32	tacn(CO)CT			76	2.67
S <sub>27</sub>	6.25	0.000	37	tacn(CO)CT	37	tacn(NO)CT			74	1.94
S <sub>28</sub>	6.28	0.002	58	tacn(CO)CT	11	tacnMCT			69	1.41
S <sub>29</sub>	6.29	0.003	59	tacn(CO)CT	12	tacnMCT			71	1.27
S <sub>30</sub>	6.32	0.003	25	MC	24	MtacnCT	11	(CO)tacnCT	60	1.72
S <sub>31</sub>	6.33	0.000	34	tacn(NO)CT	32	tacn(CO)CT			66	1.97
S <sub>32</sub>	6.33	0.003	19	MC	11	MtacnCT	10	(NO)MCT	40	3.56
S <sub>33</sub>	6.38	0.000	46	tacn(NO)CT	28	tacn(CO)CT			74	1.02
S <sub>34</sub>	6.41	0.000	40	tacn(NO)CT	35	tacn(CO)CT			75	1.80
S <sub>35</sub>	6.42	0.001	23	MC	19	(NO)MCT	15	M(CO)CT	57	1.31
S <sub>36</sub>	6.50	0.002	29	tacn(CO)CT	12	tacn(NO)CT	10	MC	51	3.18
S <sub>37</sub>	6.53	0.001	33	tacn(NO)CT	29	tacn(CO)CT			62	2.99
S <sub>38</sub>	6.53	0.001	34	tacn(CO)CT	11	MC	11	M(CO)CT	56	2.20
S <sub>39</sub>	6.55	0.000	26	tacnMCT	26	tacn(CO)CT			52	2.52
S <sub>40</sub>	6.58	0.004	33	tacnMCT	28	tacn(CO)CT			61	1.27
S <sub>41</sub>	6.61	0.000	41	tacn(NO)CT	32	tacn(CO)CT			73	1.17
S <sub>42</sub>	6.68	0.001	40	tacn(NO)CT	30	tacn(CO)CT			70	1.86
S <sub>43</sub>	6.72	0.000	41	MtacnCT	18	(CO)tacnCT			59	1.74
S <sub>44</sub>	6.76	0.016	31	tacnMCT	30	tacn(CO)CT			61	1.59
S <sub>45</sub>	6.77	0.003	36	MtacnCT	16	(CO)tacnCT			52	1.54
S <sub>46</sub>	6.78	0.000	33	tacn(NO)CT	27	tacn(CO)CT			60	2.01
S <sub>47</sub>	6.85	0.001	27	MtacnCT	17	MC	10	(CO)tacnCT	54	2.43
S <sub>48</sub>	6.86	0.001	43	tacn(NO)CT	28	tacn(CO)CT			71	1.11
S <sub>49</sub>	6.87	0.002	40	tacn(NO)CT	32	tacn(CO)CT			72	1.20
S <sub>50</sub>	6.88	0.002	29	tacn(NO)CT	25	tacn(CO)CT			54	2.10
S <sub>51</sub>	6.89	0.001	36	tacn(NO)CT	30	tacn(CO)CT			66	2.02
S <sub>52</sub>	6.93	0.000	41	tacn(NO)CT	29	tacn(CO)CT			70	1.73
S <sub>53</sub>	6.93	0.002	18	MtacnCT	18	MC	14	(NO)MCT	50	1.56
S <sub>54</sub>	6.95	0.000	29	MtacnCT	13	(CO)tacnCT	13	tacn(NO)CT	55	2.24
S <sub>55</sub>	6.99	0.000	14	M(CO)CT	14	tacn(CO)CT	13	MtacnCT	41	4.97
S <sub>56</sub>	6.99	0.002	47	tacn(CO)CT	30	tacnMCT			77	1.09
S <sub>57</sub>	7.00	0.002	34	tacn(NO)CT	30	tacn(CO)CT			64	1.67
S <sub>58</sub>	7.03	0.007	37	tacn(CO)CT	24	tacnMCT			61	1.98
S <sub>59</sub>	7.12	0.001	36	tacn(NO)CT	25	tacn(CO)CT			61	1.58
S <sub>60</sub>	7.17	0.003	24	MtacnCT	16	tacn(CO)CT	13	tacn(NO)CT	53	3.27

## A. Appendices

Table A.7.: Triplet state character analysis of **TacnMo** (DFT B3LYP-D3(BJ)/def2-SVP implicit acetonitrile).

State	$\Delta E$ [eV]	$f_{osc}$	State Character Analysis						$\sum_{i=1}^3 w_i$ [%]	PR <sub>NTO</sub>
			$w_1$ [%]	$\Omega$	$w_2$ [%]	$\Omega$	$w_3$ [%]	$\Omega$		
T <sub>1</sub>	2.57	-	27	M(NO)CT	21	(NO)C			48	1.96
T <sub>2</sub>	2.66	-	28	M(NO)CT	19	M(CO)CT		(CO)(NO)CT	59	1.25
T <sub>3</sub>	2.81	-	28	M(NO)CT	16	M(CO)CT	15	MC	59	1.37
T <sub>4</sub>	2.82	-	27	M(NO)CT	18	(NO)C	12	MC	57	1.93
T <sub>5</sub>	2.94	-	26	M(NO)CT	21	(NO)C	12	MC	59	1.99
T <sub>6</sub>	3.36	-	24	M(NO)CT	21	(NO)C	11	MC	56	1.62
T <sub>7</sub>	3.75	-	47	M(CO)CT	23	(CO)C			70	1.01
T <sub>8</sub>	4.09	-	28	M(CO)CT	28	MC			56	1.03
T <sub>9</sub>	4.16	-	30	M(CO)CT	26	MC			56	1.07
T <sub>10</sub>	4.51	-	23	M(CO)CT	18	(NO)(CO)CT	18	MC	59	1.23
T <sub>11</sub>	4.55	-	37	tacn(NO)CT	25	tacn(CO)CT			62	1.19
T <sub>12</sub>	4.56	-	36	tacn(NO)CT	28	tacn(CO)CT			64	1.09
T <sub>13</sub>	4.57	-	36	tacn(NO)CT	27	tacn(CO)CT			63	1.09
T <sub>14</sub>	4.60	-	29	M(CO)CT	23	(NO)(CO)CT			52	1.28
T <sub>15</sub>	4.61	-	21	M(CO)CT	20	MC	15	(NO)(CO)CT	56	1.23
T <sub>16</sub>	4.61	-	38	M(CO)CT	20	MC			58	1.27
T <sub>17</sub>	4.72	-	31	M(CO)CT	25	(NO)(CO)CT			56	1.18
T <sub>18</sub>	4.73	-	37	tacn(NO)CT	22	tacn(CO)CT			59	1.19
T <sub>19</sub>	4.77	-	36	tacn(NO)CT	23	tacn(CO)CT			59	1.24
T <sub>20</sub>	5.02	-	30	tacn(NO)CT	19	tacn(CO)CT	15	tacnMCT	64	1.62
T <sub>21</sub>	5.17	-	31	MC	22	M(CO)CT			53	1.23
T <sub>22</sub>	5.21	-	27	M(CO)CT	22	(NO)(CO)CT	17	MC	66	1.23
T <sub>23</sub>	5.26	-	29	M(CO)CT	22	(NO)(CO)CT			51	1.88
T <sub>24</sub>	5.28	-	25	M(CO)CT	20	(NO)(CO)CT	12	MC	57	1.69
T <sub>25</sub>	5.34	-	33	MC	17	M(CO)CT	15	(CO)MCT	65	1.26
T <sub>26</sub>	5.42	-	29	M(CO)CT	24	(NO)(CO)CT			53	1.25
T <sub>27</sub>	5.66	-	43	tacn(NO)CT	34	tacn(CO)CT			77	1.03
T <sub>28</sub>	5.75	-	43	tacn(NO)CT	33	tacn(CO)CT			76	1.16
T <sub>29</sub>	5.78	-	56	tacn(CO)CT	13	tacnMCT			69	1.06
T <sub>30</sub>	5.89	-	43	tacn(NO)CT	31	tacn(CO)CT			74	2.01
T <sub>31</sub>	5.90	-	23	MC	19	(NO)MCT	17	M(CO)CT	59	1.16
T <sub>32</sub>	5.91	-	45	tacn(NO)CT	28	tacn(CO)CT			73	1.01
T <sub>33</sub>	5.92	-	41	tacn(NO)CT	33	tacn(CO)CT			74	2.33
T <sub>34</sub>	5.97	-	47	tacn(CO)CT	20	tacnMCT			67	1.36
T <sub>35</sub>	6.00	-	24	MC	19	(NO)MCT	16	M(CO)CT	59	1.18
T <sub>36</sub>	6.04	-	24	MC	20	(NO)MCT	18	M(CO)CT	62	1.09
T <sub>37</sub>	6.07	-	37	tacn(CO)CT	10	MC	9	M(CO)CT	56	1.94
T <sub>38</sub>	6.13	-	43	tacn(NO)CT	29	tacn(CO)CT			72	1.33
T <sub>39</sub>	6.14	-	34	tacn(NO)CT	33	tacn(CO)CT			67	2.00
T <sub>40</sub>	6.23	-	41	tacn(NO)CT	29	tacn(CO)CT			70	1.24
T <sub>41</sub>	6.25	-	18	MC	14	tacn(CO)CT	14	MtacnCT	46	2.98
T <sub>42</sub>	6.27	-	32	tacn(CO)CT	32	tacnMCT			64	1.36
T <sub>43</sub>	6.28	-	22	MC	22	MtacnCT	10	(CO)tacnCT	54	2.12
T <sub>44</sub>	6.29	-	40	tacn(NO)CT	35	tacn(CO)CT			75	1.06
T <sub>45</sub>	6.29	-	42	tacn(NO)CT	33	tacn(CO)CT			75	1.10
T <sub>46</sub>	6.30	-	37	tacnMCT	27	tacn(CO)CT			64	1.11
T <sub>47</sub>	6.31	-	31	tacnMCT	28	tacn(CO)CT			59	1.77
T <sub>48</sub>	6.33	-	50	MtacnCT	24	(CO)tacnCT			74	1.01
T <sub>49</sub>	6.37	-	40	tacn(NO)CT	33	tacn(CO)CT			73	1.14
T <sub>50</sub>	6.43	-	43	MtacnCT	20	(CO)tacnCT			63	1.04
T <sub>51</sub>	6.56	-	44	tacn(NO)CT	28	tacn(CO)CT			72	1.09
T <sub>52</sub>	6.56	-	39	tacn(CO)CT	23	tacnMCT			62	2.07
T <sub>53</sub>	6.56	-	40	tacn(NO)CT	29	tacn(CO)CT			69	1.31
T <sub>54</sub>	6.57	-	39	tacn(CO)CT	23	tacnMCT			62	2.12
T <sub>55</sub>	6.57	-	37	tacn(CO)CT	23	tacn(NO)CT			60	2.27
T <sub>56</sub>	6.61	-	43	tacn(NO)CT	30	tacn(CO)CT			73	1.08
T <sub>57</sub>	6.63	-	47	MtacnCT	22	(CO)tacnCT			69	1.12
T <sub>58</sub>	6.66	-	37	tacn(CO)CT	27	tacn(NO)CT			64	2.15
T <sub>59</sub>	6.79	-	22	MtacnCT	20	MC	19	(NO)tacnCT	61	1.03
T <sub>60</sub>	6.89	-	21	MtacnCT	18	MC	16	(NO)tacnCT	55	1.28

## A. Appendices

Table A.8.: Singlet state character analysis of **DabCo** (DFT B3LYP-D3(BJ)/def2-SVP implicit acetonitrile).

State	$\Delta E$ [eV]	$f_{osc}$	State Character Analysis								PR <sub>NTO</sub>
			$w_1$ [%]	$\Omega$	$w_2$ [%]	$\Omega$	$w_3$ [%]	$\Omega$	$ \sum_{i=1}^3 w_i $ [%]		
S <sub>1</sub>	1.54	0.000	38	MdabCT	21	(NO)dabCT				59	1.01
S <sub>2</sub>	1.87	0.024	62	MdabCT	11	MC				73	1.05
S <sub>3</sub>	2.30	0.001	36	M(NO)CT	33	MC				69	1.32
S <sub>4</sub>	2.53	0.002	26	MdabCT	19	M(NO)CT	19	MC		64	2.54
S <sub>5</sub>	2.69	0.030	25	M(NO)CT	15	MdabCT	15	MC		55	2.07
S <sub>6</sub>	2.73	0.000	26	M(NO)CT	23	MC	19	MdabCT		68	1.73
S <sub>7</sub>	3.01	0.007	37	M(NO)CT	28	MC				65	1.86
S <sub>8</sub>	3.07	0.012	28	MdabCT	19	MC	16	M(NO)CT		63	1.82
S <sub>9</sub>	3.12	0.002	22	MdabCT	18	M(NO)CT	16	MC		56	2.81
S <sub>10</sub>	3.23	0.012	35	M(NO)CT	26	MC				61	2.61
S <sub>11</sub>	3.39	0.002	39	M(NO)CT	28	MC				67	1.53
S <sub>12</sub>	3.52	0.006	42	MdabCT	18	MC				60	1.25
S <sub>13</sub>	3.81	0.000	39	M(CO)CT	13	MC				52	1.98
S <sub>14</sub>	3.84	0.002	29	M(CO)CT	20	MC	15	M(NO)CT		64	3.16
S <sub>15</sub>	3.89	0.023	32	M(NO)CT	21	MC				53	2.50
S <sub>16</sub>	3.89	0.001	43	M(CO)CT	15	(NO)(CO)CT				58	1.52
S <sub>17</sub>	4.00	0.000	37	M(CO)CT	12	MC	12	(NO)(CO)CT		61	2.76
S <sub>18</sub>	4.19	0.009	43	M(CO)CT	17	(NO)(CO)CT				60	2.25
S <sub>19</sub>	4.43	0.002	40	M(CO)CT	15	MC				55	2.14
S <sub>20</sub>	4.55	0.000	52	M(CO)CT	14	(NO)(CO)CT				66	2.05
S <sub>21</sub>	4.77	0.002	54	M(CO)CT	16	(NO)(CO)CT				70	1.12
S <sub>22</sub>	5.15	0.000	40	MdabCT	23	(NO)dabCT				63	1.53
S <sub>23</sub>	5.19	0.000	38	M(CO)CT	15	MC				53	3.57
S <sub>24</sub>	5.20	0.010	27	MC	16	MdabCT	15	M(CO)CT		58	1.69
S <sub>25</sub>	5.20	0.006	52	dabC	14	MdabCT				66	1.62
S <sub>26</sub>	5.27	0.005	24	MC	17	MdabCT	15	(NO)MCT		56	1.38
S <sub>27</sub>	5.30	0.000	45	M(CO)CT	13	(NO)(CO)CT				58	1.29
S <sub>28</sub>	5.32	0.010	44	dabC	29	MdabCT				73	2.18
S <sub>29</sub>	5.36	0.004	47	dabC	19	MdabCT				66	2.12
S <sub>30</sub>	5.60	0.057	42	MdabCT	32	dabC				74	2.15
S <sub>31</sub>	5.72	0.025	66	MdabCT	13	dabC				79	1.26
S <sub>32</sub>	5.78	0.003	44	MdabCT	28	(NO)dabCT				72	1.03
S <sub>33</sub>	5.82	0.001	50	MdabCT	20	dabC				70	1.14
S <sub>34</sub>	5.82	0.005	45	MC	28	MdabCT				73	1.06
S <sub>35</sub>	5.85	0.001	43	dab(NO)CT	39	dabMCT				82	1.12
S <sub>36</sub>	5.88	0.000	53	MdabCT	18	dabC				71	1.15
S <sub>37</sub>	6.01	0.000	39	MdabCT	23	(NO)dabCT				62	1.55
S <sub>38</sub>	6.13	0.007	39	dab(NO)CT	28	dabMCT				67	1.55
S <sub>39</sub>	6.26	0.004	58	dabC	15	MdabCT				73	2.05
S <sub>40</sub>	6.30	0.001	33	MC	22	MdabCT				55	1.47
S <sub>41</sub>	6.36	0.001	59	dabC	18	MdabCT				77	1.74
S <sub>42</sub>	6.40	0.001	78	MdabCT	8	dabC				86	1.03
S <sub>43</sub>	6.40	0.000	76	dabC	11	dabMCT				87	1.04
S <sub>44</sub>	6.52	0.007	41	MdabCT	30	dabC				71	2.49
S <sub>45</sub>	6.52	0.000	67	MdabCT	8	dabC				75	1.31
S <sub>46</sub>	6.66	0.002	49	MdabCT	18	(NO)dabCT				67	1.25
S <sub>47</sub>	6.70	0.002	42	MdabCT	27	(NO)dabCT				69	1.04
S <sub>48</sub>	6.71	0.003	53	MdabCT	18	(NO)dabCT				71	1.13
S <sub>49</sub>	6.76	0.003	63	dabC	15	dabMCT				78	1.56
S <sub>50</sub>	6.79	0.001	45	MdabCT	27	(NO)dabCT				72	1.08
S <sub>51</sub>	6.81	0.000	53	MdabCT	13	(NO)dabCT				66	1.70
S <sub>52</sub>	6.81	0.002	31	MC	20	MdabCT				51	1.62
S <sub>53</sub>	6.83	0.001	49	MdabCT	19	(NO)dabCT				68	1.65
S <sub>54</sub>	6.85	0.002	18	dab(CO)CT	16	MdabCT	13	MC		47	3.90
S <sub>55</sub>	6.85	0.002	69	dab(CO)CT	12	dabMCT				81	1.20
S <sub>56</sub>	6.92	0.000	35	dab(NO)CT	25	dabMCT				60	2.12
S <sub>57</sub>	6.93	0.001	37	MdabCT	22	(NO)dabCT				59	2.39
S <sub>58</sub>	7.04	0.000	34	dab(NO)CT	24	dabMCT				58	2.80
S <sub>59</sub>	7.15	0.003	31	dabC	27	dab(CO)CT				58	3.02
S <sub>60</sub>	7.22	0.001	47	dabC	14	dab(CO)CT				61	2.64

## A. Appendices

Table A.9.: Triplet state character analysis of **DabCo** (DFT B3LYP-D3(BJ)/def2-SVP implicit acetonitrile).

State	$\Delta E$ [eV]	$f_{osc}$	State Character Analysis						$\sum_{i=1}^3 w_i$ [%]	PR <sub>NTO</sub>
			$w_1$ [%]	$\Omega$	$w_2$ [%]	$\Omega$	$w_3$ [%]	$\Omega$		
T <sub>1</sub>	1.15	-	45	MdabCT	15	dabC			60	1.06
T <sub>2</sub>	1.36	-	36	MdabCT	18	(NO)dabCT			54	1.04
T <sub>3</sub>	1.50	-	26	M(NO)CT	21	MC	18	(NO)C	65	1.46
T <sub>4</sub>	1.72	-	62	MdabCT	15	MC			77	1.11
T <sub>5</sub>	1.74	-	36	M(NO)CT	34	MC			70	1.19
T <sub>6</sub>	1.98	-	32	M(NO)CT	21	MC			53	1.60
T <sub>7</sub>	2.07	-	26	M(NO)CT	24	MC	13	(NO)C	63	2.45
T <sub>8</sub>	2.29	-	24	MC	23	M(NO)CT	16	MdabCT	63	1.93
T <sub>9</sub>	2.41	-	42	M(NO)CT	31	MC			73	1.62
T <sub>10</sub>	2.46	-	29	MdabCT	14	M(NO)CT	13	MC	56	1.98
T <sub>11</sub>	2.55	-	36	M(NO)CT	33	MC			69	1.78
T <sub>12</sub>	2.84	-	42	MdabCT	13	M(NO)CT			55	1.17
T <sub>13</sub>	2.96	-	38	M(NO)CT	28	MC			66	1.27
T <sub>14</sub>	3.32	-	29	M(NO)CT	28	MC			57	1.36
T <sub>15</sub>	3.37	-	23	MC	22	M(NO)CT	14	M(CO)CT	59	1.58
T <sub>16</sub>	3.43	-	35	M(CO)CT	15	MC	13	M(NO)CT	63	1.64
T <sub>17</sub>	3.54	-	34	M(CO)CT	15	dabC	10	MC	59	1.72
T <sub>18</sub>	3.58	-	45	M(CO)CT	14	dab(CO)CT			59	1.07
T <sub>19</sub>	3.69	-	37	dabC	23	M(CO)CT			60	2.70
T <sub>20</sub>	3.78	-	31	M(CO)CT	16	dabC	11	(NO)(CO)CT	58	2.35
T <sub>21</sub>	3.91	-	52	M(CO)CT	12	MC			64	1.34
T <sub>22</sub>	3.95	-	59	M(CO)CT	9	MC			68	1.07
T <sub>23</sub>	4.28	-	44	M(CO)CT	21	(NO)(CO)CT			65	1.02
T <sub>24</sub>	4.67	-	45	M(CO)CT	14	(NO)(CO)CT			59	1.48
T <sub>25</sub>	4.82	-	48	MdabCT	27	dabC			75	1.33
T <sub>26</sub>	4.93	-	45	dabC	21	MdabCT			66	1.92
T <sub>27</sub>	4.97	-	49	M(CO)CT	13	(NO)(CO)CT			62	1.12
T <sub>28</sub>	4.98	-	55	dabC	17	MdabCT			72	1.58
T <sub>29</sub>	5.06	-	51	M(CO)CT	14	(NO)(CO)CT			65	1.24
T <sub>30</sub>	5.14	-	32	MC	19	MdabCT			51	1.08
T <sub>31</sub>	5.19	-	28	MC	19	(NO)MCT	16	MdabCT	63	1.03
T <sub>32</sub>	5.33	-	50	dabC	27	MdabCT			77	2.04
T <sub>33</sub>	5.39	-	78	MdabCT	9	dabC			87	1.03
T <sub>34</sub>	5.42	-	47	dabC	21	MdabCT			68	2.04
T <sub>35</sub>	5.65	-	52	MdabCT	19	dabC			71	1.01
T <sub>36</sub>	5.71	-	43	MdabCT	28	(NO)dabCT			71	1.04
T <sub>37</sub>	5.74	-	54	MdabCT	19	dabC			73	1.03
T <sub>38</sub>	5.74	-	47	MC	28	MdabCT			75	1.01
T <sub>39</sub>	5.77	-	41	dab(NO)CT	39	dabMCT			80	1.16
T <sub>40</sub>	6.03	-	38	MdabCT	23	(NO)dabCT			61	1.56
T <sub>41</sub>	6.10	-	67	dabC	10	dabMCT			77	1.62
T <sub>42</sub>	6.18	-	28	dab(NO)CT	21	dabMCT	15	MdabCT	64	2.50
T <sub>43</sub>	6.23	-	47	dabC	30	MdabCT			77	2.11
T <sub>44</sub>	6.25	-	76	dabC	11	dabMCT			87	1.10
T <sub>45</sub>	6.26	-	75	MdabCT	8	dabC			83	1.08
T <sub>46</sub>	6.27	-	29	MC	19	dab(NO)CT	18	MdabCT	66	1.86
T <sub>47</sub>	6.32	-	35	dab(NO)CT	34	dabMCT			69	1.18
T <sub>48</sub>	6.36	-	78	MdabCT	8	dabC			86	1.01
T <sub>49</sub>	6.41	-	74	dabC	12	dabMCT			86	1.14
T <sub>50</sub>	6.58	-	34	dab(NO)CT	30	dabMCT			64	2.38
T <sub>51</sub>	6.62	-	48	MdabCT	17	(NO)dabCT			65	1.08
T <sub>52</sub>	6.66	-	42	MdabCT	26	(NO)dabCT			68	1.05
T <sub>53</sub>	6.69	-	53	MdabCT	18	(NO)dabCT			71	1.27
T <sub>54</sub>	6.71	-	53	dabC	18	MdabCT			71	2.15
T <sub>55</sub>	6.77	-	50	MdabCT	14	(NO)dabCT			64	1.78
T <sub>56</sub>	6.78	-	39	MC	24	MdabCT			63	1.12
T <sub>57</sub>	6.87	-	36	MdabCT	23	(NO)dabCT			59	1.55
T <sub>58</sub>	6.93	-	32	dab(NO)CT	24	dabMCT			56	3.10
T <sub>59</sub>	6.93	-	47	dab(CO)CT	12	dabMCT			59	1.78
T <sub>60</sub>	6.97	-	29	dab(NO)CT	19	MdabCT	18	dabMCT	66	2.04

## Appendix A4: IR Spectra Peak Analysis

Table A.10.: Peak analysis of all **CpMo** variants considered as potential photoproduct including intensity I [a.u.], wave number  $\tilde{\nu}$  [ $\text{cm}^{-1}$ ] (without shift correction) and respective vibrational mode: radial symmetric and antisymmetric stretching  $\nu_s$  and  $\nu_{as}$ , latitudinal scissoring  $\delta$  and rocking  $\rho$ , longitudinal wagging  $\omega$  and twisting  $\tau$  (DFT B3LYP-D3(BJ)/def2-SVP implicit acetonitrile).

Molecular species	IR-Peaks								
	$\tilde{\nu}$	I	mode	$\tilde{\nu}$	I	mode	$\tilde{\nu}$	I	mode
<b>Dissociated Species</b>									
Photosubstrate	1772	2297	$\nu_{as}(MoNO)$	1993	2371	$\nu_{as}(Mo(CO)_2)$	2079	1437	$\nu_s(Mo(CO)_2)$
solv. single CO-Diss	1717	2167	$\nu_s(MoNO) + \nu_{as}(NNO)MoCCO)$	1968	2003	$\nu_s(MoCO)$			
unsolv. double CO-Diss	1632	1648	$\nu_{as}(MoNO)$						
solv. double CO-Diss	1653	1971	$\nu_{as}(MoNO)$	2314	317	$\nu_{as}(Mo(ACN)_2)$	2330	249	$\nu_{as}(Mo(ACN)_2)$
solv. NO-Diss	1872	2467	$\nu_{as}(Mo(CO)_2)$	1964	2120	$\nu_s(Mo(CO)_2)$			
solv. CO/NO-Diss <sup>•</sup>	1929	2488	$\nu_{as}(MoCO)$						
<b>Dimerized Species</b>									
single CO-Diss	788	241	$\rho(CHCp)$	1692	3570	$\nu_{as}((MoNO)_2)$	1941	8441	$\nu_{as}((MoCO)_2)$
double CO-Diss	766	208	$\rho(CHCp)$	1611	3649	$\nu_{as}((MoNO)_2)$			
solv. double CO-Diss	787	278	$\rho(CHCp)$	1614	3622	$\nu_{as}((MoNO)_2)$	2343	277	$\nu_s((MoACN)_2)$
unsolv. single CO/NO-Diss	1634	2128	$\nu_{as}(MoNO)$	1771	2211	$\nu_{as}(MoCO)$			
solv. single CO/NO-Diss*	1699	2374	$\nu_{as}(MoNO)$	1880	2179	$\nu_{as}(MoCO)$			
<b>Isomerized Species</b>									
NO bend	1768	2275	$\nu_{as}(MoNO)$	1991	2250	$\nu_{as}(Mo(CO)_2)$	2075	1317	$\nu_s(Mo(CO)_2)$
NO half flip	1366	917	$\tau(MoNO)$	1988	1951	$\nu_{as}(Mo(CO)_2)$	2083	1586	$\nu_s(Mo(CO)_2)$
NO full flip	1751	2512	$\nu_{as}(MoNO)$	1959	2328	$\nu_{as}(Mo(CO)_2)$	2044	1584	$\nu_s(Mo(CO)_2)$
solv. single CO-Diss "bend"	1715	2146	$\nu_{as}(MoNO)$	1966	2026	$\nu_{as}(MoCO)$			
solv. single CO-Diss half flip	1247	775	$\tau(MoNO)$	1956	1989	$\nu_{as}(MoCO)$			
solv. single CO-Diss full flip	1683	2462	$\nu_{as}(MoNO)$	1930	2169	$\nu_{as}(MoCO)$			
solv. double CO-Diss half flip	1102	569	$\tau(MoNO)$	2337	179	$\nu_{as}(MoACN)$			
solv. double CO-Diss full flip	1617	2444	$\nu_{as}(MoNO)$	2297	430	$\nu_{as}(Mo(ACN)_2)$	2315	367	$\nu_s(Mo(ACN)_2)$
<b>Water-contaminated Species</b>									
single CO-Diss + 1 H <sub>2</sub> O	1713	2130	$\nu_{as}(MoNO) + \nu_{as}(NNO)MoCCO)$	1954	1856	$\nu_{as}(MoCO)$	3718	252	$\nu_s(H_2O)$
	3781	261	$\nu_{as}(H_2O)$						
unsolv. double CO-Diss + 1 H <sub>2</sub> O	426	263	$\omega(H_2O)$	1643	1701	$\nu_{as}(MoNO)$	3722	287	$\nu_s(H_2O)$
	3789	290	$\nu_{as}(H_2O)$						
solv. double CO-Diss + 1 H <sub>2</sub> O	1638	1832	$\nu_{as}(MoNO)$	2314	320	$\nu_s((MoACN)_2)$	3800	315	$\nu_{as}(H_2O)$
double CO-Diss + 2 H <sub>2</sub> O	443	445	$\omega(H_2O)$	1634	1568	$\nu_{as}(MoNO)$	3726	255	$\nu_s(H_2O)$
	3789	275	$\nu_{as}(H_2O)$	3796	301	$\nu_{as}(H_2O)$			

Multiplicity singlet except \* doublet; Charge 0 except <sup>•</sup> +1

## A. Appendices

Table A.11.: Peak analysis of all **TacnMo** variant considered as potential photoproduct including intensity I [a.u.], wave number  $\tilde{\nu}$  [ $\text{cm}^{-1}$ ] (without shift correction) and respective vibrational mode: radial symmetric and antisymmetric stretching  $\nu_s$  and  $\nu_{as}$ , latitudinal scissoring  $\delta$  and rocking  $\rho$ , longitudinal wagging  $\omega$  and twisting  $\tau$  (DFT B3LYP-D3(BJ)/def2-SVP implicit acetonitrile).

Molecular species	IR-Peaks								
	$\tilde{\nu}$	I	mode	$\tilde{\nu}$	I	mode	$\tilde{\nu}$	I	mode
<b>Dissociated Species</b>									
Photosubstrate	1772	2181	$\nu_{as}(MoNO)$	1998	2029	$\nu_{as}(Mo(CO)_2)$	2095	1192	$\nu_s(Mo(CO)_2)$
unsolv. CO-Diss*	1610	1913	$\nu(NO) + \nu_{as}(NNO)MoCCO)$	1861	1625	$\nu(NO) + \nu_s(NNO)MoCCO)$			
solv. CO-Diss•	1724	1939	$\nu_s(MoNO) + \nu_{as}(NNO)MoCCO) + \omega(CH_3)$	1972	1704	$\nu_{as}(MoCO) + \nu_s(NNO)MoCCO)$			
unsolv. NO-Diss	1729	2658	$\nu_{as}(Mo(CO)_2)$	1825	1354	$\nu_s(Mo(CO)_2)$			
solv. NO-Diss*	1843	2527	$\nu_{as}(Mo(CO)_2)$	1983	1662	$\nu_s(Mo(CO)_2)$			
solv CO/NO-Diss*	1819	2377	$\nu(CO)$	2292	362	$\nu_{as}(MoNCACN)$			
<b>Isomerized Species</b>									
NO bend*	1596	1946	$\nu_{as}(MoNO)$	1824	2398	$\nu_{as}(Mo(CO)_2)$	2952	1571	$\nu_s(Mo(CO)_2)$
NO half flip*	1326	331	$\tau(MoNO)$	1843	2030	$\nu_{as}(Mo(CO)_2)$	1973	1841	$\nu_s(Mo(CO)_2)$
NO full flip•	1757	2307	$\nu_{as}(MoNO)$	1962	297	$\nu_{as}(Mo(CO)_2)$	2059	1277	$\nu_s(Mo(CO)_2)$ $\nu(MoONO)$
solv. single CO-Diss bend*	1502	1624	$\nu_{as}(MoNO)$	1789	2274	$\nu_{as}(MoCO)$	2302	466	$\nu_{as}(MoACN)$
solv. single CO-Diss half flip*	1241	347	$\tau(MoNO)$	1781	2150	$\nu_{as}(MoCO)$	2325	296	$\nu_{as}(MoACN)$
solv. single CO-Diss full flip*	1772	2146	$\nu_{as}(MoCO)$	2265	698	$\nu_s(MoACN)$			
solv. double CO-Diss bend*	1581	1838	$\tau(MoNO)$	1862	278	$\nu_s(MoACN)$	2260	971	$\nu_s(MoACN)$
	2946	203	$\nu_s(ACNCH_3)$						
solv. double CO-Diss half flip*	929	383	$\nu(Tacn)$	1192	367	$\nu(NO)$	1787	1910	$\nu_s(ACN)$
	2292	661	$\nu_s(ACN)$	2960	267	$\nu_s(ACNCH_3)$			
<b>Water-contaminated Species</b>									
single CO-Diss + 1 H <sub>2</sub> O*	1441	239	$\omega(Tacn)$	1477	553	$\nu(NO) + \omega(Tacn)$	1769	1884	$\nu_{as}(MoCO)$
	3802	327	$\nu_{as}(H_2O)$						
solv double CO-Diss + 1 H <sub>2</sub> O*	1548	1611	$\nu_{as}(MoNO)$	1822	367	$\nu_{as}(MoCNACN)$	2940	215	$\nu_s(ACNCH_3)$
	3784	357	$\nu_{as}(H_2O)$						
double CO-Diss + 2 H <sub>2</sub> O*	1480	201	$\omega(Tacn)$	1521	306	$\tau(H_2O)$	1568	997	$\nu_{as}(MoNO)$
	2633	7164	$\nu_{as}(H_2O)$	2706	2433	$\nu_{as}(H_2O)$			

Multiplicity singlet except \* doublet; Charge 0 except • +1

## Appendix A5: DMRG-Orbital Classification, Single Orbital Entropy Values and State-specific Entanglement Diagrams

### CpMo

Table A.12.: Orbital classification and their respective single orbital entropy values for each state of CpMo (DMRG[250](30,26)-SCF/ANO-RCC-MB gas phase, natural orbitals).

Orbital index	Classification	Occ.	$Z_{s(1)}$							
			S <sub>0</sub>	S <sub>1</sub>	S <sub>2</sub>	S <sub>3</sub>	S <sub>4</sub>	S <sub>5</sub>	S <sub>6</sub>	S <sub>7</sub>
<b>Photosubstrate</b>										
1	$\pi(\text{NO})$	2	0.122	0.141	0.107	0.247	0.124	0.162	0.116	0.120
2	$\sigma^*(\text{C}^4\text{O}), \sigma^*(\text{C}^6\text{O}), \sigma^*(\text{NO})$	2	0.072	0.079	0.082	0.070	0.076	0.070	0.073	0.078
3	$\pi(\text{C}^4\text{O}), \pi(\text{C}^6\text{O}), \sigma^*(\text{NO})$	2	0.098	0.112	0.113	0.096	0.091	0.088	0.105	0.113
4	$\pi(\text{C}^4\text{O}) + \pi(\text{C}^6\text{O}) + \pi(\text{NO})$	2	0.141	0.108	0.124	0.127	0.161	0.139	0.127	0.115
5	$\pi(\text{C}^4\text{O}) + \pi(\text{C}^6\text{O}) - \sigma(\sigma(\text{NO}) + 4p(\text{Mo}))$	2	0.079	0.082	0.085	0.078	0.081	0.074	0.075	0.080
6	$\pi(\text{C}^4\text{O}), \pi(\text{C}^6\text{O})$	2	0.135	0.152	0.154	0.138	0.131	0.125	0.135	0.152
7	$\pi(\text{C}^4\text{O}) + \pi(\text{C}^6\text{O}) - \pi(\text{NO})$	2	0.159	0.138	0.132	0.175	0.149	0.148	0.145	0.134
8	$\sigma^*(\text{C}^4\text{O}), \sigma^*(\text{C}^6\text{O})$	2	0.079	0.086	0.083	0.098	0.085	0.086	0.068	0.085
9	$\pi(\text{NO}) - \pi(\text{CO})$	2	0.159	0.113	0.163	0.140	0.239	0.190	0.149	0.145
10	$\pi(\text{Cp})$	2	0.102	0.100	0.100	0.096	0.102	0.095	0.096	0.088
11	$\pi_1(4d(\text{Mo}) + \pi(\text{Cp})) - \pi^*(\text{NO})$	2	0.204	0.228	0.208	0.344	0.183	0.241	0.207	0.199
12	$\pi_2(4d(\text{Mo}) + \pi(\text{Cp}))$	2	0.164	0.409	0.393	0.161	0.173	0.159	0.367	0.395
13	$\pi_3(4d(\text{Mo}) + \pi^*(\text{NO}))$	2	0.513	0.284	0.288	0.250	0.934	1.140	0.457	0.361
14	$\pi_4(4d(\text{Mo}) + \pi^*(\text{NO}))$	2	0.531	0.795	0.665	1.120	0.485	1.070	0.538	0.589
15	$\pi_5(4d(\text{Mo}) + \pi^*(\text{C}^4\text{O}) + \pi^*(\text{C}^6\text{O}))$	2	0.209	1.000	0.995	0.219	0.274	0.219	1.020	1.020
16	$\pi_6(4d(\text{Mo}) + \pi^*(\text{C}^4\text{O}) + \pi^*(\text{C}^6\text{O})) + n(4d(\text{Mo}) - \pi^*(\text{NO}))$	0	0.544	0.1844	1.200	0.414	1.210	1.130	0.575	0.619
17	$\pi^*(\text{C}^4\text{O}) + \pi^*(\text{C}^6\text{O}) + \pi^*(\text{NO})$	0	0.438	1.000	0.382	1.170	0.346	1.080	0.376	0.720
18	$\pi^*(\text{C}^4\text{O}), \pi^*(\text{C}^6\text{O})$	0	0.216	0.210	0.236	0.230	0.304	0.231	1.020	0.223
19	$\pi_1^*(4d(\text{Mo}) - \pi^*(\text{C}^4\text{O}) - \pi^*(\text{C}^6\text{O}))$	0	0.366	0.571	0.294	0.778	0.245	0.531	0.343	1.170
20	$\pi_2^*(4d(\text{Mo}) - \pi^*(\text{C}^4\text{O}) - \pi^*(\text{C}^6\text{O}) - \pi^*(\text{NO}))$	0	0.366	0.571	0.294	0.778	0.245	0.531	0.343	1.170
21	$\delta(4d(\text{Mo}) + \pi^*(\text{Cp})) + n(4d(\text{Mo}) - \pi^*(\text{C}^4\text{O}) - \pi^*(\text{C}^6\text{O}))$	0	0.221	0.257	0.286	0.209	0.339	0.234	1.030	0.238
22	$\pi_3^*(4d(\text{Mo}) - \pi^*(\text{Cp}))$	0	0.145	0.191	0.131	0.206	0.138	0.173	0.134	0.287
23	$\pi_4^*(4d(\text{Mo}) - \pi^*(\text{Cp})) + n(4d(\text{Mo}) - \pi^*(\text{C}^4\text{O}) - \pi^*(\text{C}^6\text{O}))$	0	0.168	0.187	0.207	0.153	0.245	0.184	0.509	0.172
24	$\delta_1^*(4d(\text{Mo}) - \pi^*(\text{Cp}))$	0	0.143	0.136	0.135	0.149	0.139	0.132	0.136	0.145
25	$\delta_2^*(4d(\text{Mo}) - \pi^*(\text{Cp}))$	0	0.171	0.192	0.224	0.151	0.231	0.174	0.293	0.162
26	$5s(\text{Mo}) + (2s(\text{N}) + 2s(\text{C}^4) + 2s(\text{C}^6) + 2p_z(\text{Cp-C}))$	0	0.043	0.043	0.041	0.045	0.042	0.039	0.038	0.068
<b>Dissociation CO</b>										
1	$\pi(\text{NO}) + \pi(\text{C}^4\text{O})$	2	0.121	0.111	0.104	0.104	0.136	0.139	0.238	0.111
2	$\pi(\text{C}^4\text{O})$	2	0.118	0.138	0.109	0.109	0.146	0.130	0.119	0.135
3	$\pi(\text{C}^4\text{O}), \pi(\text{NO})$	2	0.128	0.122	0.131	0.131	0.118	0.128	0.152	0.111
4	$\pi(\text{C}^6\text{O})$	2	0.110	0.102	0.109	0.109	0.098	0.103	0.127	0.111
5	$\pi(\text{C}^6\text{O})$	2	0.110	0.102	0.109	0.109	0.098	0.103	0.118	0.111
6	$\pi(\text{C}^4\text{O}), \sigma^*(\text{NO})$	2	0.075	0.070	0.078	0.078	0.063	0.069	0.070	0.066
7	$\sigma^*(\text{C}^4\text{O}), \pi(\text{NO})$	2	0.058	0.053	0.063	0.063	0.064	0.055	0.065	0.051
8	$\pi(\text{NO})$	2	0.151	0.149	0.209	0.209	0.109	0.142	0.131	0.143
9	$\pi(\text{Cp})$	2	0.104	0.097	0.101	0.101	0.097	0.096	0.100	0.098
10	$\sigma^*(\text{C}^6\text{O})$	2	0.041	0.000	0.041	0.041	0.000	0.000	0.042	0.000
11	$\pi_1(4d(\text{Mo}) + \pi(\text{Cp}))$	2	0.209	0.193	0.201	0.201	0.222	0.233	0.287	0.202
12	$\pi_2(4d(\text{Mo}) + \pi(\text{Cp}))$	2	0.171	0.447	0.173	0.173	0.453	0.512	0.165	0.439
13	$\pi_3(4d(\text{Mo}) + \pi^*(\text{NO}))$	2	0.431	1.070	0.704	0.704	1.220	1.000	1.090	1.220
14	$\pi_4(4d(\text{Mo}) + \pi^*(\text{NO}))$	2	0.465	1.060	1.180	1.180	1.010	1.380	0.562	1.050
15	$\pi_5(4d(\text{Mo}) + \pi^*(\text{NO}))$	2	0.608	0.815	1.010	1.010	0.952	1.240	1.110	0.969
16	$\pi_6(4d(\text{Mo}) + \pi^*(\text{C}^4\text{O})) + 5s(\text{Mo})$	0	0.386	1.110	1.030	1.030	0.637	1.020	0.244	0.897
17	$\pi_1^*(\pi(4d(\text{Mo}) + \pi^*(\text{C}^4\text{O})) - \pi^*(\text{NO}))$	0	0.458	0.408	0.399	0.399	1.210	0.503	1.180	0.710
18	$\pi_2^*(4d(\text{Mo}) + \pi^*(\text{NO}))$	0	0.534	0.484	0.443	0.443	0.809	0.622	0.855	1.270
19	$\pi^*(\text{C}^6\text{O})$	0	0.126	0.119	0.126	0.126	0.113	0.119	0.143	0.127

Continued on next page

## A. Appendices

Table A.12 – *Continued from previous page*

Orbital index	Classification	Occ.	$Z_{s(1)}$							
			S <sub>0</sub>	S <sub>1</sub>	S <sub>2</sub>	S <sub>3</sub>	S <sub>4</sub>	S <sub>5</sub>	S <sub>6</sub>	S <sub>7</sub>
20	$\pi^*(C^6O)$	0	0.127	0.118	0.125	0.125	0.113	0.119	0.135	0.127
21	$\pi_3^*(4d(Mo)-\pi^*(C^4O))$	0	0.215	0.438	0.369	0.369	0.202	0.491	0.275	0.563
22	$\pi_7(4d(Mo)+\pi^*(Cp))+n(4d(Mo)-\pi^*(C^4O)-\pi^*(NO))$	0	0.385	0.352	0.321	0.321	0.605	0.414	0.760	0.356
23	$\pi_4^*(4d(Mo)-\pi^*(Cp))+n(4d(Mo)-\pi^*(C^4O))$	0	0.159	0.169	0.159	0.159	0.182	0.176	0.163	0.257
24	$\pi_5^*(4d(Mo)-\pi^*(Cp))$	0	0.181	0.190	0.188	0.188	0.224	0.268	0.268	0.175
25	$\delta_1^*(4d(Mo)-\pi^*(Cp))$	0	0.141	0.130	0.131	0.131	0.163	0.127	0.156	0.131
26	$\delta_2^*(4d(Mo)-\pi^*(Cp))$	0	0.186	0.247	0.240	0.240	0.233	0.369	0.167	0.244
<b>Dissociation NO</b>										
1	$\pi(C^4O),\pi(C^6O)$	2	0.120	0.117	0.143	0.119	0.111	0.119	0.133	0.114
2	$\pi(C^4O),\pi(C^6O)$	2	0.122	0.128	0.106	0.121	0.123	0.121	0.111	0.123
3	$\sigma^*(C^4O),\sigma^*(C^6O)$	2	0.102	0.102	0.093	0.103	0.102	0.101	0.088	0.103
4	$\sigma^*(C^4O),\sigma^*(C^6O)$	2	0.135	0.129	0.147	0.134	0.122	0.134	0.144	0.121
5	$\pi(C^4O),\pi(C^6O)$	2	0.155	0.151	0.131	0.157	0.153	0.154	0.130	0.155
6	$\pi(NO)$	2	0.015	0.015	0.126	0.014	0.111	0.234	0.112	0.112
7	$\sigma^*(C^4O),\sigma^*(C^6O)$	2	0.076	0.072	0.078	0.079	0.071	0.076	0.075	0.071
8	$\pi(NO)$	2	0.119	0.112	0.212	0.108	0.203	0.094	0.203	0.206
9	$\sigma^*(NO)$	2	0.015	0.014	0.011	0.013	0.012	0.018	0.011	0.012
10	$\pi(Cp)$	2	0.104	0.106	0.106	0.103	0.103	0.099	0.094	0.102
11	$\pi_1(4d(Mo)+\pi(Cp))$	2	0.179	0.163	0.157	0.174	0.158	0.173	0.152	0.154
12	$\pi_2(4d(Mo)+\pi(Cp))$	2	0.174	0.213	0.273	0.175	0.159	0.171	0.281	0.171
13	$4d(Mo)$	2	0.245	0.844	0.325	0.357	0.953	0.212	0.468	1.010
14	$\pi_3(4d(Mo)+\pi^*(C^4O)+\pi^*(C^6O))$	2	0.289	0.364	0.923	0.246	0.389	0.280	1.060	0.594
15	$4d(Mo)+\pi^*(NO)$	2	0.884	1.150	1.130	1.170	0.892	1.080	1.190	0.890
16	$\pi_4(4d(Mo)+\pi^*(C^4O)+\pi^*(C^6O))+\pi^*(NO)$	0	0.867	1.090	1.060	1.110	0.885	1.160	1.180	0.905
17	$\pi_5(4d(Mo)+\pi^*(C^4O)+\pi^*(C^6O))$	0	0.159	0.222	0.258	1.040	1.100	0.150	1.180	1.130
18	$\pi^*(C^4O),\pi^*(C^6O)$	0	0.232	0.237	0.195	0.220	0.195	0.228	0.185	0.217
19	$\pi_1^*(4d(Mo)-\pi^*(C^4O)-\pi^*(C^6O))$	0	0.234	0.244	0.238	0.490	0.550	0.231	0.340	0.508
20	$\delta(4d(Mo)+\pi^*(Cp))+n(4d(Mo)-\pi^*(C^4O)-\pi^*(C^6O))$	0	0.251	0.264	0.261	0.189	0.213	0.250	0.208	0.218
21	$\pi^*(NO)$	0	0.128	0.120	0.219	0.116	0.211	0.764	0.211	0.213
22	$\pi_2^*(4d(Mo)-\pi^*(C^4O)-\pi^*(C^6O))$	0	0.248	0.256	0.202	0.254	0.291	0.245	0.234	0.257
23	$\pi_3^*(4d(Mo)-\pi^*(Cp))+n(4d(Mo)-\pi^*(C^4O)-\pi^*(C^6O))$	0	0.177	0.200	0.192	0.137	0.164	0.179	0.157	0.176
24	$\pi_4^*(4d(Mo)-\pi^*(Cp))$	0	0.141	0.149	0.132	0.231	0.274	0.138	0.226	0.264
25	$\pi_5^*(4d(Mo)-\pi^*(Cp))+n(4d(Mo)-\pi^*(C^4O)-\pi^*(C^6O))$	0	0.153	0.150	0.154	0.215	0.199	0.149	0.178	0.234
26	$\delta_1^*(4d(Mo)-\pi^*(Cp))+n(4d(Mo)-\pi^*(C^4O)-\pi^*(C^6O))$	0	0.155	0.164	0.156	0.134	0.137	0.154	0.138	0.132

A. Appendices

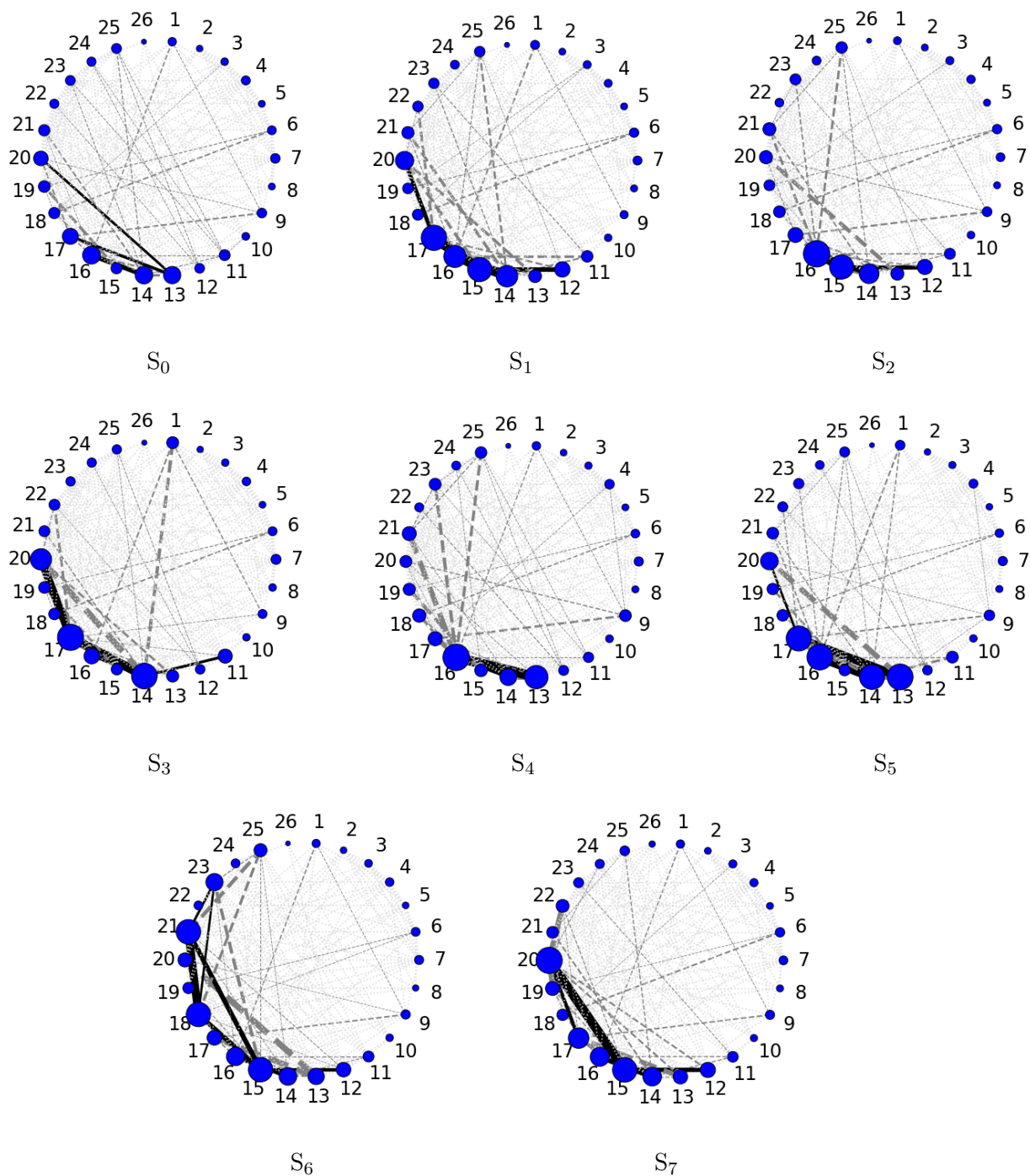


Figure A.8.: State-specific entanglement diagrams for  $\text{CpMo}$  (DMRG[250](30,26)-SCF/ANO-RCC-MB gas phase).

A. Appendices

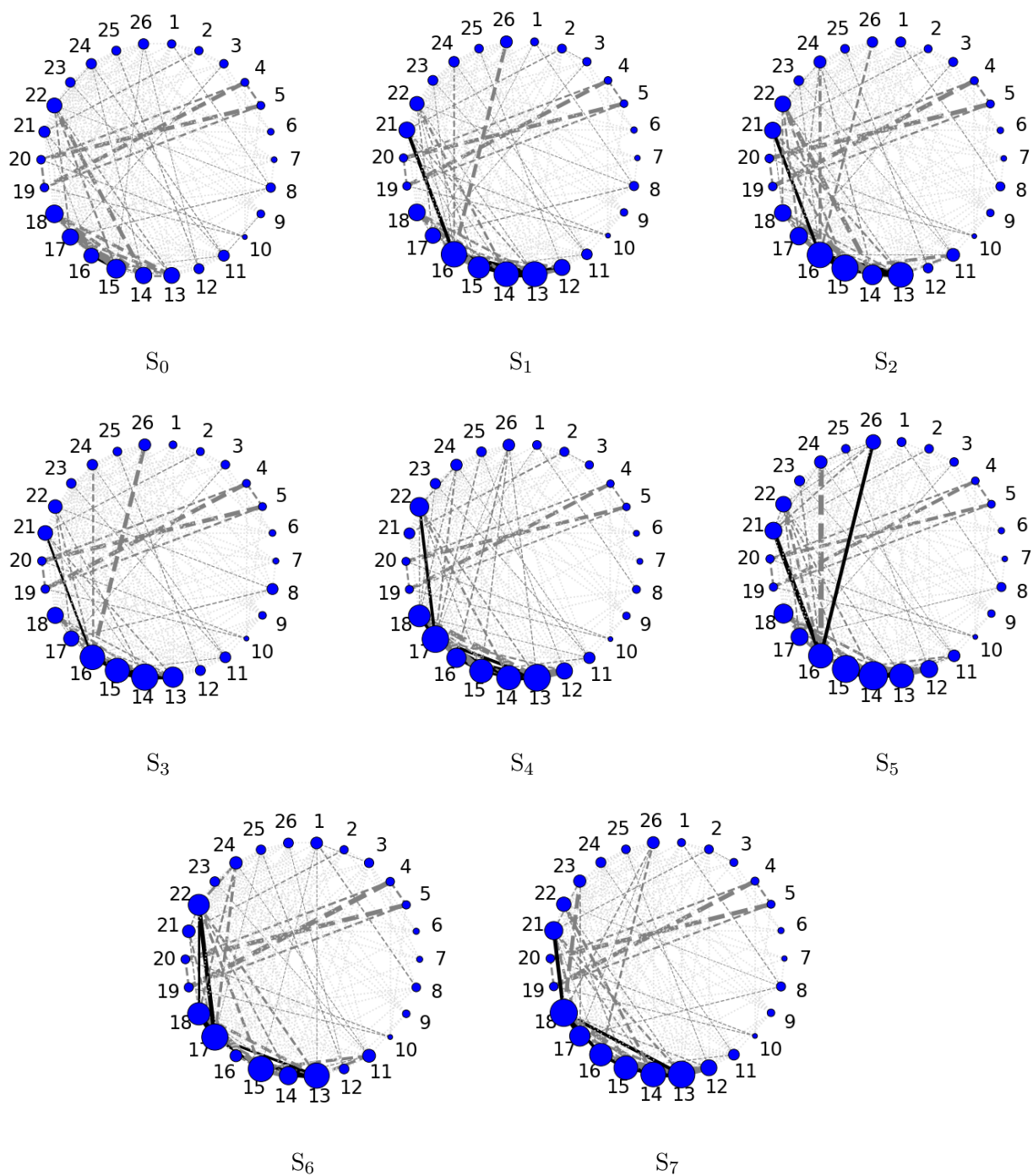


Figure A.9.: State-specific entanglement diagrams for **CpMoco<sub>diss</sub>** with a Mo-C bond length set to 10 Å (DMRG[250](30,26)-SCF/ANO-RCC-MB gas phase).

A. Appendices

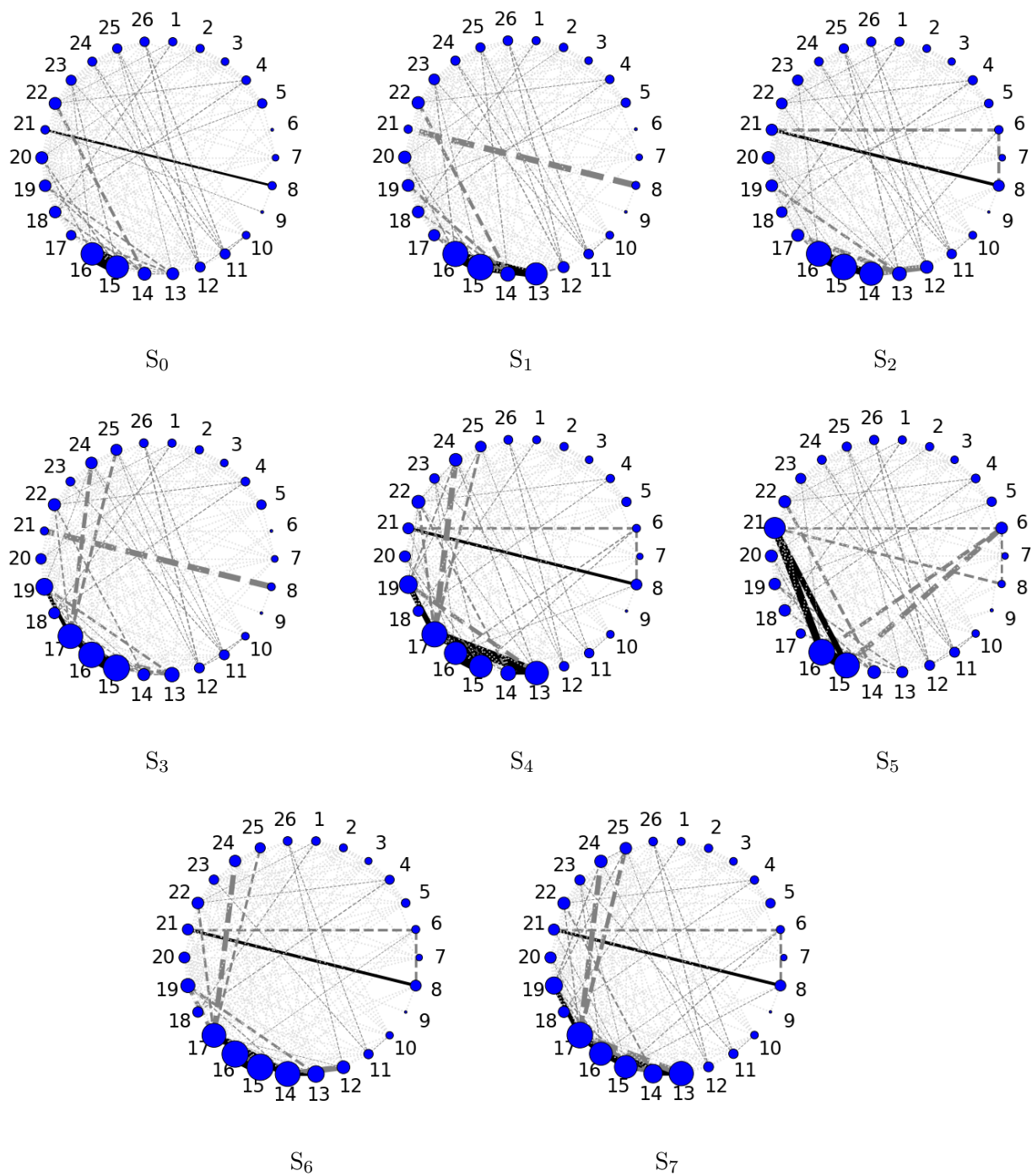


Figure A.10.: State-specific entanglement diagrams for **CpMoNOdiss** with a Mo-N bond length set to 10 Å (DMRG[250](30,26)-SCF/ANO-RCC-MB gas phase).

A. Appendices

TacnMo

Table A.13.: Orbital classification and their respective single orbital entropy values for each state of TacnMo (DMRG[250](46,33)-SCF/ANO-RCC-MB gas phase, natural orbitals).

Orbital index	Classification	Occ.	$Z_{s(1)}$							
			S <sub>0</sub>	S <sub>1</sub>	S <sub>2</sub>	S <sub>3</sub>	S <sub>4</sub>	S <sub>5</sub>	S <sub>6</sub>	S <sub>7</sub>
<b>Photosubstrate</b>										
1	$\pi(\text{NO}), \sigma(\text{Tacn})$	2	0.033	0.034	0.031	0.034	0.052	0.041	0.033	0.035
2	$\pi(\text{NO})$	2	0.084	0.089	0.086	0.085	0.145	0.118	0.086	0.085
3	$\sigma(\text{C}^6\text{O}), \sigma(\text{C}^6\text{O})$	2	0.060	0.071	0.071	0.058	0.061	0.059	0.069	0.058
4	$\sigma(\text{C}^2\text{O}), \sigma(\text{C}^4\text{O}), \sigma(\text{NO})$	2	0.044	0.050	0.053	0.044	0.047	0.049	0.049	0.042
5	$\pi(\text{C}^4\text{O}), \sigma(\text{C}^2\text{O}), \sigma(\text{NO})$	2	0.087	0.081	0.090	0.091	0.085	0.099	0.079	0.085
6	$\pi(\text{C}^4\text{O}), \pi(\text{C}^2\text{O}), \pi(\text{NO})$	2	0.091	0.087	0.072	0.113	0.099	0.089	0.082	0.104
7	$\sigma^*(\text{C}^4\text{O}), \sigma^*(\text{NO}), \text{p}(\text{N}_{\text{Tacn}})$	2	0.049	0.048	0.056	0.049	0.052	0.059	0.051	0.052
8	$\pi(\text{C}^4\text{O}), \sigma^*(\text{NO})$	2	0.079	0.095	0.085	0.082	0.078	0.074	0.089	0.074
9	$\sigma^*(\text{NO}), \pi(\text{C}^2\text{O})$	2	0.066	0.070	0.074	0.073	0.062	0.072	0.068	0.070
10	$\pi(\text{C}^2\text{O})$	2	0.075	0.087	0.087	0.074	0.074	0.073	0.084	0.057
11	$\pi(\text{C}^4\text{O}), \pi(\text{C}^2\text{O}), \pi(\text{NO})$	2	0.153	0.128	0.135	0.145	0.156	0.156	0.130	0.166
12	$\pi(\text{NO}), \sigma^*(\text{C}^4\text{O}), \sigma^*(\text{C}^2\text{O})$	2	0.098	0.091	0.097	0.140	0.094	0.123	0.094	0.129
13	$\pi(\text{NO}), \sigma^*(\text{C}^4\text{O}), \sigma^*(\text{C}^2\text{O})$	2	0.084	0.077	0.074	0.119	0.082	0.094	0.077	0.111
14	$\sigma^*(\text{CO})$	2	0.038	0.039	0.041	0.037	0.046	0.043	0.038	0.043
15	$\pi(\text{NO}), \sigma^*(\text{C}^4\text{O}), \sigma^*(\text{C}^2\text{O})$	2	0.049	0.049	0.048	0.088	0.049	0.066	0.051	0.073
16	$\sigma(\text{Tacn}), \text{p}(\text{Tacn})$	2	0.002	0.003	0.003	0.002	0.002	0.002	0.003	0.002
17	$\sigma(\text{Tacn}), \text{p}(\text{Tacn})$	2	0.001	0.001	0.001	0.001	0.001	0.001	0.001	0.001
18	$\sigma(\text{Tacn}), \text{p}(\text{Tacn}), \pi(\text{Tacn})$	2	0.010	0.012	0.012	0.013	0.010	0.010	0.010	0.013
19	$\sigma(\text{Tacn}), \text{p}(\text{Tacn}), \pi(\text{Tacn}), \text{s}(\text{Mo})$	2	0.014	0.013	0.015	0.017	0.014	0.017	0.015	0.023
20	$\sigma(\text{Tacn}), \text{p}(\text{Tacn}), \pi(\text{Tacn}), \text{s}(\text{Mo}), \text{p}(\text{Mo}), \text{d}(\text{Mo})$	2	0.015	0.018	0.016	0.015	0.019	0.015	0.018	0.016
21	$\pi_1(\text{d}(\text{Mo}) + \pi^*(\text{C}^4\text{O}) + \pi^*(\text{C}^2\text{O}) + \pi^*(\text{NO}))$	2	0.309	1.204	1.216	0.333	0.690	0.609	1.209	0.833
22	$\pi_2(\text{d}(\text{Mo}) + \pi^*(\text{NO}))$	2	0.527	0.965	0.966	0.473	1.245	1.163	1.028	0.546
23	$\pi_3(\text{d}(\text{Mo}) + \pi^*(\text{NO}))$	2	0.537	0.362	0.368	1.005	0.688	1.037	0.448	1.275
24	$\pi_1^*(\pi(\text{d}(\text{Mo}) + \pi^*(\text{C}^4\text{O})) - \pi^*(\text{NO}))$	0	0.526	1.288	1.240	1.179	0.707	1.021	0.658	0.512
25	$\pi_2^*(\pi(\text{d}(\text{Mo}) + \pi^*(\text{C}^2\text{O})) - \pi^*(\text{NO}))$	0	0.453	1.064	1.147	0.401	1.191	1.174	0.583	0.495
26	$\text{n}(\text{d}(\text{Mo}) + \pi^*(\text{C}^2\text{O}) + \pi^*(\text{C}^4\text{O}))$	0	0.210	0.217	0.223	0.270	0.309	0.235	0.566	1.149
27	$\pi_3^*(\text{d}(\text{Mo}) - \pi^*(\text{C}^4\text{O}) - \pi^*(\text{C}^2\text{O}))$	0	0.285	0.268	0.272	0.271	0.364	0.322	0.949	0.836
28	$\delta_1^*(\text{d}(\text{Mo}) - \pi^*(\text{C}^4\text{O}) - \pi^*(\text{C}^2\text{O}) - \pi^*(\text{NO}))$	0	0.373	0.440	0.378	0.336	0.632	0.484	1.021	0.335
29	$\delta_2^*(\text{d}(\text{Mo}) - \pi^*(\text{C}^4\text{O}) - \pi^*(\text{C}^2\text{O}))$	0	0.304	0.384	0.383	0.453	0.275	0.341	0.466	0.437
30	$\pi_4^*(\pi^*(\text{C}^4\text{O}) - \text{d}(\text{Mo}) + \text{p}(\text{N}_{\text{Tacn}}))$	0	0.076	0.098	0.081	0.097	0.082	0.084	0.121	0.127
31	$\pi_5^*(\pi^*(\text{C}^2\text{O}) - \text{d}(\text{Mo}) + \text{p}(\text{N}_{\text{Tacn}}))$	0	0.069	0.075	0.090	0.076	0.075	0.080	0.082	0.181
32	$\pi(\text{Tacn}) + \sigma^*(\text{Tacn})$	0	0.012	0.011	0.011	0.010	0.012	0.011	0.015	0.011
33	$\pi(\text{Tacn}) + \sigma^*(\text{Tacn})$	0	0.008	0.008	0.008	0.007	0.009	0.008	0.008	0.007
<b>Dissociation CO</b>										
1	$\pi(\text{NO}), \sigma(\text{Tacn})$	2	0.025	0.028	0.026	0.042	0.025	0.032	0.037	0.025
2	$\sigma^*(\text{NO}), \sigma(\text{Tacn})$	2	0.013	0.014	0.013	0.018	0.013	0.014	0.017	0.014
3	$\pi(\text{NO}), \sigma(\text{Tacn})$	2	0.078	0.086	0.080	0.129	0.077	0.102	0.122	0.074
4	$\pi(\text{NO}), \sigma(\text{Tacn}), \pi(\text{C}^2\text{O})$	2	0.062	0.064	0.063	0.073	0.062	0.059	0.074	0.073
5	$\sigma^*(\text{NO}), \pi(\text{C}^2\text{O})$	2	0.110	0.100	0.110	0.092	0.113	0.111	0.092	0.102
6	$\sigma^*(\text{NO}), \pi(\text{C}^2\text{O})$	2	0.092	0.093	0.093	0.095	0.094	0.084	0.094	0.100
7	$\pi(\text{NO}), \pi(\text{C}^2\text{O})$	2	0.067	0.066	0.068	0.065	0.069	0.064	0.062	0.069
8	$\sigma(\text{C}^2\text{O}), \sigma^*(\text{Tacn})$	2	0.019	0.021	0.020	0.022	0.020	0.024	0.022	0.021
9	$\sigma(\text{NO}), \pi(\text{C}^2\text{O}), \sigma^*(\text{Tacn})$	2	0.067	0.062	0.068	0.057	0.069	0.071	0.058	0.065
10	$\sigma(\text{NO}), \sigma^*(\text{Tacn})$	2	0.018	0.020	0.018	0.017	0.018	0.019	0.017	0.019
11	$\pi(\text{C}^2\text{O}), \sigma^*(\text{Tacn})$	2	0.068	0.071	0.068	0.069	0.069	0.057	0.069	0.082
12	$\sigma^*(\text{NO}), \sigma^*(\text{C}^2\text{O}), \sigma^*(\text{Tacn}), \pi(\text{Tacn})$	2	0.019	0.022	0.020	0.028	0.019	0.023	0.026	0.021
13	$\pi(\text{NO}), \sigma^*(\text{C}^2\text{O})$	2	0.091	0.092	0.092	0.088	0.093	0.069	0.086	0.133
14	$\pi(\text{NO}), \sigma^*(\text{Tacn}), \pi(\text{Tacn})$	2	0.023	0.023	0.024	0.022	0.024	0.017	0.021	0.033
15	$\pi^*(\text{C}^4\text{O})$	2	0.104	0.155	0.143	0.139	0.162	0.138	0.233	0.147
16	$\pi^*(\text{C}^4\text{O})$	2	0.193	0.159	0.141	0.139	0.088	0.141	0.085	0.148

Continued on next page

A. Appendices

Table A.13 – Continued from previous page

Orbital index	Classification	Occ.	$Z_{s(1)}$							
			S <sub>0</sub>	S <sub>1</sub>	S <sub>2</sub>	S <sub>3</sub>	S <sub>4</sub>	S <sub>5</sub>	S <sub>6</sub>	S <sub>7</sub>
17	$\sigma(C^4O)$	2	0.693	0.053	0.049	0.049	0.693	0.048	0.693	0.050
18	$p(N_{Tacn}),\pi(Tacn),p(Mo)$	2	0.010	0.009	0.010	0.010	0.011	0.011	0.010	0.012
19	$\pi_1(d(Mo)+p(N_{Tacn})),\pi(Tacn),\sigma(Tacn)$	2	0.015	0.016	0.016	0.014	0.016	0.021	0.014	0.015
20	$p(N_{Tacn}),\pi(Tacn),d(Mo)$	2	0.014	0.012	0.014	0.012	0.015	0.015	0.012	0.014
21	$\pi_2(d(Mo)+\pi^*(C^2O)+\pi^*(NO))$	2	0.963	0.276	0.964	0.468	0.960	1.069	0.428	0.389
22	$\pi_3(d(Mo)+\pi^*(NO))$	2	0.682	0.666	0.676	1.136	0.637	1.015	1.017	0.526
23	$\pi_4(d(Mo)+\pi^*(NO)+\pi^*(C^2O))$	2	0.519	0.630	0.527	0.844	0.474	0.425	0.815	1.152
24	$\pi_5(d(Mo)+p(N_{NO})+p(C^2)+\pi^*(C^2O)+\sigma(iPr_{Tacn}))$	0	1.014	0.370	1.125	1.135	1.014	0.603	1.005	1.006
25	$\pi_1^*(d(Mo)-\pi^*(NO)-\pi^*(C^2O))$	0	0.391	0.508	0.412	0.699	0.363	1.059	0.668	0.450
26	$\pi_2^*(d(Mo)-\pi^*(NO)-\pi^*(C^2O))$	0	0.616	0.580	0.558	0.422	0.564	0.726	0.378	0.482
27	$\pi_3^*(d(Mo)-\pi^*(C^2O))$	0	0.344	0.260	0.439	0.450	0.354	0.231	0.362	0.379
28	$\pi_4^*(d(Mo)-\pi^*(NO)+\pi^-(C^2O))$	0	0.377	0.405	0.394	0.466	0.360	0.554	0.459	0.333
29	$\pi^*(C^4O)$	0	1.036	0.175	0.162	0.158	0.577	0.156	0.311	0.167
30	$\pi^*(C^4O)$	0	0.600	0.179	0.160	0.158	1.031	0.159	0.829	0.167
31	$\pi_6(d(Mo)+p(N_{Tacn})-\pi^*(C^2O))$	0	0.074	0.075	0.077	0.089	0.076	0.110	0.096	0.091
32	$\pi_7(d(Mo)+p(N_{Tacn}))$	0	0.203	0.062	0.225	0.181	0.206	0.087	0.158	0.165
33	$f(Mo),p(N_{Tacn}),\pi^*(C^2O),\pi(Tacn)$	0	0.063	0.035	0.066	0.057	0.065	0.037	0.058	0.060
<b>Dissociation NO</b>										
1	$\pi(NO)$	2	0.270	0.092	0.157	0.078	0.142	0.154	0.137	0.275
2	$\pi(NO)$	2	0.129	0.081	0.271	0.094	0.272	0.277	0.247	0.138
3	$\sigma(CO)$	2	0.053	0.054	0.053	0.056	0.053	0.067	0.052	0.054
4	$\sigma^*(NO)$	2	0.018	0.695	0.015	0.696	0.017	0.016	0.014	0.018
5	$\sigma^*(C^4O)$	2	0.013	0.012	0.013	0.013	0.012	0.014	0.012	0.013
6	$\pi(C^2O)p(Tacn),\sigma(Tacn)$	2	0.060	0.065	0.061	0.064	0.056	0.054	0.061	0.058
7	$\pi(CO)$	2	0.121	0.133	0.123	0.130	0.139	0.122	0.130	0.140
8	$\pi(C^2O)$	2	0.086	0.095	0.087	0.092	0.089	0.084	0.091	0.092
9	$\pi(C^4O)$	2	0.111	0.125	0.111	0.118	0.113	0.093	0.118	0.115
10	$\pi(C^4O),\pi(C^2O)$	2	0.117	0.118	0.118	0.124	0.124	0.139	0.115	0.125
11	$\sigma^*(C^4O),\sigma^*(C^2O),\sigma(Tacn)$	2	0.038	0.038	0.038	0.040	0.037	0.043	0.036	0.038
12	$\pi(C^4O),\pi(C^2O),\sigma(Tacn)$	2	0.024	0.026	0.024	0.026	0.026	0.024	0.025	0.027
13	$\pi(C^4O),\pi(C^2O),\sigma(Tacn)$	2	0.047	0.047	0.047	0.050	0.046	0.049	0.044	0.048
14	$\sigma(C^4O),\sigma(C^2O),\sigma(Tacn)$	2	0.042	0.042	0.042	0.045	0.042	0.043	0.040	0.044
15	$\sigma(Tacn),\pi(Tacn),p(N_{Tacn})$	2	0.002	0.002	0.002	0.002	0.001	0.001	0.002	0.001
16	$\sigma(Tacn),\pi(Tacn),p(N_{Tacn})$	2	0.001	0.001	0.001	0.001	0.001	0.001	0.001	0.001
17	$\sigma(Tacn),\pi(Tacn),p(N_{Tacn})$	2	0.001	0.001	0.001	0.001	0.001	0.001	0.001	0.001
18	$\sigma(Tacn),\pi(Tacn),p(N_{Tacn})$	2	0.009	0.009	0.009	0.010	0.008	0.008	0.009	0.009
19	$\sigma(Tacn),\pi(Tacn),p(N_{Tacn}),p(Mo)$	2	0.015	0.017	0.014	0.016	0.013	0.021	0.016	0.015
20	$\sigma(Tacn),\pi(Tacn),p(N_{Tacn}),d(Mo)$	2	0.018	0.017	0.018	0.020	0.012	0.016	0.018	0.014
21	$\pi_1(d(Mo)+\pi^*(CO))$	2	0.859	0.828	0.854	0.862	0.220	0.346	0.844	0.240
22	$\pi_2(d(Mo)+\pi^*(CO))$	2	0.418	0.637	0.427	0.437	0.415	0.978	0.557	0.457
23	$\pi^*(NO),\pi_3(d(Mo)+\pi^*(CO))$	2	1.383	1.347	1.116	1.056	0.971	1.132	1.207	1.165
24	$\pi^*(NO),\pi_4(d(Mo)+\pi^*(CO))$	0	1.375	1.354	1.155	1.096	0.990	1.167	1.222	1.108
25	$d(Mo),s(Mo),p(C)$	0	0.349	0.999	0.356	0.357	0.231	0.352	1.197	0.262
26	$\pi^*(NO)$	0	0.800	0.755	0.287	0.694	0.282	0.287	0.256	0.794
27	$n(d(Mo)+\pi^*(C^4O)+\pi^*(C^2O))$	0	0.233	0.257	0.233	0.246	0.232	0.206	0.262	0.242
28	$\pi_1^*(d(Mo)-\pi^*(C^4O)-\pi^*(C^2O))$	0	0.286	0.423	0.289	0.296	0.276	0.217	0.451	0.279
29	$\pi_2^*(d(Mo)-\pi^*(C^4O)-\pi^*(C^2O))$	0	0.229	0.216	0.228	0.240	0.272	0.333	0.215	0.287
30	$\pi_3^*(d(Mo)-\pi^*(C^4O)-\pi^*(C^2O))$	0	0.350	0.372	0.351	0.358	0.314	0.303	0.378	0.322
31	$\pi_4^*(d(Mo)-\pi^*(C^4O)-\pi^*(C^2O))$	0	0.078	0.123	0.077	0.083	0.074	0.083	0.123	0.079
32	$f(Mo),pi^*(CO),p(Tacn)$	0	0.052	0.209	0.053	0.056	0.045	0.045	0.212	0.048
33	$f(Mo),pi^*(CO),p(Tacn)$	0	0.038	0.085	0.039	0.040	0.035	0.038	0.083	0.036

A. Appendices

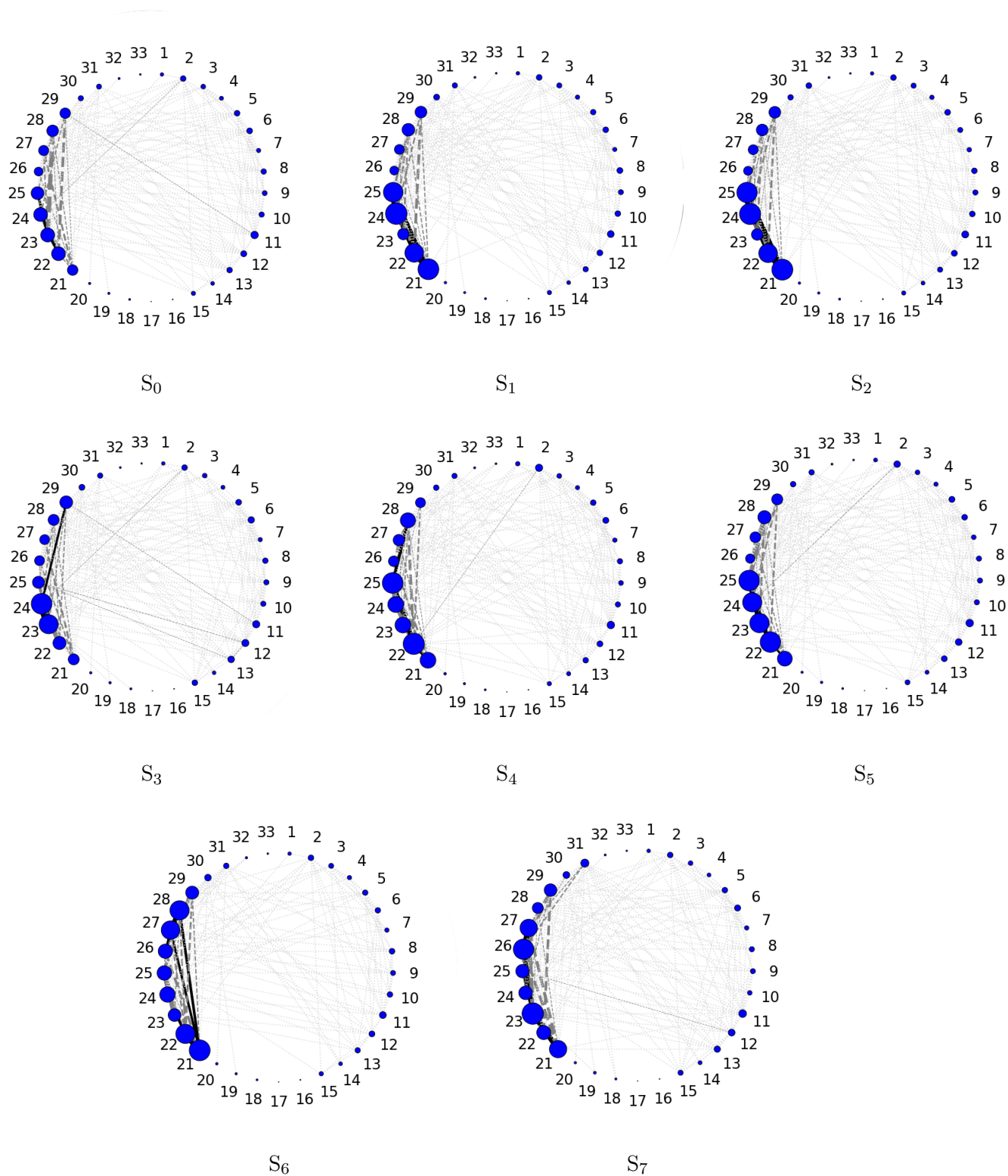


Figure A.11.: State-specific entanglement diagrams for **TacnMo** (DMRG[250](46,33)-SCF/ANO-RCC-MB gas phase).

A. Appendices

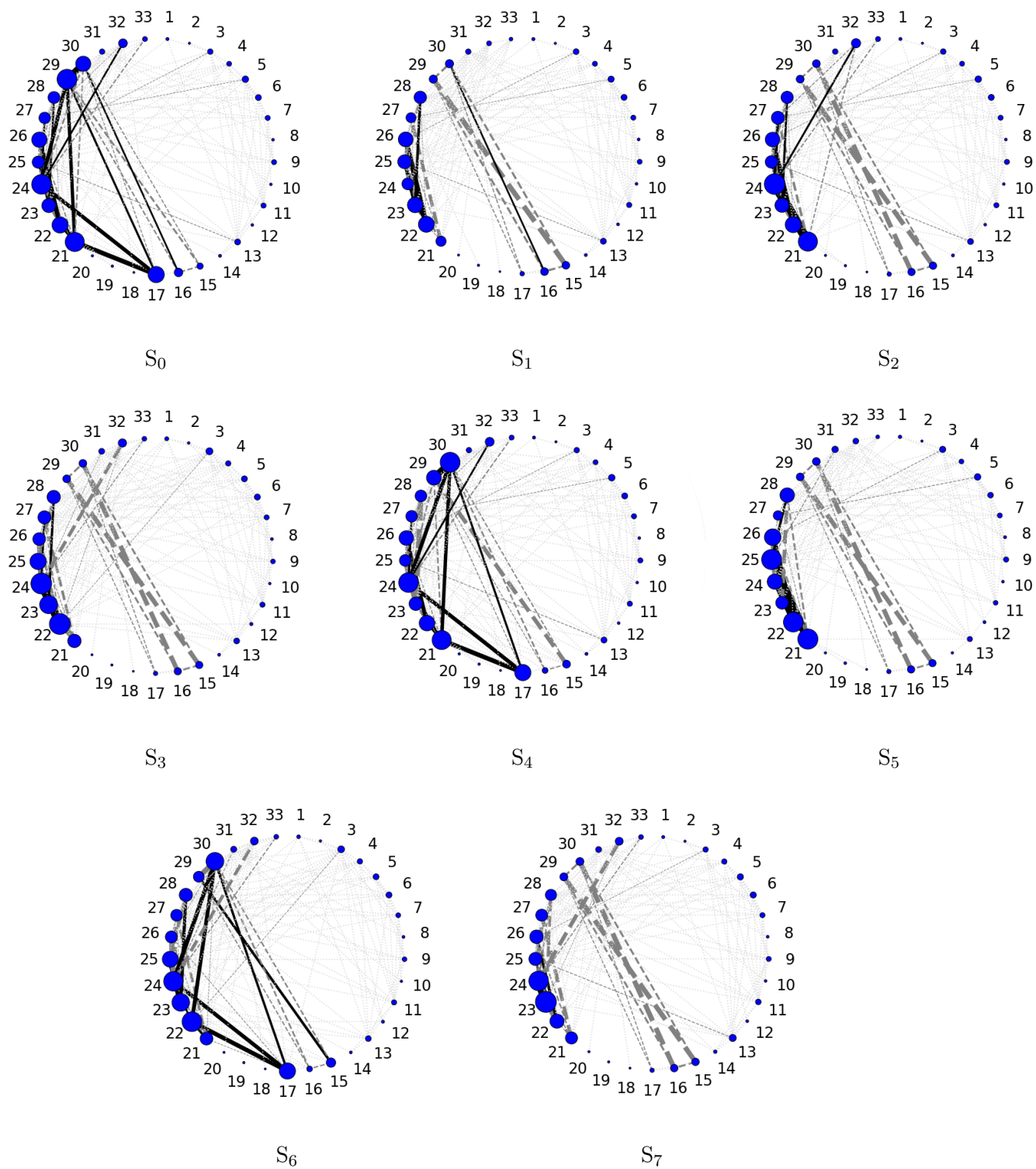


Figure A.12.: State-specific entanglement diagrams for **TacnMocoDiss** with a Mo-C bond length set to 10 Å (DMRG[250](46,33)-SCF/ANO-RCC-MB gas phase).

A. Appendices

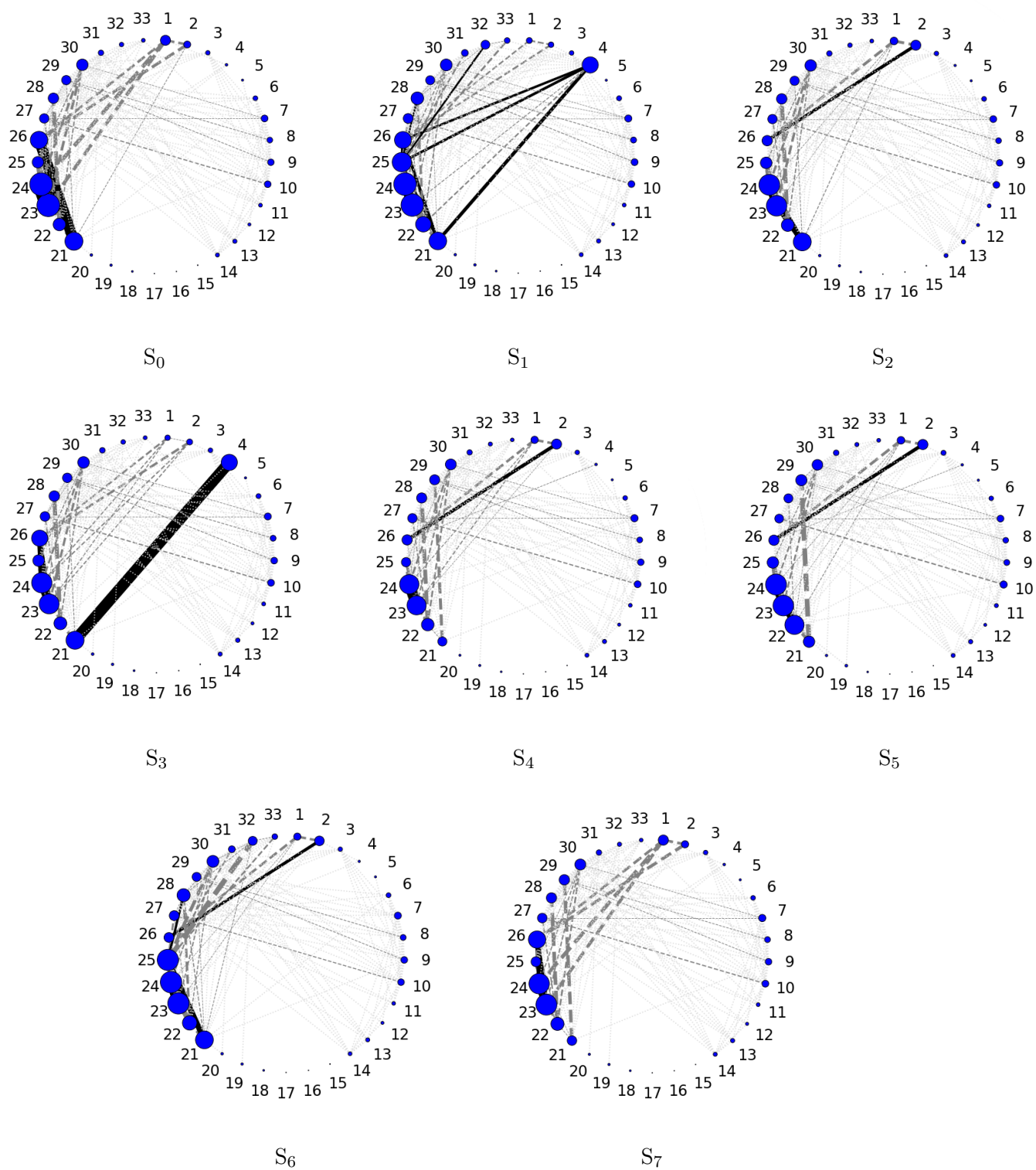


Figure A.13.: State-specific entanglement diagrams for **TacnMoNOdiss** with a Mo-N bond length set to 10 Å (DMRG[250](46,33)-SCF/ANO-RCC-MB gas phase).

A. Appendices

DabCo

Table A.14.: Orbital classification and their respective single orbital entropy values for each state of DabCo (DMRG[250](38,26)-SCF/ANO-RCC-MB gas phase, natural orbitals).

Orbital index	Classification	Occ.	$Z_{s(1)}$								
			S <sub>0</sub>	S <sub>1</sub>	S <sub>2</sub>	S <sub>3</sub>	S <sub>4</sub>	S <sub>5</sub>	S <sub>6</sub>	S <sub>7</sub>	
<b>Photosubstrate</b>											
1	$\sigma(\text{Dab}), \pi(\text{Dab})$	2	0.052	0.054	0.051	0.052	0.050	0.053	0.050	0.053	
2	$\pi(\text{CO})$	2	0.133	0.131	0.129	0.132	0.127	0.129	0.126	0.135	
3	$\pi(\text{CO})$	2	0.111	0.113	0.141	0.106	0.121	0.114	0.112	0.110	
4	$\sigma^*(\text{CO})$	2	0.085	0.123	0.082	0.080	0.078	0.108	0.072	0.077	
5	$\sigma(\text{Dab}), p(\text{Dab}), \sigma^*(\text{CO})$	2	0.053	0.045	0.048	0.051	0.048	0.049	0.047	0.049	
6	$\pi(\text{NO})$	2	0.097	0.112	0.137	0.125	0.142	0.129	0.171	0.088	
7	$\sigma^*(\text{CO}), d(\text{Co}), \sigma(\text{Dab})$	2	0.043	0.078	0.053	0.079	0.055	0.114	0.071	0.047	
8	$\sigma(\text{CO}), d(\text{Co}), \pi(\text{Dab})$	2	0.057	0.107	0.078	0.131	0.050	0.181	0.064	0.064	
9	$\pi(\text{Dab}), \sigma(\text{Dab})$	2	0.054	0.040	0.037	0.048	0.038	0.057	0.041	0.049	
10	$\pi(\text{NO})$	2	0.219	0.188	0.156	0.129	0.149	0.221	0.142	0.246	
11	$\pi(\text{NO}), \sigma(\text{Dab}), \pi(\text{Dab})$	2	0.067	0.060	0.054	0.045	0.050	0.067	0.048	0.071	
12	$\pi(\text{Dab}), \sigma(\text{Dab}), p(\text{O}), p(\text{Co})$	2	0.057	0.081	0.065	0.049	0.047	0.113	0.042	0.050	
13	$\pi(\text{Dab}), \sigma(\text{Dab}), d(\text{Co})$	2	0.064	0.198	0.110	0.092	0.156	0.092	0.117	0.106	
14	$n(d(\text{Co}) + \pi(\text{NO}))$	2	0.128	1.008	0.471	0.198	0.083	1.124	0.142	0.393	
15	$\pi_1(d(\text{Co}) + p(\text{N}_{\text{Dab}}))$	2	0.249	0.198	0.746	0.489	0.566	0.369	0.400	0.485	
16	$\pi_2(d(\text{Co}) + p(\text{N}_{\text{Dab}}))$	2	0.329	0.270	0.801	0.644	0.670	0.405	0.464	0.572	
17	$\pi_3(d(\text{Co}) + \pi^*(\text{NO}) + \pi^*(\text{CO}))$	2	0.604	0.951	0.428	0.743	0.652	0.903	0.663	0.781	
18	$\pi_4(d(\text{Co}) + p(\text{N}_{\text{Dab}})) + \sigma(\text{NO})$	2	0.757	0.931	0.883	1.215	0.858	0.684	0.922	1.083	
19	$\pi_5(d(\text{Co}) + \pi^*(\text{NO}))$	2	1.054	1.197	1.316	1.230	1.275	1.095	1.347	1.242	
20	$n(d(\text{Co}) + \pi(\text{Dab}))$	0	0.400	1.247	1.252	1.073	1.208	0.554	1.066	0.707	
21	$\pi_1^*(d(\text{Co}) - \pi^*(\text{CO}))$	0	0.473	0.314	0.323	0.553	0.380	0.592	0.388	0.873	
22	$\pi_2^*(d(\text{Co}) - \pi^*(\text{CO}))$	0	0.394	0.383	0.382	0.365	0.405	0.416	0.418	0.428	
23	$n(\pi_3^*(\text{Dab}) + d(\text{Co}) + \pi(\text{NO}))$	0	0.330	0.408	0.427	0.478	0.474	0.464	0.501	0.332	
24	$\pi_3^*(\pi^*(\text{NO}) + d(\text{Co}) + \pi^*(\text{Dab}))$	0	0.909	1.057	1.103	1.178	1.170	0.950	1.248	0.899	
25	$\pi_4^*(\pi^*(\text{NO}) + d(\text{Co}))$	0	1.023	1.137	1.123	1.158	0.924	1.368	0.899	1.344	
26	$f(\text{Co}), p(\text{N}_{\text{Dab}}), p(\text{C}_{\text{Dab}})$	0	0.214	0.253	0.248	0.249	0.187	0.418	0.184	0.323	
<b>Dissociation CO</b>											
1	$\pi(\text{CO})$	2	0.098	0.283	0.174	0.254	0.097	1.113	0.135	0.271	
2	$\pi(\text{CO})$	2	0.286	0.089	0.256	0.171	0.285	0.879	0.236	0.124	
3	$\sigma(\text{Dab})$	2	0.014	0.014	0.013	0.013	0.013	0.013	0.013	0.017	
4	$\sigma(\text{Dab})$	2	0.016	0.016	0.012	0.012	0.016	0.015	0.012	0.012	
5	$\pi(\text{NO})$	2	0.134	0.135	0.040	0.040	0.139	0.133	0.077	0.042	
6	$\sigma(\text{Dab}), \pi(\text{Dab})$	2	0.031	0.031	0.020	0.020	0.031	0.031	0.022	0.021	
7	$\sigma(\text{Dab}), \pi(\text{Dab}), \sigma(\text{NO})$	2	0.011	0.011	0.014	0.013	0.012	0.011	0.012	0.014	
8	$\sigma(\text{NO})$	2	0.018	0.018	0.031	0.030	0.025	0.018	0.022	0.044	
9	$\sigma^*(\text{CO})$	2	0.693	0.693	0.693	0.693	0.693	0.047	0.693	0.693	
10	$n(d(\text{Co}) + \pi(\text{NO}), \sigma(\text{Dab}))$	2	0.134	0.135	0.150	0.152	0.107	0.135	0.137	0.227	
11	$n(d(\text{Co}) + \pi(\text{NO}), \sigma(\text{Dab}))$	2	0.102	0.102	0.121	0.121	0.079	0.102	0.110	0.176	
12	$\pi(\text{NO}), \sigma(\text{Dab}), \pi(\text{Dab})$	2	0.051	0.051	0.081	0.081	0.049	0.051	0.071	0.086	
13	$\pi_1(d(\text{Co}) + p(\text{N}_{\text{Dab}})), \sigma(\text{Dab})$	2	0.027	0.028	0.028	0.028	0.027	0.027	0.058	0.029	
14	$n(d(\text{Co}) + \pi(\text{Dab}))$	2	0.169	0.169	0.134	0.131	0.134	0.167	0.355	0.135	
15	$n(d(\text{Co}) + \pi(\text{NO}))$	2	0.106	0.106	0.203	0.207	0.090	0.104	0.059	0.069	
16	$n(d(\text{Co}) + \pi(\text{Dab}))$	2	0.287	0.292	0.091	0.091	0.180	0.300	1.107	0.118	
17	$d(\text{Co}), d(\text{ONO})$	2	0.779	0.780	0.545	0.599	0.552	0.779	0.536	1.073	
18	$n(d(\text{Co}) + \pi(\text{Dab}))$	2	0.400	0.401	1.094	1.111	1.037	0.399	0.464	0.727	
19	$\pi_2(d(\text{Co}) + \pi^*(\text{NO}))$	2	0.942	0.945	0.336	0.334	0.898	0.951	0.729	0.328	
20	$\pi(d(\text{Co}) + \pi(\text{Dab}))$	0	1.245	1.245	0.897	0.901	1.302	1.241	1.050	1.036	
21	$\pi^*(\text{CO})$	0	0.897	0.414	1.122	0.801	0.768	1.090	1.064	0.811	
22	$\pi^*(\text{CO})$	0	0.416	0.891	0.802	1.121	0.293	0.784	0.679	1.123	
23	$\pi_3(d(\text{Co}) + \pi^*(\text{NO}))$	0	0.995	0.994	0.388	0.385	1.161	0.987	0.645	0.467	

Continued on next page

## A. Appendices

Table A.14 – *Continued from previous page*

Orbital index	Classification	Occ.	$Z_{s(1)}$							
			S <sub>0</sub>	S <sub>1</sub>	S <sub>2</sub>	S <sub>3</sub>	S <sub>4</sub>	S <sub>5</sub>	S <sub>6</sub>	S <sub>7</sub>
24	$\pi^*(\text{Dab})$	0	0.129	0.129	0.146	0.145	0.143	0.125	0.133	0.136
25	$n(f(\text{Co})+\pi^*(\text{NO}))$	0	0.647	0.646	0.295	0.294	0.798	0.645	0.427	0.324
26	$n(f(\text{Co})+\pi^*(\text{NO}))$	0	0.188	0.190	0.338	0.340	0.179	0.189	0.375	0.326
<b>Dissociation NO</b>										
1	$\pi(\text{CO})$	2	0.145	0.140	0.156	0.125	0.161	0.128	0.163	0.158
2	$\pi(\text{CO})$	2	0.147	0.143	0.125	0.162	0.130	0.160	0.122	0.122
3	$\sigma(\text{CO}),\sigma(\text{Dab})$	2	0.049	0.047	0.070	0.065	0.071	0.064	0.056	0.059
4	$\pi(\text{CO}),\sigma(\text{Dab})$	2	0.054	0.052	0.056	0.066	0.057	0.065	0.047	0.047
5	$\sigma(\text{Dab}),\pi(\text{Dab})$	2	0.046	0.043	0.055	0.051	0.056	0.050	0.048	0.047
6	$\pi(\text{NO})$	2	0.273	0.144	0.133	0.149	0.265	0.268	0.145	0.141
7	$\sigma(\text{Dab}),\pi(\text{Dab})$	2	0.015	0.014	0.014	0.014	0.014	0.014	0.014	0.013
8	$\sigma(\text{Dab}),\pi(\text{Dab})$	2	0.009	0.009	0.009	0.009	0.009	0.009	0.008	0.009
9	$\sigma(\text{Dab}),\pi(\text{Dab})$	2	0.009	0.008	0.008	0.009	0.009	0.009	0.009	0.008
10	$\sigma(\text{Dab}),\pi_1(\pi(\text{Dab})+p(\text{Co}))$	2	0.037	0.035	0.055	0.055	0.056	0.055	0.043	0.043
11	$\pi_2(\pi(\text{Dab})+p(\text{Co}))$	2	0.039	0.038	0.034	0.043	0.037	0.043	0.039	0.038
12	$\pi_3(\pi(\text{Dab})+d(\text{Co}))$	2	0.035	0.034	0.086	0.079	0.081	0.077	0.120	0.128
13	$\pi(\text{NO})$	2	0.134	0.279	0.270	0.291	0.130	0.133	0.274	0.265
14	$\sigma(\text{NO})$	2	0.018	0.017	0.017	0.017	0.018	0.018	0.016	0.015
15	$n(\pi(\text{Dab})+d(\text{Co}))$	2	0.187	0.175	0.140	0.143	0.151	0.145	0.139	0.128
16	$\pi_4(\pi(\text{Dab})+d(\text{Co}))$	2	0.223	0.215	0.333	0.171	0.348	0.185	0.564	0.562
17	$\pi_1^*(\pi(\text{Dab})-d(\text{Co}))$	2	0.271	0.261	0.341	0.246	0.352	0.253	0.477	0.510
18	$\pi_5(d(\text{Co})+\pi^*(\text{CO}))$	2	0.455	0.447	1.151	1.086	1.143	1.118	1.147	1.181
19	$\pi(\text{NO}),\pi(\text{Dab})$	2	0.978	1.158	1.048	1.197	0.794	1.058	1.347	1.380
20	$\pi(\text{NO}),\pi(\text{Dab})$	0	1.194	1.154	1.150	1.330	1.076	1.361	1.363	1.374
21	$\pi_6(d(\text{Co})+\pi^*(\text{CO}))$	0	0.522	0.513	0.609	1.196	0.641	1.202	0.621	0.667
22	$\pi_2^*(d(\text{Co})+\pi^*(\text{CO}))$	0	0.393	0.373	1.126	0.469	1.125	0.499	1.183	1.180
23	$\pi_3^*(d(\text{Co})+\pi^*(\text{CO}))$	0	0.230	0.215	0.200	0.223	0.213	0.229	0.225	0.229
24	$\pi^*(\text{Dab})$	0	0.158	0.151	0.160	0.154	0.166	0.152	0.149	0.152
25	$\pi(\text{NO})$	0	0.792	0.289	0.281	0.301	0.789	0.791	0.291	0.274
26	$\pi_4^*(d(\text{Co})+\pi^*(\text{CO}))$	0	0.127	0.116	1.003	0.105	1.006	0.123	0.871	0.799

A. Appendices

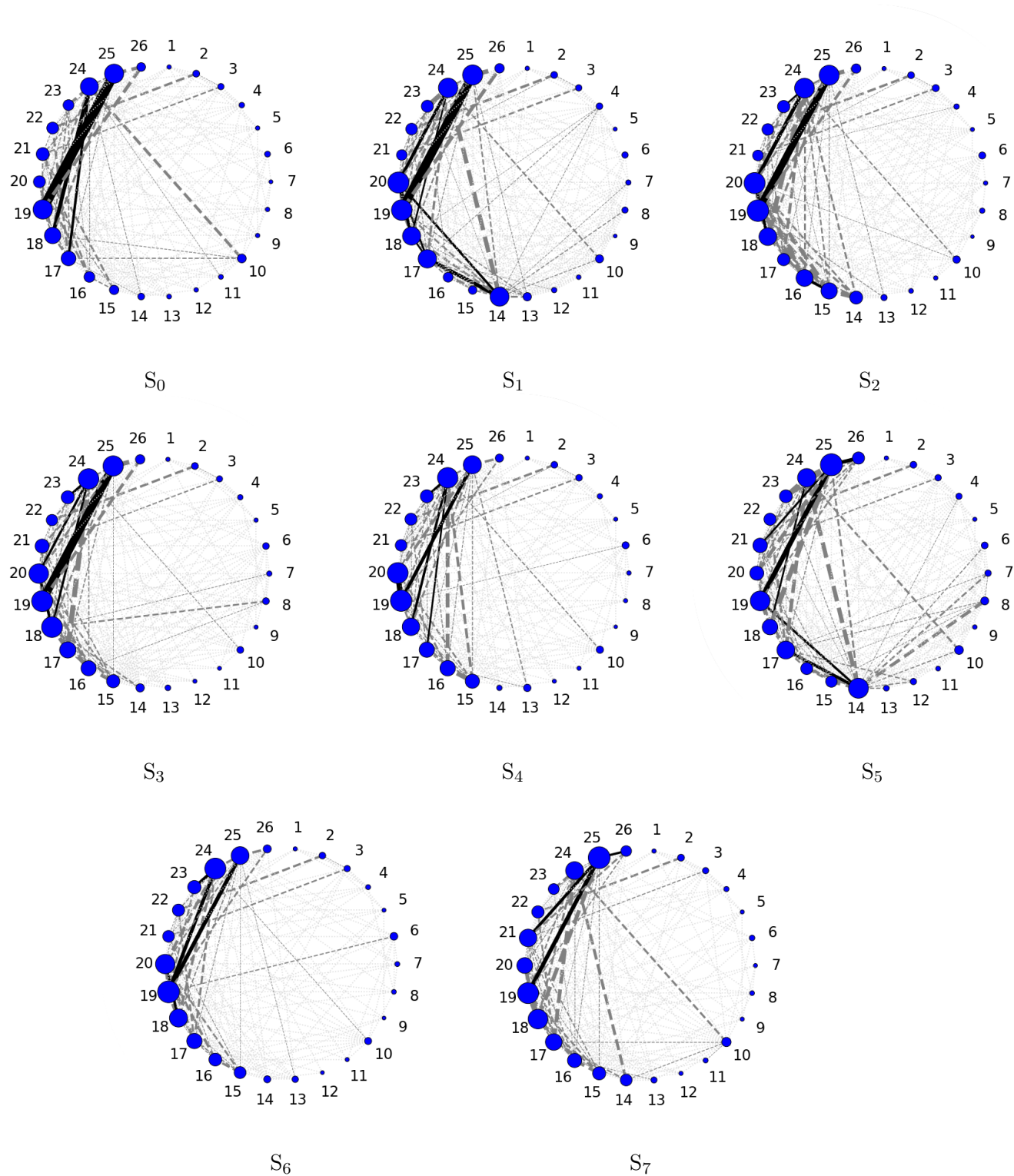


Figure A.14.: State-specific entanglement diagrams for **DabCo** (DMRG[250](38,26)-SCF/ANO-RCC-MB gas phase).

A. Appendices

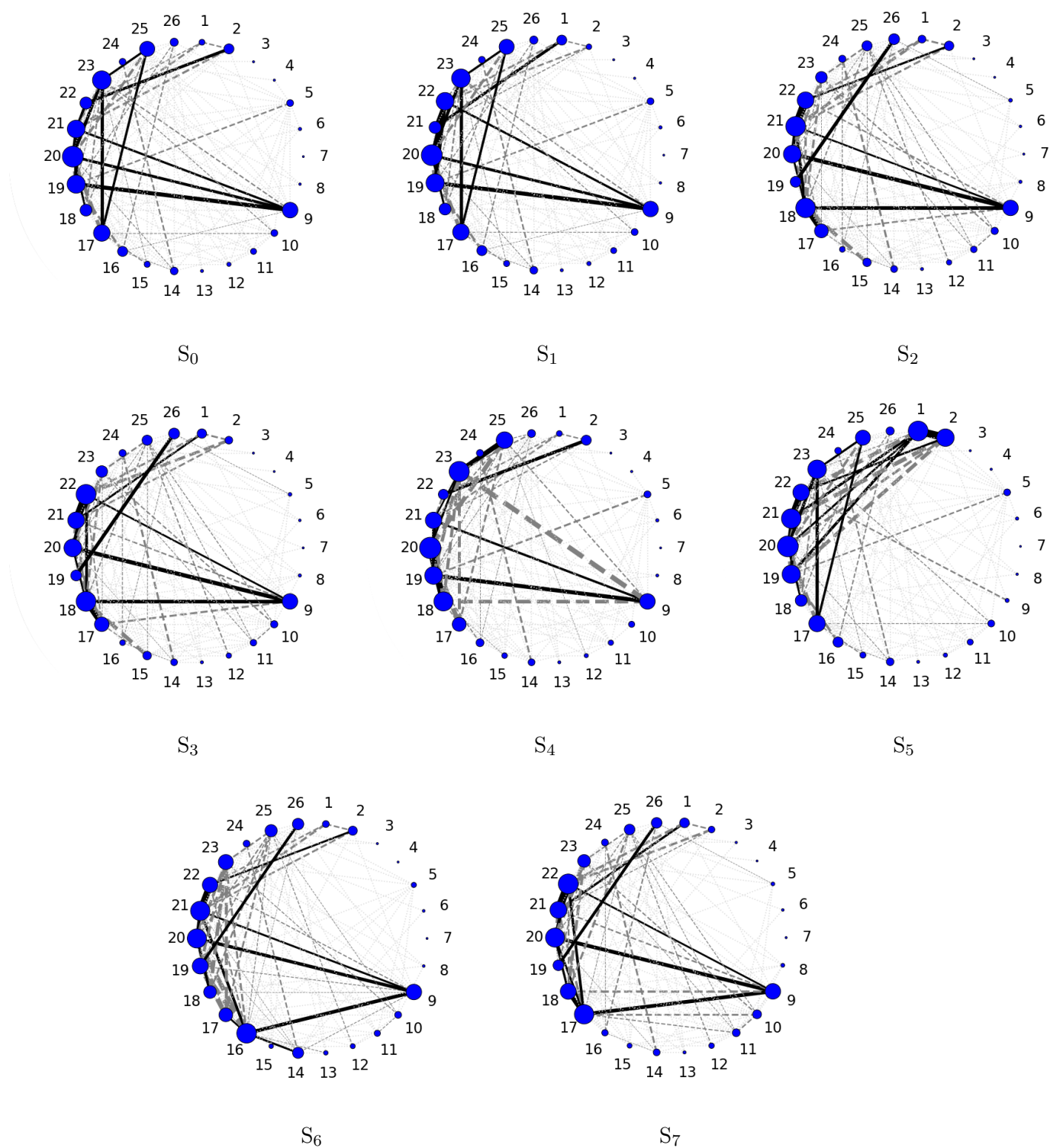


Figure A.15.: State-specific entanglement diagrams for **DabCocodiss** with a Mo-C bond length set to 10 Å (DMRG[250](38,26)-SCF/ANO-RCC-MB gas phase).

A. Appendices

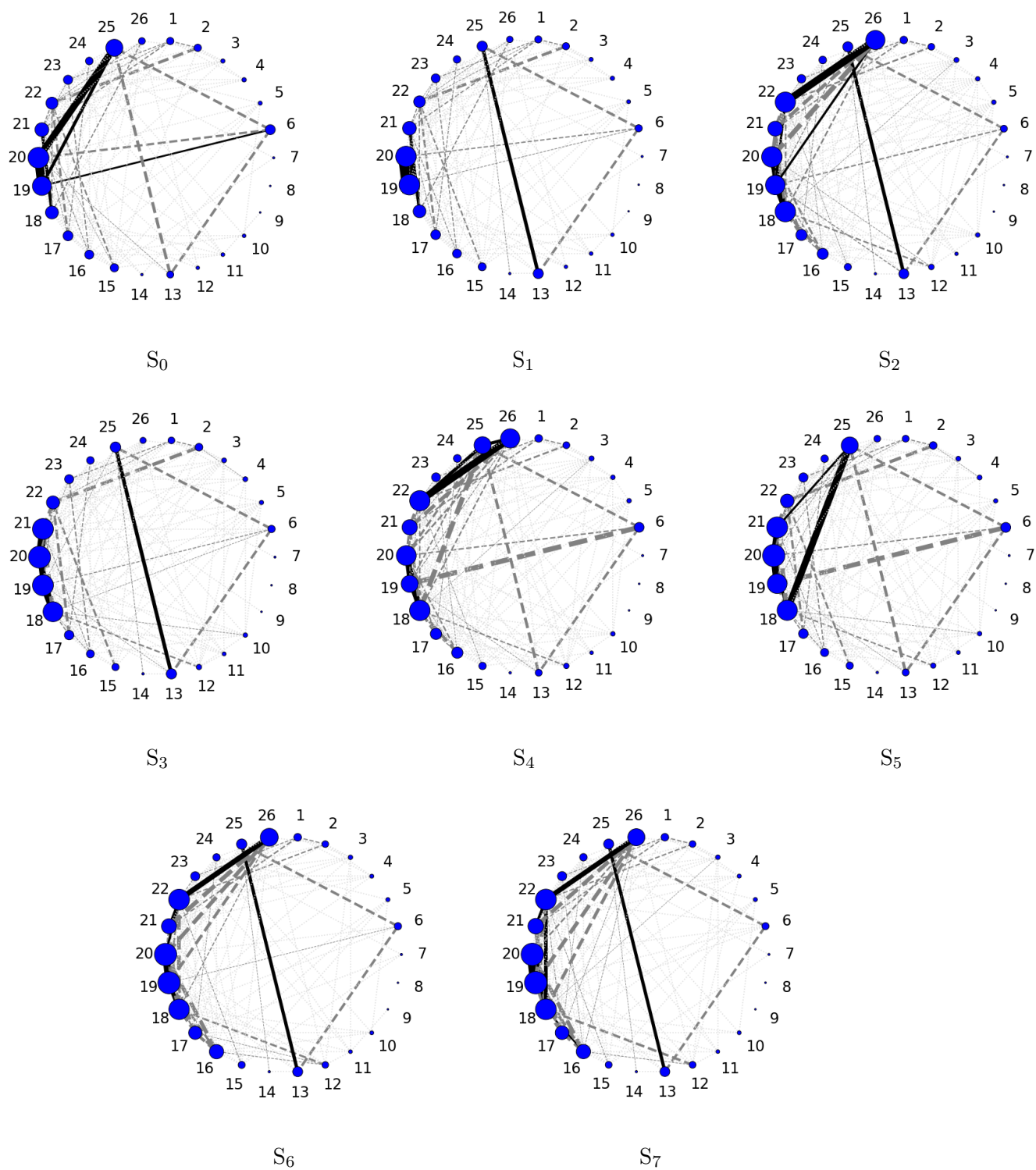


Figure A.16.: State-specific entanglement diagrams for **DabCONodiss** with a Mo-N bond length set to 10 Å (DMRG[250](38,26)-SCF/ANO-RCC-MB gas phase).

## Appendix A6: Potential Energy Scans CpMo Including Triplet States

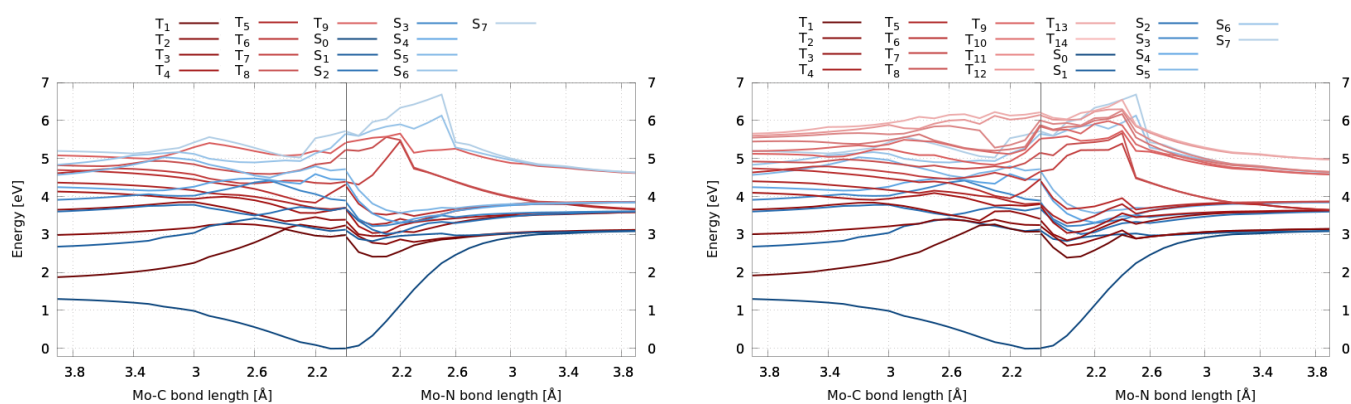


Figure A.17.: 1D-Potential energy scans along the Mo-C<sub>CO</sub> and Mo-N<sub>NO</sub> bond dissociation including 8 singlet states and 9 triplet states (*left*) and 8 singlet states and 14 triplet states (*right*). (CASSCF(6,10)/ANO-RCC-VDZP gas phase).

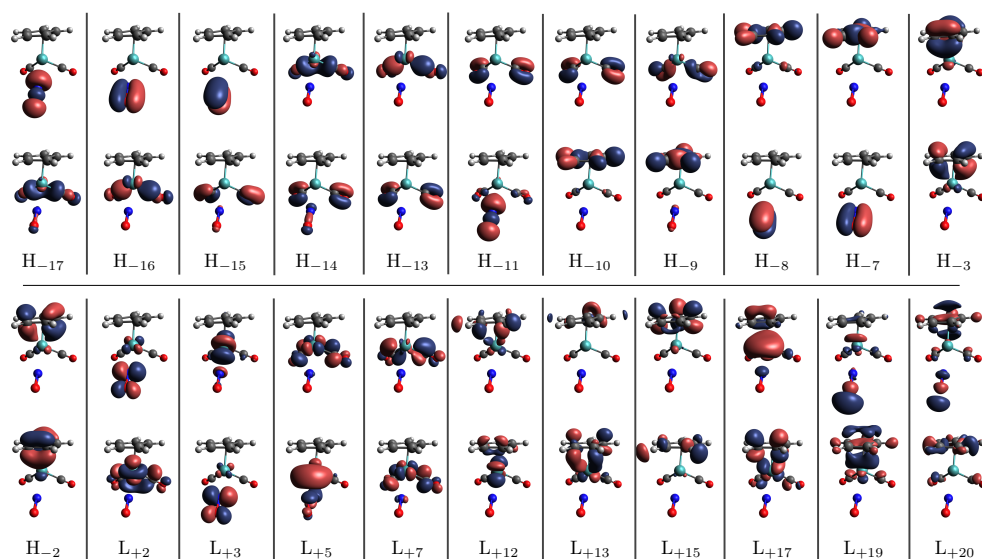


Figure A.18.: Comprehensive comparison of the state-averaged orbital set used for the computation of 8 singlet states and 9 triplet states (*upper row*) and 8 singlet states and 14 triplet states (*bottom row*) at Mo-N<sub>NO</sub> bond length of 2.4 Å (CASSCF(6,10)/ANO-RCC-VDZP gas phase, natural orbitals).

## Appendix A7: SOC Component Comparison of CpMo

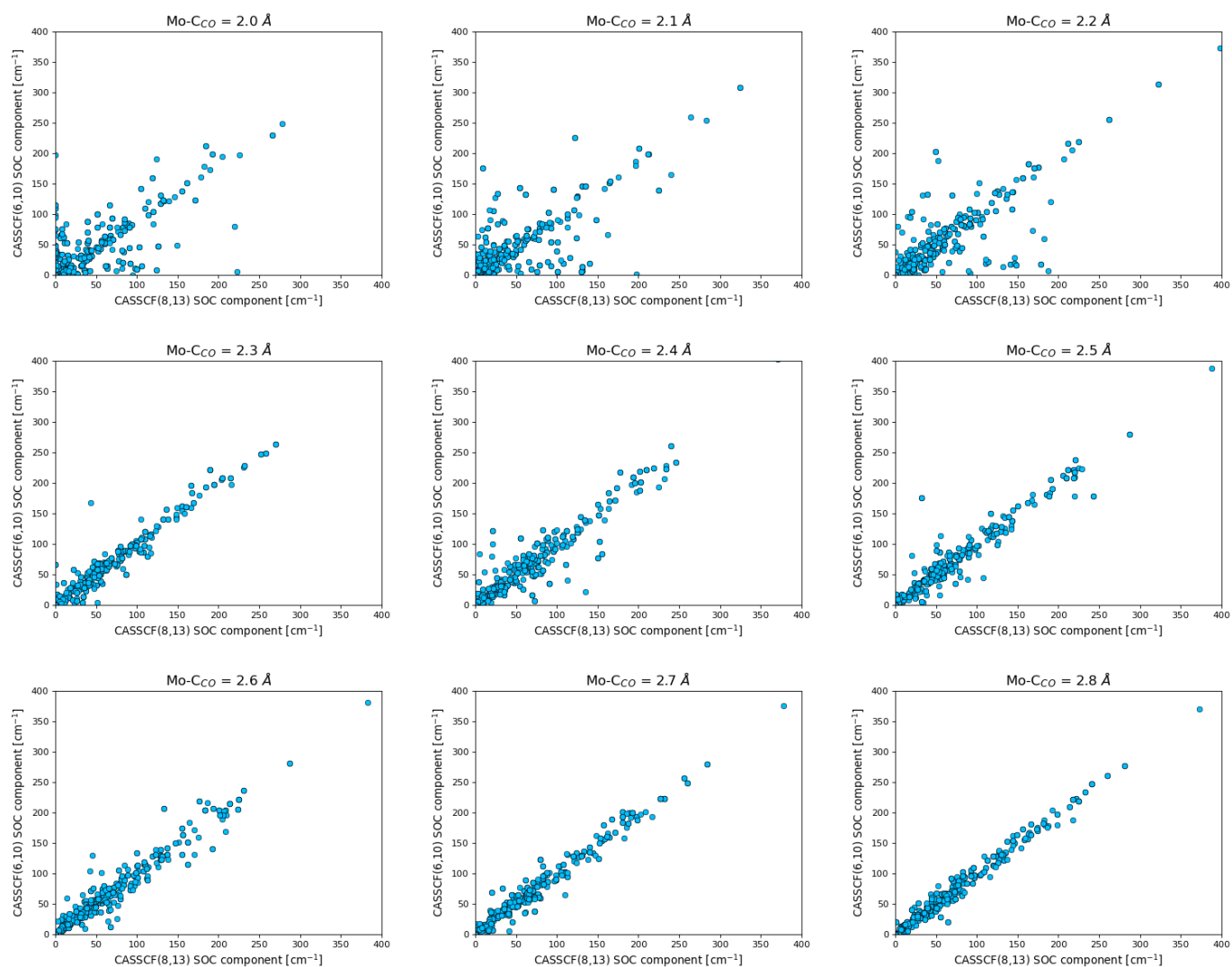


Figure A.19.: SOC component comparison for the CO-dissociation of **CpMo** computed on CASSCF(6,10) and CASSCF(8,13) level of theory (*part I*).

## A. Appendices

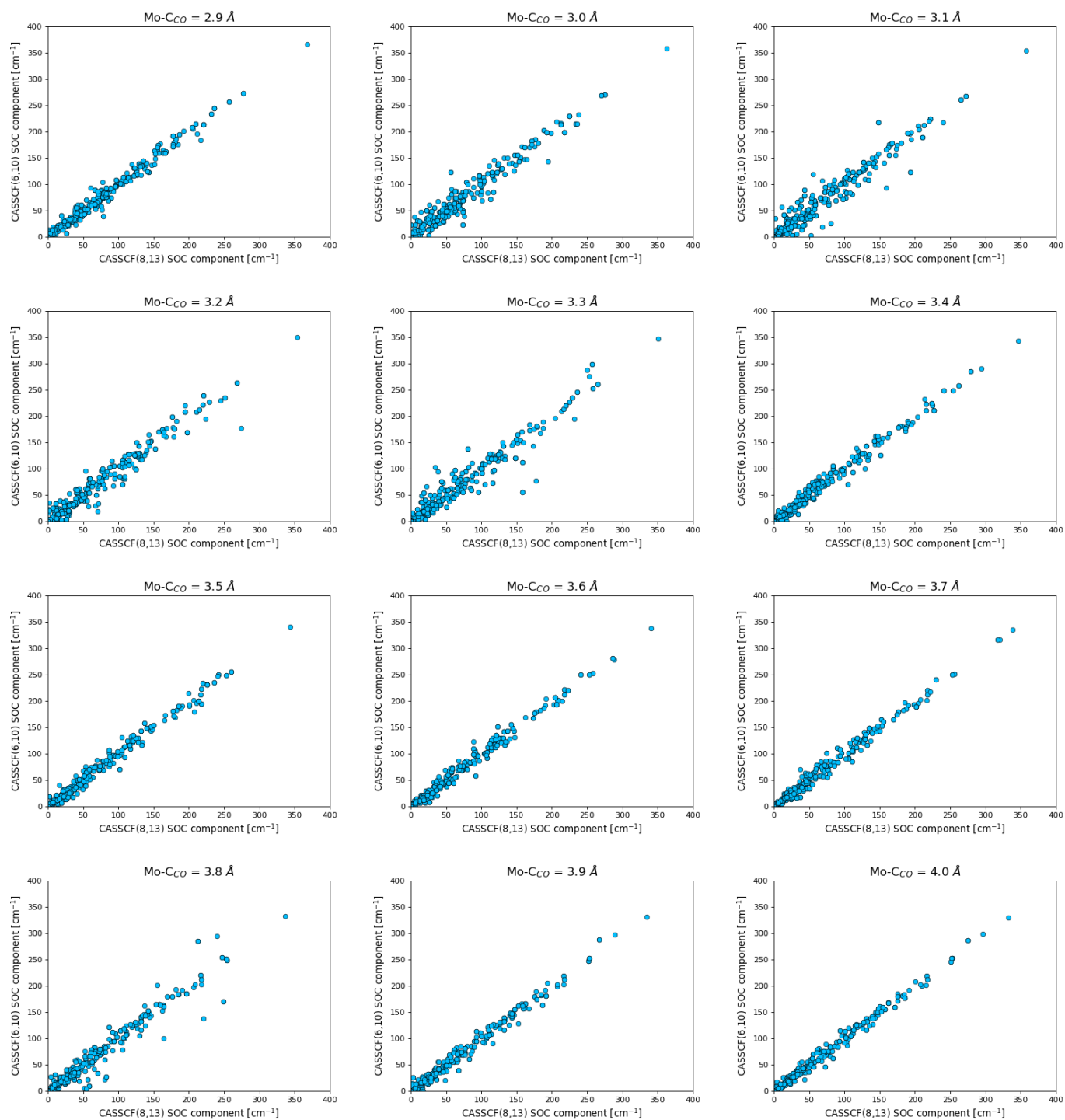


Figure A.20.: SOC component comparison for the CO-dissociation of  $\text{CpMo}$  computed on CASSCF(6,10) and CASSCF(8,13) level of theory (*part II*).

## A. Appendices

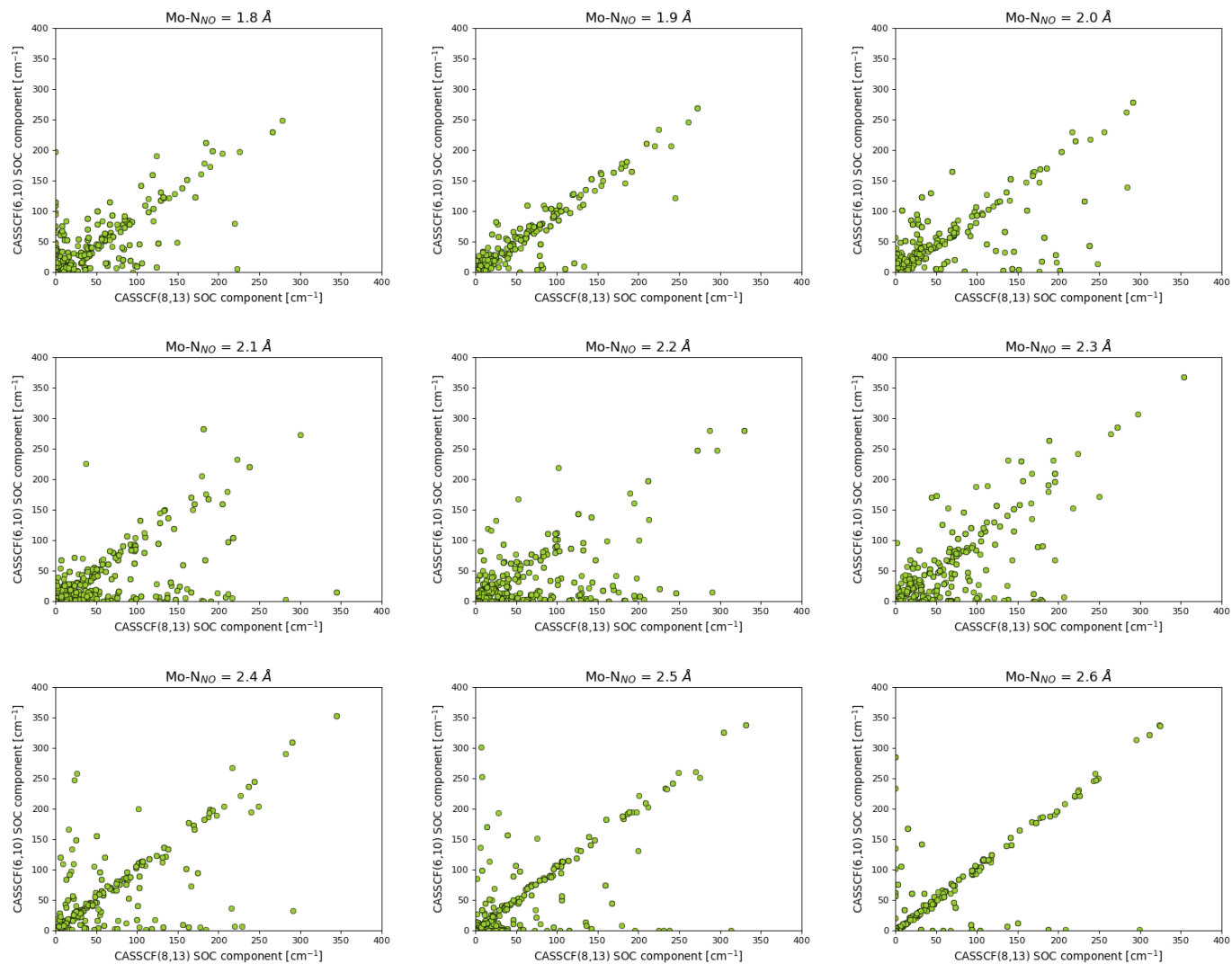


Figure A.21.: SOC component comparison for the NO-dissociation of **CpMo** computed on CASSCF(6,10) and CASSCF(8,13) level of theory (*part I*).

## A. Appendices

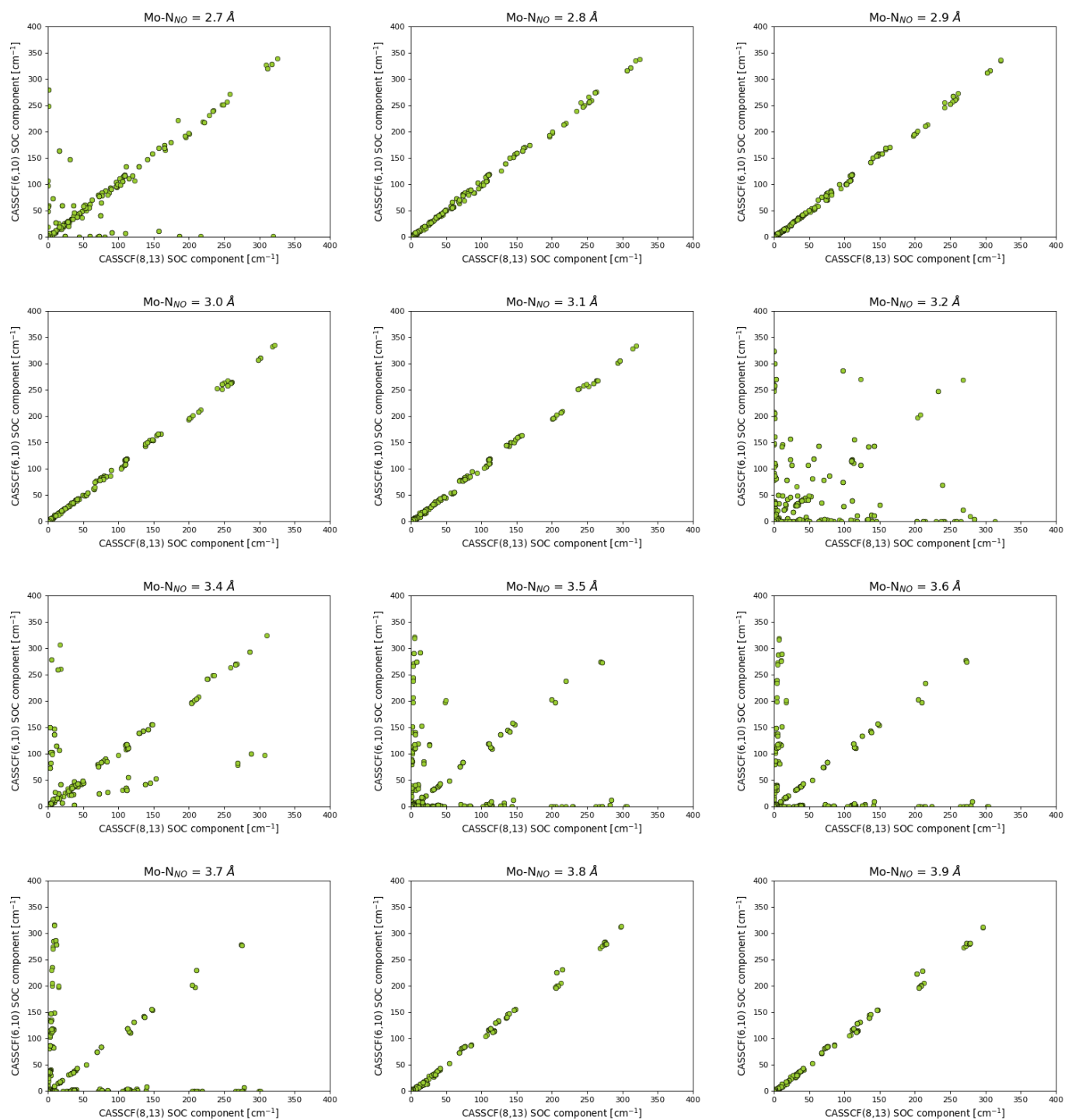


Figure A.22.: SOC component comparison for the NO-dissociation of CpMo computed on CASSCF(6,10) and CASSCF(8,13) level of theory (*part II*).

## Appendix A8: Add-on to DabCo

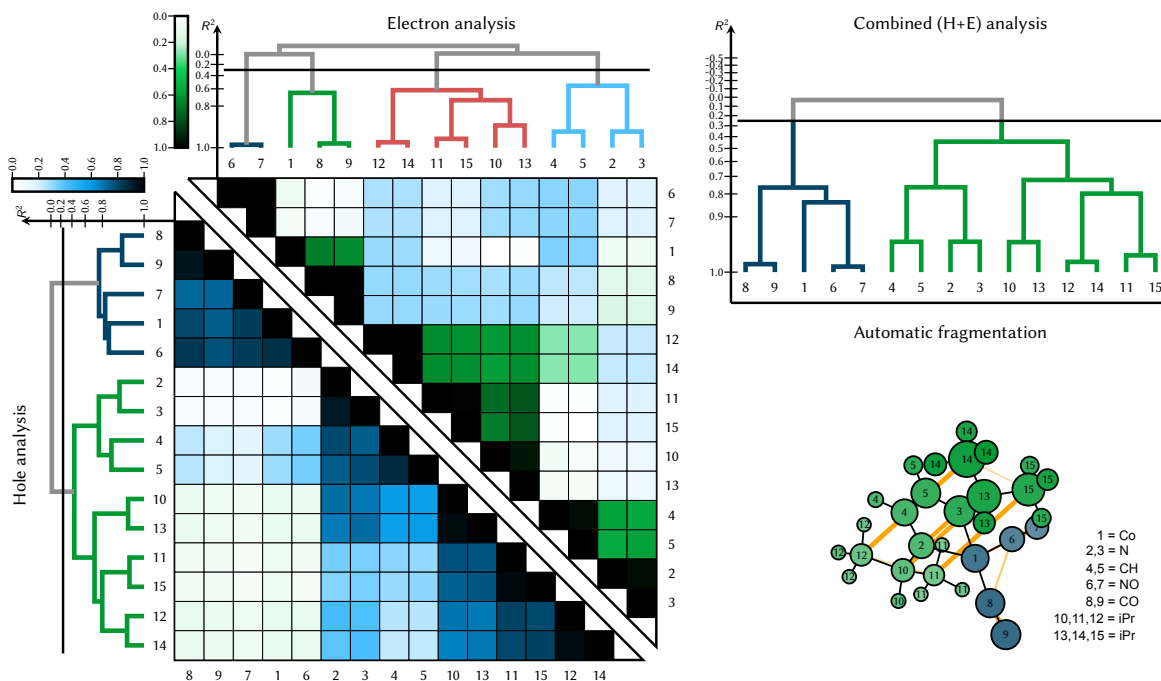


Figure A.23.: Hierarchical clustering analysis of **DabCo** with (*left*) the correlation matrices of the excitation hole (*lower left triangular matrix*) and the excited electron (*upper left triangular matrix*) with the respective dendrograms showing the clustering scheme to each correlation matrix and (*right*) the combined dendrogram with the threshold of 0.45 as indicated by the black vertical line, as well as the to this threshold corresponding clustering scheme depicted on the molecular geometry (TD-DFT B3LYP-D3(BJ)/def2-SVP implicit toluene).